Providing current forecasts for the 2012 Olympic Sailing Competition

by means of a finite element based numerical flow model

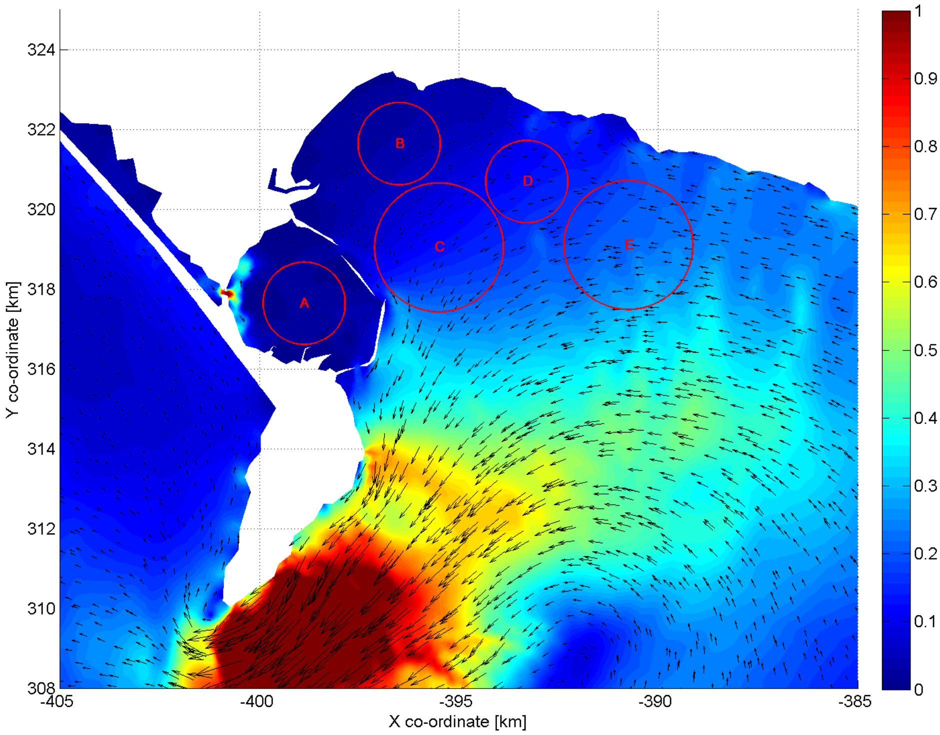

S.E. Poortman

March 16, 2011

Svašek Hydraulics

Delft University of Technology
Faculty of Civil Engineering
Section of Fluid Mechanics

MSc Thesis
Delft University of Technology

Providing current forecasts for the 2012 Olympic Sailing Competition

by means of a finite element based numerical flow model

Sanne E. Poortman
March 16, 2011

Supervising committee:
Prof.dr.ir. G.S. Stelling
Dr.ir. R.J. Labeur
Dr.ir. J.A. Keuning
Ir. M.J.G. van den Boomgaard

Abstract

The Olympic Summer Games of 2012 will be held in London and surroundings, United Kingdom. In the sailing category, the Netherlands will be represented by the Dutch Olympic Sailing Team. To increase the knowledge of the prevaling currents in the Olympic sailing area, which are especially of importance when there is little wind, the Dutch Olympic Sailing Team wants to use specific current forecasts. By adjusting their strategy to the current forecasts, the current forecasts will assist the Dutch Sailing Team to achieve the optimal performance during the 2012 Olympic Sailing Competition.

This project therefore focuses on studying and modelling the flow in the sailing area of the 2012 Olympic Sailing Competition, located partly in the Portland Harbour and partly in Weymouth Bay, in order to generate accurate and reliable current forecasts in the Olympic sailing area during the 2012 Olympic Sailing Competition by means of a numerical flow model. The area of interest is known for its tidal eddies and large flow velocities around Portland Bill, and together with a strongly fluctuating bathymetry, the current pattern can be very complex.

In order to provide current forecasts, it is important to have knowledge of the physical processes which induce currents in the area considered. Therefore, the several current–inducing processes have been discussed during a literature study. From this literature study follows that the main flow in the sailing area is the tidal flow, which is the driving force behind the tidal eddies, which have flow velocities of the same order of magnitude. The tidal flow normally has a logarithmic vertical velocity distribution.Therefore, the tidal flow can well be modelled by means of depth–averaged models, which assumes a logarithmic velocity profile. The flow velocities corresponding to other current–inducing processes are one or two orders of magnitude smaller than the order of magnitude of the flow velocities corresponding to the tidal flow, by which the currents induced by most of these processes are negligible. The wind– and wave–induced currents however, may amount up to several percent of the wind speed, and may therefore have a significant influence on the flow in the area.

In order to further increase the knowledge of (the flow in) the area of interest, bathymetric, water level, current, wind and wave data has been gathered. Sufficient sources which provide reliable bathymetric and water level data are available. For both wind and wave data, several sources are available as well. The accuracy of the data is however questionable, although the data does give a good impression of the wind and wave conditions. The available current data however, originates from the late seventies and early eighties, is considered outdated. Since the objective is provide current forecasts, information on the current is of vital importance. Therefore, sailed current measurements have been performed in the area of interest. The current measurements have shown that the tide in the area of interest is ebb dominated, and that the vertical velocity distribution is nearly logarithmic. According to the survey results it is therefore justified to model the flow by means of a depth–averaged model.

To provide for current forecasts, the two–dimensional depth–averaged numerical flow model FINEL2D, which has the finite element method (FEM) as numerical basis, has been used. FINEL2D has adopted the discontinuous Galerkin method to solve the shallow water equations, complemented by a Riemann solver according to Roe to account for the fluxes trough the element boundaries. A disadvantage of the Roe solver is the production of numerical diffusion; it is however demonstrated that this diffusivity plays a minor role.

FINEL2D is applied to the so–called European Continental Shelf Model (ECSM), which model domain is fairly large and covers most of the north–west European continental shelf. The TPXO model is used to enforce boundary conditions on the model. This model provides water level data, based on TOPEX/Poseidon satellite data, in the form of the amplitude and phase of 13 harmonic constituents, at every 0.5 degree.

During the calibration process, several different values of the Nikuradse bottom roughness have been applied to the model in order to investigate which value of the bottom roughness leads to model results which deviate least from the measured flow velocities and directions. It appeared a Nikuradse roughness of 0.035 m is best. However, a phase shift was still visible in the model results. Therefore, the bottom roughness has been adjusted locally as well. The bottom roughness around Portland Bill, where the subsoil is rocky, and the bottom roughness at the Shambles Bank, where large sand dunes are existing, have been increased to 0.25 m. The model results have been improved by this adjustment.

During the literature study it is concluded that wind and waves may have a significant influence on the flow in the area of interest; the influence of wind and waves is therefore investigated. For waves, the influence appears to be limited to the breaker zone, which is located outside the racing areas. The influence of waves on the flow can therefore be considered negligible. Wind however does have a significant influence on the flow in the racing area, and induces, depending on the wind direction, gyres in the racing area or a strong current along the coast. The strength of the wind–induced current and the size of the flow features are sensitive to the wind speed and wind direction. The shape of the flow features is sensitive to the phase of the tide; the strength of wind–induced current however not. The water levels at Weymouth therefore have a negligible influence on the locally generated gyres.

Since the influence of wind on the flow is large, it has been investigated if it is possible to account for the wind–induced current in the current forecasts. A way to account for the wind–induced current is by linking the numerical flow model to wind predictions, or by composing several wind scenarios which are calculated before the start of the 2012 Olympic Sailing Competition. Each competition day, the scenario which corresponds best to the current wind conditions is taken. Since it is difficult to obtain accurate and reliable wind predictions, uncertainties are present in the wind data and in turn, uncertainties arise in the model results. Besides, no flow velocities have been measured in the sailing area during wind, by which it is difficult to calibrate the model for the wind.Due to the above mentioned limitations, it is difficult to provide reliable and accurate forecasts of the wind–induced current.

In conclusion it can be stated that the flow in the sailing area of the 2012 Olympic Sailing Competition can be modelled well by means of the two–dimensional depth–averaged numerical flow model FINEL2D. The model results correspond well to the during the survey measured flow velocities and flow directions. Accounting for the wind in the current forecasts is however difficult.

Acknowledgements

This thesis is the result of the Hydraulic Engineering Master of Science program at the faculty of Civil Engineering and Geosciences at Delft University of Technology, The Netherlands. This study has been carried out under the guidance of the section of Environmental Fluid Mechanics in cooperation with Svašek Hydraulics.

I would like to thank Gerard Dam, who automatically took over the supervision at Svašek Hydraulics during the maternity leave of Marloes, for his help and guidance during the survey and the FINEL2D calculations, and for reading my draft report so carefully. I would like to thank Marloes van den Boomgaard, my supervisor at Svašek Hydraulics, for her enthusiasm and introducing me to the subject, and Robert Jan Labeur, my supervisor at Delft University of Technology, for his critical view. Furthermore, I would like to thank the other members of my committee and all employees of Svašek Hydraulics for their help and support, and Frans Winterswijk, for sailing me across the North Sea and the English Channel. Finally, I would like to thank my family and friends, who have been supporting me during not only during this study, but during my entire education at Delft University of Technology.

Sanne Poortman
March 16, 2011

Contents

Chapter 1

General

1.1 Introduction

The Olympic Summer Games of 2012 will be held in London and surroundings, United Kingdom. The Olympic Games 2012 will feature a total of 26 sports, among which sailing, which will feature ten classes. The Dutch Olympic Sailing Team will represent The Netherlands in several of these classes.

To increase the knowledge of the prevailing currents in the Olympic sailing area, which are especially of importance when there is little wind, the Dutch Olympic Sailing Team will use specific current forecasts. By adjusting their strategy to the current forecasts, the current forecasts will assist the Dutch Sailing Team to achieve the optimal performance during the Olympic Games 2012.

During the Olympic Summer Games of 2008, in Qingdao, China, the Dutch Olympic Sailing Team, which has won two silver medals, made use of current forecasts as well. These current forecasts, supplied by Svašek Hydraulics, have been obtained by using the by Svašek Hydraulics in–house developed two–dimensional depth–averaged numerical flow model FINEL2D, which is based on the finite element method. Since the Dutch Olympic Sailing Team was pleased with the current forecasts, the team has asked Svašek Hydraulics to provide the current forecasts during the Olympic Games 2012 again.

1.2 Area of interest

The area of interest is the sailing area of the 2012 Olympic Sailing Competition, which is located on the south coast of England, near Weymouth and Portland, as shown in figure 1.1. The area is known for its tidal eddies and large flow velocities around Portland Bill, and together with a strongly fluctuating bathymetry, the current pattern can be very complex.

Since the flow velocity of the tidal flow has the same order of magnitude as the speed of a sailing boat (roughly $\mathcal{O}(10^0)$ m/s), the flow has a significant influence on the velocity of the sailing boat with respect to the ground, especially when there is little wind. Besides, the magnitude and directions of the currents may vary over the racing area, and therefore profit can be gained by sailing a course where the current is most advantageous. A flow velocity difference of 0.2 m/s for example, gets a sailor 60 m ahead of its competitors in only 5 minutes. Therefore, knowledge of the current pattern in the sailing area can be very useful to the sailors.

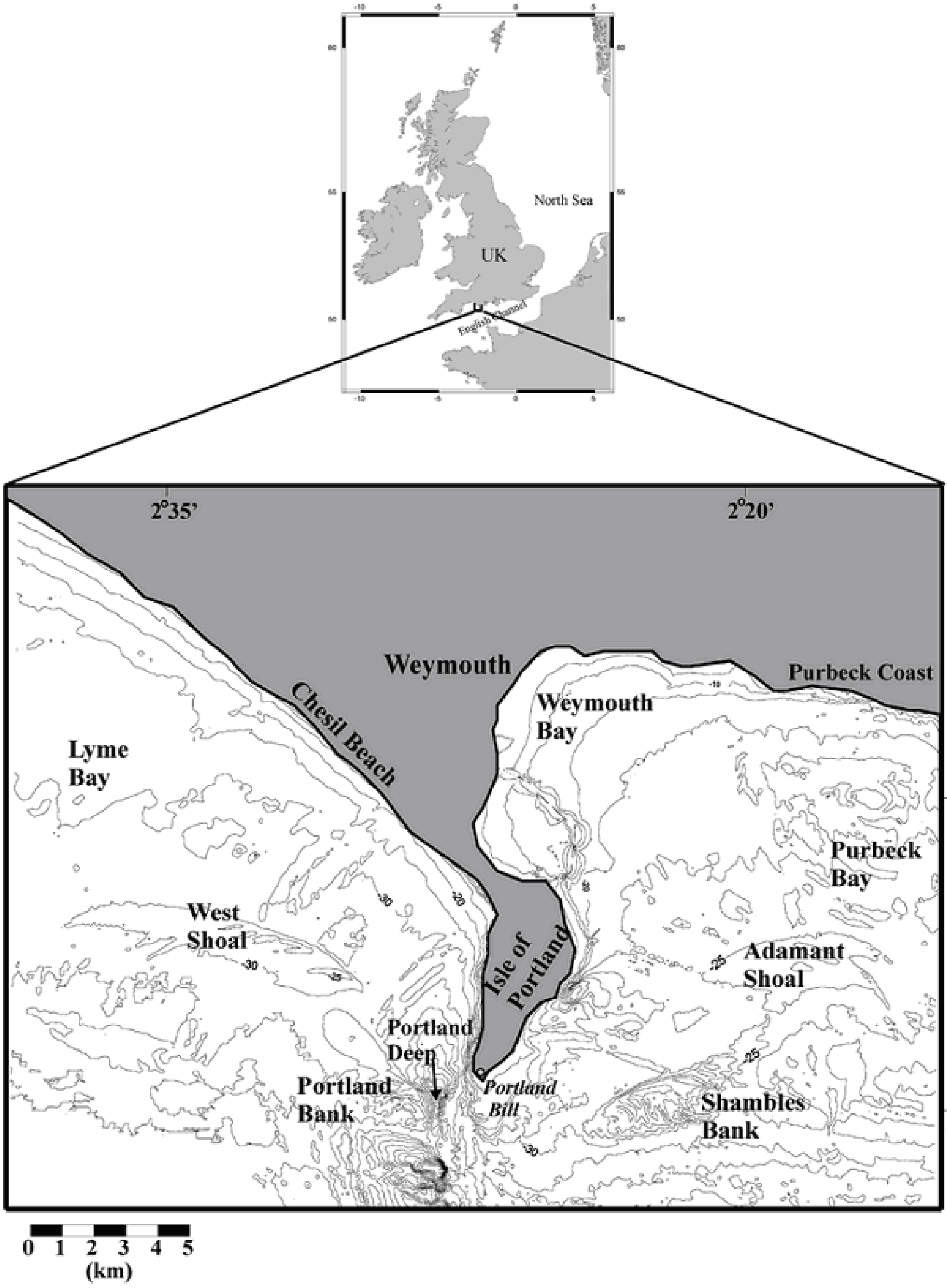

Figure 1.1: Bathymetric map Weymouth and Portland, based on UK Hydrographic Office Fair Sheets [1]

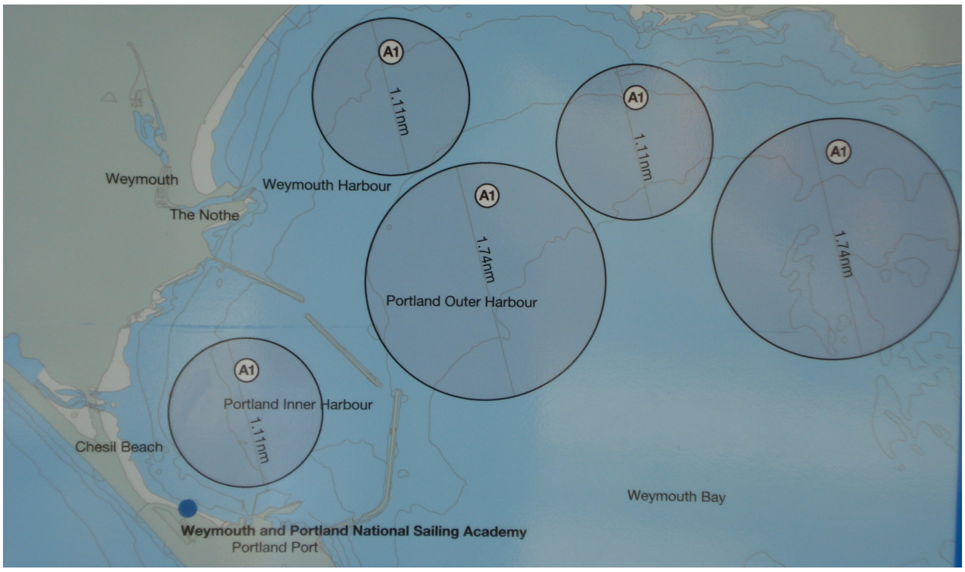

Figure 1.2: Racing areas of the Olympic Games 2012 in the Portland Harbour and Weymouth Bay (provided by the Dutch Water Sports Association (Watersportverbond))

The Olympic sailing area itself is situated partly in Weymouth Bay and partly in Portland Harbour. In the sailing area several circles will be assigned, which are the actual racing areas. The provisional racing areas for the Olympic Games 2012 are given in figure 1.2; the final racing areas may deviate from the areas given in figure 1.2, but will be at similar locations.

1.3 Objective

This project focuses on studying and modelling the flow in the sailing area of the Olympic Games 2012, located partly in Portland Harbour and partly in Weymouth Bay, in order to generate accurate and reliable current forecasts in the Olympic sailing area during the Olympic Games 2012 by means of a numerical flow model.

Differences in magnitude and direction of the flow over the racing area and when and where these differences exactly occur are of main importance to the sailing team. The slack tide, which may occur at different moments at different locations, is therefore significant as well.

1.4 Methodology

In order to study the flow in the sailing area of the Olympic Games 2012, a literature study on the current-inducing processes will be performed. The literature study has to reveal which of the processes are dominant, and which of the processes may be neglected. Besides, available current, water level, bathymetric, wind and wave data will be gathered and analysed. Since not enough current data is available, a survey plan will be set up in order to achieve the data by performing measured sailed current measurements oneself. The obtained current data will subsequently be thoroughly analysed.

Subsequently, the numerical flow model which will be used to model the flow in the area of interest will be considered. The results from the literature study and the data analysis will be used to determine whether it is allowed to use a depth–averaged model to provide current forecasts during the Olympic Games 2012, or whether a three–dimensional model is necessary. The model domain will be determined, which among others will depend on the availability of boundary conditions, and the properties of the numerical flow model. Besides, a conscious choice on the element size has to be made.

While the model is being calibrated, the sensitivity of the model will be investigated by means of varying several input parameters, for instance the bottom friction. Finally, the influence of external forces, like wind and waves, on the model results, so far calculated with tidal forces only, will be investigated. Wind data will be gathered to determine the prevailing wind conditions, which in turn will be enforced onto the model. The influence of the waves depends on the direction of the waves, and since it is difficult to solve for the waves directly, it is necessary to run a separate model to get a good spatial distribution of the wave fields in the model area. This will be the SWAN model, which is already linked to several of the numerical flow models.

1.5 Outline report

Knowledge about the physical processes which induce currents in the sailing area of the Olympic Games 2012 is presented in Chapter 2. Besides, available current, water level, bathymetric, wind and wave data of the area of interest is considered in this chapter. Chapter 3 proceeds with discussing the performed measurements and presenting the survey results. After that, the numerical flow model used to provide the current forecasts is discussed in Chapter 4. General information on the used numerical flow model is given and the calibration process is described. Following this, the influence of external forces such as wind and waves is investigated in Chapter 5. The final current forecasts are subsequently presented in Chapter 6. The conclusions and recommendations can be found in Chapter 7.

Chapter 2

Current inducing processes

In order to provide current forecasts, it is important to study the physical processes which induce currents in the area considered. Therefore, first a description of the area of interest will be given. From literature, the physical processes occurring in the area of interest will subsequently be identified. These processes will be considered in sections 2.2 to 2.7. By means of determining the scales of each of these processes' features, and by determining the order of magnitude of the flow velocities corresponding to each process, it will be investigated which of these processes are pre–dominant in the area of interest. Since the sailing boats experience the flow in the surface layer only, the vertical structure of the phenomena has to be investigated as well. Besides, available data considering the processes will be discussed.

2.1 Portland Harbour and Weymouth Bay

As already mentioned in section 1.2, the area of interest is the sailing area of the Olympic Games 2012, and is located partly in Weymouth Bay and partly in Portland Harbour. Portland Harbour is a man made harbour with an area of about $10\,\mathrm{km}^2$ and is on the south–western side connected with an intertidal area, called the Fleet, see figure 2.1. The inner harbour area is sheltered by breakwaters on the eastern side and is enclosed by a natural spit on the western side, which connects the Portland peninsula with the mainland. Along the coastline of Weymouth Bay, the coast varies from sandy and pebbled beaches to a jagged rocky coast.

2.1.1 Bathymetry

The bathymetry is strongly fluctuating in the entire Olympic sailing area, although the sailing area is shallow; the depth in Portland Harbour does not exceed $-10\,\mathrm{m}$ above chart datum (CD). In Weymouth Bay and the adjacent Purbeck Bay, the depth does hardly exceed $-30\,\mathrm{m}$ CD, see also figure 1.1, figure 2.1 and figure 2.2. Larger depths, up to $-80\,\mathrm{m}$ CD, are only found south–west of Portland Bill.

Since the sea bed topography has a significant influence on the flow patterns, it is important to have accurate and up to date bathymetric data. Various data is available from several sources. The bathymetric data provided by General Bathymetric Chart of the Oceans (GEBCO) however, is composed of data from several sources and is therefore not normalised with respect to a certain level, as for instance Chart Datum. It appeared that differences up to $40\,\mathrm{m}$ with respect to the more reliable North–West European Shelf Operational Oceano-

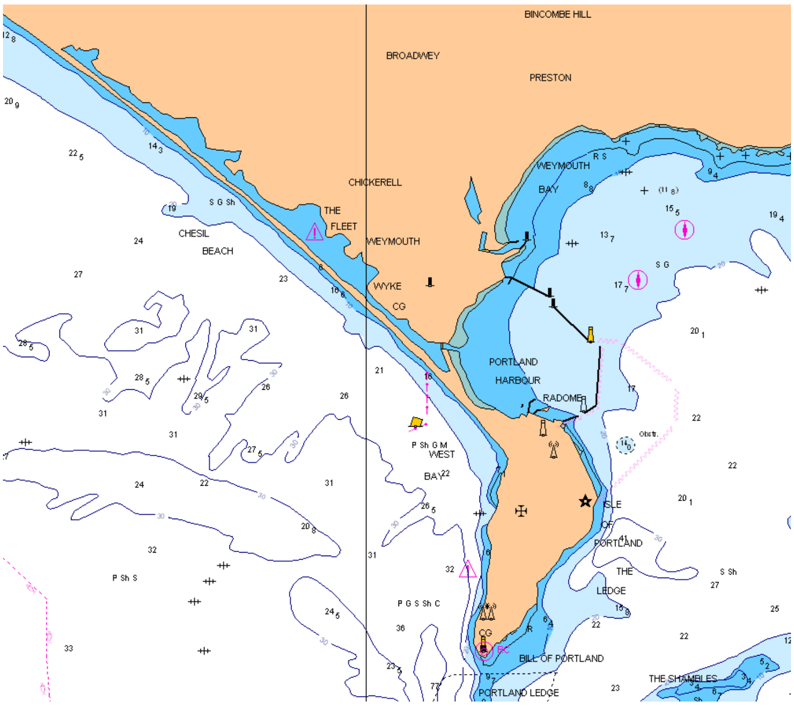

Figure 2.1: Overview of the Weymouth and Portland area, including several depth contour lines (extracted from NaviCharT navigation aid system)

graphic System (NOOS) bathymetric data occurred. Therefore, the GEBCO data will not be used for the bathymetry.

The NOOS bathymetric data is contrary to the GEBCO data normalised, and is therefore more reliable. NOOS provides bathymetric data every nautical mile which is accurate enough throughout most of the model domain.

Close to Weymouth and Portland, the area of interest, more refined bathymetric data is desired. In order to obtain this data, two Admiralty nautical charts of the area of interest, chart 2255 – Approaches to Weymouth and Portland (version 2010), and chart 2615 – Bill of Portland to The Needles (version 2005), have been digitised. The result is shown in figure 2.2. By using the NOOS bathymetric data (version 2008) and the digitised nautical charts, sufficient accurate bathymetric data is available.

2.2 Water levels

This section discusses the tidal wave in the area of interest as well as the shape of the tidal curve and the corresponding tidal asymmetries. Available data considering water levels in the area of interest, which are influenced mainly by the tide, is discussed as well.

2.2.1 Tidal system

The tide in the English Channel propagates from west to east and is dominated by the M_2–constituent. Therefore, the tide is a so–called semi–diurnal tide and has a tidal period of 12 h and 25 min. Figure 2.3 indicates that the tidal range varies widely across the Channel.

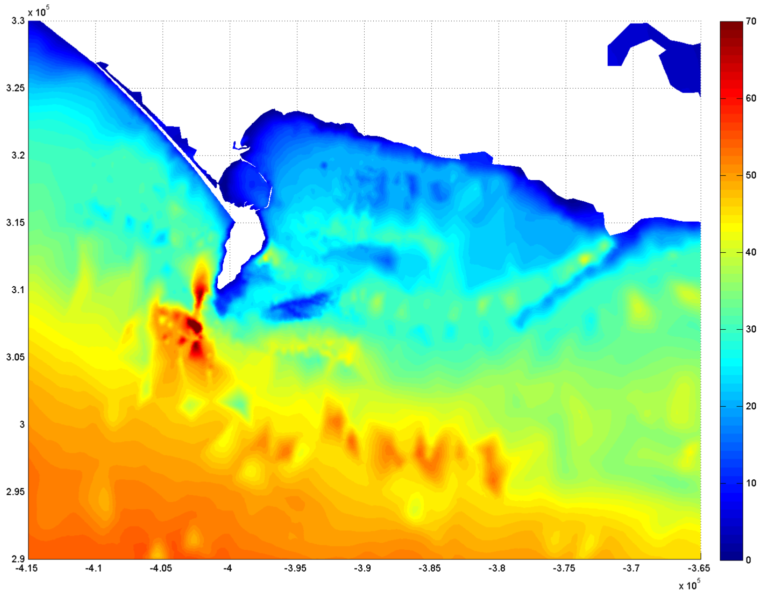

Figure 2.2: Bathymetry of the Weymouth and Portland area according to digitised Admiralty Charts. Depths are in meters, with respect to Chart Datum.

Tide levels Portland – 50°34′N 2°26′W	
Height in meters above datum	
Mean High Water Spring	2.1
Mean High Water Neap	1.4
Mean Low Water Neap	0.8
Mean Low Water Spring	0.1

Table 2.1: Tide levels in the Weymouth and Portland area according to Admiralty Chart 2255

At Weymouth, the tidal range has a maximum of approximately 2.5 m. The tidal levels are shown in table 2.1. Besides, according to figure 2.3, Weymouth is located close to an (inland) amphidromic point, which is located about 60 km east of Weymouth, near the Isle of Wight.

According to the National Tidal and Sea Level Facility [15] of the UK National Oceanography Centre, the three principal harmonic constituents together with the M_2–constituent are the S_2, O_1 and K_1–constituents, see also table 2.2. Due to the propagation of the tidal wave in shallower areas and frictional effects, other components, for instance the non–linear M_4, MS_4 and M_6–constituents might become important as well.

Figure 2.4 shows an example of observed water levels at Weymouth during several tidal cycles. A double low water is clearly visible, especially during spring tides. The second low water occurs 3 to 4 hours later than the first low water, and may at springs, on occasions be lower than the first. This can also be seen in figure 2.4. Whether the area is ebb or flood dominant, i.e. whether the ebb flow velocity or the flood flow velocity is largest, will be discussed in Chapter 3, where an extensive analysis on the water level variations will be performed.

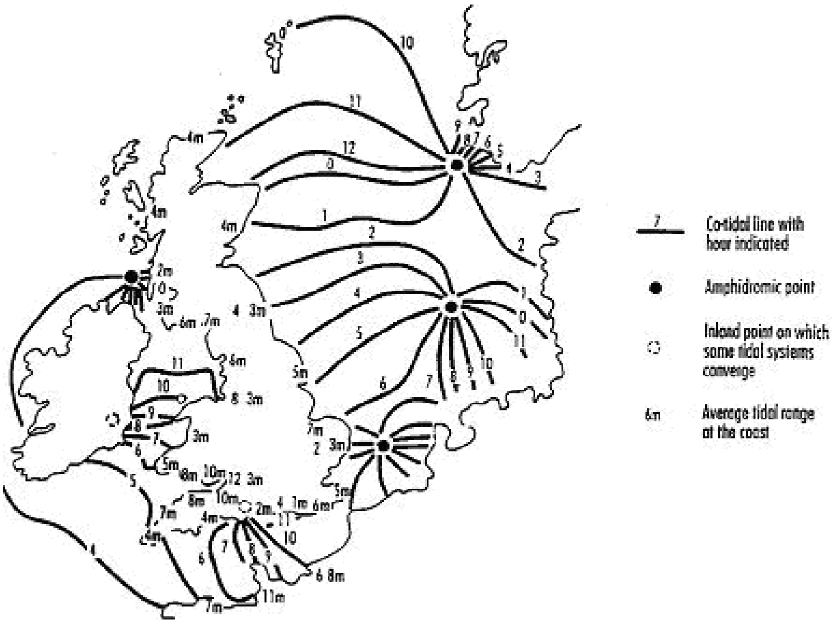

Figure 2.3: Amphidromic points, co–tidal lines and tidal range around the British coast [7]

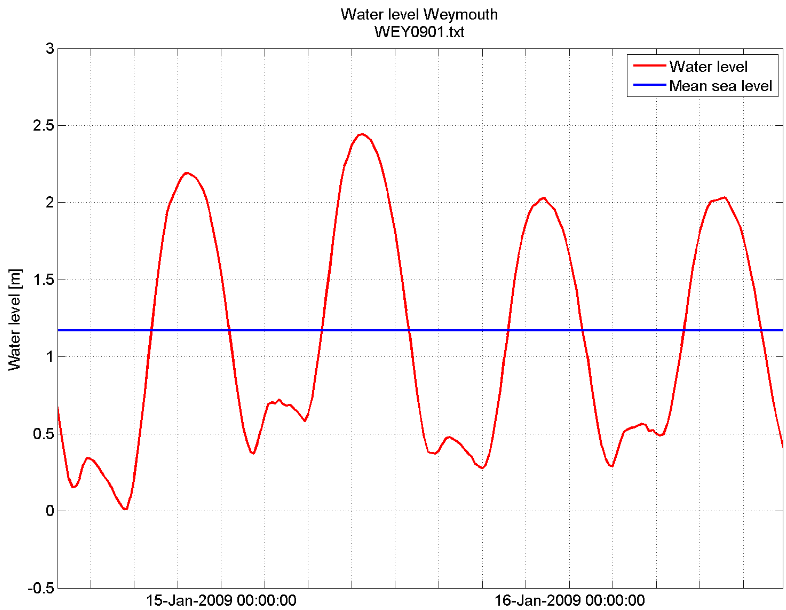

Figure 2.4: Example of the tide at Weymouth (data from [15])

Location	z_0	O_1		K_1		M_2		S_2	
		H[m]	g[°]	H[m]	g[°]	H[m]	g[°]	H[m]	g[°]
Weymouth	1.169	0.049	348.70	0.089	111.85	0.595	190.69	0.309	242.06

Table 2.2: Principal harmonic constituents [15]

Figure 2.5: UK Tide Gauge Network [15]

2.2.2 Water level data

The United Kingdom disposes of an extensive tide gauge network to provide for water level data, shown in figure 2.5. By means of this network, observed water levels with an interval of 15 minutes and long observational periods are available at 44 locations throughout the UK, indicated with the red dots in figure 2.5. The British Oceanographic Data Centre (BODC) has already performed a quality check and by that flagged the improbable values, null values and interpolated values. Furthermore, plots of the datasets show no exceptional highs and lows in its course, and the data can therefore be considered reliable.

The UK Tide Gauge Network provides water level data only for locations along the UK coastline. For water level data in the open ocean, the TPXO[1] model can be used, which provides the 13 principal harmonic constituents of the tidal wave at every quarter degree over the entire ocean. However, one has to bear in mind that the TPXO model provides model data instead of measured data. Besides, the TPXO model is calibrated by means of TOPEX/Poseidon and Jason satellite data, which has relatively large intervals. As a result, the TPXO model calculates the deep water constituents, which have a low frequency, fairly good, but the shallow water constituents on the other hand, which have higher frequencies, are less well generated.

A comparison of the TPXO constituents of a point near Newlyn (see figure 2.5) with the results of a tidal analysis on observed water levels at Newlyn can be found in appendix A. The comparison has shown considerable deviations in the shallow water constituents calculated by means of the TPXO model with respect to the astronomical tide. Therefore, it is concluded that the TPXO data is less reliable in coastal seas and cannot be used for shallow water.

[1] http://volkov.oce.orst.edu/tides/TPXO7.2.html

Tidal streams referred to high water at Devonport			
50°35′03″N 2°24′08″W			
Hours	Direction [°]	Speed at spring [m/s]	Speed at neap [m/s]
-6	163	0.3	0.1
-5	150	0.35	0.1
-4	146	0.3	0.1
-3	143	0.25	0.05
-2	233	0.05	0.0
-1	330	0.15	0.05
0	323	0.25	0.05
+1	333	0.35	0.1
+2	001	0.25	0.05
+3	115	0.2	0.05
+4	139	0.15	0.05
+5	147	0.25	0.05
+6	161	0.25	0.05

Table 2.3: Tidal streams in the Weymouth and Portland area according to Admiralty Chart 2255

The TPXO model is known to perform better in deep water, since the tide in deep water is not influenced by shallow water effects which causes for instance the M_4 constituent, and since the tide is hardly influenced by frictional effects which causes for instance the M_6 constituents. Therefore, the tide in deep water mainly consists of constituents with a low frequency only. These constituents can be better measured by satellites than constituents with higher frequencies, since the satellites only pass a few times a day by which they are not able to measure water level fluctuations with a higher frequency. Since tidal constituents with a higher frequency, e.g. the M_4 and the M_6 constituent, are absent in deep water, the TPXO model performs fairly good in deep water.

2.3 Currents

This section discusses the tidal current as well as the formation of tidal eddies in the area of interest. Special attention will be paid on the flow separation process, which is a prerequisite for eddy formation. Moreover, the eddy generation process curves the tidal flow, which thereupon leads to the generation of secondary circulations. The tidal influence in the inner Portland Harbour due to the filling and emptying of the adjacent intertidal areas is discussed thereafter. Finally, available data considering currents in the area of interest is discussed.

2.3.1 Tide

The tide along the British south coast propagates from west to east, and the tidal flow is directed parallel to the coastline. During rising water the general direction of the flow is from west to east and during falling water the direction of the flow is from east to west. The flow velocities corresponding to the tidal flow are $\mathcal{O}(10^0)$ m/s. An overview of the tidal streams in the Weymouth and Portland area is given in table 2.3. The phase difference between the water levels and the flow velocities will be discussed in Chapter 3.

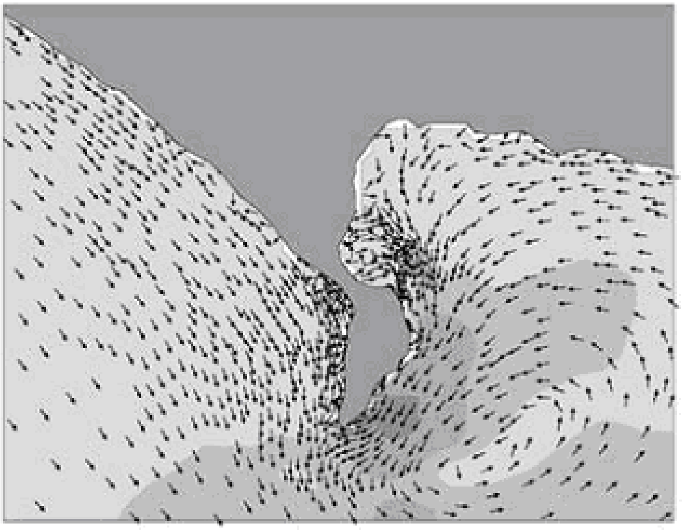

Figure 2.6: Computed current pattern five hours after high water [1]

Since frictional effects on the tidal flow are larger near shore, the flow velocity is lower close to the coast. Therefore, slack tide usually occurs earlier near the coast than in the deeper areas.

2.3.2 Eddy formation

Several studies as well as the Admiralty tidal stream atlases reveal that transient eddies are formed on the alternate sides of the Portland peninsula with the reversal of the tide. According to Signell and Geyer [13], transient tidal eddies arise when streamlines separate. In the area of interest, the tidal flow separates near Portland Bill, which is located at the tip of the Portland peninsula. The eddy which is subsequently generated at the eastern side of the headland, is shown in figure 2.6 and extends over the entire Weymouth and Purbeck Bays. The tidal eddies therefore influences the flow in the entire sailing area under normal conditions to large extent. On the western side of the headland a similar eddy is formed; see figure 2.7. The flow pattern in figure 2.6 and figure 2.7 are both obtained by means of a depth-averaged numerical flow model [1].

As mentioned before, a prerequisite for eddy formation, is that the flow separates. In order to explain the flow separation process, first the situation without bottom friction is considered. Since streamlines converge as the flow reaches an obstacle and diverge when the flow has past the obstacle's tip, the flow accelerates as it reaches the headland and starts decelerating when it has past the headland tip. Due to the Bernoulli effect, the water level drops as the flow velocity increases and a pressure minimum can be found at the location of the maximum velocity, which is at the tip of the headland. Therefore, a positive pressure gradient can be found upstream and a negative pressure gradient downstream of the headland tip.

The negative pressure gradient downstream of the headland tip counteracts the flow. Depending on the amount of advective flux of momentum coming from upstream, which among others depends on the wall friction, the flow might even turn back. In order to maintain continuity, the deceleration of the alongshore flow must be counterbalanced by an

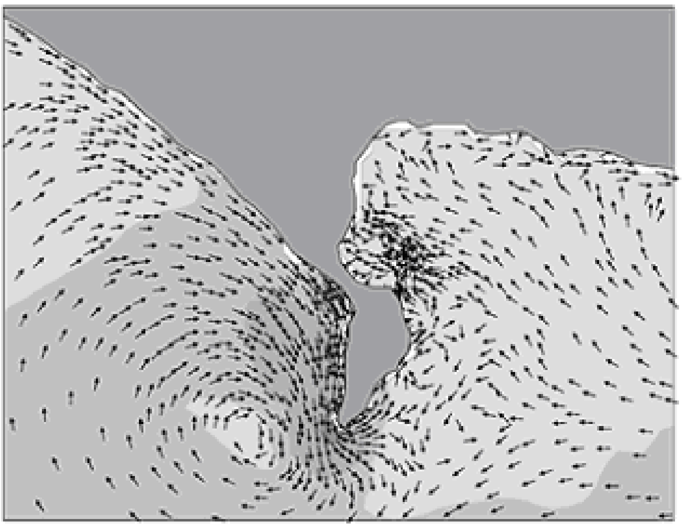

Figure 2.7: Computed current pattern one hour before high water [1]

offshore flow. Since this offshore flow directs the flow away from the headland boundary, the flow will separate when the alongshore flow velocity has reached zero [13].

In coastal seas however, bottom friction may not be neglected. When bottom friction is considered, the pressure must balance both bottom friction an advection, by which the pressure minimum is located downstream of the velocity maximum [13]. The bottom friction also alters the way momentum is extracted from the flow and changes the relation between the pressure gradient and the point of flow separation as well. It appears that at small distances from the coast, and when viscous effects are negligible, the bottom friction causes the flow to separate as soon as an adverse pressure gradient is established [13].

Whether the flow separates or not depends on whether the pressure gradient changes from favouring to adverse or not. Signell and Geyer [13] have obtained an expression for the pressure gradient, in which the separate terms represent the contributions of local acceleration, advection and friction. The relative size of these terms determines the nature of the pressure gradient along the headland. It appears that flow separation only occurs when the advection term dominates both the local acceleration and the friction term in the momentum equation. When evaluating the advection–local acceleration ratio and the advection–friction ratio, it turns out both ratios have an essential dependence on the aspect ratio, which is the ratio between the length and the width of the headland. Advection will quickly dominate as this ratio increases, therefore when the sharpness of the headland increases [13].

It appears that the nature of the transient tidal eddies is controlled by the same ratios [13]. For a fixed aspect ratio, the advection–friction ratio can be represented by the frictional Reynolds number, based on bottom friction instead of viscosity:

$$Re_f = \left[\frac{H}{c_f a}\right] \tag{2.1}$$

In this parameter, also used by Wolanski et al. [19] as a measure of the nature of island wakes, H represents the water level, c_f the friction coefficient and a the headland width.

The advection–local acceleration ratio can be expressed by the Keulegan–Carpenter num-

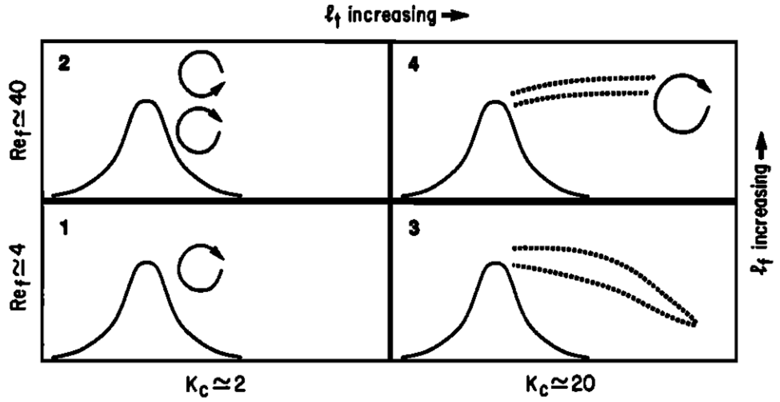

Figure 2.8: Nature of the flow for values of K_c and Re_f [1]

ber:

$$K_c = \left[\frac{u_0}{\omega a}\right] \tag{2.2}$$

Here u_0 represents the flow velocity, and ω the angular speed. Figure 2.8 shows the nature of the flow for both parameters.

Around the Isle of Portland, the water depth is approximately 30 m and the flow velocity approximately 1 m/s. The width of the headland is approximately 2500 m. The bottom friction is assumed 0.003. The angular velocity of the semi–diurnal tide is $1.405 \cdot 10^{-5}$ rad/s. For the flow around the Isle of Portland, the frictional Reynolds number and the Keulegan–Carpenter number are approximately:

$$Re_f = \frac{30}{0.003 \cdot 2500} = 4 \tag{2.3}$$

$$K_c = \frac{1}{2500 \cdot 1.405 \cdot 10^{-5}} \approx 3 \tag{2.4}$$

Since these ratios are comparable, the frictional decay scale and the tidal excursion are comparable as well, and while time dependent effects are important, the friction is strong enough to decay vorticity over a tidal cycle. A tidal eddy is formed during each half tidal cycle, but the eddies do not interact with the eddy formed in the subsequent tidal cycle [13]. The above described flow regime, specified by the two parameters and by regime 1 in figure 2.8, corresponds with the flow regime depicted in figure 2.6 and figure 2.7, which is obtained by means of a numerical flow model.

2.3.3 Residual flow

The study of Bastos et al. [1] on the tidal flow around Portland Bill also reveals the residual flow pattern, which is represented in figure 2.9. The tidal eddies, which are shown in figure 2.6 and figure 2.7, are also visible in the residual flow pattern, which confirms the significance of these eddies in the tidal flow. The residual flow however, is the average flow over a tidal cycle, whereas a sailing match usually does not last longer than a few hours. Therefore, the residual flow is not important in case of current forecasts for the Dutch Olympic Sailing Team.

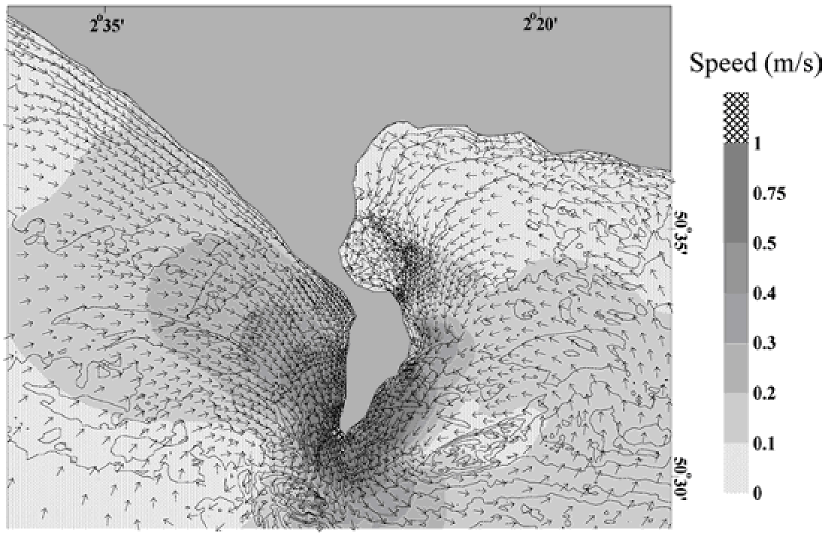

Figure 2.9: Computed residual flow, derived by averaging the depth-averaged current over a tidal cycle [1]

2.3.4 Secondary circulations

Until now, only the horizontal structure of the tidal flow is considered, but the vertical structure of the flow influences the current pattern as well. Due to frictional effects, the flow velocity near the bottom is significantly lower than the flow velocity in the remainder of the water column. The vertical structure of the tidal flow is therefore considered approximately logarithmic. This logarithmic velocity distribution in combination with the curvature of the tidal flow due to the formation of tidal eddies, causes secondary circulations.

The curvature of the tidal flow leads to a centrifugal force directed normal to the main flow, in the outward direction of the bend. Since the centrifugal force is proportional to the square of the flow velocity, and the velocity distribution is logarithmic, the centrifugal force varies over the vertical. The centrifugal force is compensated by a barotropic cross–stream pressure gradient, which, when integrated over depth, leads to a hydrostatic force directed to the inside of the curve. Since the resulting pressure gradient is constant over depth, the resulting accelerations are directed to the outward at the surface, and are directed inward near the bottom. These resulting accelerations cause a secondary flow, with flow velocities of $\mathcal{O}(10^{-2})$ m/s. In case of a tidal eddy, this means the water diverges at the surface and converges at the bottom, which causes upwelling in the centre of the eddy. The downwelling, which is expected at the outer edge of the eddy, is usually less clearly noticeable, unless there is a solid boundary located near the outer edge of the eddy [6].

Since the centrifugal force is proportional to the square of the flow velocity of the stream-wise flow, the secondary circulation is sensitive to the vertical structure of the tidal flow. Therefore, it is difficult to predict the magnitude of the secondary circulation. Besides, the secondary circulation depends on the eddy viscosity, and the Coriolis force may also have a significant influence, see section 2.4. Moreover, there are other factors, e.g. wind stress (section 2.5) or density differences (section 2.7), which can cause circulations which may overshadow the curvature–induced secondary circulation [8].

Although the flow velocities of the secondary circulation are small, the secondary circulation may have a significant influence on both the dynamics and kinematics of the flow [8]. Due to the transversely varying flow, the advection differs. This differential advection influences the horizontal dispersion by transporting fluid across the shear zone and spreads the vorticity over the eddy [8]. Because it is difficult to predict the exact magnitude of the circulation, it is arduous to quantify the influence of the secondary flow on the eddy generating processes. Since the order of magnitude of the flow velocities corresponding to the secondary circulations is small compared to the order of magnitude of the tidal flow velocities, it is assumed the secondary circulation may be neglected.

2.3.5 Tidal influence in the Portland Harbour

As shown before in figure 2.1, Portland Harbour is connected with the Fleet, a large intertidal area with a length of about 12 km. The basin fills and empties every tidal cycle. Because of the basin's size, the discharge into the inner harbour is high and the tidal flow in and out of the harbour is clearly noticeable. Therefore, the tide also influences current patterns within Portland Harbour.

2.3.6 Current data

The current patterns in the area of interest can be very complex. Since the objective is to provide current forecasts, current data is necessary in order to establish the accuracy of the computed current forecasts. In the database of the British Oceanographic Data Centre (BODC) a large amount of current datasets can be found. A closer look on the datasets however revealed that the current measurements originate from the late seventies and early eighties. Since the bathymetry has a significant influence on the current patterns, and the bathymetry is, through the years, liable to alterations, the reliability of the datasets is questionable. The current datasets are therefore considered outdated and will not be used.

Since current measurements are of vital importance, it is decided to perform current measurements oneself. In Chapter 3 the measurements will be discussed and the datasets achieved during the survey analysed.

2.4 Coriolis force

Due to earth's rotation, each portion of its surface has an angular velocity about a vertical axis and therefore has vorticity, called the planetary vorticity. Due to this vorticity a force, the so–called Coriolis force, acts on a particle as it moves over the earth's surface. In the Northern Hemisphere the Coriolis force deflects the flow to the right. The Coriolis force is usually only of importance when considering large scale phenomena. When studying regions which are much smaller than the earth's radius, in the order of 10 to 100 km, the f–plane approximation can be applied, which considers the Coriolis force constant. Since Weymouth is located at 50° N, f is approximately 10^{-4} 1/s.

In a similar manner as the flow curvature induces a secondary circulation, the Coriolis force induces one. Since the Coriolis force deflects the flow to the right, the Coriolis–induced secondary circulation is dependent on the direction of the flow, contrary to the curvature–induced circulation. This means the Coriolis–induced circulation and the curvature–induced circulation reinforce for a cyclonic eddy and oppose for an anti–cyclonic eddy. For both cases,

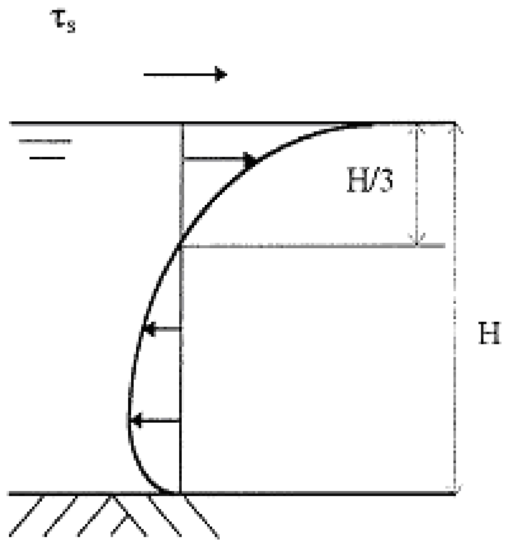

Figure 2.10: Vertical velocity distribution for constant wind in a closed basin [2]

the corresponding flow velocities are $\mathcal{O}(10^{-2})$ m/s and therefore negligible compared to the tidal flow.

According to Bastos et al. [1], the vorticity in the centre of the tidal eddies, which is vorticity relative to the earth, reaches values up to $25 * 10^{-4}$ 1/s. Therefore, the relative vorticity is an order larger than the planetary vorticity, which makes the Coriolis force negligible for most of the eddy generating processes. In other situations however, e.g. when an eddy is almost entirely damped by bottom friction, it is possible the Coriolis force does has an significant influence. Therefore, the Coriolis force will not be neglected.

2.5 Wind

Pressure differences in the atmosphere result in wind, blowing from high pressure areas to low pressure areas. This wind, which acts on the water surface, causes for a constant depth drift currents in the direction of the wind. In turn, in case of for instance a closed basin, these drift currents cause the water level to rise in the direction of the flow and to lower in opposite direction. The pressure gradient which is associated with this water level gradient, induces a flow near the bottom, the so–called return flow, directed opposite to the direction of the drift currents. The flow velocity of the drift currents amounts to a small percentage of the wind velocity. The corresponding flow velocity of the wind–induced currents is $\mathcal{O}(10^{-1})$ m/s and may, since the flow velocity corresponding to the tidal flow is $\mathcal{O}(10^{0})$ m/s, have a significant influence on the current pattern.

When a closed basin is considered, with a spatially constant wind acting on the water surface, the vertical velocity distribution is similar to the distribution in figure 2.10, with a depth–averaged velocity of zero. The velocity turning point is located at one–third of the depth counting from the surface, and is obtained by taking the bottom stress half the wind stress and by considering the eddy viscosity constant over depth [10]. In case of turbulent flow however, the eddy viscosity is a function of depth, and another distribution is for instance

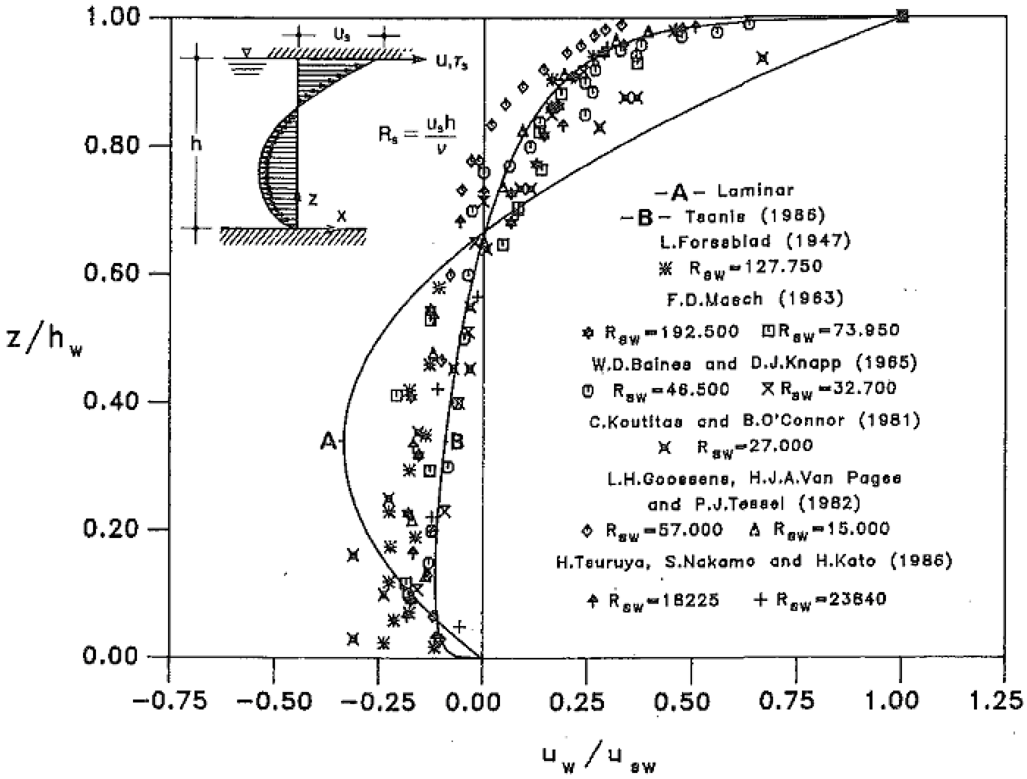

Figure 2.11: Velocity distributions in wind-induced currents [10]

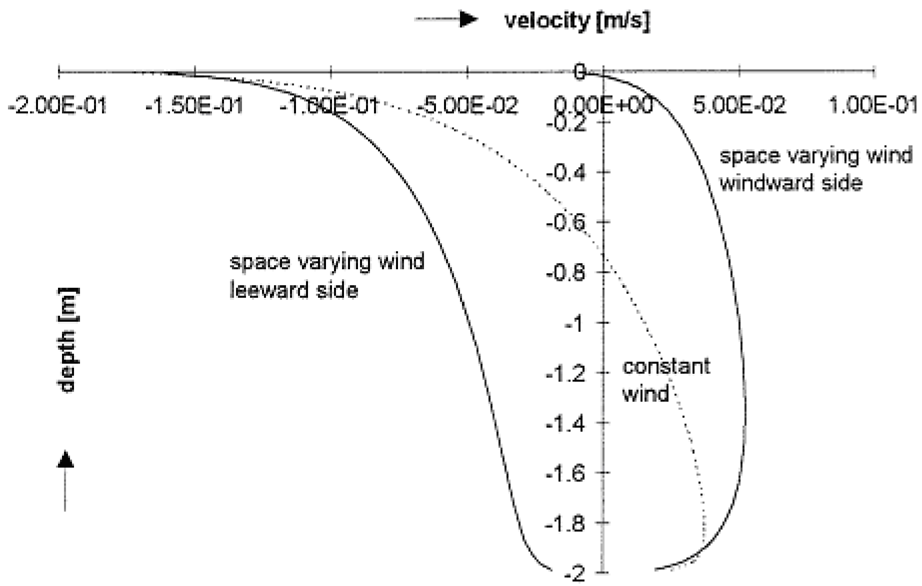

Figure 2.12: Velocity distribution changes by spatially varying wind [2]

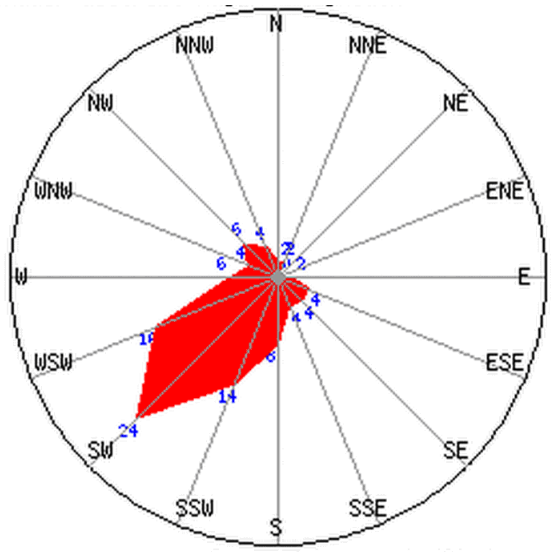

Figure 2.13: Wind rose for Weymouth, in August, based on 1.5 years of observations. [17]

more appropriate. Solutions for several eddy viscosity models in wind-induced currents are compared by Tsanis [10]. The resulting velocity distributions, depicted in figure 2.11, show substantial variations, which indicates it is important to consider the appropriate eddy viscosity model when obtaining the vertical velocity profile in wind–induced currents.

When however a spatially varying wind acts on the sea surface, the result will be a spatial surface shear stress. This leads to surface gradients, and therefore pressure gradients, in both the direction of the wind and the direction perpendicular to the wind. The vertical velocity distribution will therefore vary spatially as well and the velocity distributions change into those similar to for instance the distributions in figure 2.12. The depth–averaged velocity in these vertical velocity distributions is, in contrary to the distributions in figure 2.10 and figure 2.11, non–zero.

In reality however, the bottom topography cannot be considered flat and variations in depth are present. When a bottom topography with straight and parallel depth contours and a wind blowing along those depth contours is considered, the water level gradient appears to be constant over the cross–section and to be inversely proportional to the average water depth. The pressure gradient force however, is determined by the local depth. Since at an average depth the pressure gradient force and the wind force balance, the wind force dominates in areas shallower than the average depth, causing currents in the direction of the wind. In areas deeper than the average depth, the pressure gradient force dominates, causing an upwind flow. The above mentioned currents in both shallow and deep areas oppose, but in the end the streamlines have to close, resulting in the so–called topographical gyres [4]. The topographical gyres can be considered as a two–dimensional flow feature; the flow is approximately constant over depth. Since the depth variations are larger with respect to the absolute depth, these topographical gyres in generally occur in shallow areas.

Despite the fact that depth variations and spatially varying wind are responsible for variations in the vertical velocity distribution of wind–induced currents, the direction of the wind–induced current at the water surface is in general in the direction of the wind. The flow velocity of the wind driven current amounts up to several percent of the wind velocity [20].

Wind speed [Beaufort scale]	8	7	6	5	4	3
Probability of exceedence [%]	0	0	4	16	54	81

Table 2.4: Probability of exceedence wind speed for Weymouth, in August, based on 6 years of observations. [18]

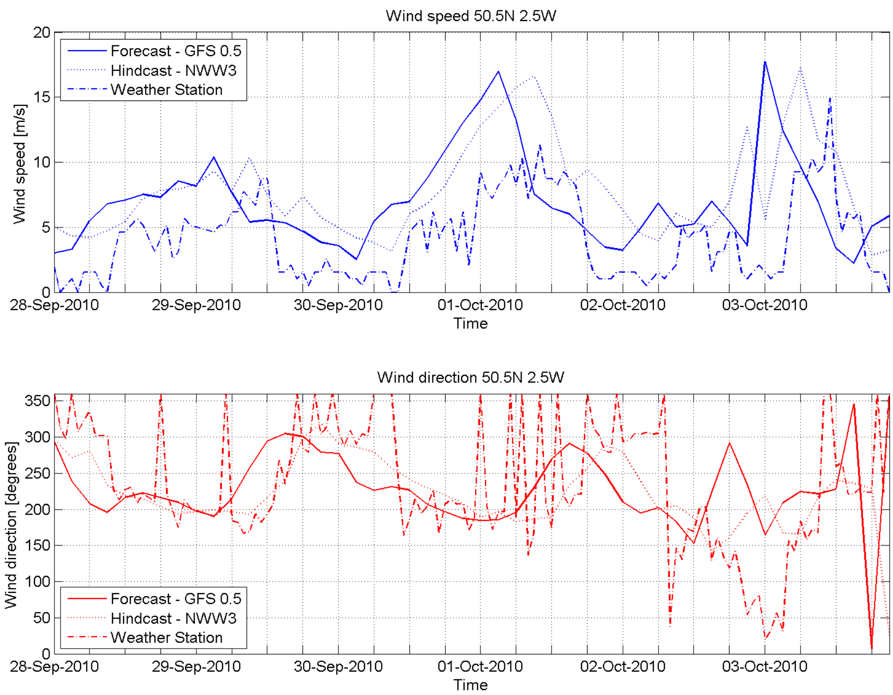

Figure 2.14: Wind data following from the Weymouth weather station, the GFS0.5 forecast model and the NWW3 hindcast model

2.5.1 Wind data

The influence of the wind on the current pattern depends on the wind speed, wind direction, bathymetry, the duration of the wind and the fetch. Therefore, information on the wind climate and wind data are considered important. Some statistics on the wind climate of Weymouth in August are given in figure 2.13 and table 2.4. The wind rose in figure 2.13 is based on 1.5 year of observations. The statistics of table 2.4 are based on amply 6 years of wind predictions. Besides statistics, real time wind data, wind forecasts and wind hindcasts are provided by several sources, such as local weather stations and databases.

Figure 2.14 shows wind data provided by a Weymouth weather station [16], the Global Forecast System 0.5 (GFS0.5), and the NOAA Wave Watch 3 (NWW3)hindcast model. The courses of the wind velocity and direction provided by the three sources roughly correspond. However, the GFS0.5 results seems to lag behind with respect to the NWW3 and Weymouth weather station data. Besides, the data provided by the Weymouth weather station frequently shows peaks in the wind direction. Which of these sources is most reliable is difficult to determine. Since the differences in the data shown in figure 2.14, it is always important to be critical towards the provided wind data.

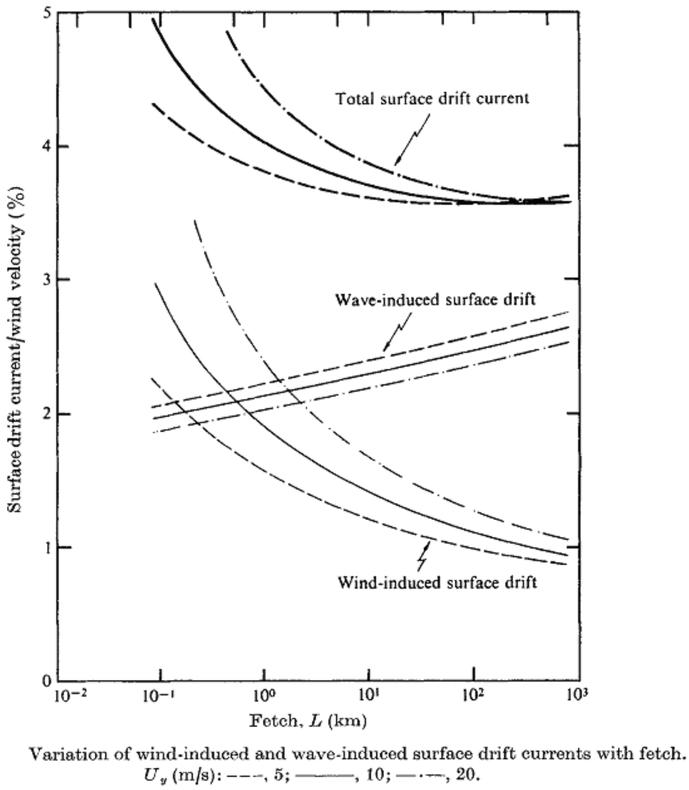

Figure 2.15: Total surface drift current [20]

2.6 Waves

Waves occur with a wide variety of angular frequencies. Waves with a low frequency are for instance tidal waves, which have already been considered in section 2.2. Both wind–generated waves which have a high frequency and the so–called seiches which are generated by amplification of waves from the intermediate frequency band, will be discussed here.

2.6.1 Wind waves

The same wind which causes the wind–induced currents, transmits energy to the water when blowing across the surface. From the instabilities which are generated due to this wind, waves are formed. Different circumstances contribute to the height of these waves, among others the wind velocity, the duration of the wind and the fetch. These wind–generated waves are, contrary to tidal waves, short waves, seen from a hydrodynamic point of view, which means vertical accelerations may not be neglected. According to the linear wave theory, the water particles move in closed orbits, circular in case of deep water or elliptical in case of intermediate depths and shallow water.

According to Stokes' higher order wave theory however, where superharmonic components are superposed onto the fundamental component (following from the linear wave theory), the particle paths are no longer closed orbits. This leads to a surface drift current, the so–called Stokes drift, in the direction of the wave propagation. Depending on the fetch and the wind velocity, the flow velocity of the Stokes drift amounts a small percentage of the wind velocity. The total surface drift, which is the sum of the wind–induced and wave–induced current, may therefore obtain values up to 5% of the wind velocity, as shown in figure 2.15. The corresponding flow velocities are $\mathcal{O}(10^{-1})$ m/s. Therefore, the wave–induced currents may have a significant influence on the current pattern.

2.6.2 Seiches

Besides the high–frequency wind waves and the low–frequency tidal waves, waves in the intermediate–frequency band might occur. According to De Jong [11], moving meso–scale atmospheric convection cells following a cold front passing over relatively warm water, induce surface wind speed fluctuations which in turn generate these intermediate–frequency waves at sea. In case the frequency of the incoming waves in a harbour basin is near the eigenfrequency of the basin, the incoming waves are amplified, giving rise to standing waves in the harbour basin, so–called seiches. Due to resonance, a scarcely noticeable wave at sea can be sufficient to generate a significant response in the harbour.

Another category seiches is generated during thunder storm events and occur usually in the late summer. A temporary increase in atmospheric pressure and wind speed is held accountable for the generation of a so–called soliton wave [11], a sole wave which preserves its shape along a large distance. This type of seiche is also known as meteo–tsunamis.

No records have been found which describe seiche events of the first category in either the Portland Harbour or the Weymouth Harbour. Haslett et al. [9] describes a single possible meteo–tsunami event in Weymouth Bay, 1939, but no other records on meteo–tsunamis in the area have been found. Therefore, seiches in the area of interest are not expected and the effect of seiches on the flow near Weymouth will be neglected.

2.6.3 Wave data

Several sources, such as the DEFRA strategic wave monitoring network for England and Wales (WaveNet), the Channel Coastal Observatory (COO) and the NWW3 model, provide real time wave data, wave forecasts and wave hindcasts. Unfortunately, WaveNet has a limited number of wave buoys, and not all wave data available at the COO is quality checked yet. Wave conditions for the closest NWW3 location (50.5°N 2.5°W) to Weymouth (50.6°N 2.45°W) and non–checked wave data from the COO (50.62°N 2.41°W) are shown in figure 2.16. Since the distance to Weymouth is significant (circa 15 km) in case of the NWW3 data, and since the COO data is not checked yet, it is important to be critical towards the provided wave data.

Wave statistics however, are available, and provided by the CCO. The average significant wave height, peak period and wave direction are shown in table 2.5. The wave direction at Weymouth and the corresponding significant wave height are shown in the wave roses of figure 2.17. The statics are based on 6 years of observations by the Weymouth wave buoy (50.62°N 2.41°W).

According to the statistics of table 2.5 and figure 2.17, the wave direction is throughout the year approximately south–east. The wave direction according to the NWW3 data, shown in figure 2.16, is however south–west. The difference in the wave data is mainly due to different locations. The Weymouth wave buoy is located in Weymouth Bay itself; the NWW3

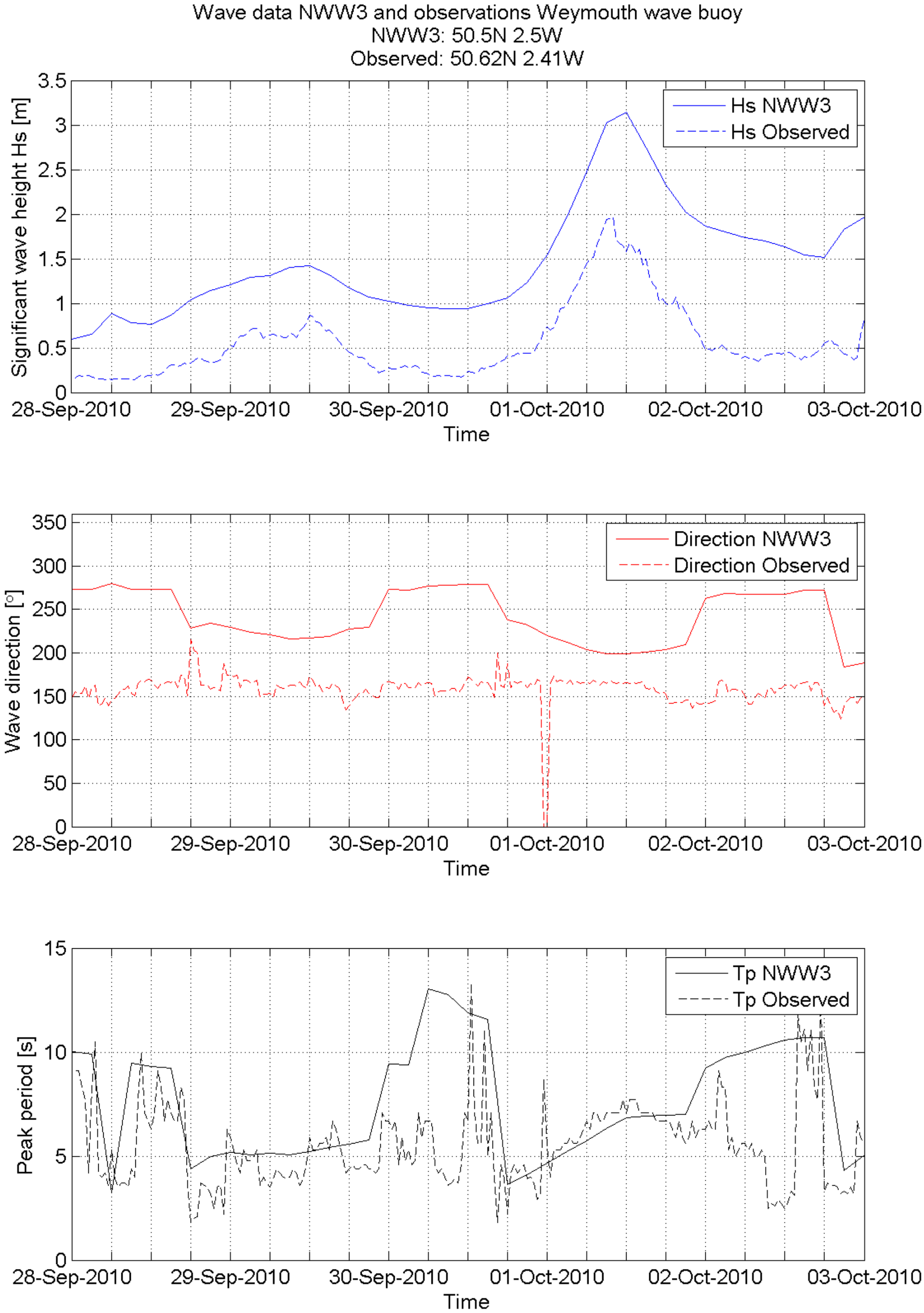

Figure 2.16: NWW3 wave data and observed wave data

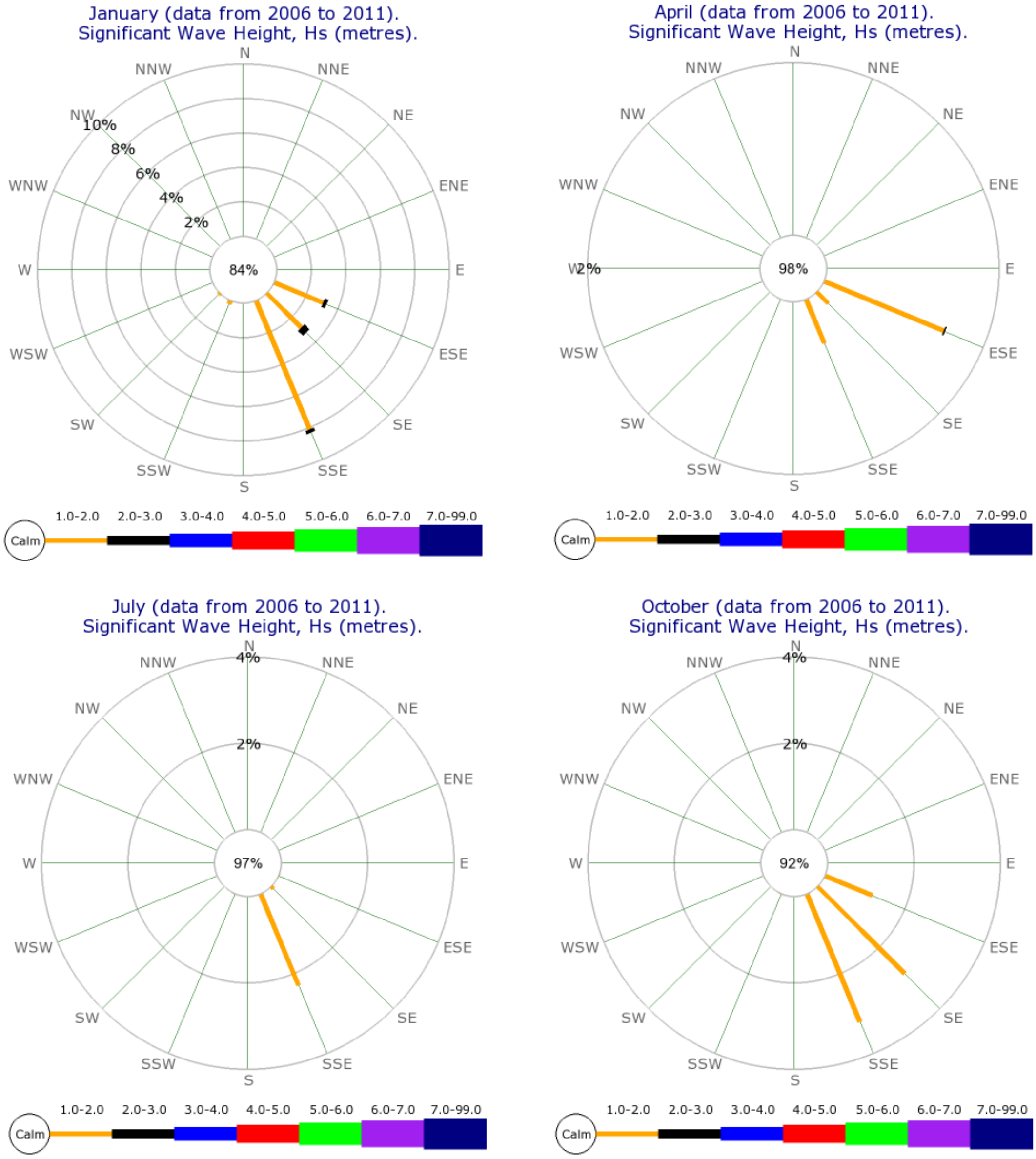

Figure 2.17: Wave roses for the wave direction and significant wave height for the Weymouth wave buoy, provided by the CCO.

Month	H_s [m]	T_p [s]	Direction [°]
January	0.63	7.8	154
February	0.54	8.1	155
March	0.46	6.9	159
April	0.37	6.2	149
May	0.4	5.8	150
June	0.31	5.9	155
July	0.4	5.4	165
August	0.37	5.2	161
September	0.4	5.7	154
October	0.49	6.2	154
November	0.56	6.5	158
December	0.55	6.9	150

Table 2.5: Wave statistics Weymouth wave buoy

location is located a little south–west of Portland Bill, where the waves are not sheltered by the mainland.

2.7 Density currents

Density currents are induced by density differences or stratification in either the horizontal or vertical plane. Since density is a function of pressure as well as potential temperature and salinity, density differences may have several causes. When barotropic flow is considered, density is a function of pressure only, and highs and lows in the water surfaces determine the direction and strength of the flow. In case of baroclinic flow however, density differences may occur as a result of temperature differences (for instance caused by heating of the water surface due to solar radiation), and as a result of salinity differences (for instance caused by river discharges) as well.

The baroclinic pressure gradient which arises as a result of the density differences due to for instance river discharge, is dependent on the type of stratification. In the example depicted in figure 2.18, where the fresh water is located on the landward side and the saltier water on the seaside, the baroclinic pressure gradient varies linearly over depth. The resulting force is therefore directed towards the land. This is shown in the top figure of figure 2.18. The barotropic pressure gradient on the other hand, which arises due to water level differences, is constant over the vertical and directed to the seaside, see the middle figure of figure 2.18. By adding both pressure gradients, the resulting pressure gradient is directed seaward at the surface and landward at the bottom, resulting in a similar vertical velocity distribution. This is shown in the bottom figure of figure 2.18. In the Rhine region of freshwater influence, where the river discharge varies between $2,000\,\mathrm{m}^3/\mathrm{s}$ and $20,000\,\mathrm{m}^3/\mathrm{s}$, the velocity of the estuarine baroclinic flow into the North Sea is $\mathcal{O}(10^{-2})$ m/s [14].

The river discharging into the sailing area is the River Wey, a small river with a length of 9 km, which rises in Upwey. At Broadwey (see figure 2.1), close to its origin, the average discharge, measured by a gauging station of the UK Gauging Station Network of the Centre of Ecology and Hydrology (CEH) amounts $0.32\,\mathrm{m}^3/\mathrm{s}$, and the maximum discharge is about $1.3\,\mathrm{m}^3/\mathrm{s}$. Because of the river's limited discharge, it is expected that the river discharge has

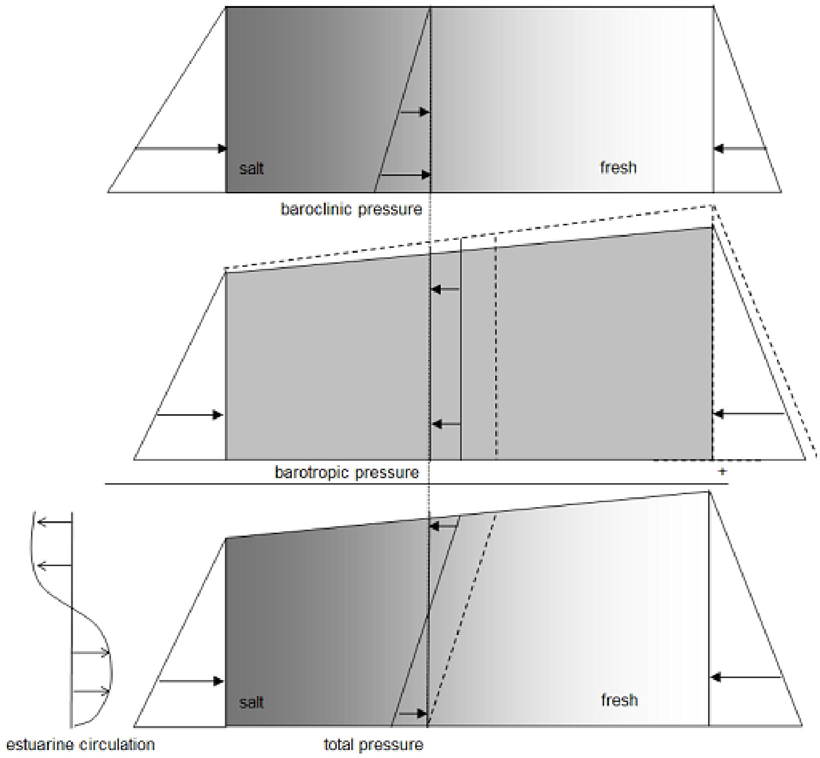

Figure 2.18: Estuarine circulation due to density differences [3]

no significant influence on the stratification in the sailing area.

2.8 Conclusion

In the preceding sections, several physical processes and the resulting flow mechanisms have been considered. The order of magnitude of the flow velocities corresponding to these flow mechanisms are summarised in table 2.6. Table 2.6 shows that the main flow in the sailing area is the tidal flow, which is the driving force behind the tidal eddies. The tidal eddies have flow velocities of the same order of magnitude as the tidal flow. The tidal flow normally has a logarithmic vertical velocity distribution, by which the velocity is approximately constant over most of the vertical.

The wind– and wave–induced drift currents have flow velocities one order of magnitude smaller than the flow velocities of the tidal flow. For drift currents, the vertical velocity may vary over the vertical. Since the flow velocity and flow direction in the surface layer are most important to the Dutch Olympic Sailing Team, it is important to keep an eye on the vertical velocity profile of the flow in case of wind and waves.

Both the curvature–induced and the Coriolis–induced circulation have flow velocities two orders of magnitude smaller than the tidal flow velocity and are consequently negligible. The same holds for the density currents. In case of clear density differences and a large river discharge, as applies for the Rhine region of freshwater influence, the flow velocities only amount to $\mathcal{O}(10^{-2})$ m/s. Because of the limited discharge of the River Wey, the effect will be significantly smaller than indicated in table 2.6 and will therefore be negligible.

Flow mechanism	u $[ms^{-1}]$	*Remarks*
Tidal flow	$\mathcal{O}(10^0)$	
Tidal eddies	$\mathcal{O}(10^0)$	For tidal flow of $\mathcal{O}(10^0)$ m/s
Curvature–induced circulation	$\mathcal{O}(10^{-2})$	For tidal flow of $\mathcal{O}(10^0)$ m/s
Coriolis–induced circulation	$\mathcal{O}(10^{-2})$	For tidal flow of $\mathcal{O}(10^0)$ m/s
Wind–induced drift current	$\mathcal{O}(10^{-1})$	
Wave–induced drift current	$\mathcal{O}(10^{-1})$	
Density current	$\mathcal{O}(10^{-2})$	For river discharges of $\mathcal{O}(10^4)$ m/s

Table 2.6: Flow velocities of the separate flow mechanisms

Besides the current–inducing processes, the preceding sections discuss bathymetric, water level, current, wind and wave data. While considering bathymetric data from several sources, the GEBCO data has proven to be unreliable. However, sufficient bathymetric data is provided by the NOOS bathymetric data and by digitised Admiralty nautical charts.

The UK Tide Gauge Network, consisting of 44 tide gauge locations along the entire English coast, provides observed water level data with intervals of 15 minutes between the data points. Due to the quality check performed by the BODC before releasing the datasets, the data can be considered reliable. Besides, the TPXO model provides boundary conditions in the form of the 13 largest tidal constituents. Since the TPXO model is calibrated by means of satellite data, the model generated the shallow water constituents less good, and is therefore particularly useful in deep water. Due to both the expanse of the UK Tidal Gauge network and the reliability of the data, and the availability of the TPXO model, sufficient reliable water level observations are available, and extra water level measurements do not have to be performed.

Since the objective of this thesis is to provide current forecasts, the availability of sufficient current data is of vital importance. The current measurements available at the BODC are however considered outdated, and no other current observations is disposed of. Therefore, it is decided to perform current measurements oneself, which will be further discussed in Chapter 3.

Several sources provide wind and wave data, both as forecast and as hindcast model data. Besides, real time measurements are available. However, the data provided by the sources differs, and the data is difficult to check on reliability. Basically enough data is available, but one should be careful when using the data.

Chapter 3

Field measurements

In Chapter 2 several current inducing processes and available data considering these processes is discussed. It appears sufficient reliable data is available at several sources considering water levels, bathymetry, wind and wave data. Current data has been found in the database of the British Oceanographic Data Centre (BODC), however, this data appeared to be originating from the late seventies and early eighties. Since the bathymetry has a significant influence on the current patterns, and the bathymetry is trough the years liable to alterations, the reliability of the current data is questionable. The current datasets found in the database of the BODC is therefore considered outdated and will not be used. In order to gather the necessary current data for this study, several different measurements have been performed. A description of these measurements, which have been performed in late September 2010, and the results of these measurements are discussed in this chapter.

3.1 Survey

To gather the necessary current data, both sailed current measurements have been performed. The most eminent measurements have been the sailed current measurements. An advantage of sailed current measurements with respect to fixed current measurements, is that the sailed currents measurements offer the opportunity of mapping the current pattern in the entire area, instead of only measuring the current at a single fixed point.

During the survey, sailed current measurements have been performed along several transects. In order to get a good picture of both the tidal eddy and the current pattern in the sailing area of the Olympic Games 2012, it was chosen to sail along a north–south directed transect which crosses the sailing area, and along an east–west directed transect, by which a part of the tidal eddy should be measured. The length of the transects is set to approximately 5 km, which is long enough to measure a large part of the tidal eddy and cover the sailing area, but short enough to keep the time interval between two data points limited.

Transect	Direction	From	To
A	North–South	50°34′48″N 2°23′30″W	50°37′48″N 2°23′30″W
B	East–West	50°35′00″N 2°24′00″W	50°35′00″N 2°19′00″W
C	North–South	50°35′00″N 2°23′00″W	50°32′00″N 2°23′00″W

Table 3.1: Lines of direction

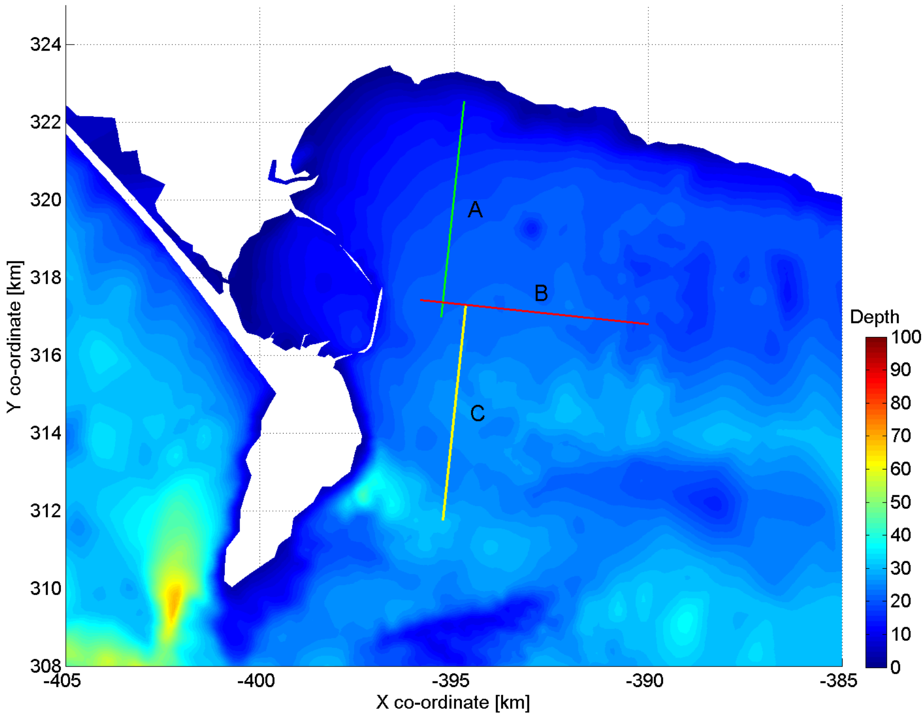

Figure 3.1: Transects

For each transect, measurements have been performed over an entire tidal cycle, thus over 13 successive hours. From literature and tidal stream atlases it turns out the flow velocities near Portland Bill, located at the southern tip of the headland, reaches up to 7 knots, which is approximately 3.5 m/s. Given that the tide is the driving force behind the flow, and that the tide is subject to spring–neap tide variations, the flow velocity will also be subject to spring–neap tide variations. Since the flow velocity at Portland Bill is rather high, the difference of the flow velocity during spring tide and neap tide will be substantial. Given that the tidal flow in turn is the driving force behind the generation of the tidal eddy in the sailing area, it is expected that distinct differences in the development of the eddy during spring and neap tide are noticeable. The sailed current measurements have therefore been performed during both spring and neap tide.

While surveying along the north–south directed transect (A), it appeared that the tidal flow along this transect was rather weak, despite the measurements were performed during spring tide. Therefore, it was decided not to perform the sailed current measurements along this transect again. Instead, measurements have been performed along a transect further south (C). An overview of the performed surveys and transects is given in figure 3.1 and in table 3.2. In table 3.1 the co-ordinates of the sailed transect are given.

During the survey the flow was measured by an the Acoustic Doppler Current Profiler (ADCP), which was fixed to the vessel by means of a frame. An ADCP transmits pulses with a fixed frequency, which are reflected by the water particles. Due to the movement of these particles with respect to the ADCP, a frequency shift occurs, the so–called Doppler shift,

Date	Activity
27/09/2010	Preparations
28/09/2010	Transect A
29/09/2010	Transect B
30/09/2010	Portland Harbour. Sailed Transect B once
01/10/2010	Transect C
02/10/2010	Transect B

Table 3.2: Overview of the performed surveys

which is a measurement for the flow velocity of the water particles. With four bundles of pulses, an ADCP is able to determine both the velocity and direction of the flow over almost the entire vertical. By linking the ADCP to a GPS system with DGPS, the current data is automatically corrected for the vessel speed.

In Chapter 2 it is concluded that sufficient reliable water level observations are available, also at Weymouth, and that water level measurements do not have to be performed. However, the water level observations originating from the BODC are released not until three months after the measurements have been performed, as the BODC first carries out a quality check. For the time frame of this study, it was necessary to have the water level data earlier. Therefore, water level measurements have been performed after all. The water level measurements have been performed by means of a Valeport pressure sensor, which has been fixed to the quay in the Weymouth Harbour. Water level observations have been obtained over 5.5 days.

More details on the survey can be found in Appendix D[1], in which the full survey report is presented. In the Appendix, the conditions in which the survey is performed are for example discussed, and all the results are presented.

3.2 Results

This section is used to discuss both the measured water levels and flow velocities. The measured water levels will be compared to tidal predictions. Where the water levels deviate, an explanation will be searched for. The current measurements will thereafter be used to classify the tidal flow in the area. Besides, the measured vertical velocity distribution will be investigated.

Only a selection of the obtained data, results representative for all measurements and some erratic results, will be considered here. An overview of all the survey results can be found in Appendix D.

3.2.1 Water level

Figure 3.2 shows the measured water levels and the raw water level data originating from the NTSLF [15], which seem to correspond perfectly. Besides both measured water level datasets, the high and low waters at Weymouth, according to astronomical predictions, published in the Reeds Nautical Almanac 2010 [12], are indicated in the graph. All water levels are with

[1]Some overlap between this chapter and Appendix D may occur, since Appendix D also serves as a stand alone survey report.

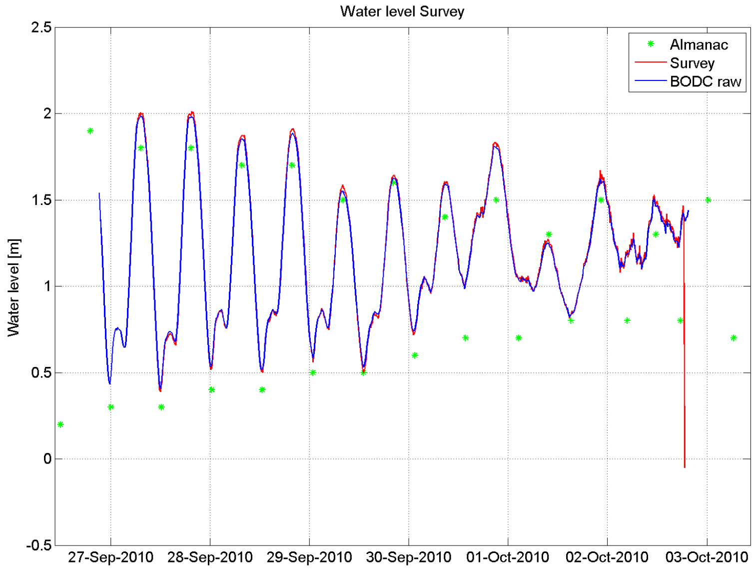

Figure 3.2: Measured and (by means of a tidal analysis) predicted water levels at Weymouth [15]. Water levels are given in meters with respect to Chart Datum.

respect to Chart Datum (CD), and only the first low waters are included in the predictions; the second low water occurs 3 to 4 hours after the first.

The times of high and low waters according to the Almanac and the measurements correspond well. The water levels however deviate. When taking the weather conditions in consideration (see Appendix D), it appears the deviation is largest when the wind speed was high, and very small when the wind speed was low. Therefore, the weather conditions are probably responsible for the water level deviations.

3.2.2 Tidal classification

The measured water levels are, however scaled, shown again in figure 3.3. The dotted vertical lines indicate the slack tide. The flood period seems to last longer than the ebb period, however, the second low water is in this figure included in the flood period. The true flood period is thus shorter than figure 3.3 indicates. To classify the tide in the area of interest, the measured flow velocities are plotted (by a red line) in the figure as well. The slack tide appears to occur approximately 4 hours after high water and approximately 5 hours after the first low water. The tidal wave therefore has the character of a progressive wave. Furthermore, the graph shows that the maximum ebb flow velocity is higher than the flood flow velocity, which indicates the tide is ebb dominated.

3.2.3 Flow pattern and vertical velocity distribution

The top figure of figure 3.4 shows several vertical velocity profiles. During the survey, every 20 s a velocity sample has been produced, which represents the average over those 20 s. Since the time span is very short, not all fluctuations due to turbulence are not averaged out of the results. The separate vertical velocity distributions become very jagged due to these

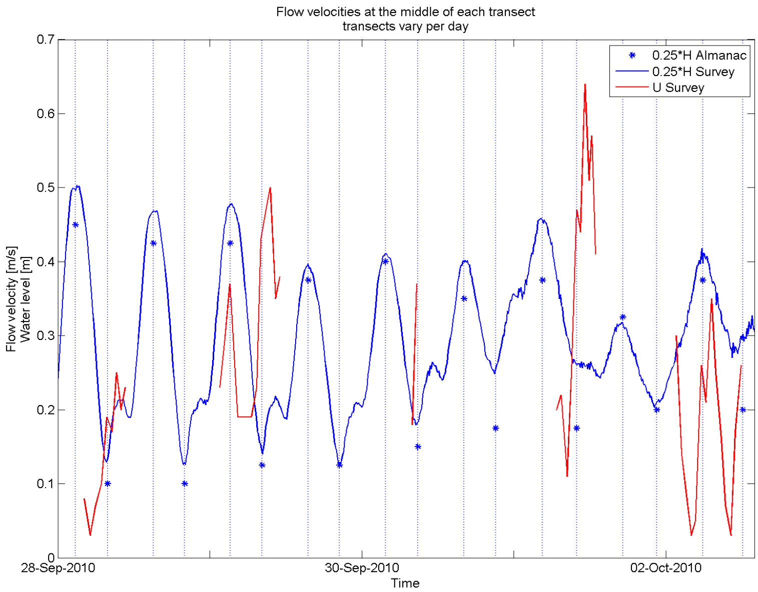

Figure 3.3: Ebb and flood tidal periods

fluctuations. To determine whether for instance 3D–effects have been measured, it is desirable to filter these fluctuations out of the signal. Each vertical velocity profile therefore represents the average velocity profile of a single transect.

The middle figure of figure 3.4 shows the vertical velocity profile on a semi–logarithmic scale. The bottom figure shows the flow directions. In figure 3.5, the measured flow velocity along the transects corresponding to the transects of figure 3.4 are shown. All measurements have been achieved by sailing along the east–west transect.

Flood tide

The flood velocity profile of figure 3.4 (indicated with a red line), sailed on the morning of September 29^{th} along transect B, is representative for nearly all velocity profiles measured during flood tide and has a nearly logarithmic shape. The second plot in figure 3.4 confirms this. For a perfectly logarithmic profile however, the lines in the second graph of figure 3.4, which shows the average vertical velocity profile on a semi–logarithmic scale, would have to be a perfectly straight lines through z_0 (the bottom). A small deviation to this straight line is visible. Near the surface, there is a clear kink in the semi–logarithmic plot. When considering figure 3.6, which shows the velocity profiles of all transects sailed on September 29^{th}, the kink appears to be visible in every profile. However, the direction of the kink appears to be alternately to and fro. Since the survey vessel sailed to and fro as well, the kink near the surface layer is assumed to be an effect of the return flow alongside the survey vessel.

The third graph in figure 3.4 shows the flow direction. The flow direction during flood tide appears to be approximately 50 °. Near the bottom, the flow direction becomes somewhat higher. This is assumed to be an effect of the beginning of the slack tide, which usually starts at the bottom.

Figure 3.5(a) shows the flood flow along transect B corresponding to the flood velocity

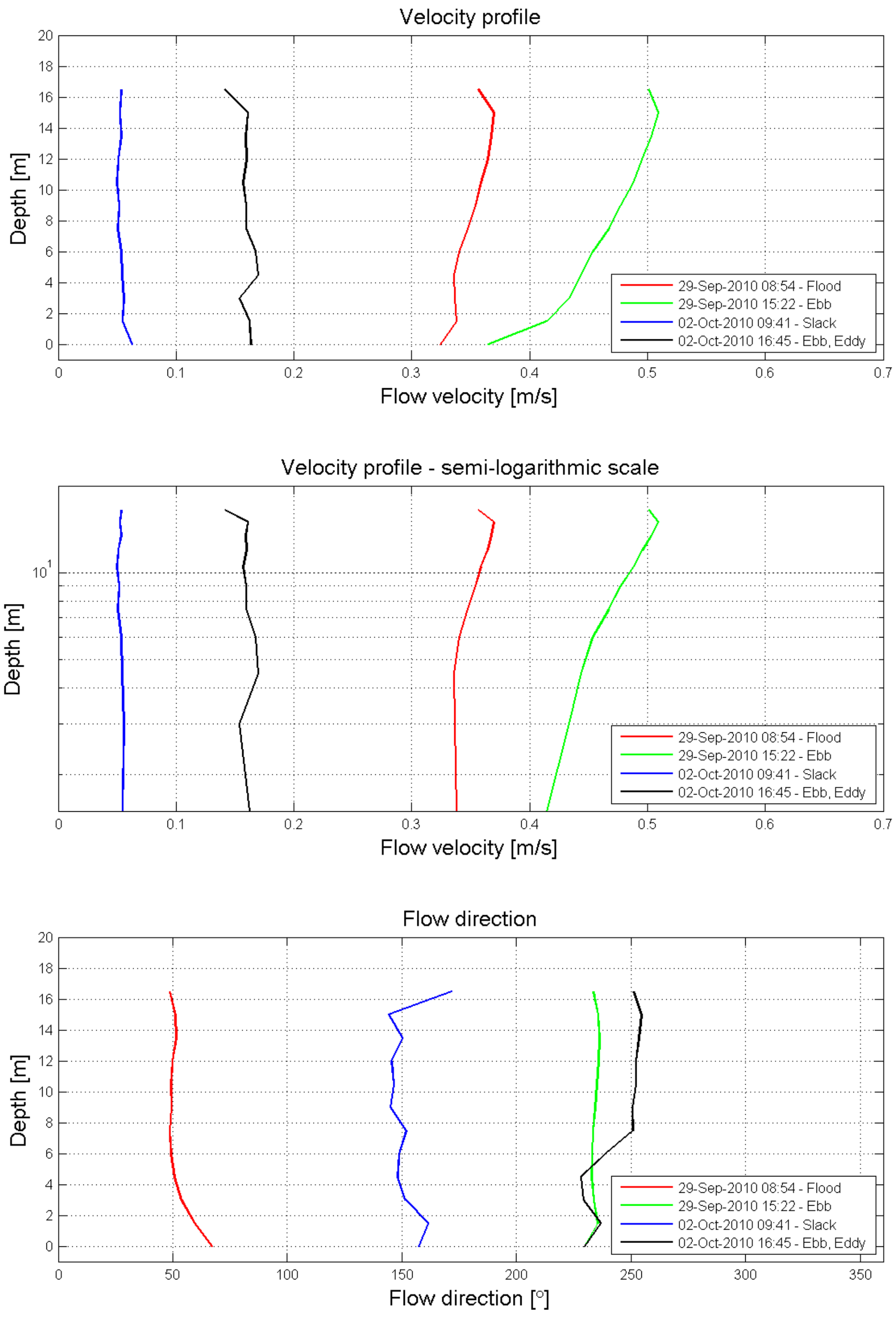

Figure 3.4: Measured vertical velocity distribution during flood tide, ebb tide and at slack tide, at transect B

profile of figure 3.4. Figure 3.5(a) shows that the flow direction varies along the transect. The flow on the eastern side of the transect deflects somewhat to the east compared to the flow on the western side of the transect. The variation of the flow along the transect is expected to be due to the geometry of the area.

Ebb tide

The ebb velocity profile of figure 3.4 (indicated with a green line), sailed on the afternoon of September 29^{th} along transect B, is representative for nearly all velocity profiles measured during ebb tide. The vertical velocity distribution is again nearly logarithmic. In the second graph of figure 3.4, the same deviation in the velocity profile is visible as in velocity profile of the flood transect. Again the return flow alongside the survey vessel is assumed to be responsible for these deviations.

The flow direction during ebb tide varies according to figure 3.5(b) along the transect, but is on average approximately $235\,^{\circ}$. The flow on the western side of the transect is directed more to the south than the flow on the eastern side of the transect. The flow again seems to follow the geometry of the area.

Slack tide

The slack velocity profile of figure 3.4 (indicated with a blue line), sailed on the morning of October 2^{nd} along transect B, clearly deviates from the above considered profiles. The velocity is nearly zero, and the average flow direction along the transect is approximately $150\,^{\circ}$. The third plot of figure 3.5 shows a changing flow direction over the transect. Taking this in consideration as well, the flow can be classified as slack tide.

Tidal eddy

The flow of the ebb flow shown in figure 3.5(d), sailed on the afternoon of October 2^{nd}, differs from the representative ebb flow shown in 3.5(a). The flow shown in figure 3.5(d) is measured at the beginning of the ebb period, by which the flow velocities are lower than in figure 3.5(a). The transient tidal eddy is still present in the area, and part of the tidal eddy has been measured. Its influence is clearly visible in figure 3.5(d); the flow turns almost $180\,^{\circ}$ along the transect.

The transient tidal eddy in the area of interest arises at the beginning of the flood tide. During flood, the eddy becomes slowly bigger, until it extends over the entire area of interest. The ebb flow, when it has become strong enough, subsequently washes the tidal eddy away, and enforces a new tidal eddy on the other side of the Portland peninsula. The transient tidal eddy in the area of interest is therefore only shortly present during ebb tide.

3.3 Conclusion

As mentioned in Chapter 2.2, the racing area of the Olympic Sailing Games 2012 is known for its transient tidal eddies. These tidal eddies have been observed during several of the sailed current measurements. Figure 3.4 and figure 3.5 show the results of the survey for several transects. Both the vertical velocity profiles and the flow patterns during flood tide, ebb tide and at slack tide are drawn. The graphs show no 3D–effects.

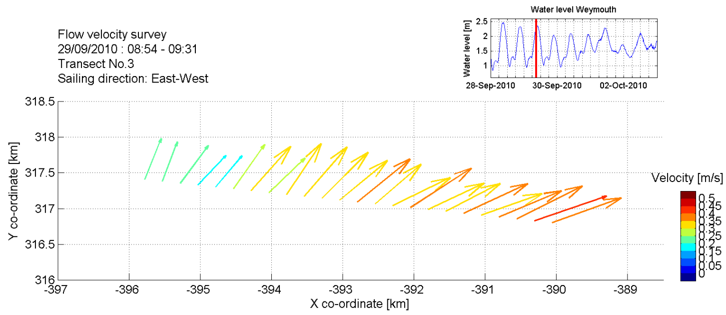

(a) Flood tide along transect B

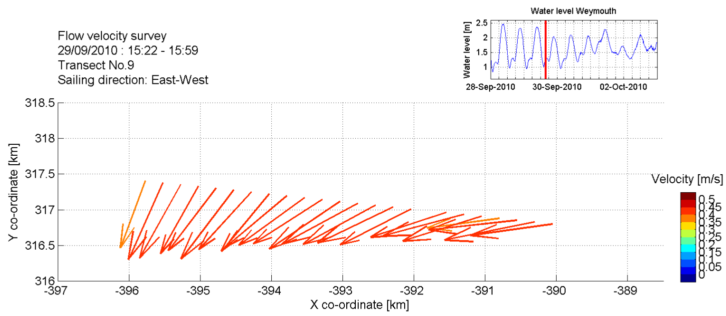

(b) Ebb tide along transect B

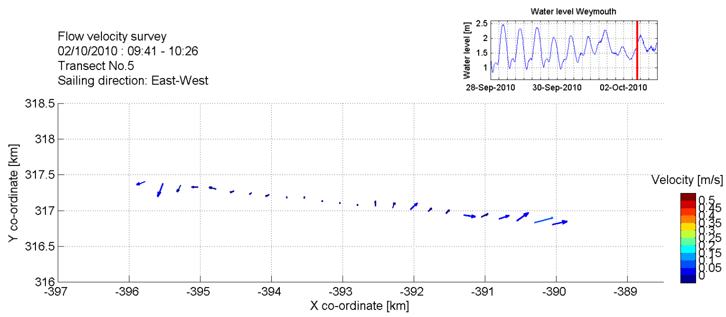

(c) Slack tide along transect B

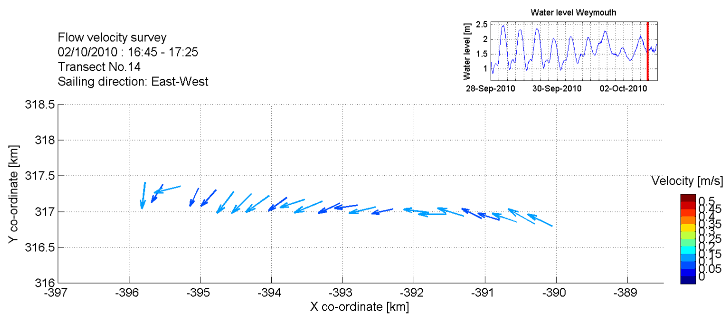

(d) Ebb tide along transect B, including the tidal eddy

Figure 3.5: Measured vertically averaged flow velocity for the transects corresponding to figure 3.4

Chapter 2 concludes that the available current data is insufficient. By performing the measurements described in this chapter, the gap in the data is narrowed. Based on the result of the measurements it can be concluded that depth averaging of the flow is allowed, since no 3D–effects in the vertical velocity profile have been observed.

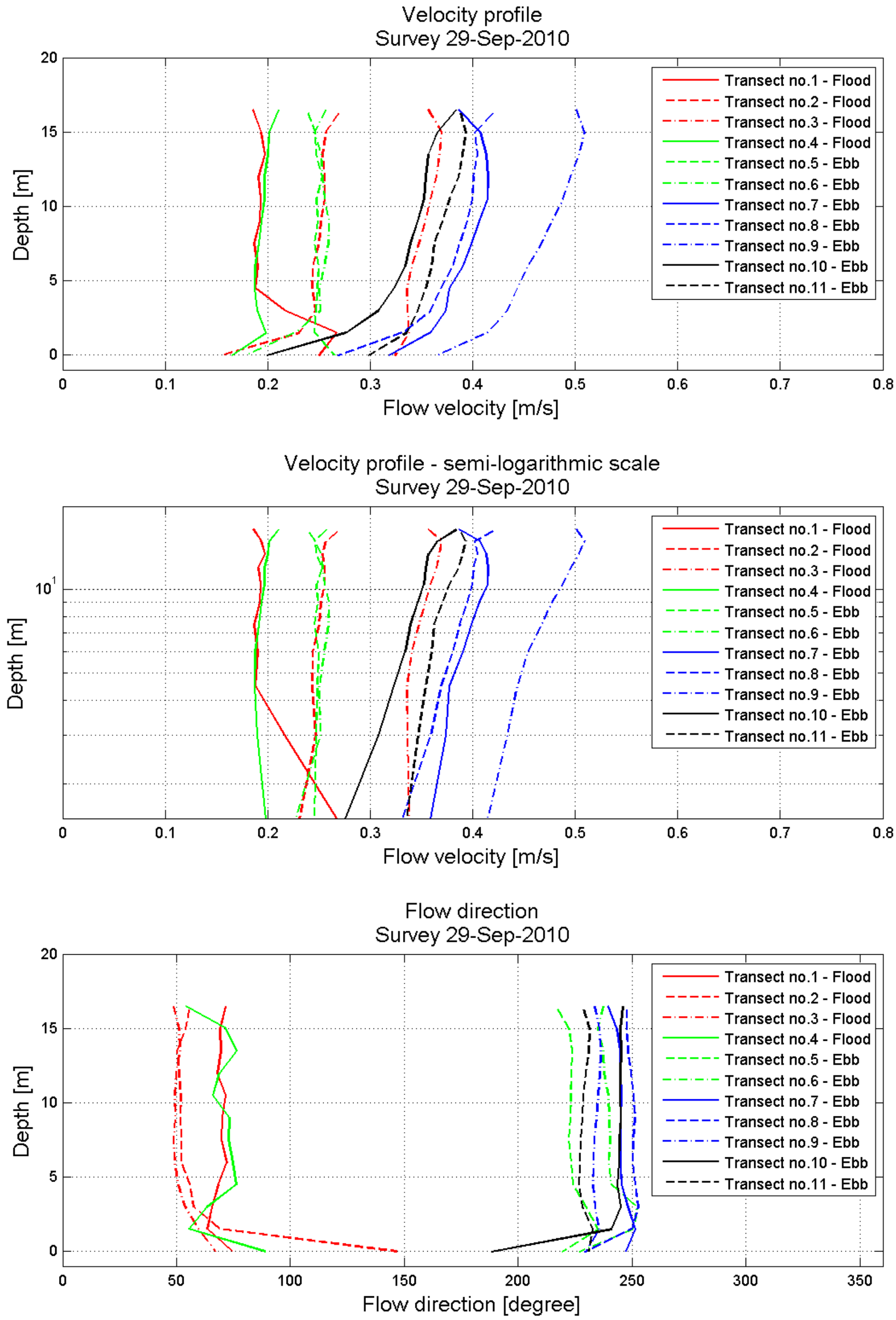

Figure 3.6: Measured vertical velocity distribution for the transects B sailed on September 29^{th}

Chapter 4

Numerical flow model

The current forecasts in the sailing area of the Olympic Games 2012 will be provided by means of a numerical flow model. In section 4.1, a technical description of the numerical flow model used to provide the current forecasts is given. Section 4.2 will thereafter further elaborate on the properties of the numerical model for this specific case, e.g. on the model domain and the computational grid applied. The model calibration process will be considered in section 4.3, where the final model properties will be given as well. Finally, the validation will be considered in section 4.4.

4.1 FINEL2D

Chapter 3 concludes that the vertical velocity profile of the flow is nearly logarithmic. Since the velocity of the main flow is therefore almost constant over the vertical, a two–dimensional, numerical flow model can be used. The effects of other currents can be considered negligible or can easily be superposed to the model results. Therefore, the by Svašek Hydraulics in–house developed two–dimensional depth–averaged numerical flow model FINEL2D[1], which has the Finite Element Method (FEM) as numerical basis, will be used to obtain current forecasts in the sailing area of the Olympic Sailing Games 2012. Both an explicit and implicit version are available[2]; the explicit version will be used.

This section will briefly discuss the depth–integrated shallow water equations, which are the basis of the flow module of FINEL2D. Subsequently, the solution method used to solve these equations will be briefly considered. Special attention will be paid to the numerical diffusivity of the flow model. Besides, it will be discussed how the numerical model accounts for external forces, e.g. wind stresses. Other modules than the flow module, such as e.g. the morphological module MORFIN, will not be discussed here.

4.1.1 Shallow water equations

The water motion can in general be described by the Navier–Stokes equations and the continuity equation. These equations can be simplified by assuming:

[1] http://www.finel.nl

[2] Despite they carry the same name, the two FINEL2D models are two different models, instead of two versions of the same model. The models are popularly designated as the explicit and implicit version to make a distinction, although this is just one of the differences.

- Hydrostatic pressure;
- Uniform velocity in vertical direction;
- Constant density.

Integrating over the vertical and applying these assumptions, results in the well–known shallow water equations, in which equation 4.1 represents the continuity equation and equations 4.2 and 4.3 represent the momentum balance in the x–direction respectively y–direction.

$$\frac{\partial h}{\partial t} + \frac{\partial uH}{\partial x} + \frac{\partial vH}{\partial y} = 0 \tag{4.1}$$

$$\frac{\partial Hu}{\partial t} + \frac{\partial Hu^2}{\partial x} + \frac{\partial Huv}{\partial y} - fHv + gH\frac{\partial h}{\partial x} - \frac{1}{\rho}\left(\tau_{x,b} + \tau_{x,w} + \tau_{x,r}\right) = 0 \tag{4.2}$$

$$\frac{\partial Hv}{\partial t} + \frac{\partial Huv}{\partial x} + \frac{\partial Hv^2}{\partial y} + fHu + gH\frac{\partial h}{\partial y} - \frac{1}{\rho}\left(\tau_{y,b} + \tau_{y,w} + \tau_{y,r}\right) = 0 \tag{4.3}$$

In which:

$$H = h + z_b \tag{4.4}$$

Here u and v represent the flow velocity in the x–direction respectively y–direction, h, z_b and H the water level, bottom level and water depth, f the Coriolis force, g the gravitational acceleration, ρ the density of water and τ_b, τ_w and τ_r the bottom shear stress, the wind shear stress and the radiation stress. Turbulent stresses are not taken into account and the application of the model is therefore restricted to advection dominated flow only.

4.1.2 Solution method

FINEL2D explicit uses FEM to decretise the differential equations. Typical for FEM is that the model domain is divided into a number of elements, in this case triangles. The physical variables are represented by discrete values in each element. The computational mesh can be generated using e.g. grid generator TRIANGLE, which generates a grid with triangular elements. The boundaries of the flow domain can easily be followed and the resolution can be adjusted locally, through which high resolution can be obtained in the area of interest and low resolutions in the area where this is allowed [5]. Besides, the grid boundaries and resolutions can be clicked in Google Earth, by which grid generation has become relatively easy.

The discontinuous Galerkin method is adopted to solve for the differential equations. Within this method, the water level and the two horizontal velocity components are taken constant in each element. This is shown in figure 4.1. To apply the discontinuous Galerkin method, the equations of motion, shown in equations 4.1, 4.2 and 4.3, are rewritten as:

$$\frac{\partial}{\partial t}U + \frac{\partial}{\partial x}F_x + \frac{\partial}{\partial y}F_y = S_1 + S_2 \tag{4.5}$$

In which:

$$U = \begin{pmatrix} H \\ uH \\ vH \end{pmatrix}, \quad F_x = \begin{pmatrix} uH \\ u^2H + \frac{gH^2}{2} \\ uvH \end{pmatrix}, \quad F_y = \begin{pmatrix} vH \\ uvH \\ v^2H + \frac{gH^2}{2} \end{pmatrix},$$

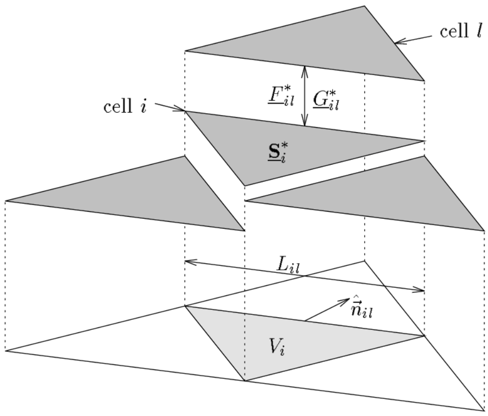

Figure 4.1: Discontinuous Galerkin Method [5]

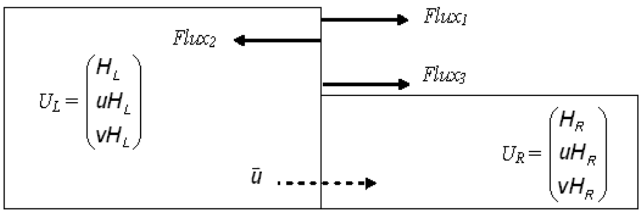

Figure 4.2: Discontinuity at element boundary, with Roe fluxes, for subcritical flow [5]

$$S_1 = \begin{pmatrix} 0 \\ gH\dfrac{\partial z_b}{\partial x} \\ gH\dfrac{\partial z_b}{\partial y} \end{pmatrix}, \quad S_2 = \begin{pmatrix} 0 \\ \dfrac{1}{\rho}\tau_{x,tot} - fv \\ \dfrac{1}{\rho}\tau_{y,tot} + fu \end{pmatrix}$$

For the discontinuous Galerkin method, the rewritten equations of motion are integrated over each element, resulting in:

$$\int_\Omega \frac{\partial}{\partial t} U \, \mathrm{d}\Omega + \int_\Gamma (F_x \cdot n_x + F_y \cdot n_y) \, \mathrm{d}\Gamma = \int_\Omega (S_1 + S_2) \, \mathrm{d}\Omega \tag{4.6}$$

In equations 4.6 and 4.5, Ω represents the element surface, Γ the element boundary and n the outward pointing unit vector normal to the element contour. Furthermore, F_x and F_y represent the fluxes, and contain the advective terms with the pressure gradient and mass flux. S_1 and S_2 represent the source terms, where S_1 contains the influence of the bottom slope and S_2 contains the external forces, e.g. the Coriolis force and shear stresses [5].

The flow variables are defined in the centre of the elements, whereby the fluxes F_x and F_y are not known beforehand. The fluxes can be constructed by solving a local Riemann problem. The explicit version of FINEL2D applies the approximate Riemann solver according to Roe, to calculate the fluxes over the boundaries. Besides F_x and F_y, S_1 is also taken into account by the Roe solver, since the bottom level within an element is taken constant, and the bottom slope is therefore not known beforehand as well [5]. The Roe solver calculates the bottom slope by means of the bottom levels in the separate elements.

To solve the local Riemann problem, equation 4.5 is rewritten to:

$$\frac{\partial}{\partial t} U + \frac{\partial F_x}{\partial U} \frac{\partial U}{\partial x} + \frac{\partial F_y}{\partial U} \frac{\partial U}{\partial y} = S_1 \tag{4.7}$$

Here, $\frac{\partial F_x}{\partial U}$ and $\frac{\partial F_y}{\partial U}$ represent the flux Jacobians. Neglecting the source term, this can subsequently be rewritten to:

$$\int_{\Omega} \frac{\partial}{\partial t} U \, \mathrm{d}\Omega + \oint A \left(U_{neighbour} - U \right) \mathrm{d}\Gamma = 0 \tag{4.8}$$

Here, $U_{neighbour}$ represents the flow in the neighbouring element. Matrix A is defined by:

$$A = \left(\frac{\partial F_x}{\partial U}, \frac{\partial F_y}{\partial U} \right) \cdot \vec{n} \tag{4.9}$$

Matrix A, as defined in equation 4.9, has three real eigenvalues, which form the characteristics along which the fluxes propagate. The abrupt change in flow variables at every element boundary can be interpreted as two step waves and a shear wave, which, in case of subcritical flow, propagate downstream along two of the characteristics and upstream along one characteristic, as sketched in figure 4.2. Every element has tree boundaries on which the three Roe fluxes are determined, by means of the eigenvalues, eigenvectors and wave strengths. These fluxes along the three boundaries together, by adding them to the flow variables of the element, determine the total change of the flow variables in an element in one time step [5].

In mathematical terms, the Roe solver in FINEL2D is a first order upwind scheme. This scheme does cause some numerical diffusion, which will be further discussed in section 4.1.3, but guarantees strict mass and momentum conservation. Furthermore, the explicit integration in time in FINEL2D restricts the time step. The time step is therefore controlled automatically, in order to achieve optimal performance [5].

4.1.3 Turbulence modelling

The explicit version of FINEL2D will be used to perform the calculations, because it has several advantages with respect to the implicit version. These advantages are:

- Performs calculations in parallel, i.e. several processors can be drawn on at the same time;
- TPXO points (only reliable in deep water) can be taken as boundary conditions, since there is barely a limit on the size of the model domain;
- Directly linked to e.g. the wave model SWAN.

The solver in FINEL2D has however the disadvantage of causing numerical diffusion. Since the transient tidal eddies are the most distinct features of the flow in the sailing area of the Olympic Games 2012, it is important that the tidal eddies are modelled sufficiently accurate. Due to the formation of the tidal eddies, horizontal velocity gradients arise and the horizontal eddy viscosity may become important, and this numerical diffusion may become a problem.

The artificial horizontal eddy viscosity, which is responsible for the diffusion, in the explicit version of FINEL2D can be estimated according to the following equation:

$$\nu_t^H = \frac{1}{2}|u|\Delta x \tag{4.10}$$

Here ν_t^H represents the horizontal eddy viscosity, $|u|$ the average flow velocity of the main flow and Δx the size of the grid elements. With an average flow velocity of 1 m/s and elements with a grid size of 500 m, the viscosity in the explicit numerical flow model is approximately 250 m^2/s. Considering the flow properties however, a good estimation for the true eddy viscosity would be $\mathcal{O}(10^{-1})$ m^2/s or even $\mathcal{O}(10^{-2})$ m^2/s. This eddy viscosity is however based on diffusivity only. When accounting for dispersion as well, the true eddy viscosity will be $\mathcal{O}(10^{0})$ m^2/s or $\mathcal{O}(10^{-1})$ m^2/s. The difference between the calculated eddy viscosity and this estimation is several orders of magnitude, and the explicit model is therefore believed too dissipative.

Since the difference in eddy viscosity is large, several test runs with both models explicit version of FINEL2D and the implicit version of FINEL2D, where the viscosity can be set manually, have been performed in order to examine the influence of the viscosity on the model results. The set up of these test runs, and the result from the test runs are discussed in Appendix B.

Both the implicit and explicit versions of FINEL2D have shown similar results, when elements with a grid size of 100 m were used. The corresponding eddy viscosity in the explicit model is approximately 50 m^2/s. The difference in flow velocities are approximately only $\mathcal{O}(10^{-2})$ m/s, and the influence of the viscosity can therefore be considered actual, but limited. Moreover, the differences in flow velocity decrease when the computational grid will be further refined, by which is it justified to use the explicit version of FINEL2D to provide the current forecasts. The refinement of the mesh will be further discusses in section 4.2.2.

4.1.4 External forces

FINEL2D takes the influence of external forces into account by defining the wind shear stress, bottom friction, wave–induced shear stress and the Coriolis force separately for every element, and by integrating these stresses over the element surface. The paragraphs below discuss the several stresses in more detail. The explicit version of FINEL2D does not take turbulent shear stresses into account. When this is desirable, the other FINEL2D version, the so–called implicit version, should be used. Section 4.1.3 and Appendix B have shown this is not essentially necessary.

Wind shear stress

To account for the wind drag on the water surface, the wind shear stress is calculated in each element by using both the wind speed and wind direction at 10 m elevation, and a wind drag factor. The wind shear stress is calculated by:

$$\frac{1}{\rho}\tau_{x,w} = C_D\left(u_{wind,10} - u\right)\sqrt{(u_{wind,10})^2 + (v_{wind,10})^2} \tag{4.11a}$$

$$\frac{1}{\rho}\tau_{y,w} = C_D\left(v_{wind,10} - v\right)\sqrt{(u_{wind,10})^2 + (v_{wind,10})^2} \tag{4.11b}$$

Here, C_D represent the wind drag.

Bottom friction

To account for the influence of bottom roughness on the flow, the bottom shear stress is calculated in each element by applying the following equations:

$$\frac{1}{\rho}\tau_{x,b} = -u\frac{g\sqrt{u^2+v^2}}{C^2H} \tag{4.12a}$$

$$\frac{1}{\rho}\tau_{y,b} = -v\frac{g\sqrt{u^2+v^2}}{C^2H} \tag{4.12b}$$

Here, C represents the bottom roughness, which can be given by specifying one of the following parameters:

- The Nikuradse roughness k_n;
- The Chézy value C;
- The Manning roughness n.

For generating current forecasts in the Weymouth and Portland area, the Nikuradse roughness is applied. For each element, a separate roughness is defined. The Nikuradse roughness is converted into the bottom roughness by applying:

$$C = 18\log\left(\frac{12H}{k_n}\right) \tag{4.13}$$

Wave–induced shear stress

In FINEL2D wave fields can be included in the calculations. The wave fields however, have to be generated by other software, e.g. the wave model SWAN, and have to be interpolated to the FINEL2D mesh. FINEL2D can be linked directly to SWAN in order to do so.

Coriolis force

Due to the rotation of the earth, the flow direction deviates to the right on the Northern Hemisphere. The influence of earth's rotation on the flow direction, is in the momentum equations captured by the Coriolis terms, and depends on the latitude. The Coriolis force is given by:

$$f = 2\Omega\sin(\phi) \tag{4.14}$$

Here, ϕ represents the model latitude and Ω represents the angular velocity of the earth, which is $7.27 \cdot 10^5$ rad/s. The latest FINEL2D version, version 7.0, is used. This version has the option of defining the latitude for each element separately.

4.2 European Continental Shelf Model

To provide current forecasts for the 2012 Olympic Sailing Competition, FINEL2D is applied onto the so–called European Continental Shelf Model (ECSM), which is shown in figure 4.3. This section will be used to discuss the model domain, the boundary conditions and the computational mesh.

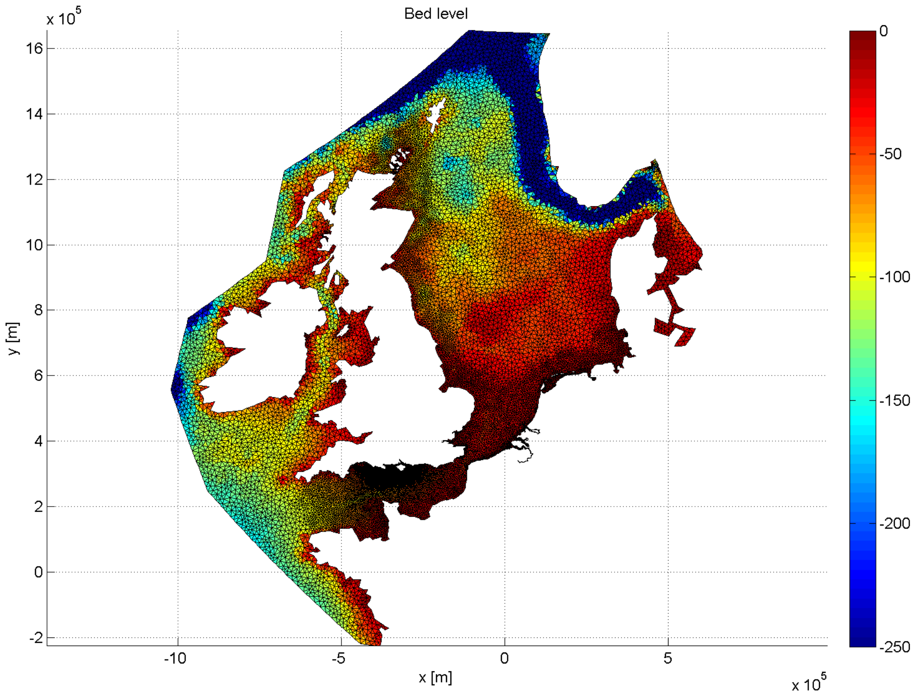

Figure 4.3: European Continental Shelf Model

4.2.1 Model domain and boundary conditions

The model domain of the ECSM model is fairly large. The model boundaries follow a large part of the North–West European coast, and the boundaries facing sea are all located in the deeper parts of the Atlantic Ocean. The availability of reliable and accurate boundary conditions have been the main reasons to choose such a large model domain.

Boundary conditions in the form of water levels can be provided by the TPXO model, which provides the 13 principal harmonic constituents of the tidal wave at every quarter degree over the entire ocean. Section 2.2.2 and Appendix A, discuss the reliability of the TPXO model and conclude that the TPXO model is only reliable in deep water, which means the model boundaries have to be placed in deep water by which the model domain becomes fairly large. When it is desirable to keep the model domain limited (the model shown in figure 4.3 consists of approximately 200.000 elements), e.g. to keep the calculation time limited, reliable boundary conditions can be achieved by nesting. In that case a (smaller) model, with for instance the size of the English Channel, can be nested into a larger model which has its boundaries in deep water.

However, FINEL2D is a powerful model and is able to perform calculations in parallel mode, i.e. several processors can be drawn on at the same time, by which there are hardly limits on the size of the model domain, and the calculation time for the ECSM model is still limited. Since nesting can be a tricky and time consuming procedure, it is decided to use the fairly large ECSM model and apply the TPXO model version 7.2 onto the model boundaries. The provided constituents are the M_2, S_2, N_2, K_2, K_1, O_1, P_1, Q_1, MF, MM, M_4, MS_4 and the MN_4 constituent.

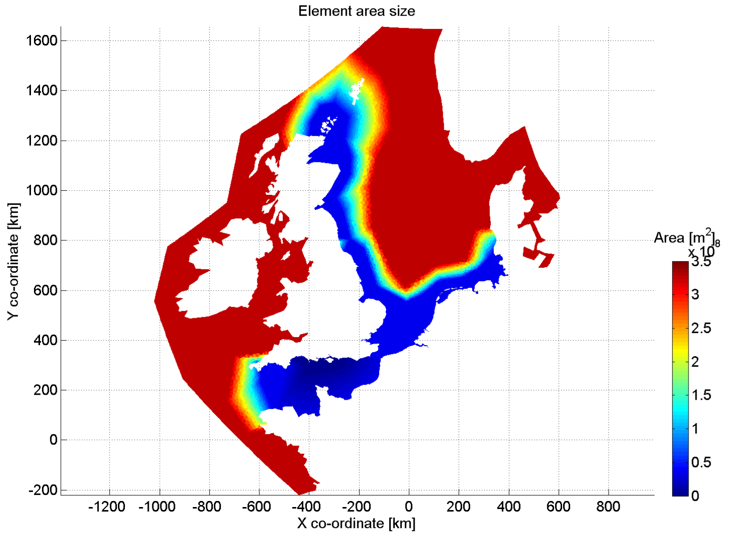

(a)

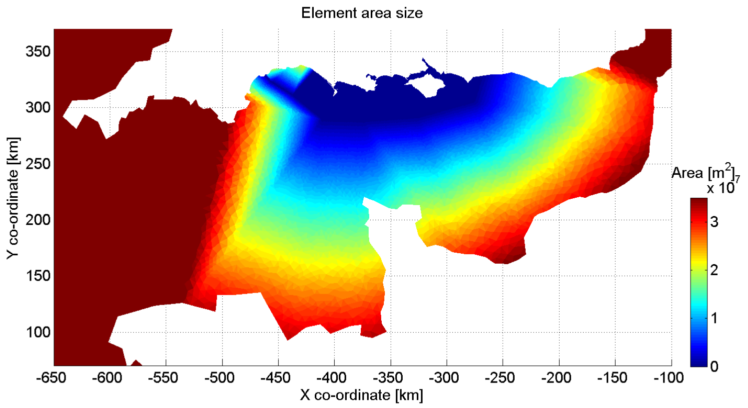

(b)

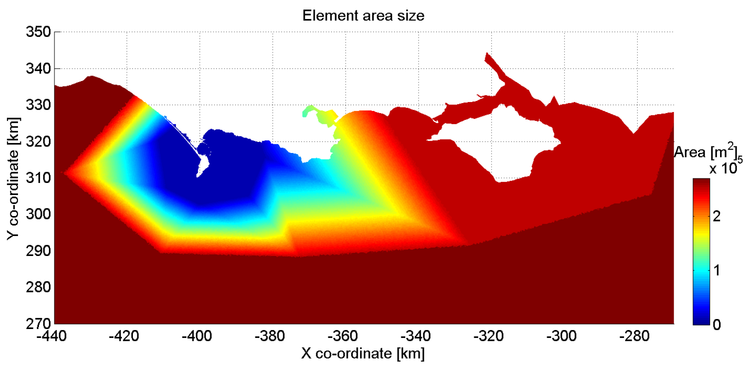

(c)

Figure 4.4: Maximum element size of the ECSM computational mesh

4.2.2 Mesh

FINEL2D uses FEM to decretise the differential equations. Typical for FEM is that the model domain is divided into a number of elements, in this case triangles, by which the element size may vary throughout the model domain. This way, a high resolution can be obtained in the area of interest, which is the Weymouth and Portland area, and low resolutions in the area where this is allowed. Therefore, the model domain has been divided into several areas before the mesh was generated, and each area has been given a maximum element size. The maximum element size varies from 12 km by 12 km at the sea boundaries to 100 m by 100 m in the Weymouth and Portland area.

In section 4.1.2 it appeared the solver of FINEL2D has the disadvantage of producing some numerical diffusion. Section 4.1.3 and Appendix B subsequently, have further elaborated the subject, and have shown that the eddy viscosity, which is responsible for this numerical diffusion, is related to the element size. The model results for a mesh with elements of maximum 500 m by 500 m in the area of interest, have been compared to model results for a mesh with elements of maximum 100 m by 100 m in the area of interest. Since the difference in flow velocity was only $\mathcal{O}(10^{-2})$ m/s, the influence of the eddy viscosity on the model results has been considered actual, but limited.

In order to further exclude numerical diffusion, the mesh is further refined once more, with elements of maximum 75 m by 75 m in the area of interest. The differences in flow velocities achieved with this refinement is only $\mathcal{O}(10^{-3})$ m/s, and are therefore considered negligible. Since the calculation time is related linearly to the number of elements, and hence increases with each refinement, and the latest refinement had hardly any affect, no further refinements have been performed. The maximum element size in the area of interest is therefore set to 100 m by 100 m. Figure 4.4 shows graphically how the maximum element size varies throughout the model domain. The computational mesh of the ECSM model itself, which is generated with the grid generator TRIANGLE, is visible in figure 4.3. The mesh consists of approximately 200.000 elements.

4.3 Calibration

In order to achieve the optimal model performance, the ECSM model is calibrated by comparing the model results to the survey results and by adjusting the settings of the numerical flow model where necessary. Thus, the global latitude is replaced by a latitude for each grid element separately, and an optimal model play–in time[3], which finally has been set to 3 days, has been found. Besides, adjustments have been made in the bottom roughness. First, the global roughness is adjusted in order to account for the water levels. The flow velocities and directions have improved by these adjustments as well. Next, in order to further improve the flow velocities and directions, adjustments in the bottom roughness have been made locally. These adjustments, and the influence of these adjustments on the water levels and flow velocities, will be discussed more extensively in the following sections.

4.3.1 Global Nikuradse roughness

In order to calibrate the numerical model, adjustments of the global bottom roughness have been made. First, the sensitivity of the numerical model to the bottom roughness is investi-

[3]Time the numerical flow model needs to remove transients from the solution.

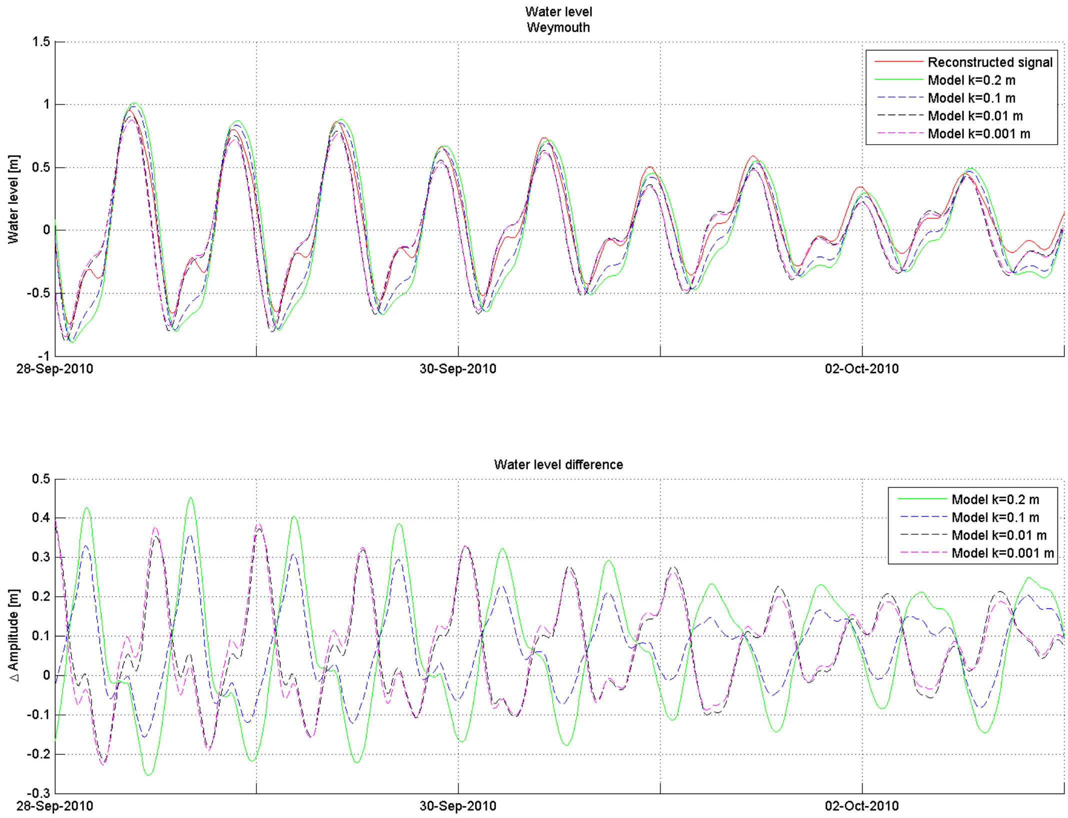

Figure 4.5: Water levels at Weymouth for several roughnesses. The reconstructed signal are predicted water levels, based on by tidal analysis obtained harmonic constituents.

gated, by simply trying several different global roughnesses. The Nikuradse roughnesses used are:

- $k_n = 0.001\,\text{m}$;
- $k_n = 0.01\,\text{m}$;
- $k_n = 0.1\,\text{m}$;
- $k_n = 0.2\,\text{m}$.

The computed water levels at Weymouth for these roughnesses, which are shown in figure 4.5, show that varying the roughness has a distinct influence on the water levels, which means the numerical flow model is sensitive to the bottom roughness. Figure 4.5 also shows the difference between the model results and tidal predictions based on an extensive tidal analysis. A Nikuradse roughness between 0.01 m and 0.1 m seems best for Weymouth. When however considering the water levels at other locations in the English Channel, it appears a Nikuradse roughness between 0.01 m and 0.1 m, is not ideal everywhere. For the water levels at Devonport for instance, shown in figure 4.6, a Nikuradse roughness between 0.1 m and 0.2 m results in better water levels. Due to the model's sensitivity to the bottom roughness, it is

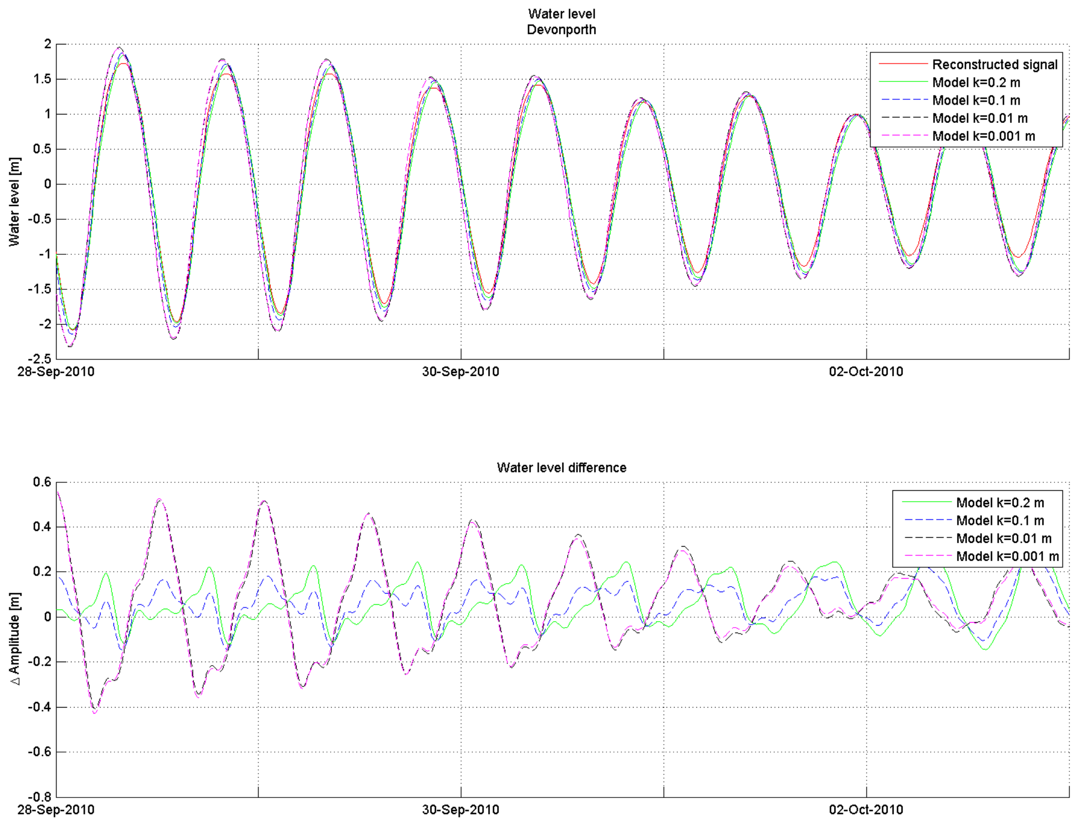

Figure 4.6: Water levels at Devonport for several roughnesses. The reconstructed signal are predicted water levels, based on by tidal analysis obtained harmonic constituents.

difficult to model the water levels perfectly everywhere. Since however the area of interest is the Weymouth and Portland area, it is decided to concentrate on finding the global roughness which gives the best results for the water levels at Weymouth, even if the water levels at e.g. Devonport become less good. In the next section, the water levels at other locations will be calibrated as well, by adjusting the roughness locally.

In order to investigate the influence of the bottom roughness on the flow, time series of the flow velocities and flow directions of 4 locations (A, B, C and D) are compared to time series of the measured flow velocities and directions at those locations. The locations considered are shown in figure 4.7. The measurements at the fifth and sixth location (E and F) indicated in the graph will be used for the verification of the flow model.

The flow velocities and flow directions for location A and B are shown in figure 4.8; the flow velocities and flow directions for location C and D in figure 4.9. For the flow velocities, a Nikuradse roughness between 0.01 m and 0.1 m seems best as well. For the flow directions however, a roughness between 0.1 m and 0.2 m, and therefore a higher roughness than for the water levels seems more appropriate. Remarkable is the phase shift up to several hours which occurs in the flow due to variations in the bottom roughness. The absolute flow velocity seems less sensitive to the variations.

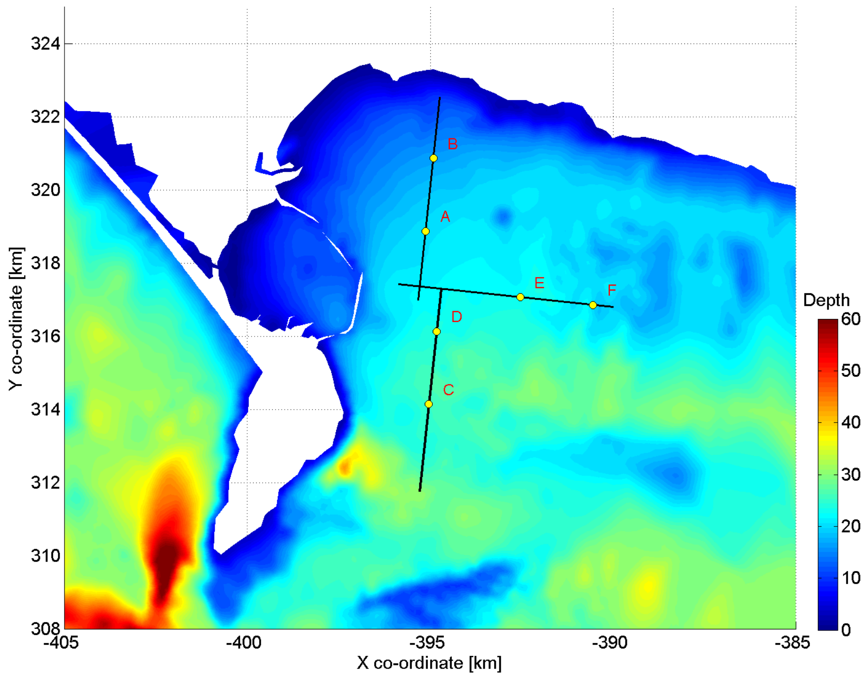

Figure 4.7: Locations used to calibrate the flow velocities

Since the flow direction is very sensitive to variations of the bottom roughness, it is expected that this flow direction can be further improved by means of increasing the bottom roughness locally, which will be considered in the next section. Therefore, it is decided to focus on finding the Nikuradse bottom roughness which leads to the water levels respectively flow velocities, which match the measurements flow velocities. A systematic investigation of the roughness value has been carried out. The water levels at Weymouth for a Nikuradse roughness of 0.05 m, 0.035 m and 0.02 m are shown in figure 4.10. The flow velocities and flow directions at locations A and B are shown in figure 4.11; the results for location C and D are shown in figure 4.11.

A roughness of 0.035 m is considered best for the water levels. The water level deviation amounts approximately 10 %. Since the objective is to provide current forecasts, the water levels are less important. A water level deviation of maximum 10 % is therefore acceptable. For the flow velocities, Nikuradse roughnesses of 0.035 m and 0.05 m lead to approximately equal deviations. In general, the differences between the measured flow velocity and the modelled flow velocity are $\mathcal{O}(10^{-2})$ m/s, which is approximately 10 % as well. Since the water levels have a better reproduction with a roughness of 0.035 m, a Nikuradse bottom roughness of 0.035 m is finally chosen as the global Nikuradse roughness.

4.3.2 Local Nikuradse roughness

In the preceding section, it has become clear that the global Nikuradse roughness, which is set to 0.035 m, is not ideally chosen with respect to the water levels of some locations outside the Weymouth and Portland area. By adjusting the bottom roughness locally, it has been tried

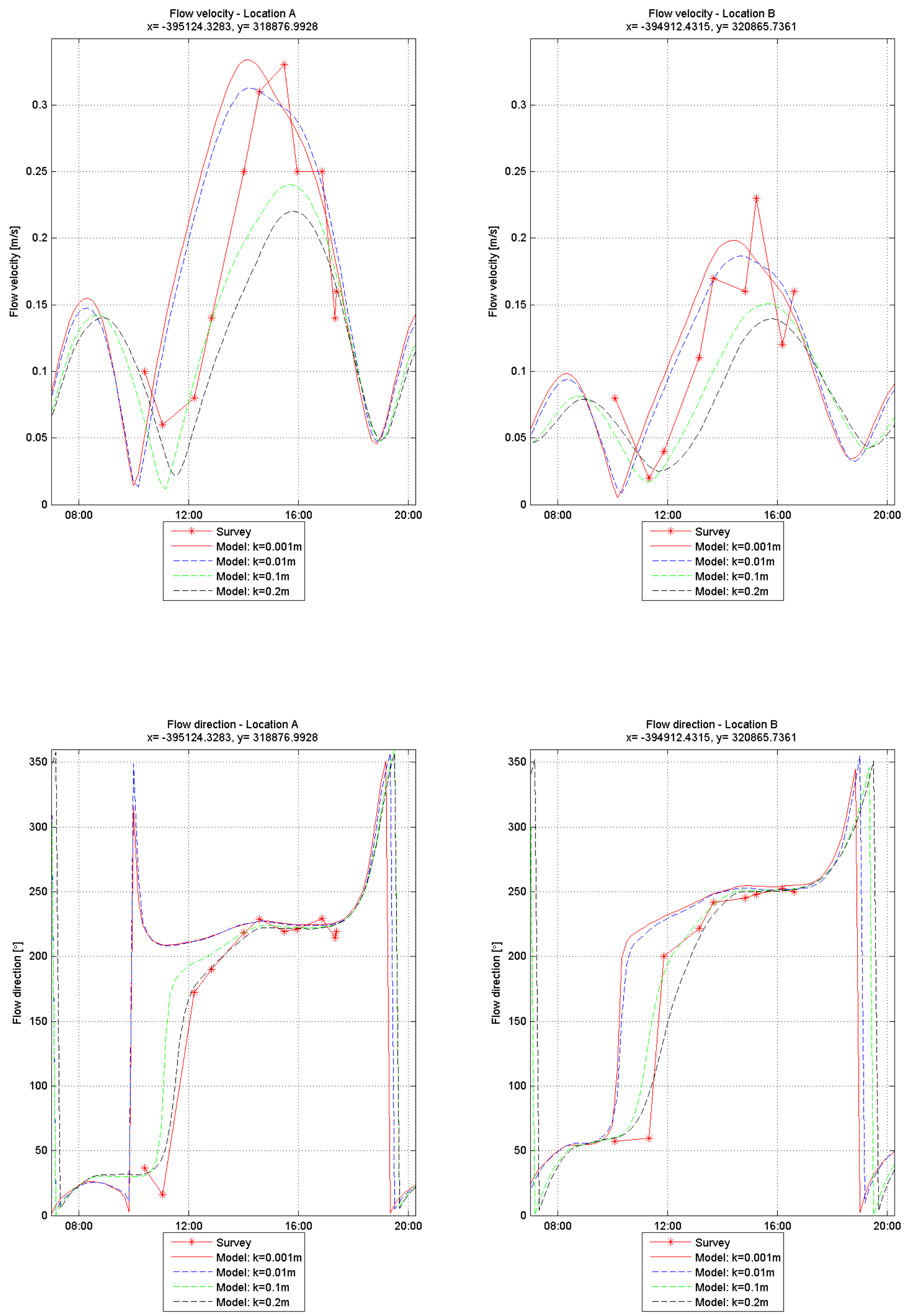

Figure 4.8: Flow velocity and direction at locations A and B

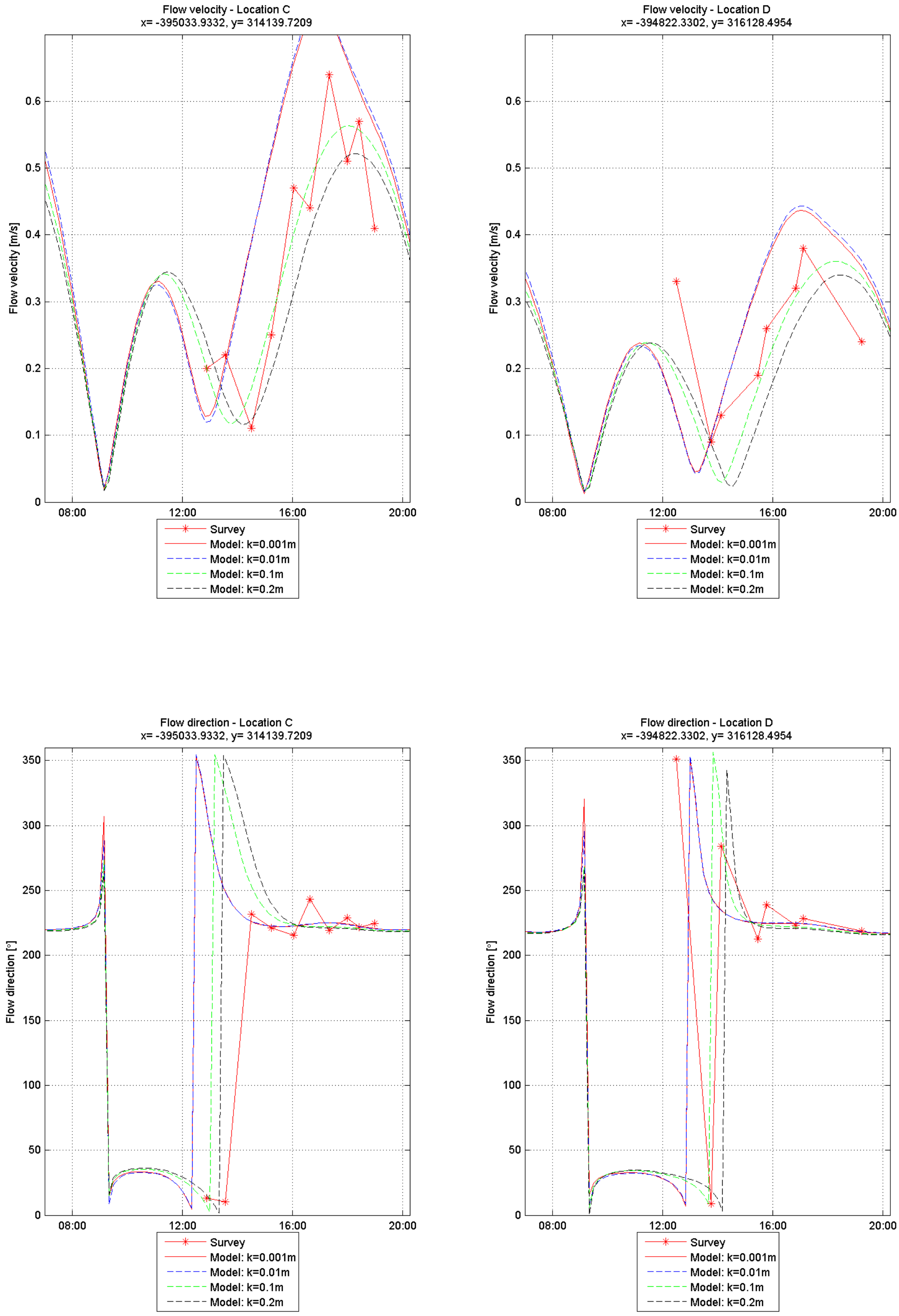

Figure 4.9: Flow velocity and direction at locations C and D

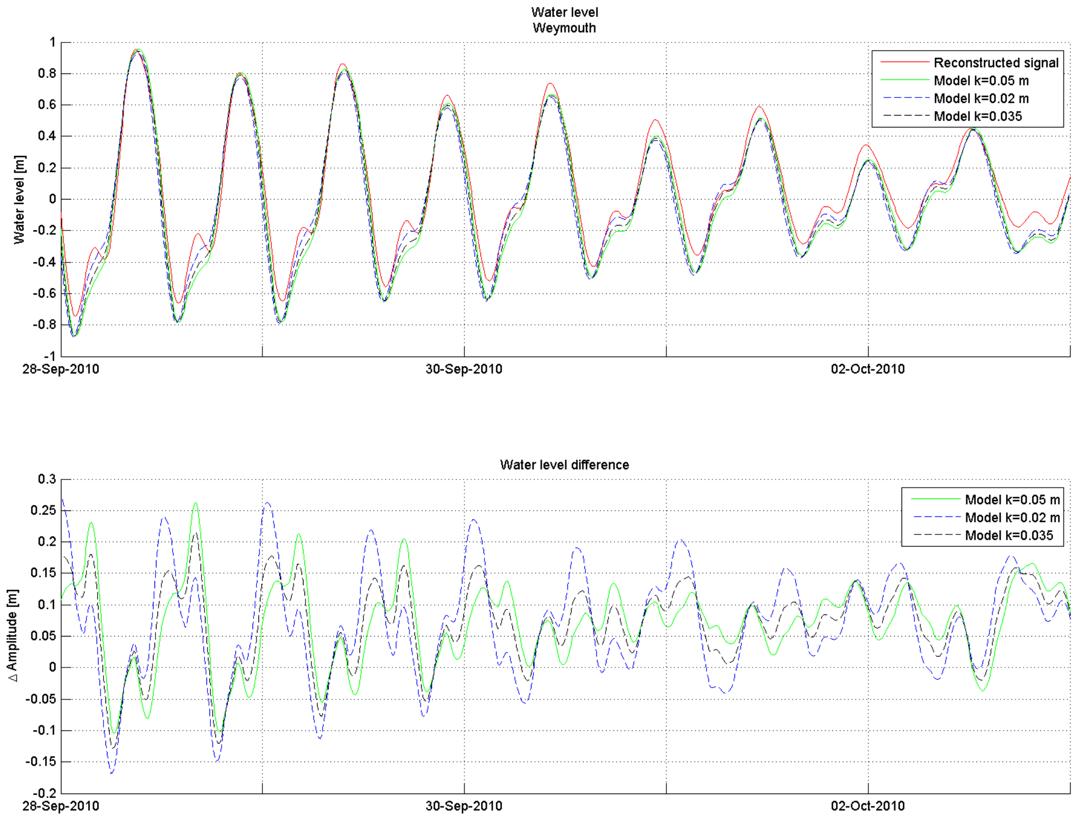

Figure 4.10: Water levels at Weymouth for several roughnesses. The reconstructed signal are predicted water levels, based on by tidal analysis obtained harmonic constituents.

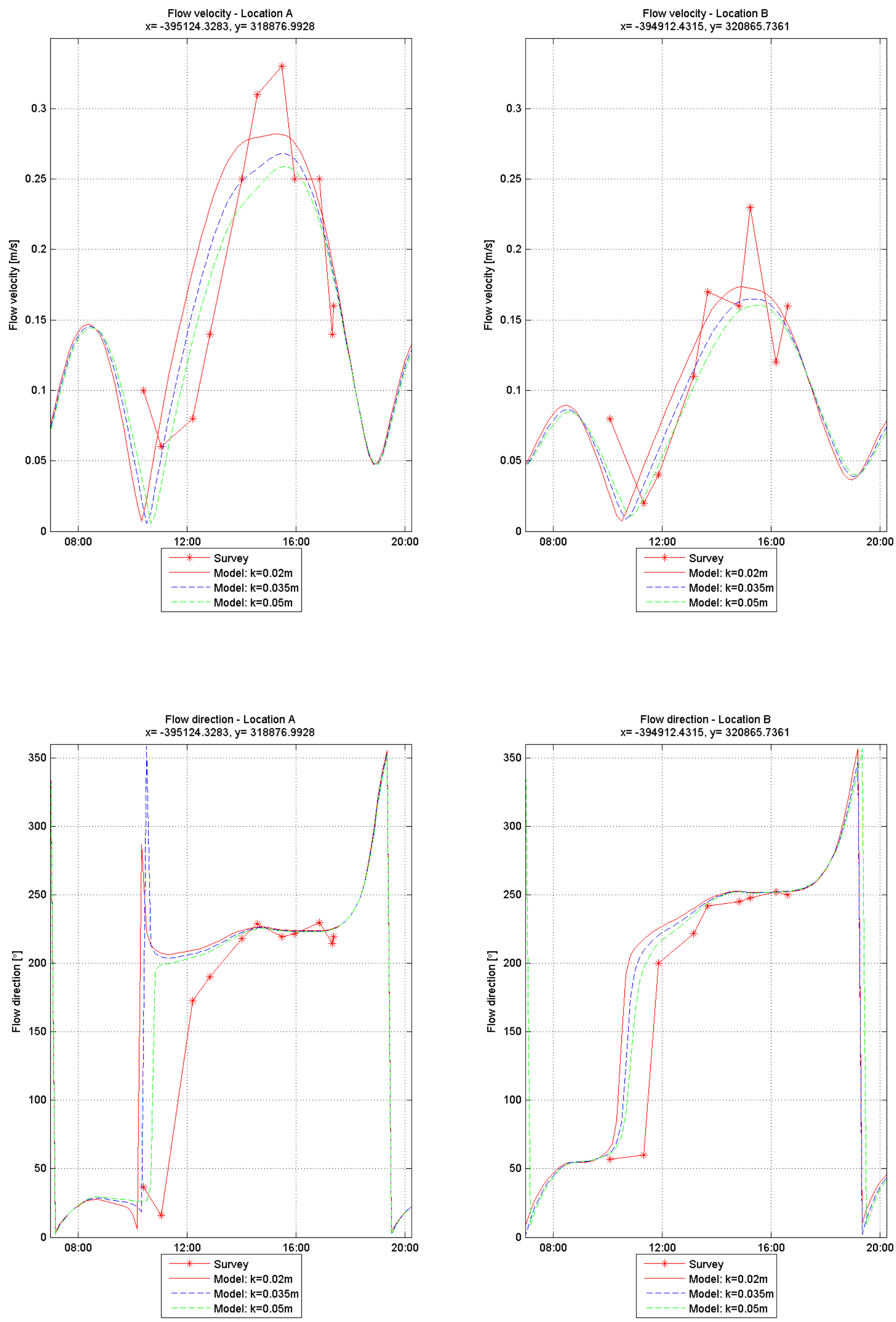

Figure 4.11: Flow velocity and direction at locations A and B

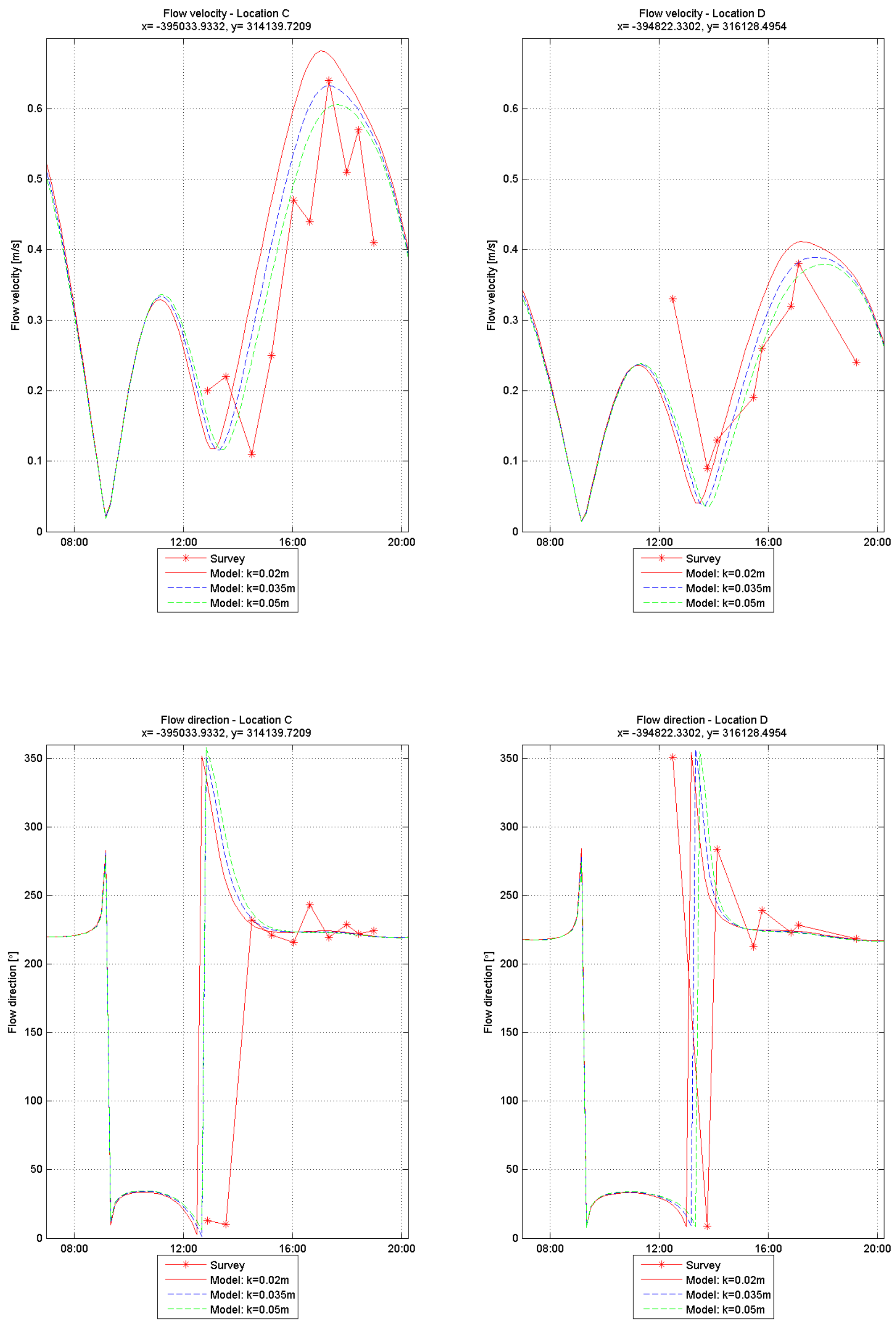

Figure 4.12: Flow velocity and direction at locations C and D

to improve the water levels outside the Weymouth and Portland area. These adjustments however, appeared to have a significant influence on the water levels in the Weymouth and Portland area. Since it is difficult to model to water levels correctly throughout the entire model domain, it is decided to focus on the Weymouth and Portland area only.

Now the water levels and absolute flow velocities in the Weymouth and Portland area are modelled fairly good, the flow directions are considered. The measured flow and the modelled flow for a global roughness of 0.035 m are given in figure 4.14 for location A and B, and in figure 4.15 for location C and D. Especially in the flow velocities and directions at location A, B and C, a phase lag of approximately half an hour is visible. Since the flow direction has appeared to be very sensitive to variations of the bottom roughness, it is expected this phase lag in the flow can be influenced by adjusting the bottom roughness locally.

In order to determine where to adjust the bottom roughness, the bottom composition is examined. In section 2.1 is already mentioned that parts of the coast are rocky. Besides, the Shambles Bank, a bank with large sand dunes, is located east of Portland Bill. The bottom roughness in these two areas is significantly larger than in the rest of the area, and therefore the Nikuradse roughness of these areas is increased; a Nikuradse roughness of 0.25 m is taken as a start value. A gradual transition between the area with the Nikuradse roughness of 0.035 m and the area with the roughness of 0.25 m is made as well. The top figure of figure 4.13 shows the Nikuradse bottom roughness in the Weymouth and Portland area in the new situation. Since FINEL2D calculates the flow by means of the Chézy roughness, the Chézy roughness for the Weymouth and Portland area is shown in the bottom figure of figure 4.13. The figure indicates that the Chézy roughness around the Portland peninsula and at the Shambles bank is between approximately $50\,\mathrm{m}^{(}0.5)/\mathrm{s}$ and $60\,\mathrm{m}^{(}0.5)/\mathrm{s}$, which are realistic values for the bottom roughness.

The model results with and without the locally adjusted bottom roughness are shown in figure 4.14 and figure 4.15 as well. For both locations A, B, C and D a clear phase shift towards the measurements has occurred. Locations A, B and C still have a minor phase shift, but in case of location D, the phase shift is considered to be a little to large. Despite that minor phase shifts are still present, the model results have been clearly improved by increasing the bottom roughness locally to 0.25 m. The water levels are not affected by the local adjustment of the bottom roughness. Since the differences between the measurements and the model results have become so small, it is decided not to further adjust the bottom roughness.

4.4 Validation

The ECSM model is validated by comparing the measured flow velocity and direction at location E and F to the model results. The results are shown in figure 4.16 and figure 4.17. The figures show that the model results correspond fairly well to the measured flow velocities and directions. The modelled flow velocities and directions along the transects have been compared to the measured flow velocities and directions along the transects as well. Examples of the results of the comparison of the measured and modelled flow velocities and directions for transect A are shown in figure 4.18, for transect B in 4.19 and for transect C in figure 4.20. For the sake of completeness, the results for all other sailed transects are given in Appendix E. Separate graphs of both the flow velocity and flow direction are given in the two top figures of figure 4.18 until figure 4.20, in order to indicate the absolute difference in

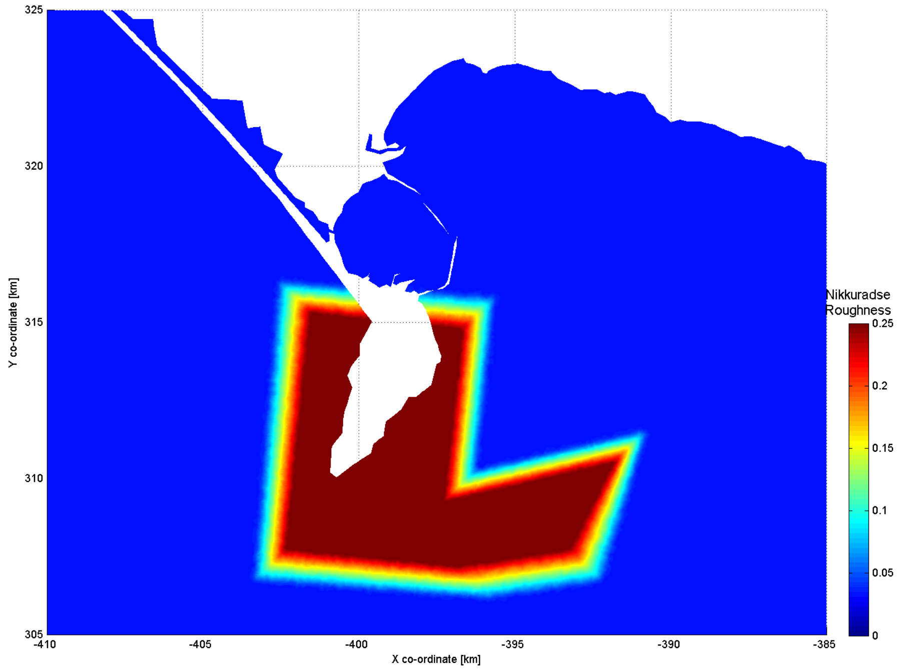

(a) Roughness according to Nikuradse

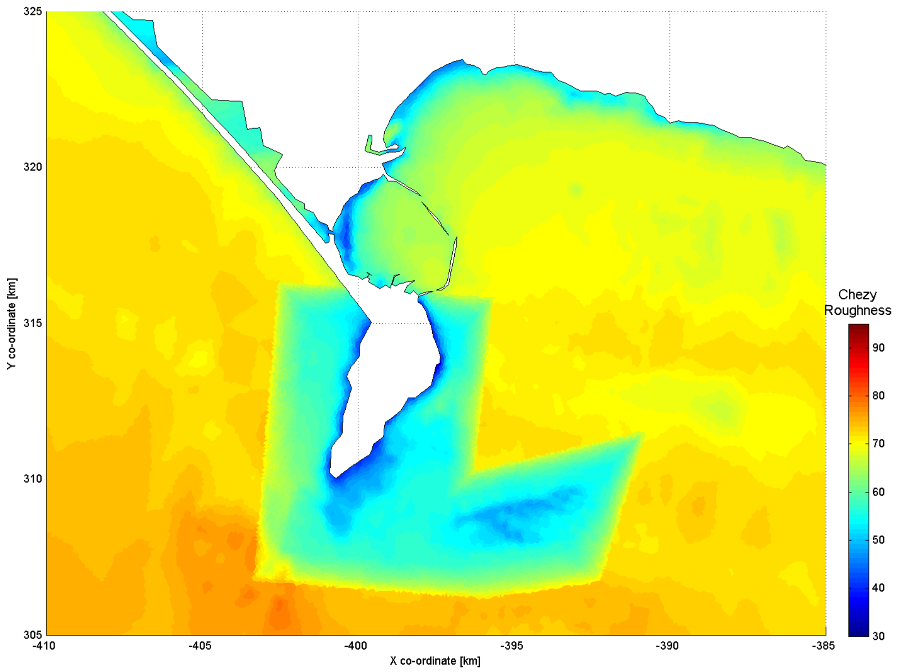

(b) Roughness according to Chézy

Figure 4.13: Bottom roughness in the Weymouth and Portland area

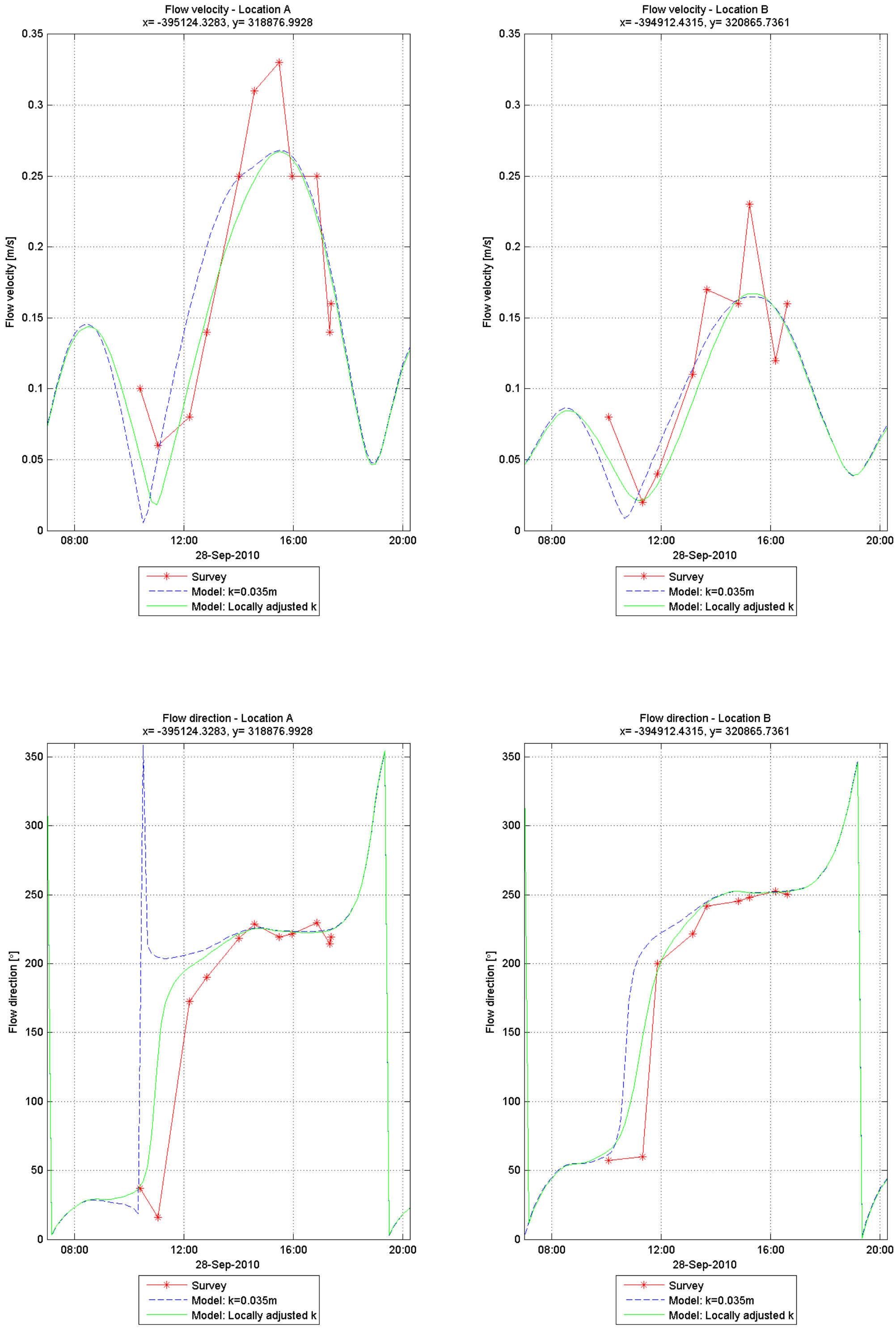

Figure 4.14: Flow velocity and direction at locations A and B

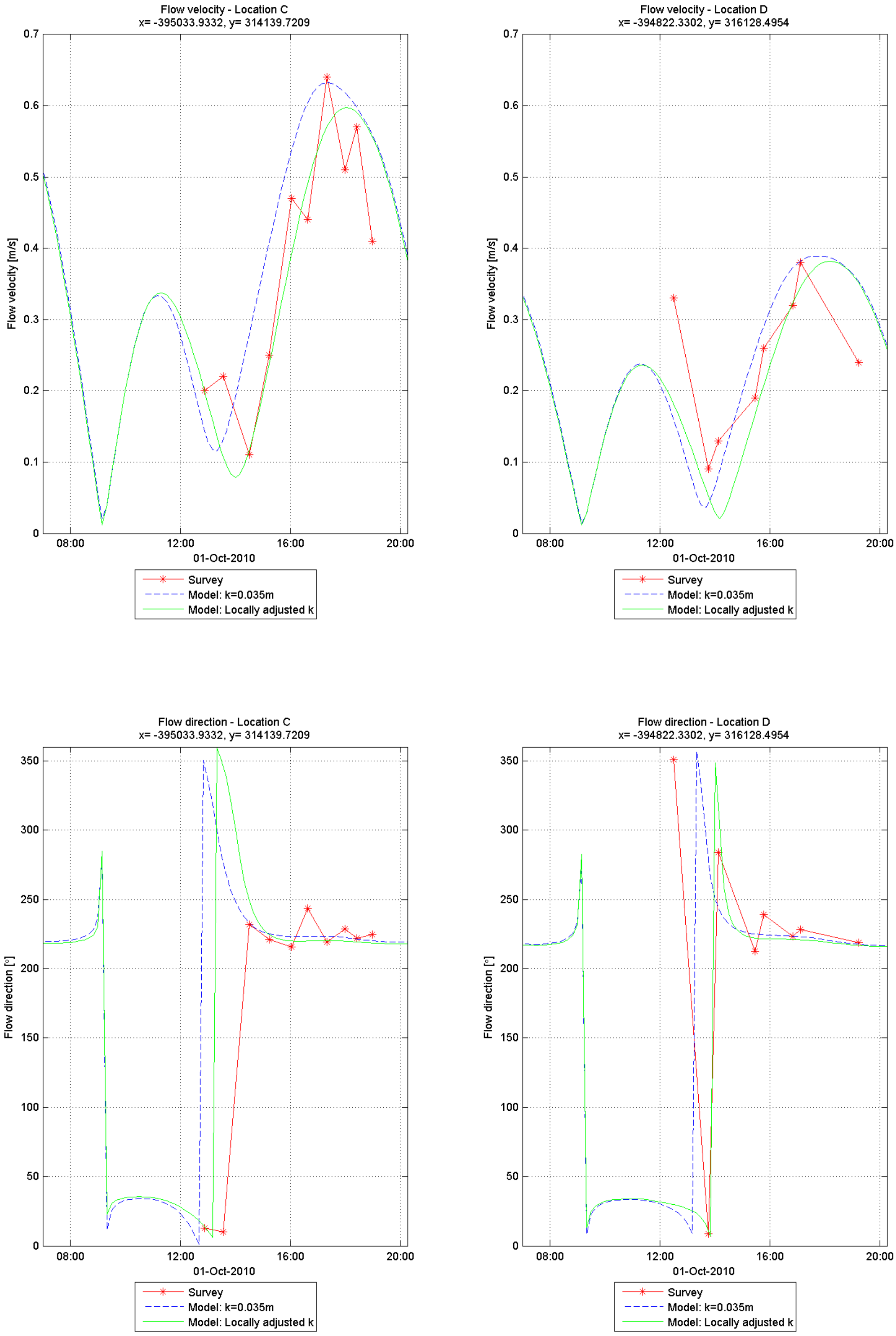

Figure 4.15: Flow velocity and direction at locations C and D

velocity and direction. In the bottom figure, the flow is visualised by means of vectors, by which the direction of the vector indicates the flow direction, and both the colour and the length of the vector indicate the flow velocity.

Figure 4.18 until figure 4.20 and the figures in Appendix E show that the model results correspond fairly well to the measured flow velocities and directions. Where figure 4.16 and figure 4.17 have shown that the flow is modelled good considering time series, these figures indicate that the flow is modelled spatially correct as well. Since both variations of the flow in space and in time are of importance to the Dutch Olympic Sailing Team, and the measured and modelled flow correspond good, the numerical flow model can be well used to provide current forecasts for the 2012 Olympic Sailing Competition. Further adjustments to the model settings are considered unnecessary.

4.5 Conclusion

Since in Chapter 3 is concluded that the vertical velocity distribution of the flow in the sailing area of the 2012 Olympic Sailing Competition is nearly logarithmic, and the main flow is therefore almost constant over the vertical, it has been decided to use the two–dimensional, depth–averaged numerical flow model FINEL2D. The solver of the explicit version of FINEL2D produces some numerical diffusion. Since the artificial horizontal eddy coefficient, which is responsible for this diffusion, is coupled to the size of the grid elements, the numerical diffusion can be limited by taking the size of the grid elements sufficiently small. From a comparison of the flow modelled by the explicit version of FINEL2D and the flow modelled by the implicit version of FINEL2D, where the horizontal eddy viscosity can be set manually, can be concluded that mesh is sufficiently fine for elements with a maximum size of 100 m by 100 m.

In order to calibrate the numerical flow model, the bottom roughness has been adjusted both globally and locally. For the Weymouth and Portland area, a global Nikuradse bottom roughness of 0.035 m has resulted in fairly good reproductions of the water levels and the flow. For other locations throughout the English Channel, other roughnesses have appeared to be more appropriate. By adjusting the bottom roughness locally, it had been tried to calibrate the water levels at other locations as well. It is however concluded that it is too difficult to model the water levels correctly throughout the entire model domain. Therefore, it has been decided to focus on the Weymouth and Portland area only.

Compared to the measurements, a phase shift was still visible in the model results for a Nikuradse roughness of 0.035 m. By increasing the bottom roughness in the area around the Portland peninsula and at the Shambles bank to 0.25 m, the model results have shifted towards the measurements. The water levels and the strength of the flow have however not been affected by the adjustment.

When considering time series of the measured and modelled flow, the measured and modelled flow correspond good. When considering the flow spatially, the measured and modelled flow correspond good as well. Since both variations in time and space are of importance to the Dutch Olympic Sailing Team, and the flow is modelled correctly is both space and time, the numerical flow model can well be used to provide current forecasts for the 2012 Olympic Sailing Competition.

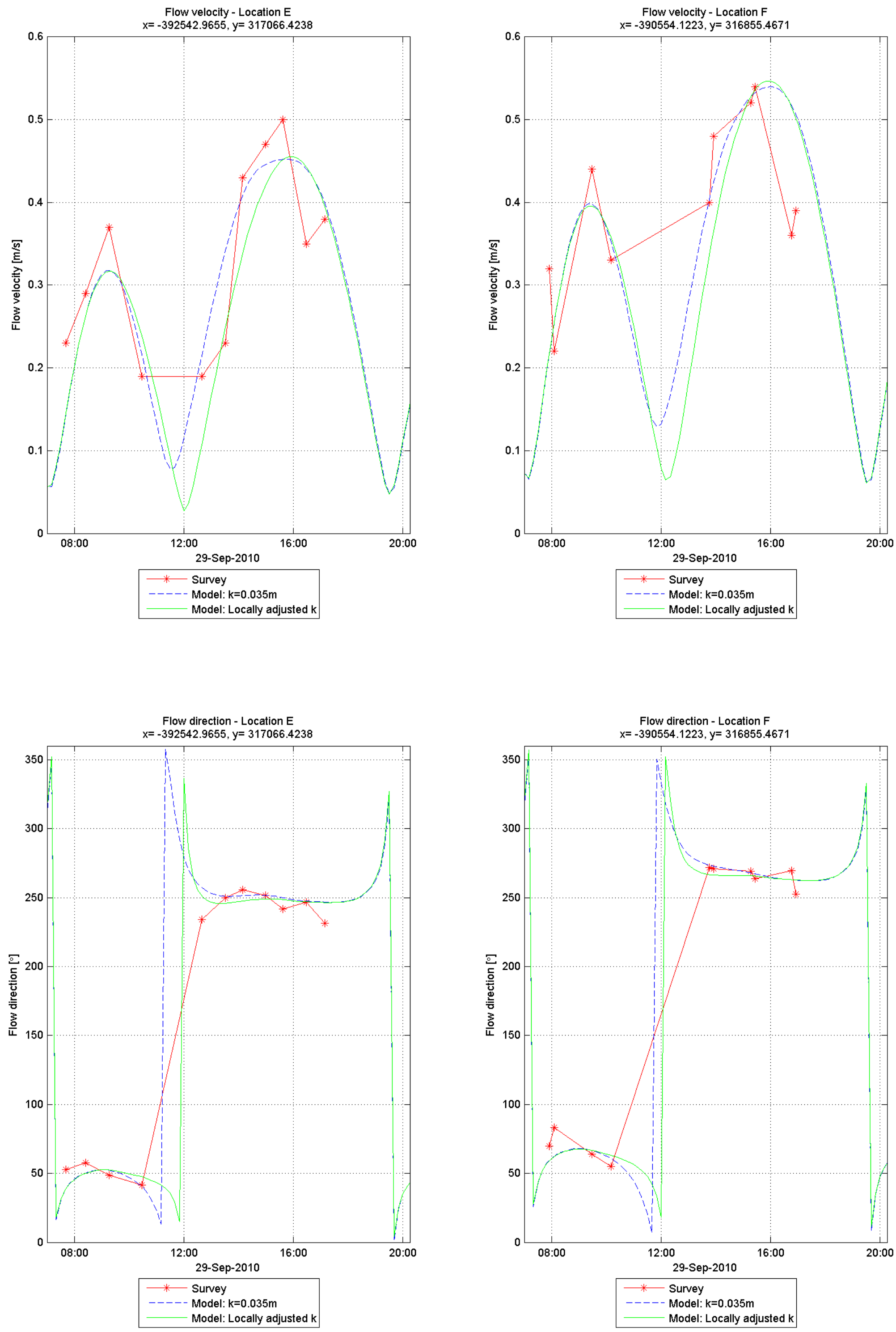

Figure 4.16: Flow velocity and direction at locations E and F, part (1)

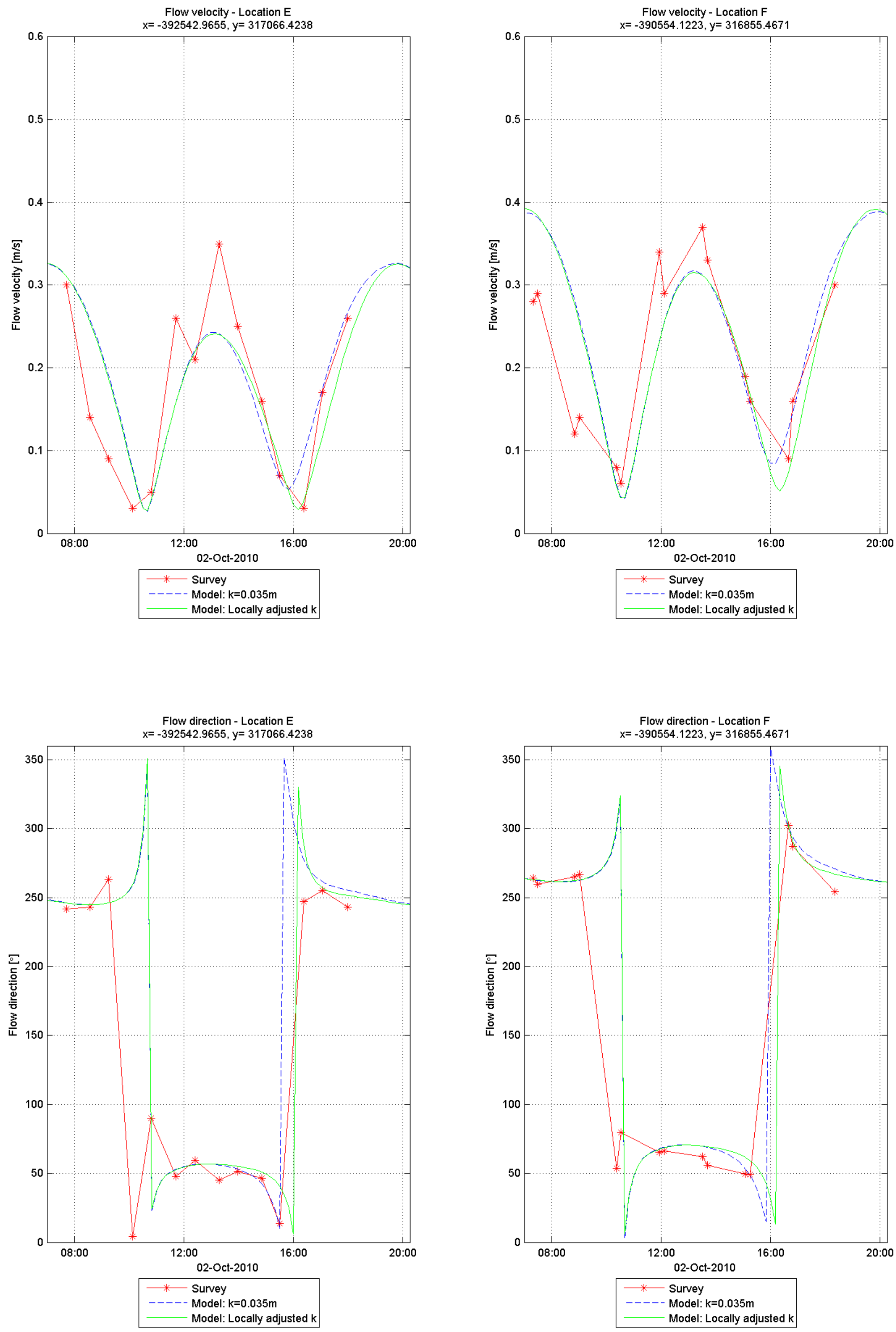

Figure 4.17: Flow velocity and direction at locations E and F, part (2)

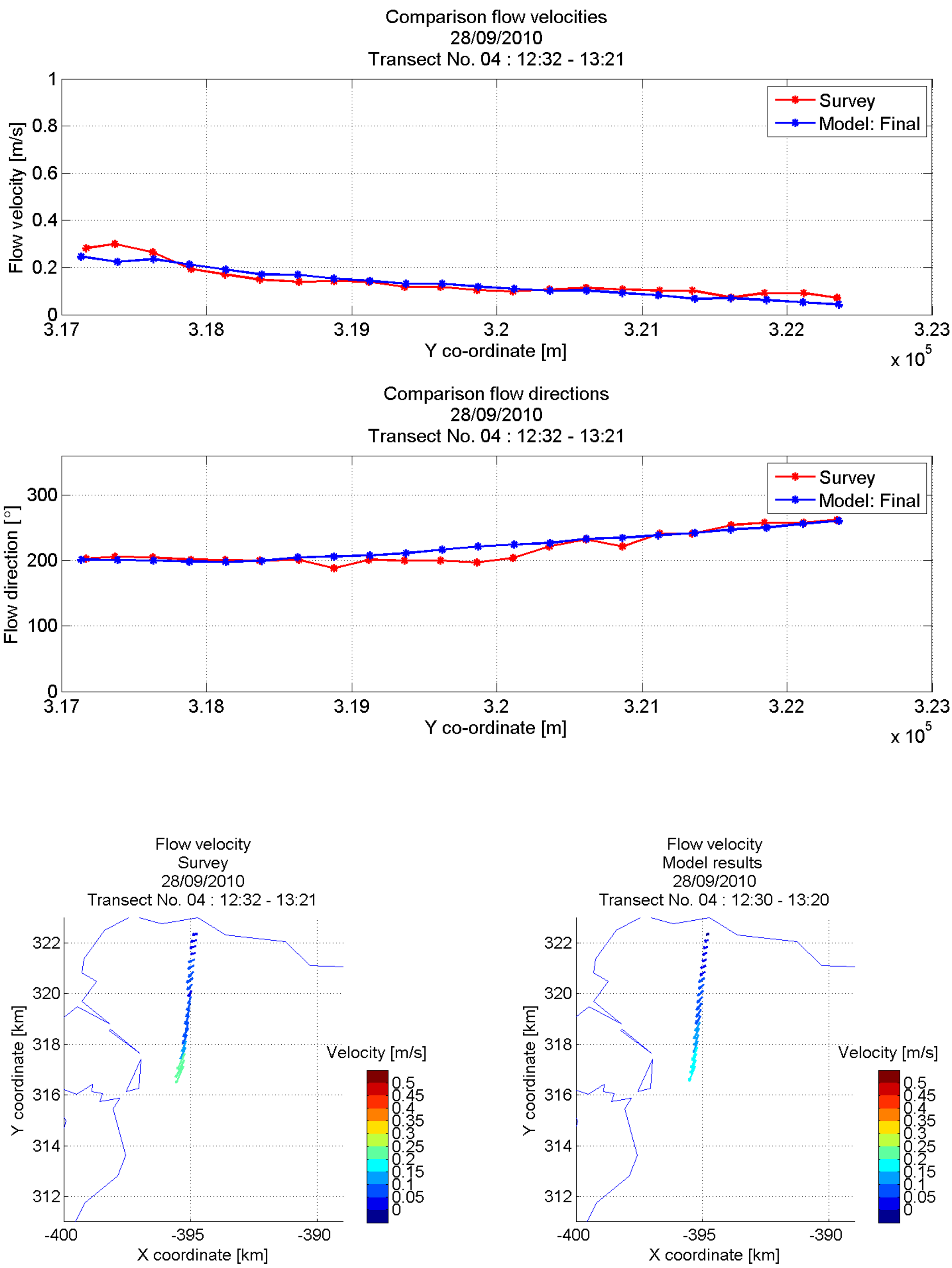

Figure 4.18: Measured and modelled flow velocity and direction along transect A

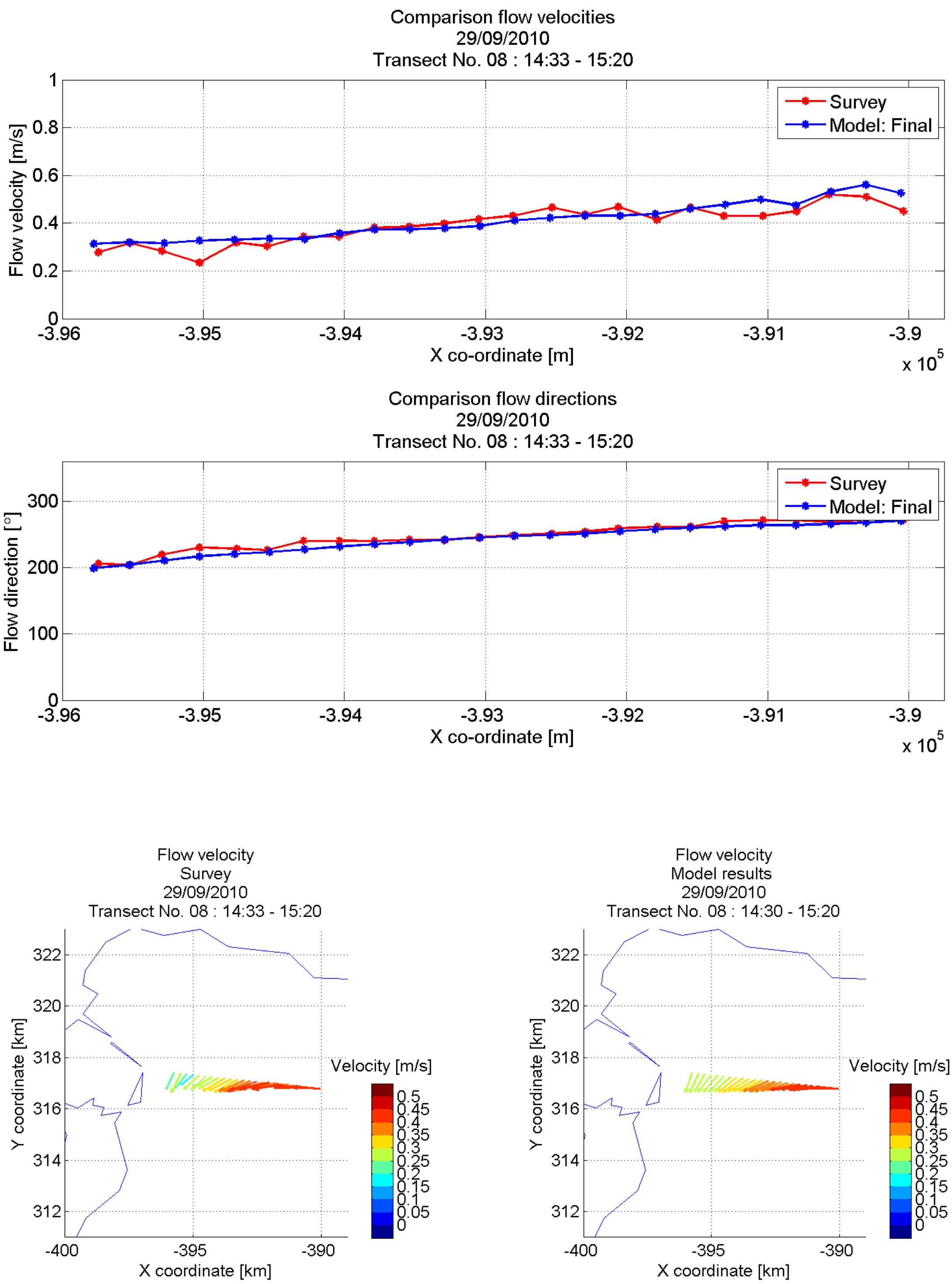

Figure 4.19: Measured and modelled flow velocity and direction along transect B

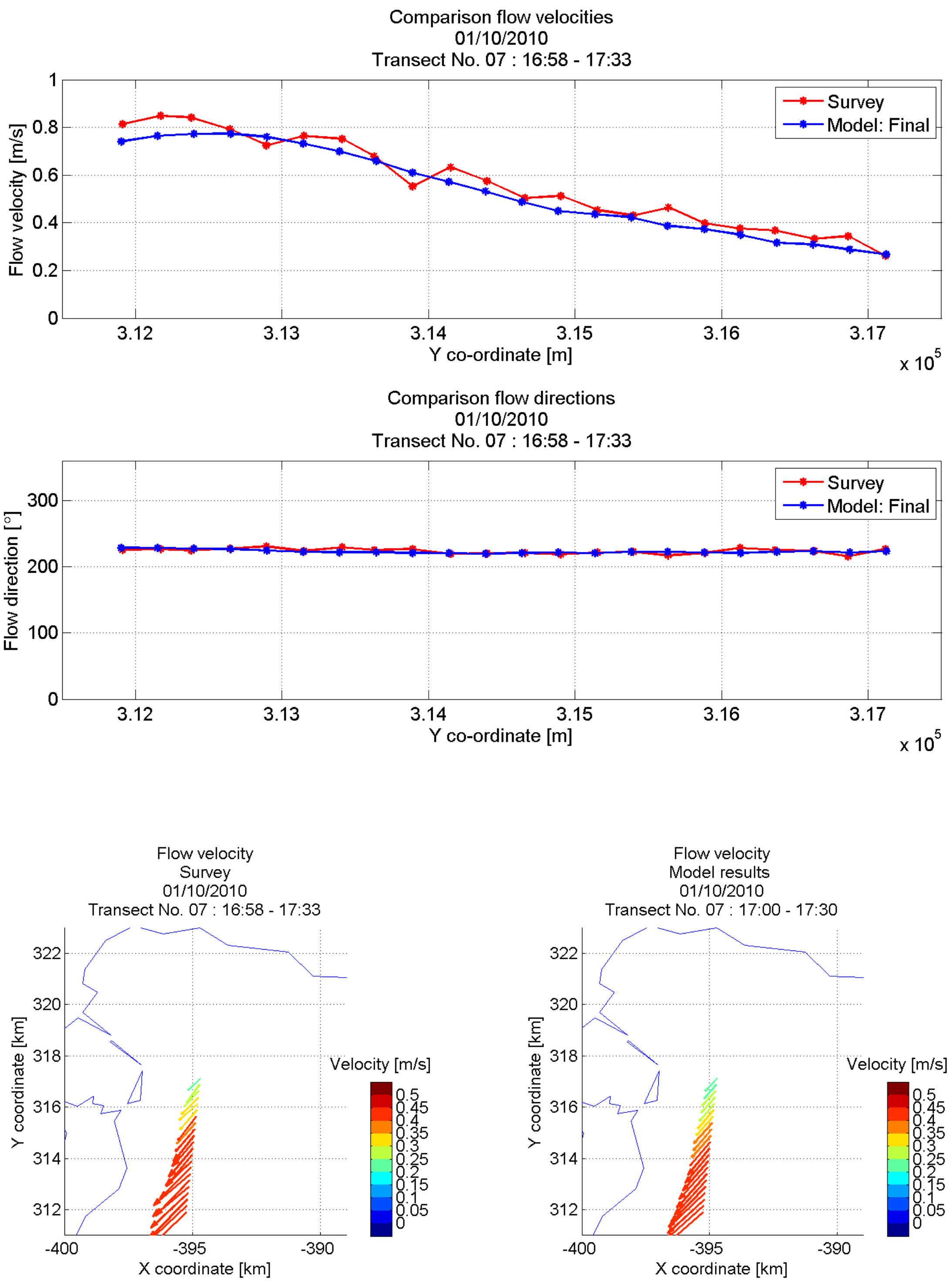

Figure 4.20: Measured and modelled flow velocity and direction along transect C

Chapter 5

Wind and wave influence

In Chapter 4, the numerical flow model, is based on the tide only. In reality however, wind and waves influence the flow as well. In Chapter 2 it is concluded that this influence, especially the influence of wind on the flow, can be significant. The influence of wind and waves on the flow will therefore be investigated in this chapter. In section 5.1, the influence of wind on the flow will be discussed. The wave influence will subsequently be considered in section 5.2. If the wind or wave influence is indeed significant, it becomes interesting to investigate whether it is possible to link the numerical flow model to on–line wind and wave forecasts. This will be discussed in section 5.3.

5.1 Wind–induced flow

Section 2.5 discusses the theory behind the wind–induced currents, and states that the wind–induced current is generally in the direction of the flow, and may amount up to several percent of the wind velocity. The corresponding wind–induced flow velocities are $\mathcal{O}(10^{-1})$ m/s. More complex situations arise when the wind varies spatially or in time, or when variations in depth are present in relatively shallow areas and so–called topographical gyres arise.

In order to estimate the influence of the wind on the current pattern, several wind fields have been imposed to the numerical flow model. The imposed wind has been constant in both space and time. This will be discussed in section 5.1.1. The resulting flow and water levels for these wind fields have been compared to the modelled flow and water levels where no wind is imposed. Besides, the sensitivity to the wind speed and direction will be considered. The sensitivity of the wind–induced current to the horizontal tide and the vertical tide will be considered in section 5.1.2.

5.1.1 Sensitivity to the wind speed and the wind direction

In order to get a first impression of the wind influence, a southern wind of 19 m/s (Beaufort 8) and a southern wind of 7 m/s (Beaufort 4) respectively, have been imposed to the model[1]. The computed water levels are shown in figure 5.1. Figure 5.2 and figure 5.3 show the resulting current patterns for a southern wind of Beaufort 8 respectively Beaufort 4. The currents shown are the currents during the maximum ebb flow velocity at spring tide; other phases of

[1]These wind conditions are selected in order to get a first impression of the wind influence in upper bound and normal conditions. No racing conditions have been considered.

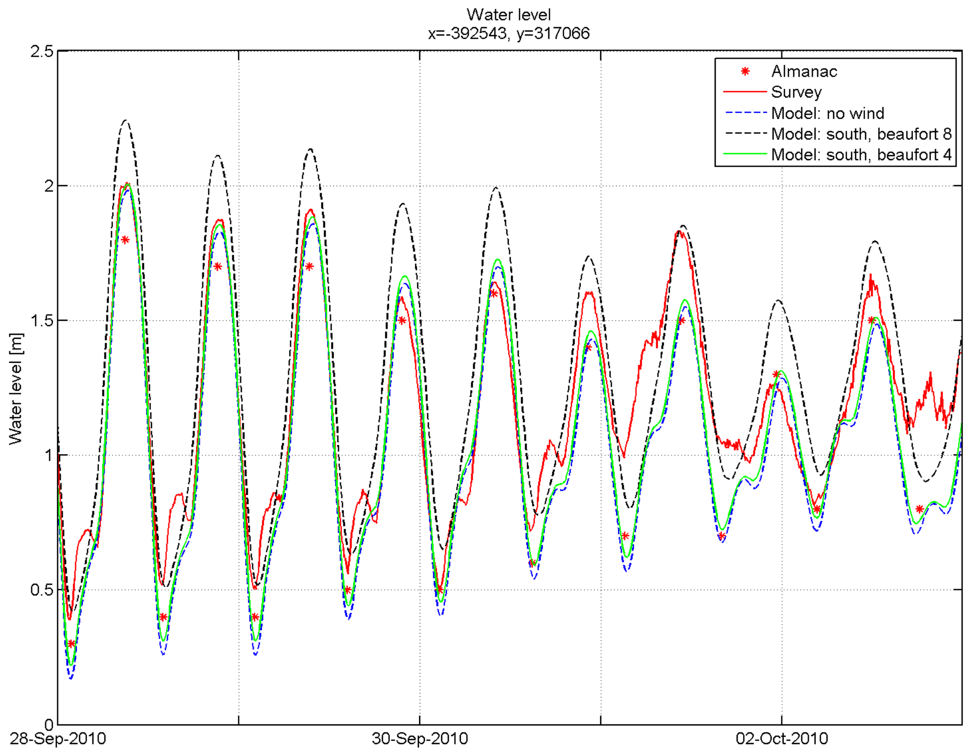

Figure 5.1: Water levels at Weymouth for no wind, a uniform southern wind, Beaufort 8, respectively a uniform southern wind, Beaufort 4. Water levels are in meters with respect to Chart Datum.

the tide will be considered in section 5.1.2. The value of the applied wind drag coefficient is 0.0026; the other model settings are as discussed in Chapter 4.

A water level set up is clearly visible in figure 5.1, which is assumed to arise due to wind forcing the water towards the coast. Since the imposed wind fields are constant in space, similar water level set ups arise throughout the model domain. Since the water levels in the model domain and the flow in the model domain are related, the water level set up influences the modelled large scale flow as well. The influence of the water level deviations on the flow will be more extensively discussed in section 5.1.2 and section 5.3.

The first graph in figure 5.2 and figure 5.3 shows the current pattern in the Weymouth and Portland area, which is the area of interest, based on the tide only. The second graph shows the current pattern (for the same time) which arises when the wind field is imposed to the numerical flow model. The third graph shows the difference between the second and the first graph, and therefore shows the wind–induced currents only. In all graphs, the racing areas are indicated as well.

Both figure 5.2 and figure 5.3 show approximately the same current pattern, although the wind–induced current in figure 5.2 is almost twice as strong as in figure 5.3. The figures show that the wind indeed has a significant influence on the current, since the wind–induced current reaches flow velocities of 0.4 m/s and 0.2 m/s respectively , which is in the same order of magnitude as the tide–induced flow velocities.

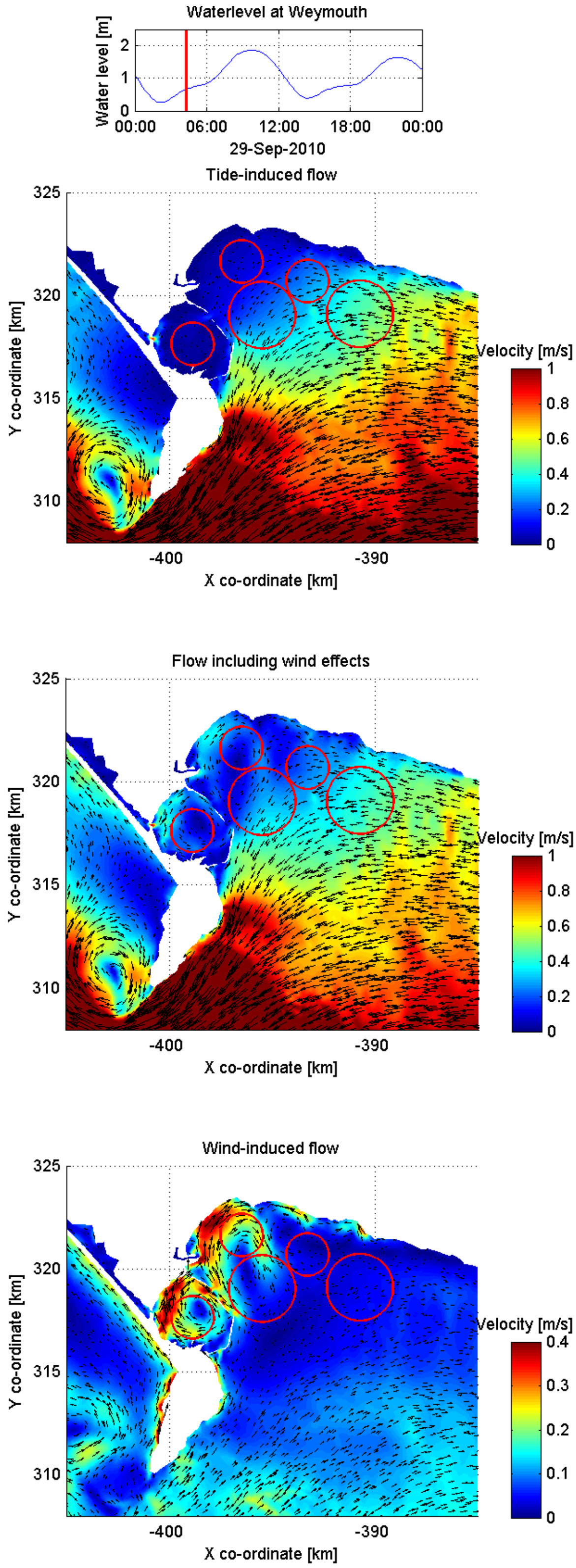

Figure 5.2: Model results for the maximum ebb flow during spring tide for a southern wind, Beaufort 8.

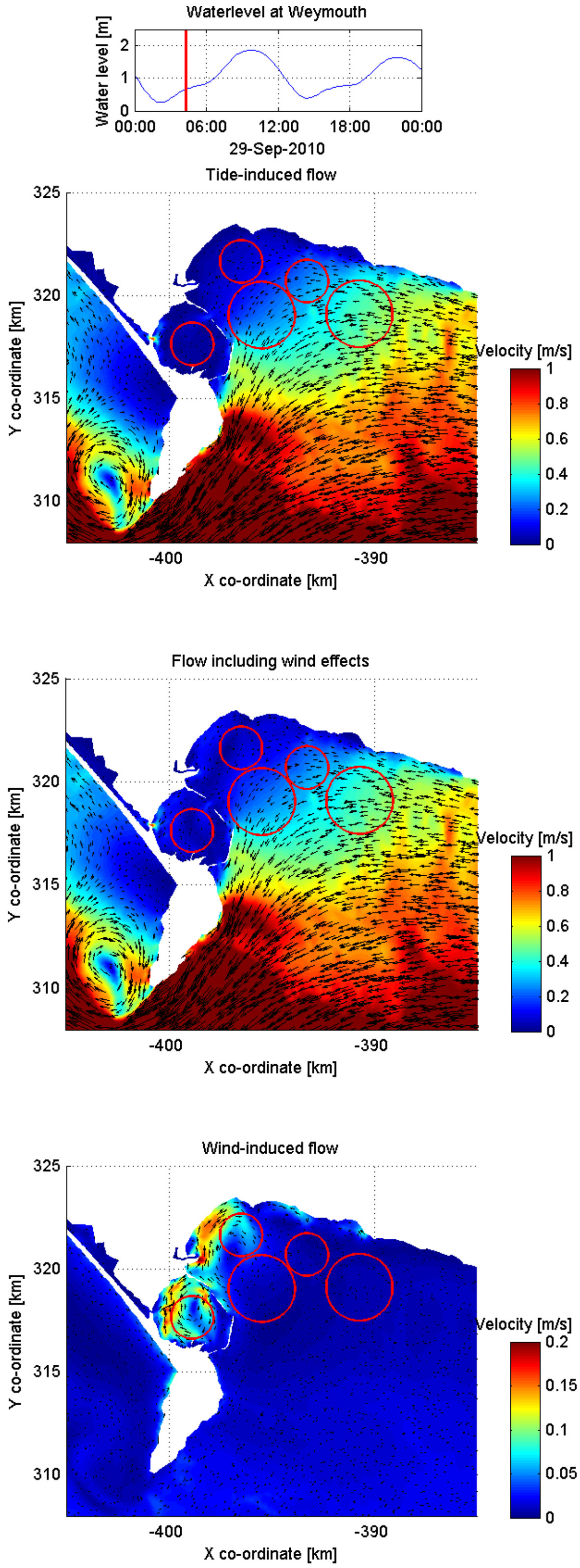

Figure 5.3: Model results for the maximum ebb flow during spring tide for a southern wind, Beaufort 4.

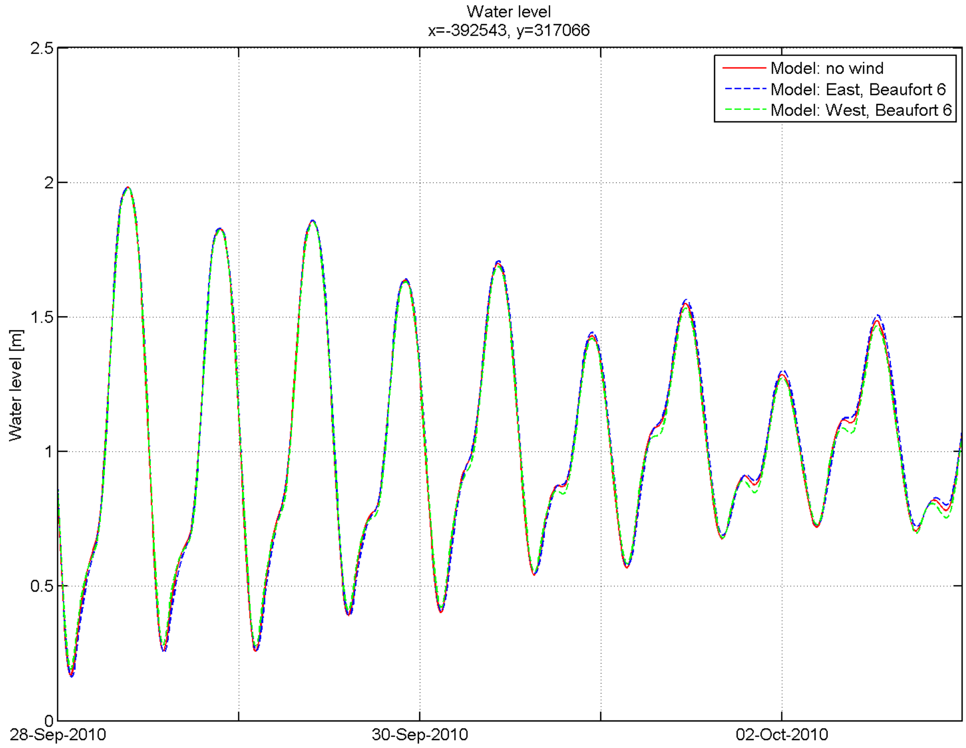

Figure 5.4: Water level in case of no wind, a uniform eastern wind and a uniform western wind of Beaufort 6

Remarkable as well are the 3 gyres, which are all located in the Olympic sailing area. Two of the gryes are located in Weymouth Bay; one in Portland Harbour. Next to the flow velocities, the flow direction is, especially due to the gyres, largely influenced as well. When comparing the gyres in figure 5.2 and in figure 5.3, it appears the gyres in figure 5.2 are larger than the gyres in figure 5.3. What is the boundary of the gyre during a Beaufort 4 wind, can be the centre of the gyre during a Beaufort 8 wind. The spatial distribution of the wind influence on the flow depends therefore on the wind speed.

Since the wind largely influences the flow velocity and direction, and since the spatial distribution of the wind–induced current depends on the wind speed, it is interesting to further investigate the influence of wind for other wind speeds and directions. In order to get an impression of how the size of the gyres varies with the wind speed, southern winds of 12.3 m/s (Beaufort 6) respectively 2.5 m/s (Beaufort 2) have been imposed to the numerical flow model as well. The resulting wind–induced currents during maximum ebb flow are presented in figure 5.5(a) respectively figure 5.5(b). The resulting total current pattern and the wind–induced current during other phases of the tide can be found in Appendix C. Remarkable is the small difference between the gyres for a wind of Beaufort 2 (figure 5.5(b)) and a wind of Beaufort 4 (figure 5.3). When the wind speed further increases to e.g. Beaufort 6 (figure 5.5(a)) and Beaufort 8 (figure 5.2), the gyres appear to expand quickly, which presumes the relation between the wind speed and the strength of the wind–induced current is non–linearly. Equation 4.11a and equation 4.11b, which represent the relation between the flow velocity, wind speed and wind friction, confirm this presumption.

To investigate the wind influence for wind from other directions than south, an eastern, northern and western wind of 12.3 m/s (Beaufort 6) have been imposed to the model , which is assumed to be the maximum wind speed for which the races of the 2012 Olympic Sailing Competition take place. The wind–induced currents for these uniform wind fields are shown in figure 5.5(c) until figure 5.5(e). The results for both the water levels, the total current pattern and the wind–induced currents during other phases of the tide are presented in Appendix C.

In case of a northern wind (figure 5.5(c)), the wind influence is similar to the influence for a southern wind, however the flow direction is opposite, and there is a wind set down instead of a wind set up. When imposing an eastern (figure 5.5(d)) respectively western wind (figure 5.5(e)), the gyres are no longer present. Instead, a current, in western respectively eastern direction, concentrating along the coast arises. The wind–induced current for a western wind is similar to the wind–induced current for an eastern wind, though slightly stronger and in opposite direction. On the water levels at Weymouth however, which are shown in figure 5.4, both the eastern and western wind seem to have little effect.

The in the above paragraphs described gyres only arise in the sailing area, which is a fairly shallow area. The theory behind these wind–induced gyres is discussed in section 2.5, where is stated that the gyres are two–dimensional flow features having a constant velocity over depth. Outside the Olympic sailing area, the wind seems to have hardly any effect on the flow. In Chapter 4 and Appendix E is shown that the measurements and the modelled flow are almost exactly the same. While surveying along transect A, it has been calm, and the above described gyres have therefore not been measured during the survey. The model results for the wind–induced current along transect A can therefore not be validated. While performing the sailed currents measurements along transect B and C, the wind speed has however amounted up to Beaufort 8 (see Appendix D). Since the measurements have however shown that the wind has negligible effect on the flow outside the sailing area, the focus will be on the wind–induced current in the Olympic sailing area in the remainder of this section.

5.1.2 Sensitivity to the horizontal and vertical tide

In the preceding section, the wind–induced current during the maximum ebb flow has been considered. In this section, the wind–induced currents during other phases of the tide for a southern wind with a wind speed of Beaufort 6 will be discussed. The resulting current patterns are shown in figure 5.6. The tidal phases considered are:

- The maximum flood flow during spring tide;
- The flow during slack tide;
- The maximum ebb flow during neap tide;
- The maximum flood flow during neap tide.

The maximum ebb flow during spring tide has already been considered in figure 5.5(a).

When comparing the wind–induced current during maximum ebb at spring tide (figure 5.5(a)) with the wind–induced current during maximum flood at spring tide (figure 5.6(a)) for a wind speed of Beaufort 6, it appears that the strength of the wind–induced currents are approximately equal. The shape of the two gyres in Weymouth Bay has however been changed. Compared to the shape of the gyres during ebb, the middle gyre is larger during

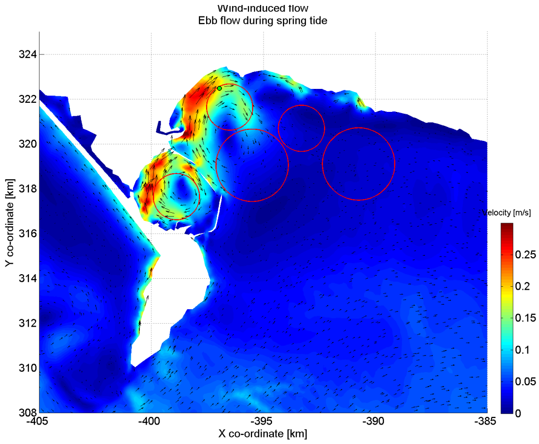

(a) Wind–induced current for a southern wind, Beaufort 6.

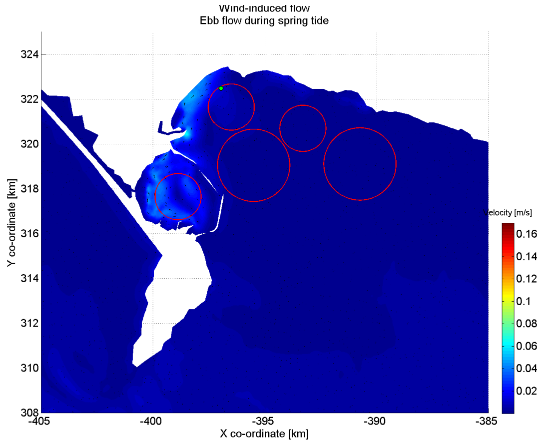

(b) Wind–induced current for a southern wind, Beaufort 2.

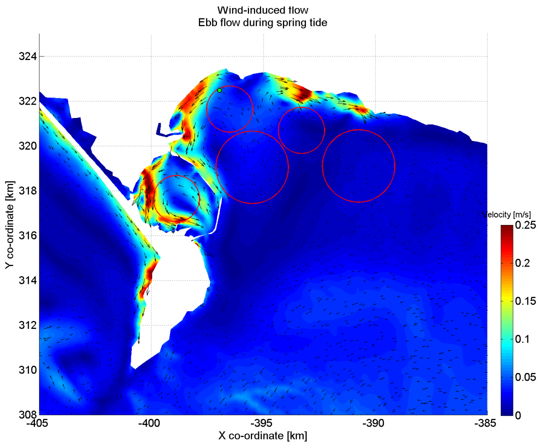

(c) Wind–induced current for a northern wind, Beaufort 6.

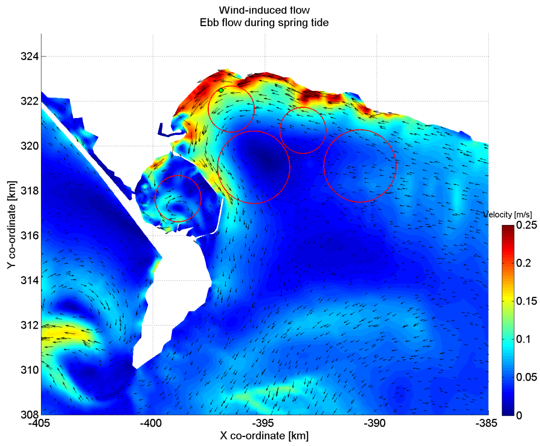

(d) Wind–induced current for an eastern wind, Beaufort 6.

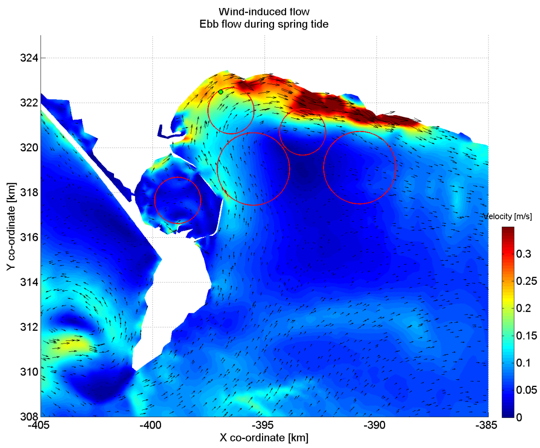

(e) Wind–induced current for a western wind, Beaufort 6.

Figure 5.5: Wind–induced currents during maximum ebb flow for several wind speeds and directions.

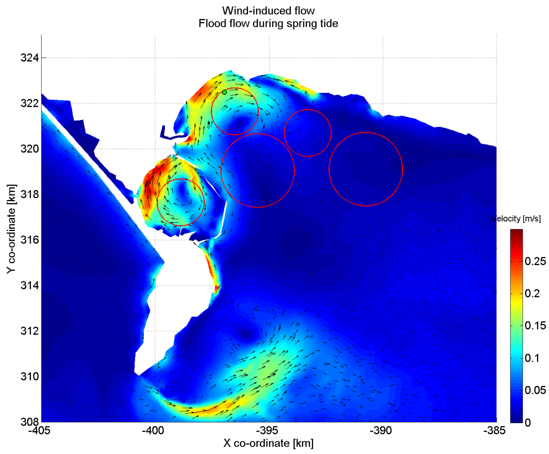

(a) Maximum flood flow during spring tide

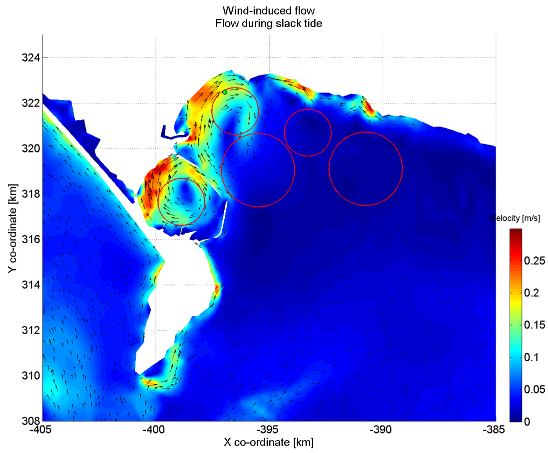

(b) Flow during slack tide

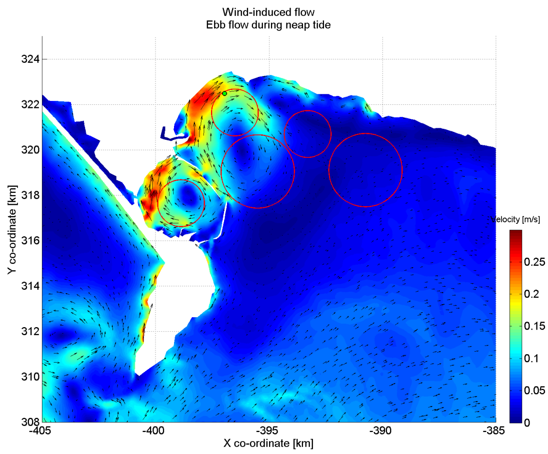

(c) Maximum ebb flow during neap tide

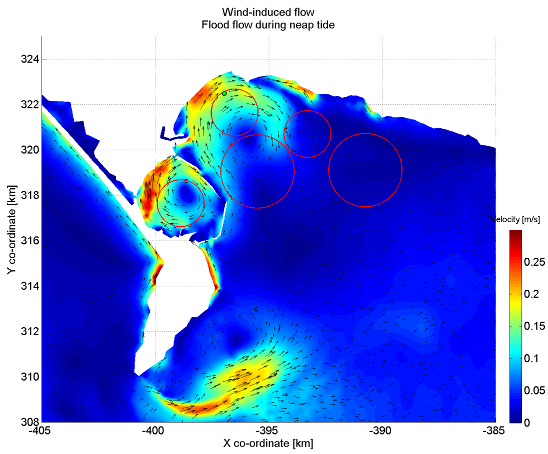

(d) Maximum flood flow during neap tide

Figure 5.6: Model results for the flow for a southern wind, Beaufort 6.

flood and the top gyre has squeezed towards the coast. During neap tide, see figure 5.6(c) and figure 5.6(d), the gyres have the same shape as during spring tide, but the flow velocity at the south–western side of the gyres in Weymouth Bay has increased. Remarkable about the wind–induced current during flood flow is the current east of the Portland peninsula. Since the Shambles bank, a sand bank, is located here, it is assumed that the wind–induced current arises here due to the limited depth. During slack tide, see figure 5.6(b), the middle gyre is larger than during ebb, but smaller than during flood. For the top gyre, the opposite holds. The shape of the gyres in Weymouth Bay during slack tide seems to be in a transition between the shape during ebb and the shape during flood. The flow direction of the tide therefore seems to influence the size of the separate gyres. Therefore, the wind–induced current can be considered sensitive to the horizontal tide.

In the preceding paragraph is noticed that the strength of the wind–induced current is approximately constant throughout the tidal cycle. The water level in the area of interest, which is the vertical tide, seem to have no or hardly any influence on the strength of the wind–induced current. In order to investigate the exact variation of the strength of the

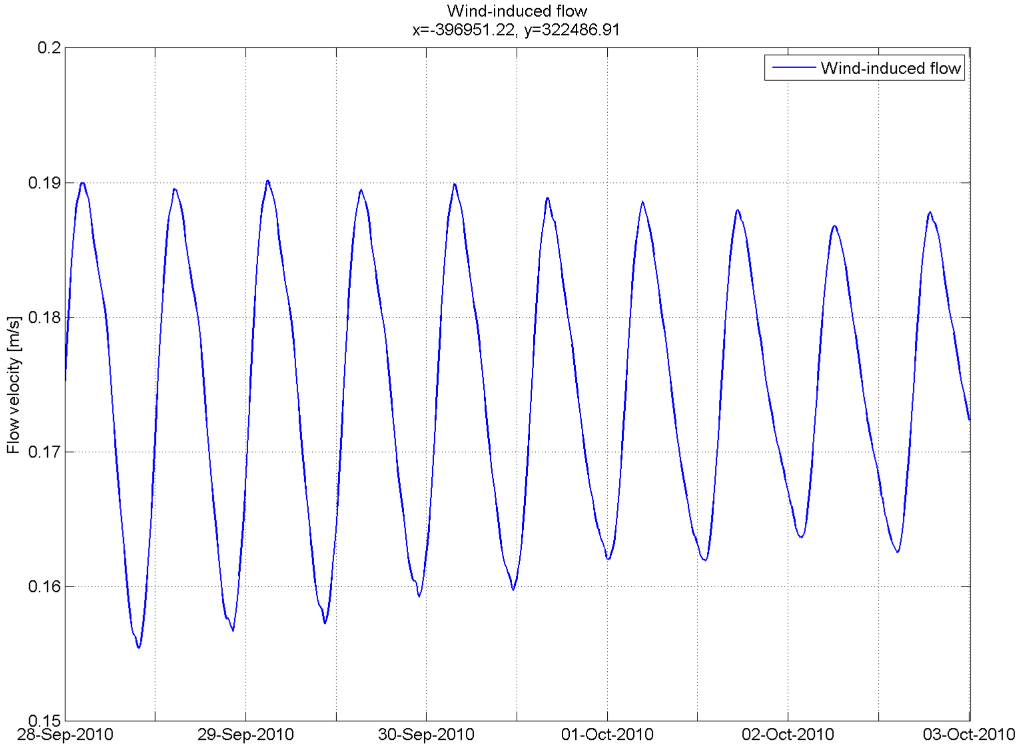

Figure 5.7: Flow velocity wind–induced current at the boundary of the most northern racing area.

wind–induced current, the strength of the wind–induced current at the boundary of the most northern racing area (the green dot in figure 5.6) is shown in figure 5.7. Figure 5.7 indicates that the flow velocity does change over the tidal cycle, and that spring tide and neap tide slightly influence the strength of the flow. The absolute differences in the flow velocity over a tidal cycle are however only $\mathcal{O}(10^{-2})$ m/s. Since the absolute differences in flow velocity over a tidal cycle are so small, the influence of the vertical tide on the locally generated wind–induced current can be considered negligible. The water level however does influence larger scale currents. This will be more extensively discussed in section 5.3.

5.1.3 Conclusion

From the preceding sections can be concluded that the influence of the wind on the current in the Olympic sailing area is indeed significant. The velocities corresponding to the wind–induced current are $\mathcal{O}(10^{-1})$ m/s. Depending on the wind direction, gyres or a current concentrated along the coast arise. Outside the sailing area, the wind seems to have hardly any effect, which has been confirmed by the measurement (see section 5.1.1). The flow velocities and the size of the flow features in the Olympic sailing area are both depending on the wind speed and wind direction. The (horizontal) tide influences the size and shape of the flow features as well. The strength of the wind–induced flow on the other hand, is hardly influenced by the (vertical) tide, by which the wind–induced current in the Olympic sailing

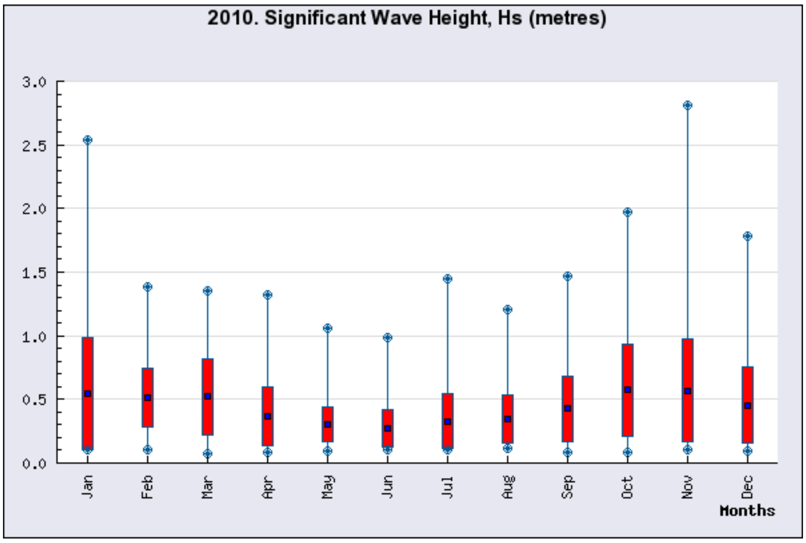

Figure 5.8: CCO Statistics for the significant wave height in 2010 for the Weymouth wave buoy. The blue square indicates the average significant wave height. The blue circle indicates the extremes of the significant wave height.

area can be considered independent of the water levels.

The wind–induced gyres which arise in the Olympic sailing area, are two–dimensional flow features. The wind–induced current can therefore be considered constant over depth, and FINEL2D should therefore be able to model the wind–induced current. However, the current along transect A, which crosses the sailing area and therefore the gyres, has only been measured when it was calm, by which the gyres have not been measured. The model results for the wind–induced current can therefore not be validated.

Since in general the influence of the wind on the flow is large, it is interesting to investigate whether the wind–induced current can be accounted for in the numerical flow model, by for instance linking the model to on–line wind forecasts. This will be discussed in section 5.3.

5.2 Wave–induced flow

In section 2.6 the wave–induced currents are discussed. Just like the wind–induced flow, the wave–induced flow may amount up to several percent of the wind speed. In reality however, these velocities are only achieved in case of breaking waves, which is usually close to the coast. Especially because the racing areas for the 2012 Olympic Sailing Competition are located close to the coast, it is interesting to investigate what the influence of waves on the current pattern is. Therefore, wave fields have been imposed to the numerical flow model, by using the SWAN functionality of FINEL2D, which calculates the wave fields for the flow computations. The SWAN function is however not available in FINEL2D version 7.0. Therefore, version 6.20 is used. A disadvantage of this version is that only a global latitude can be defined, instead of a latitude for each element separately. However, the deviations which arise are negligibly small.

According to statistics of the Channel Coastal Observatory (CCO), the significant wave height in the Weymouth and Portland area hardly exceeds 1.5 m. The statistics for the significant wave height H_s in 2010 are shown in figure 5.8, where the blue square indicates

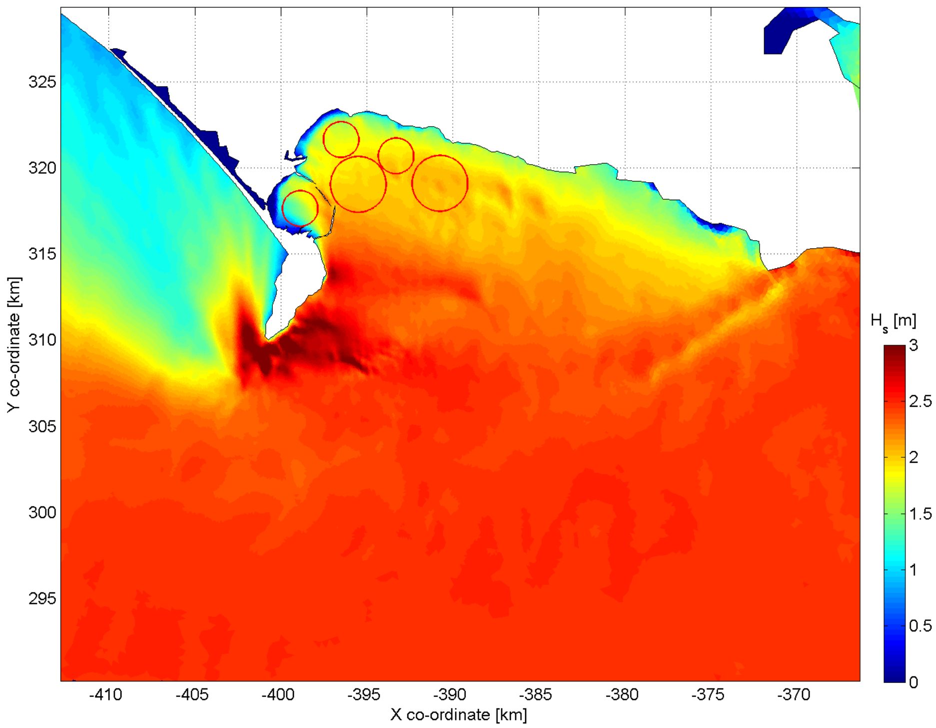

Figure 5.9: Significant wave height of the waves imposed to the numerical flow model. On the southern and eastern boundaries of the SWAN model waves with a significant wave height of 2.5 m, a peak period of 8 s and a direction of 135 ° have been imposed.

the average significant wave height, and the blue circle indicates the maximum significant wave height. Incidentally, this wave height has also occurred during the survey (see figure D.3). The peak period corresponding to these waves has been approximately 8 s (figure D.3); the wave direction approximately south–west. To get an impression of the wave influence for upper bound wave conditions, the above described waves have been imposed on the model first. In order to obtain waves with a significant wave height of 1.5 m in the area of interest, higher waves have to be imposed on the SWAN boundaries. Therefore, waves with a significant wave height of 2.5 m, a peak period of 8 s and a direction of 135 ° have been imposed on the southern and eastern SWAN boundaries. This wave field can be considered a realistic wave field. No waves have been imposed on the western boundary, since waves from the south–west propagate propagate away from the area of interest, instead of in the area of interest. The SWAN wave field, which is not imposed to the entire model, but only on the area of interest, is shown in figure 5.9.

Figure 5.10 shows the resulting wave–induced current, which has been obtained by current pattern based on the tide only from the current pattern including wave effects. Since the difference between the flow with and without waves seems to be small, only the wave–induced current itself is presented in the figure. The racing areas of the 2012 Olympic Sailing Competition are indicated by means of red circles. The wave–induced flow appears to be weak and negligible in most of the sailing area. Only close to the coast, where the waves break, the

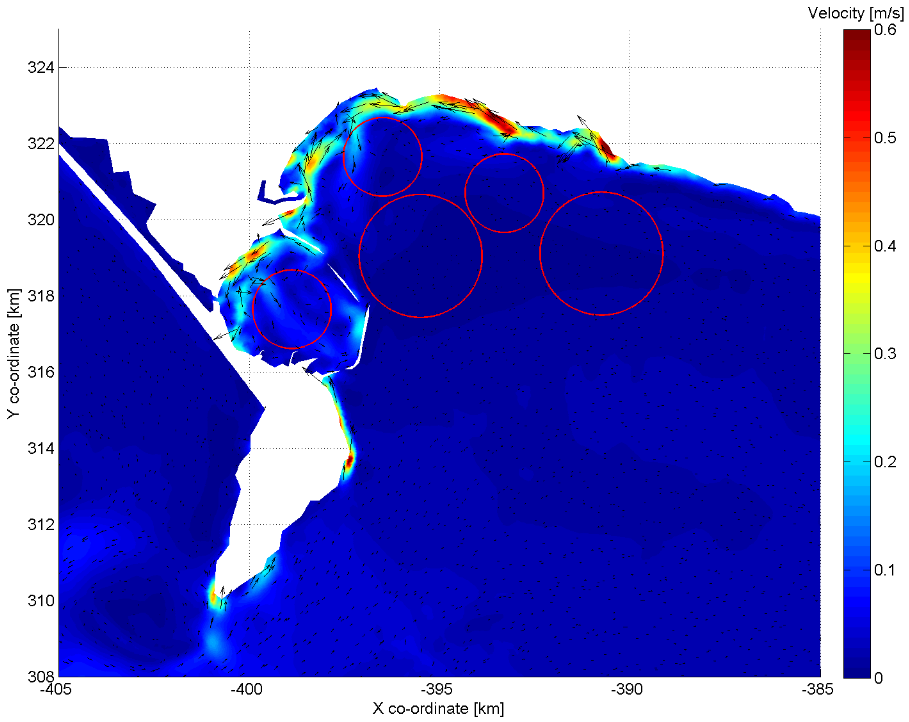

Figure 5.10: Wave–induced flow for waves from the south–west during maximum ebb flow. The wave field is shown figure 5.9.

effect is larger. The flow in the racing areas however, which are located close to the coast as well, is not influenced by the wave–induced current, except for the two most westerly located racing areas.

Since the wave field shown in figure 5.9 only occurs in case of extreme winds and the races of the 2012 Olympic Sailing Competition will be cancelled in case of these strong winds, it is assumed that the wave conditions of figure 5.9 will not occur during the races. In order to investigate if the two most westerly racing areas are also influenced by the wave–induced currents during racing conditions, another wave field has been imposed to the numerical flow model. The peak period respectively wave direction are equal to the peak period and wave direction of the first wave field, i.e. 8 s respectively 135 °; the significant wave height is decreased to 1.5 m. The significant wave height in the Weymouth and Portland area for this wave field is shown in figure 5.11.

The resulting wave–induced current for this second wave field is shown in figure 5.12. Compared to the wave–induced current shown in figure 5.10, the wave–induced current has become less strong. The flow in the two most westerly racing areas, is no longer influenced by the wave–induced current. Only close to the coast, which is the area where the waves break, the wave influence is clearly visible.

It can be concluded that the wave–induced flow in the racing areas during racing conditions is negligible; the areas are located far enough outside the coast. Despite that the waves do not influence the flow in the racing areas, the waves are of importance to the Dutch Olympic Sailing Team, since the waves enforce wave forces on the sailing boat. The question how to

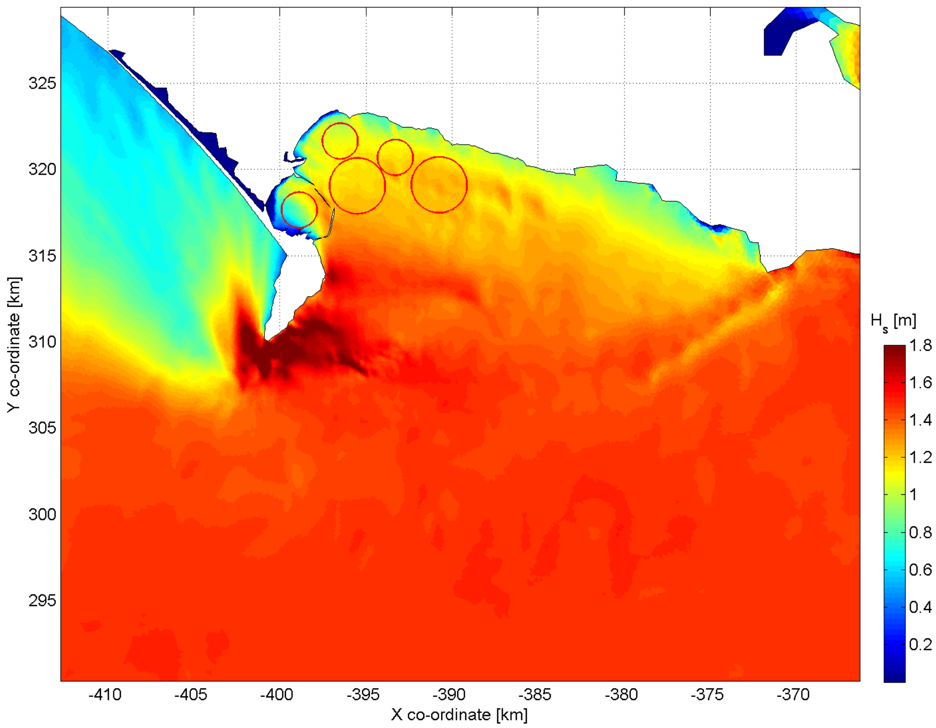

Figure 5.11: Significant wave height of the second wave field imposed to the numerical flow model. On the southern and eastern boundaries of the SWAN model waves with a significant wave height of 1.5 m, a peak period of 8 s and a direction of 135 ° have been imposed.

deal best with waves and wave forces on the boat, is a matter of sailing techniques and tactics as well. This subject is outside the scope of this thesis.

5.3 Including wind effects in the model results

The ECSM model, the numerical flow model which will be used to provide current forecasts with, is until now based on the tide only. According to the theory discussed in Chapter 2, wind and waves may also influence the flow significantly. In the preceding sections, the influence of wind and waves on the flow is investigated. It appears that the influence of waves on the current is negligible under sailing conditions, except for areas close to the coast, but that wind influences the flow to a large extent. Since the scope of the model computations is to provide reliable and accurate current forecasts, and the wind influences the flow to such an extent, it might be interesting to include wind fields in the computation.

A way to include wind in the computations is by linking the model to on–line wind predictions. In order to do so, wind predictions have to be available. In the predictions however, an uncertainty is always present. This wind deviation enlarges the error which is already present in the model. When wind predictions are used to include the wind–induced current in the model results, the predictions have to be accurate and reliable. A numerical model which

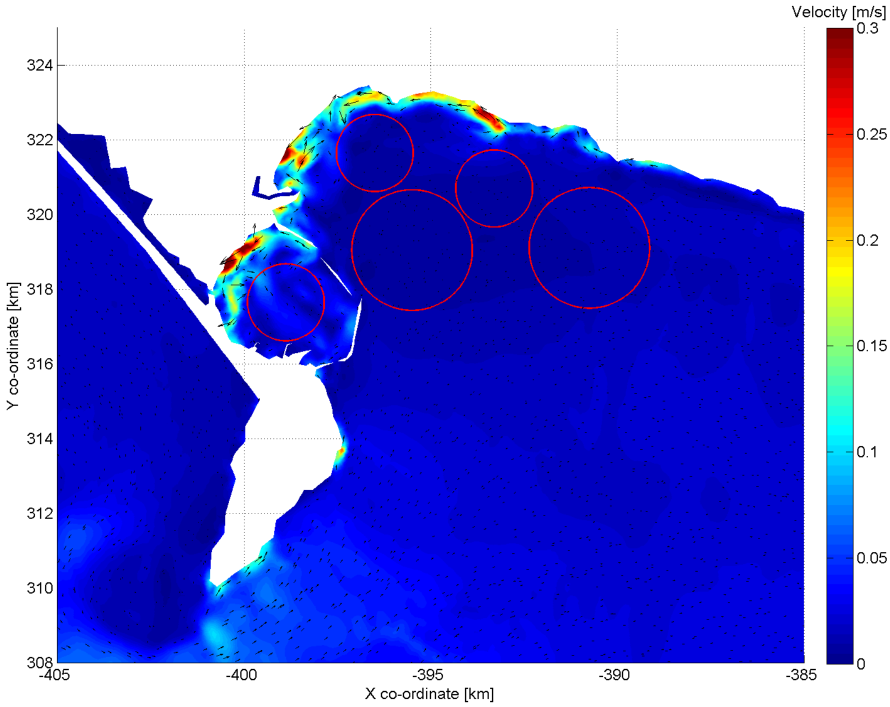

Figure 5.12: Wave–induced flow for waves from the south–west during maximum ebb flow. The wave field is shown in figure 5.11.

provides wind predictions is already described in section 2.5, where the prediction provided by the model is compared to wind observations. The predictions and the observations show approximately the same trend, but still clearly deviate. The uncertainty in the predictions including wind is therefore fairly large.

Another way to account for the wind is by composing several simplified wind scenarios, and calculate the flow for all these scenarios well before the start of the Olympic Games 2012. On the day of the races, the model results for the scenario which fits best for the current wind conditions are taken and used for the current forecasts for that specific day. This method has several disadvantages as well. Since reliable current forecasts are desired and the wind–induced current depends on both the wind speed and wind direction, much scenarios have to be calculated in order to always have an appropriate scenario available for which the wind conditions deviate only little from the true wind conditions, which takes up much (calculation) time. Besides, a constant wind is imposed to the entire model in case of wind scenarios, while the true wind varies in both space and time. This spatially constant wind leads to large errors in the modelled water levels. The gyres which arise in the Olympic sailing area, are however only influenced by the local wind conditions. Moreover, the wind–induced current in the Olympic sailing area is considered independent of the water levels, and the wind–induced current in the Olympic sailing area is therefore not influenced by the errors in the water levels.

Errors in the water levels due to deviations of the imposed wind form the true wind are present throughout the entire model domain. The water levels hardly influence the locally generated gyres, but do influence the larger scale flow, among others the flow through the English Channel. Errors in the water levels thus enforce an error in the modelled flow, by which the flow in the Olympic sailing area is influenced by the water levels after all. When the error in the imposed wind is reduced, the error in the flow will be reduced as well. Even when the imposed wind equals the true wind, deviations in the water levels may still be present due to the influence of e.g. air pressure gradients. Uncertainties in both the water levels and the flow are therefore always present when wind is imposed to the numerical flow model.

From the above, it can be concluded that it is difficult to obtain reliable and accurate current forecast when the wind–induced current is accounted for. The flow is influenced by the wind both globally and locally. Since the current along transect A, which crosses the sailing area and therefore the gyres, has only been measured when it was calm, no data is available to validate the numerical flow model, and the reliability of the model with respect to the local influence of the wind cannot be proven. Moreover, no data is available to investigate the influence of the wind on the larger scale flow. Besides, errors in the current forecasts may arise due to uncertainties in the available wind forecasts.

Chapter 6

Current forecasts

Now the numerical flow model has been calibrated and the influence of wind and waves has been discussed, results in the form of current forecast can be generated. The serviceability of the current forecasts provided by the numerical flow model, will be discussed in section 6.1. The presentation of the current forecasts and the preferences of the Dutch Water Sports Association (in Dutch: Watersportverbond) on the presentation of the forecasts will be considered in section 6.2.

6.1 Serviceability

In Chapter 4 is concluded that the numerical flow model models the tidal flow in both space and time fairly good. However, deviations of the modelled flow and water levels with respect to the measurements are still present. These deviations are presented in table 6.1. The deviations in the phase of the water levels, the phase of the flow, the gradients of the flow and the flow direction are several percent, by which the phase of the water levels, the phase of the flow, the gradients of the flow and the flow direction can be considered accurately modelled. Larger deviations are present in the water levels and the flow velocity. The water levels are however less important, by which the deviations in the water levels of approximately 10 percent are acceptable.

The relative deviations of the modelled flow velocities with respect to the measured flow velocities amounts up to 15 percent, while, contrary to the water level, the flow velocity is an important aspect of the current forecasts. A comparison of the modelled and measured flow

	Deviation
Water level	± 10%
Flow velocity	± 15%
Flow direction	± 5%
Phase (water level)	± 2%
Phase (velocity)	± 5%
Phase (direction)	± 5%
Velocity gradient	± 2%

Table 6.1: Deviations of the modelled flow and water levels, based on the tidal flow only, with respect to the measurements.

	Deviation
Water level	± 30%
Flow velocity	unknown
Flow direction	unknown
Phase (water level)	± 5%
Phase (velocity)	unknown
Phase (direction)	unknown
Velocity gradient	unknown

Table 6.2: Deviations of the modelled flow and water levels, under the influence of wind, with respect to the measurement. Where the deviations is considered unknown, no measurements are available.

velocity for each separate sailed transect can be found in Appendix E. It appears that despite that the relative deviation amounts up to 15 percent, the absolute differences are in general less than 0.05 m/s. Besides, the modelled flow velocity is sometimes higher and sometimes lower than the measured flow velocity, from which a trend in the deviations seems not to be present. Therefore, it is difficult to further improve the model performance with respect to the flow velocity.

The relative deviations of the modelled flow and water levels with respect to the measured flow and water levels when wind is imposed to the numerical flow model are given in table 6.2. Compared to the forecasts where no wind is taken into account, the deviation in the water levels is significantly larger. These deviations are so large that they may cause errors in the larger scale currents; the exact influence is however unknown. The deviations considering the flow in the Olympic sailing area are unknown as well, since no measurements along transect A, which crosses the sailing area and the wind–induced gyres, have been performed when there was wind. Since the numerical flow model cannot be validated with respect to the wind–induced flow, uncertainties are present in the current forecasts when wind is accounted for.

In Chapter 4 the size of the grid elements in the area of interest has been set to a maximum element size of 100 m by 100 m. For larger elements, the numerical flow model becomes to diffusive, and the model results become less accurate. For smaller elements however, the performance of the numerical flow model does not further increase. Spatially, the level of detail reaches its maximum for an element size of 100 m by 100 m.

From the above can be concluded that the current forecasts based on the tidal flow only are reasonably accurate. Besides, the forecasts are more detailed in both space and time then other available information on the currents as for instance the Admiralty tidal stream atlases. The current forecasts can therefore be considered as useful information for the Dutch Olympic Sailing Team.

When wind is accounted for, several uncertainties are present in the results, and the forecasts become less useful. The model performance can be improved by performing measurements in the Olympic sailing area under various wind conditions so that the modelled gyres can be validated. Uncertainties in the model results will however remain present, among other due to uncertainties in the wind data. Therefore, it is advised not to include wind effects in the current forecasts. A rough indication of the wind–induced current in the Olympic sailing area can however be given.

6.2 Presentation

The Dutch Water Sports Association has indicated to have certain preferences in the way in which the current forecasts are supplied. The Dutch Water Sports Association would like to receive current forecasts for both the training period in 2011 and for the period in which the Olympic Games 2012 take place. For each day, they would like to receive forecasts for the time span between approximately 8 AM and 8 PM, in the form of:

- Plots showing the current pattern for every hour, two plots per A4 page, in order to get an impression of the currents for that day;
- Plots showing the current pattern for every 10 minutes, one plot per A4 page, in order to study the currents for the time span in which the actual race takes place in more detail;
- Animations which show the the current pattern for each separate day;
- Detail plots which show the current pattern for each racing area separately, for every 10 minutes, one plot per A4 page, in order to be able to focus on the flow for a specific racing area.

Both the plots and the animations will visualise the strength of the flow by means of colour, which gives an indication for the flow velocity. Vectors are shown as well, which indicate both the flow velocity (by the length of the vector) and the flow direction (by the direction of the vector). On request of the Dutch Water Sport Association, the vectors are plotted on a rectangular grid and the velocities are given in m/min. The water level corresponding to the flow is given in a small sub–plot.

Preliminary examples of the different plots are shown in figure 6.1 till figure 6.7, where figure 6.1 shows an example of the hourly plots, figure 6.2 shows an example of the 10 minutes plots, and figure 6.3 until figure 6.7 show examples of the detail plots for each racing area. All figures are displayed in reduced size.

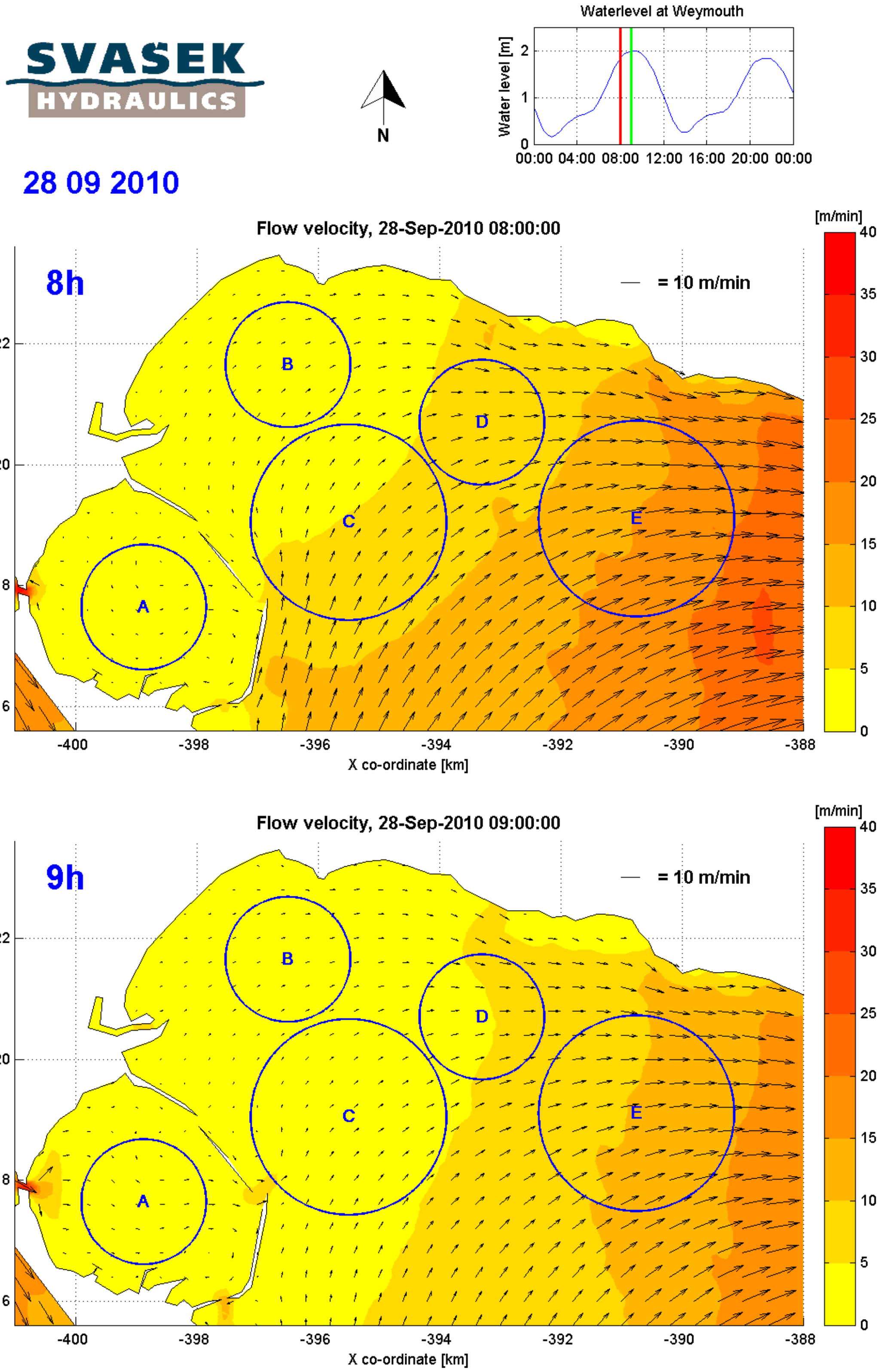

Figure 6.1: Example of an hourly plot

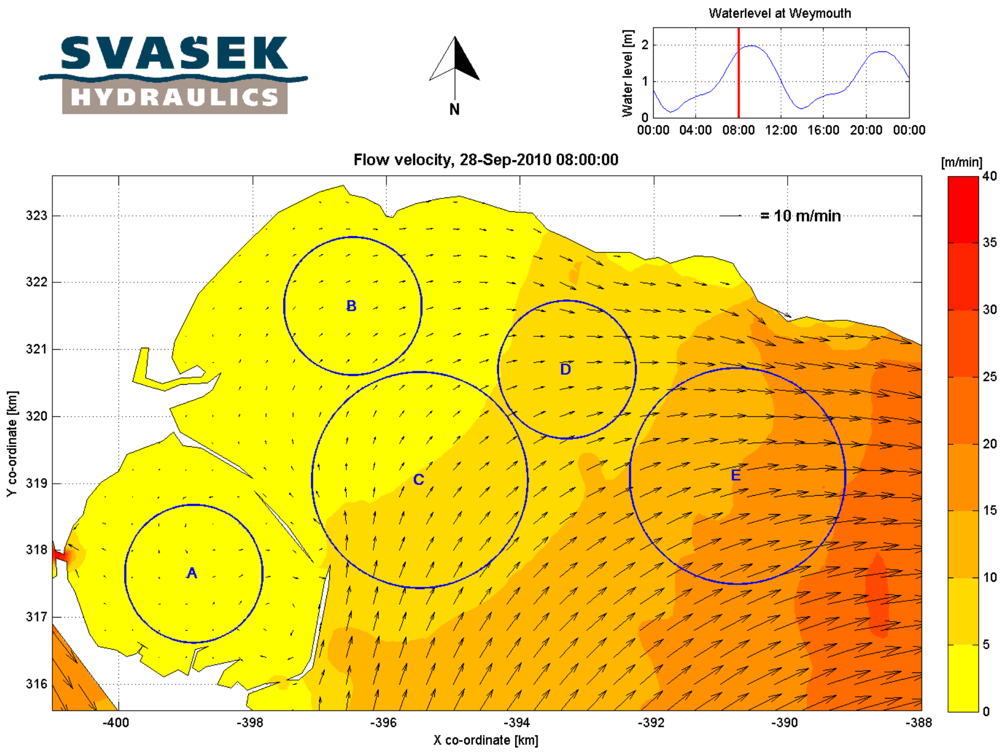

Figure 6.2: Example of a 10 minute plot

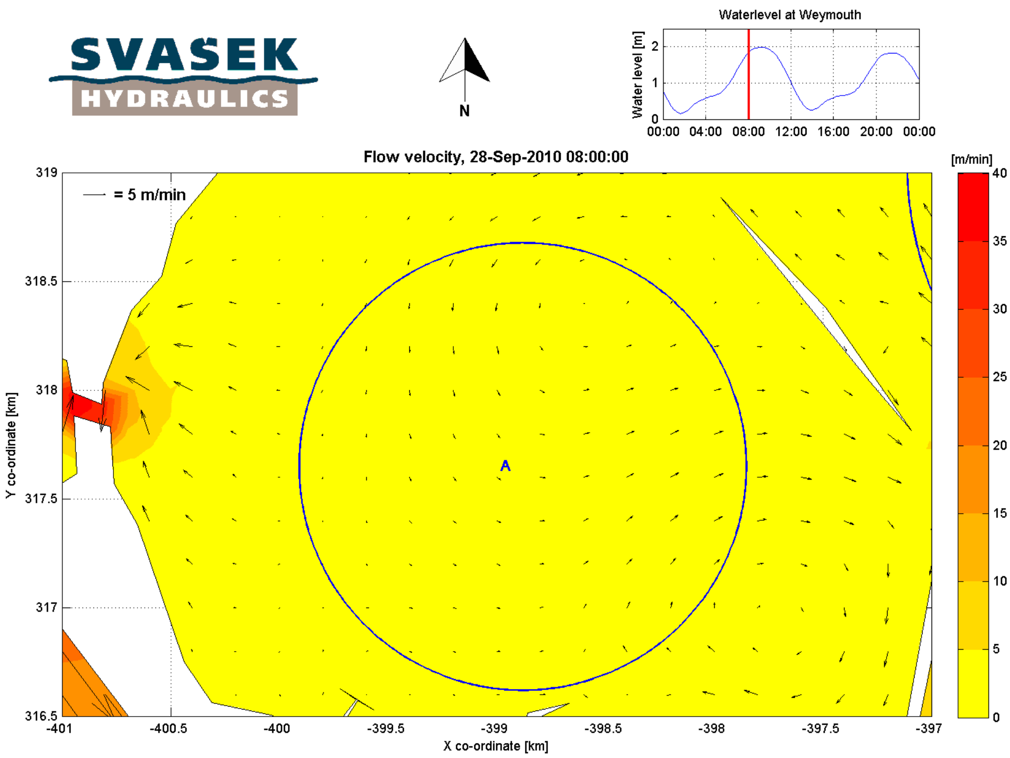

Figure 6.3: Example of a detail plot for racing area A

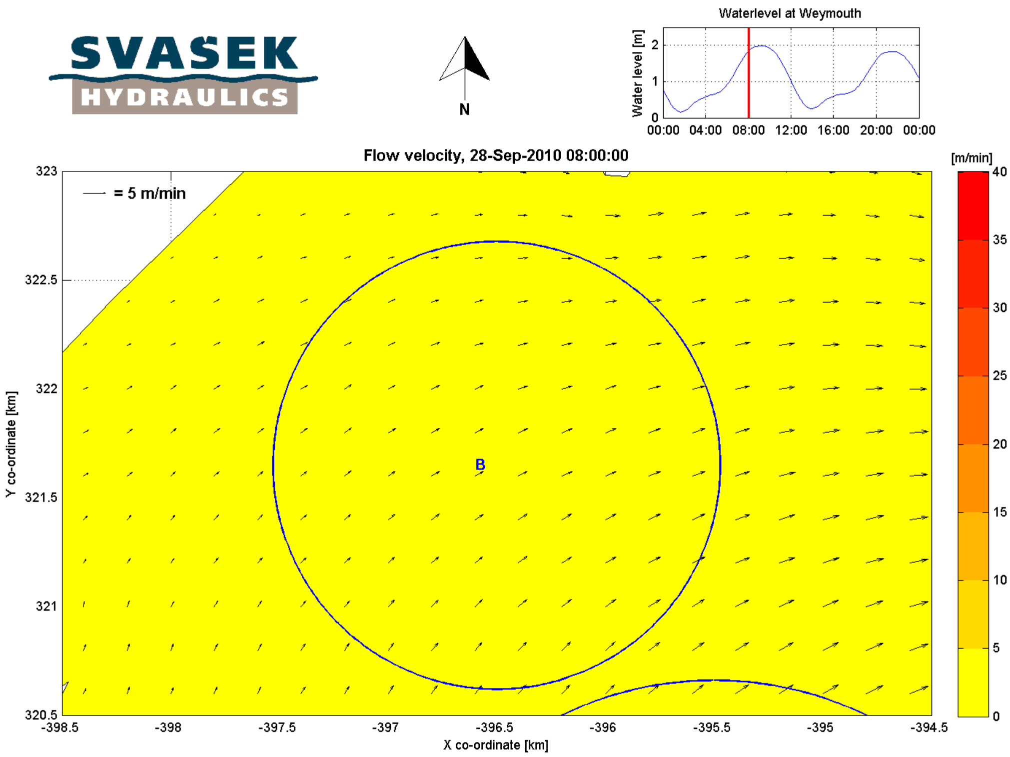

Figure 6.4: Example of a detail plot for racing area B

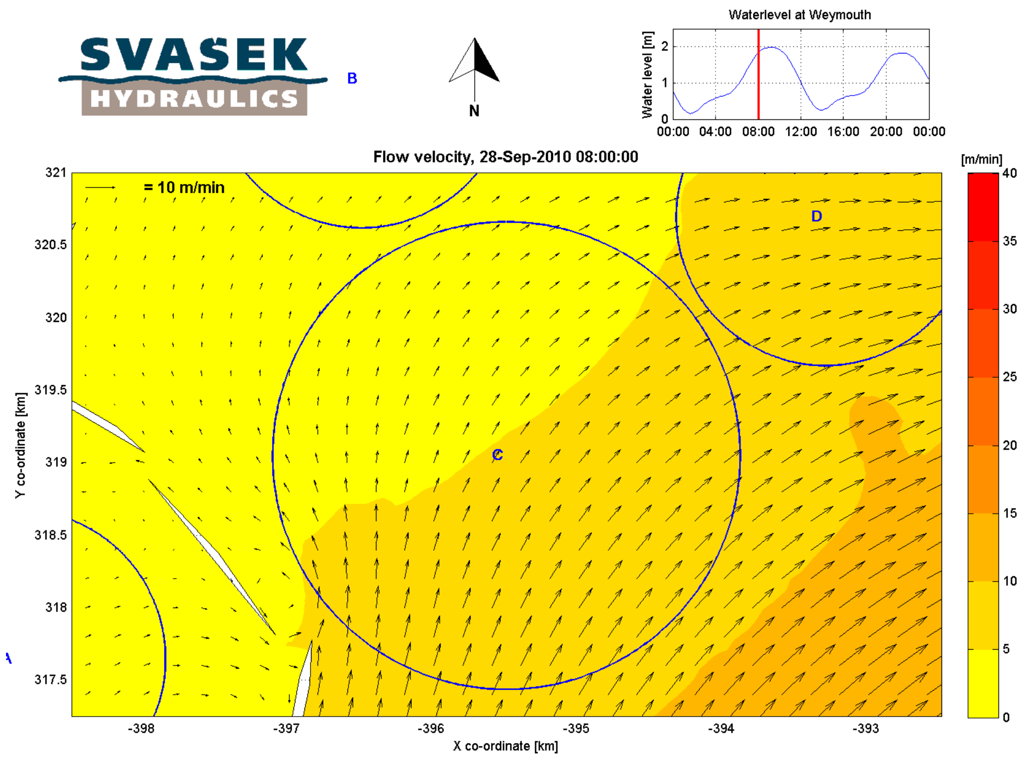

Figure 6.5: Example of a detail plot for racing area C

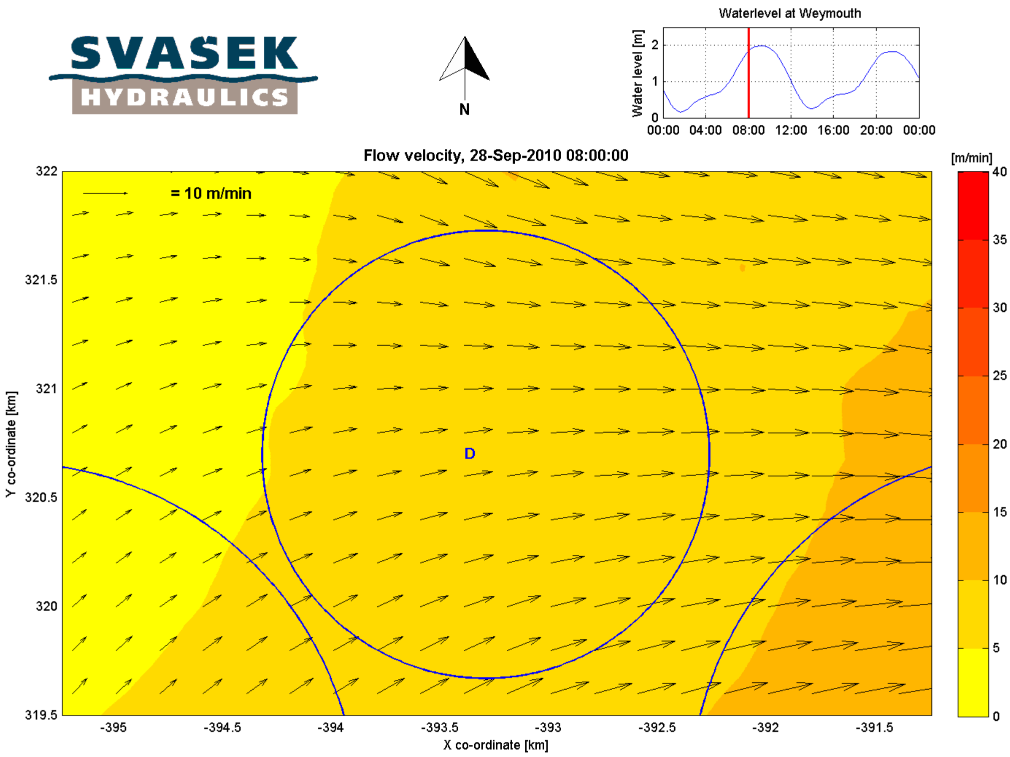

Figure 6.6: Example of a detail plot for racing area D

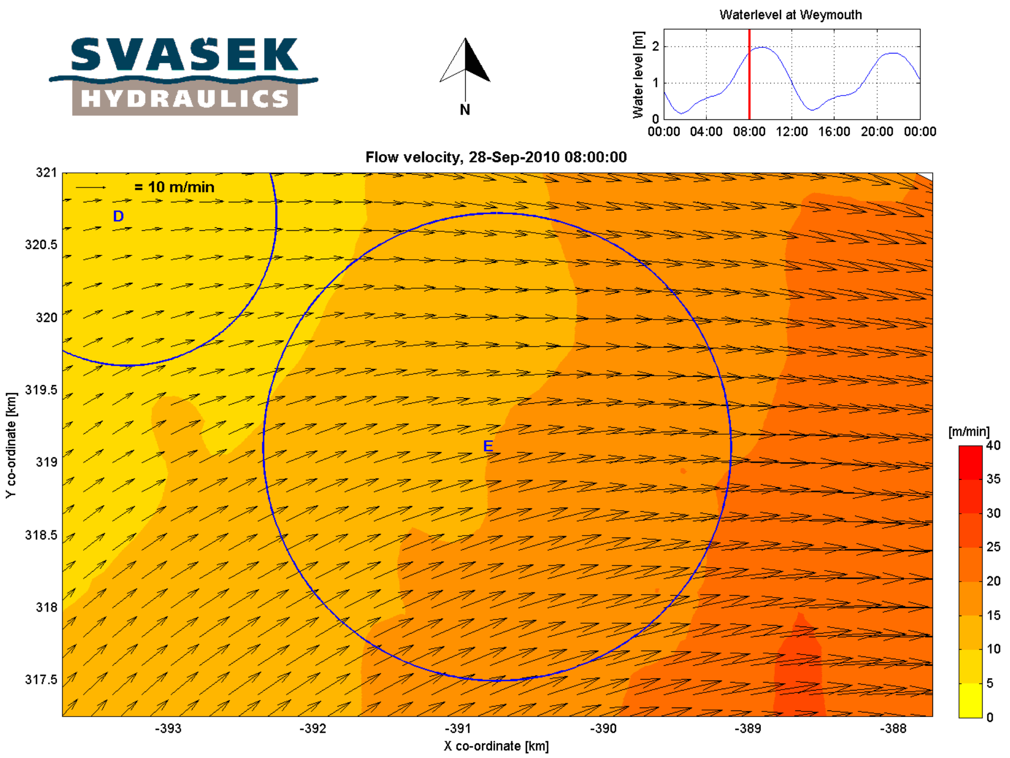

Figure 6.7: Example of a detail plot for racing area E

Chapter 7

Conclusions and recommendations

The objective of this thesis is to study and model the flow in the sailing area of the 2012 Olympic Sailing Competition, located partly in Portland Harbour and partly in Weymouth Bay, in order to generate accurate and reliable current forecasts in the Olympic sailing area during the 2012 Olympic Sailing Competition by means of a numerical flow model.

Based on the literature study and the survey, several conclusions can be drawn:

- According to the literature study of current–inducing processes, applied to the area of interest, the tidal flow is the main flow process in the Olympic sailing area. Most other current–inducing processes can be neglected; only wind and waves may have an influence on the flow.

- The available current data, originating from the late seventies and early eighties, is considered outdated. New current measurements, carried out in this study, show that the vertical velocity profile in the area of interest is nearly logarithmic, and that the flow direction is constant over the depth. Therefore, it is justified to average the flow over the depth.

The flow in the Olympic sailing area has been modelled by means of the depth–averaged numerical flow model FINEL2D. With respect to modelling the flow, several conclusions can be drawn:

- The currents in the sailing area of the 2012 Olympic Sailing Competition can well be modelled by means of FINEL2D. The model results correspond well to the measured flow velocities and flow directions. Besides, the water levels in the area of interest and the time of slack are reproduced good as well.

- The model is sensitive to the size of the grid elements. With respect to the calculation time, relatively large elements are best. In order to limit the numerical diffusion, which is a numerical artefact of the solver of FINEL2D, small elements are best. The element size has finally been taken such that both the calculation time and the numerical diffusion are acceptable, and is set to 100 m by 100 m.

- The computed flow velocities are sensitive to the bottom roughness. By adjusting the bottom roughness, the water levels, flow velocities and flow directions throughout the model domain respond; the phase of the flow responds somewhat stronger than the flow velocities and the water levels. Adjusting the bottom roughness locally has led to further improvements of the phase of the flow.

The literature study shows that wind and waves may have a significant influence on the flow. Therefore, special attention has been paid to wind and waves. With respect to these external forces, the conclusions are:

- Waves only influence the flow in the breaker zone. The racing areas are located outside the breaker zone. The waves therefore have a negligible influence on the flow in the racing areas.
- Wind has a significant influence on the flow in the sailing area. Depending on the wind direction, gyres in the Olympic sailing area or strong currents concentrated along the coast arise. The flow velocities corresponding to the wind–induced current in the area of interest are in the same order of magnitude as the tide–induced current in area of interest, which is $\mathcal{O}(10^{-1})$ m/s.
- It is difficult to obtain reliable and accurate forecasts of the wind–induced current, since uncertainties in the computed wind influence on the flow and water levels arise due to uncertainties in wind data. Besides, the modelled flow in the Olympic sailing are cannot be validated since no currents have been measured along transect A, which crosses the Olympic sailing area and therefore the wind–induced gyres, during wind.

With respect to the flow in the area and the performance of the numerical flow model some recommendations can be given as well:

- Measure the current in the Olympic sailing area during various wind conditions. The influence of the wind on the flow in the sailing area can thus be further investigated.
- Investigate the influence of the wind on the larger scale current.

Bibliography

[1] A.C. Bastos, M.B. Collins, and N.H. Kenyon. Water and sediment movement aroud a coastal headland: Portland Bill, Southern UK. *Ocean Dynamics*, 53:309–321, 2003.

[2] L.M. van der Bend. The Amsterdam Bosbaan: a top class rowing course? A study of lane differences. Master's thesis, Delft University of Technology, 1998.

[3] G.J. de Boer. *On the interaction between tides and stratification in the Rhine Region of Freshwater Influence.* PhD thesis, Delft University of Technology, 2009.

[4] G.T. Csanady. *Circulations in the Coastal Ocean.* D. Reidel Publishing Company, 1982.

[5] G. Dam and L. de Wit. *Technical and user manual FINEL2D, version 6.15.* Svašek Hydraulics, F edition, 2009.

[6] E. Deleersnijder, A. Norro, and E. Wolanski. A three-dimensional model of the water circulation around an island in shallow water. *Continental Shelf Research*, 12(7/8):891–906, 1992.

[7] Department for Environment, Food and Rural Affairs. Saltmarsh Management Manual. `http://www.saltmarshmanagementmanual.co.uk/Whatissaltmarsh.htm`. Retrieved August 2010.

[8] W.R. Geyer. Three-dimensional tidal flow around headlands. *J. Geophys. Res.*, 98(C1):955–966, 1993.

[9] S.K. Haslett, H.E. Mellor, and E.A. Bryant. Meteo-tsnuami hazard associated with thunderstorms in the United Kingdom. *Physics and Chemistry of the Earth*, 34:1016–1022, 2009.

[10] I.K.Tsanis. Simulation of wind-induced water currents. *J. Hydr. Eng.*, 115(8):1113–1134, 1989.

[11] M.P.C. de Jong. *Origin and prediction of seiches in Rotterdam harbour basins.* PhD thesis, Delft University of Technology, 2004.

[12] A. du Port. *Reeds Nautical Almanac 2010.* A & C Black Publishers Ltd., 2009.

[13] R.P. Signell and W.R. Geyer. Transient eddy formation around headlands. *J. Geophys. Res.*, 96(C2):2561–2575, 1991.

[14] J.H. Simpson. Physical processes in the ROFI regime. *J. Mar. Syst.*, 12:3–15, 1997.

[15] National Tidal and Sea Level Facility. Tidal predictions: Harmonic constants Weymouth. `http://www.pol.ac.uk/ntslf/`. Retrieved July 2010.

[16] Weymouth Weather. Weymouth weather data. `http://www.weymouth-weather.co.uk/`. Retrieved December 2010.

[17] Windfinder. Wind statistics Weymouth. `http://www.windfinder.com/windstats/windstatistic_weymouth.htm`. Retrieved August 2010.

[18] WindGURU. Monthly statistics Weymouth. `http://www.windguru.cz/nl/historie_statsw.php`. Retrieved August 2010.

[19] E. Wolanski, J. Imberger, and M.L. Heron. Island wakes in shallow coastal waters. *J. Geophys. Res.*, 89(C6):10,553–10,569, 1984.

[20] J. Wu. Wind-induced drift currents. *J. Fluid Mech.*, 68(1):49–70, 1975.

List of Figures

List of Tables

AppendixAppendix

Appendix A

The TPXO model

In order to determine the reliability of the TPXO model in shallow water, a comparison of the TPXO constituents of a TPXO point near Newlyn (see figure 2.5) and the constituents resulting from a tidal analysis on observed water levels at Newlyn has been made. This comparison has shown considerable deviations. Table A.1 shows the harmonic constituents following from the TPXO model and compares them with the 13 largest harmonic constituents following from a tidal analysis of observed water levels. It appears that 5 of the 13 constituents derived from the observed water levels, with significant amplitude, do not appear in the TPXO list. Furthermore, there are considerable differences in amplitude for all constituents. The phase however seems to correspond well.

In figure A.1 subsequently, the tide according to the TPXO model is extracted from the astronomical prediction. The difference between both shows deviations up to 0.75 m. The astronomical tide minus the tide according to the tidal analysis on the water level observations is also shown in the graph. Deviations still reach up to 0.40 m, but are significantly smaller than the deviations the TPXO model shows.

Since the difference between the harmonic constituents is particularly noticeable in the shallow water constituents, and the tide at Newlyn, calculated by means of the TPXO constituents show relatively large deviations compared to the astronomical tide, it is concluded that the TPXO data is less reliable in coastal seas and cannot be used for shallow areas.

The TPXO model is known to perform better in deep water, since the tide in deep water is not influenced by shallow water effects which causes for instance the M_4 constituent, and since the tide is hardly influenced by frictional effects which causes for instance the M_6 constituents. Therefore, the tide in deep water consists of constituents with a low frequency only. Since these constituents can be better measured by satellites than constituents with higher frequencies, the TPXO model performs fairly good in deep water.

TPXO		Observed	
Constituent	Amplitude	Constituent	Amplitude
M_2	1.81	M_2	1.58
S_2	0.62	S_2	0.53
N_2	0.36	N_2	0.29
K_2	0.17	K_2	0.14
M_4	0.11	$\boldsymbol{NU_2}$	**0.09**
K_1	0.07	$\boldsymbol{L_2}$	**0.09**
O_1	0.06	M_4	0.09
MS_4	0.06	K_1	0.06
MN_4	0.04	MS_4	0.05
P_1	0.02	$\boldsymbol{MU_2}$	**0.05**
Q_1	0.02	O_1	0.05
MF	0.01	$\boldsymbol{2N_2}$	**0.05**
MM	0.01	$\boldsymbol{MSF}$	**0.04**

Table A.1: Largest harmonic constituents following from the TPXO model and a tidal analysis of observed water levels at Newlyn

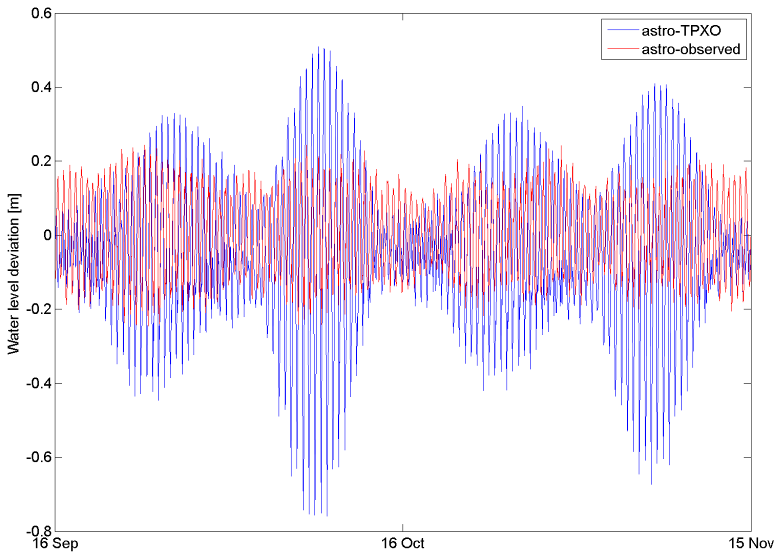

Figure A.1: TPXO harmonic constituents and harmonic constituents following from a tidal analysis on observed water levels at Newlyn, both compared to the astronomical prediction

Appendix B

Diffusivity of FINEL2D

Since the difference in eddy viscosity is large, several test runs with both the implicit version of FINEL2D, where the viscosity can be set manually, and the explicit version of FINEL2D have been performed in order to examine the influence of the viscosity on the model results. The properties of the models for these test runs are given in table B.1, and the used models are shown in figure B.1(a) and figure B.1(b). Both the viscosity and the time discretisation method vary throughout the different model runs. Figure B.2 shows the model results for an arbitrary point in time.

The current pattern in figure B.2(b), computed by means of the first order upwind scheme, corresponds well to the pattern in figure B.2(c), computed with the first order accurate Euler implicit method, although the flow velocities in figure B.2(b) are slightly smaller. The pattern in figure B.2(a), computed by means of the first order upwind scheme, corresponds good as well, however the flow velocities are clearly lower compared to the flow velocities in figure B.2(b).

Since the grid size determines the viscosity in the explicit version of FINEL2D, it is assumed that the deviations in flow velocities in figure B.2(a) and figure B.2(b) are due to sensitivities to the viscosity. The difference in flow velocities are approximately only $\mathcal{O}(10^{-2})$ m/s, and the influence of the viscosity can therefore be considered actual, but limited. Moreover, the differences in flow velocity decrease when the computational grid will be further refined. Therefore, it is concluded that the influence of the numerical diffusivity caused by the solver of the explicit version of FINEL2D is negligible. However, the grid elements have to be sufficiently small.

	Implicit	*Explicit – coarse*	*Explicit – fine*
k $[-]$	0.01	0.01	0.01
ν_t^H $[m^2s^{-1}]$	0.001	≈ 250	≈ 50
Max area element $[m]$	$500 \cdot 500$	$500 \cdot 500$	$100 \cdot 100$
Time discretisation	Euler Implicit	Upwind	Upwind
Accuracy	1^{st} order	1^{st} order	1^{st} order
Model	Channel	ECSM	ECSM

Table B.1: Model properties test runs

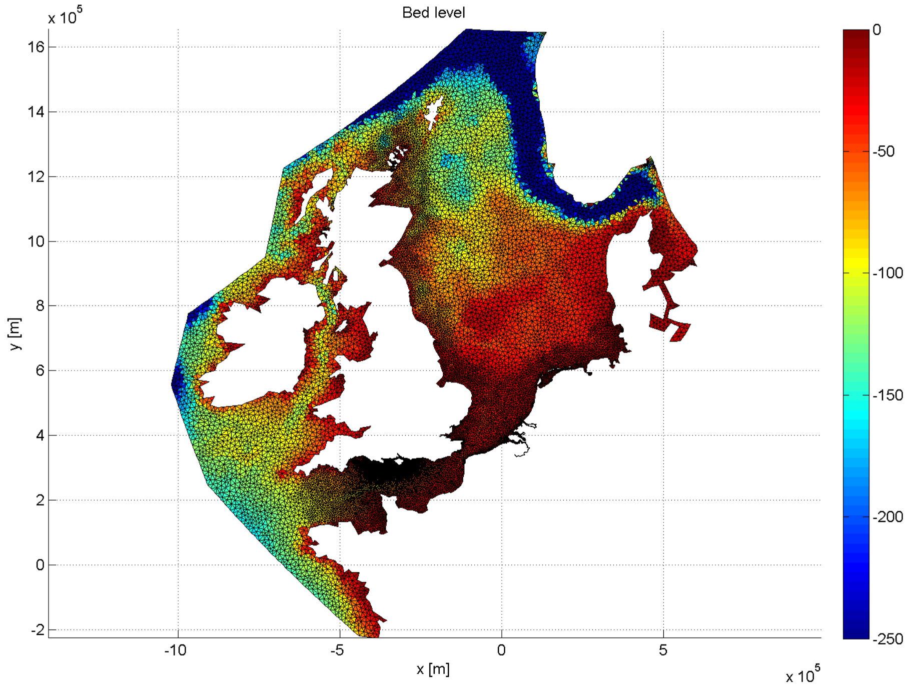

(a)

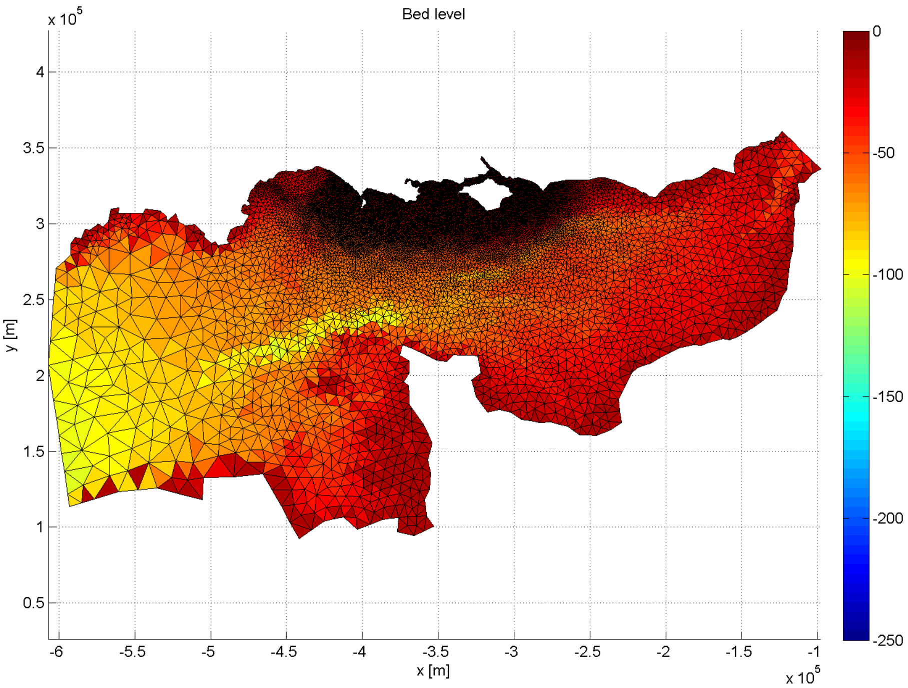

(b)

Figure B.1: (a) ECSM model (b) Channel model

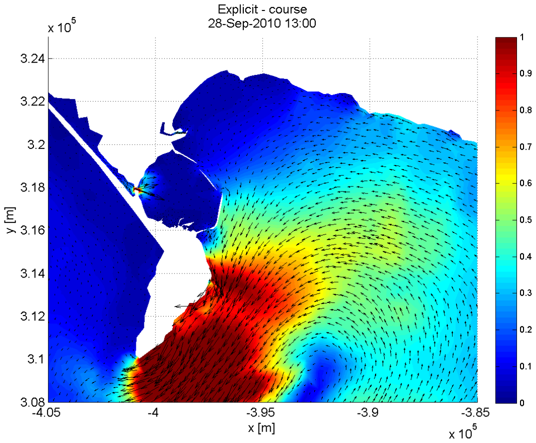

(a) Model results for the explicit version of FINEL2D. The elements are large compared to the elements of figure B.2(b).

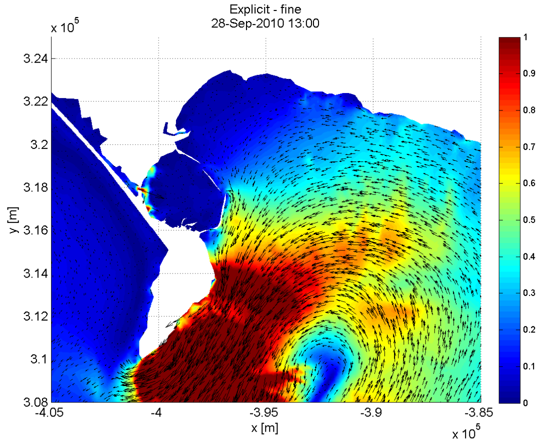

(b) Model results for the explicit version of FINEL2D. The elements are small compared to the elements of figure B.2(a).

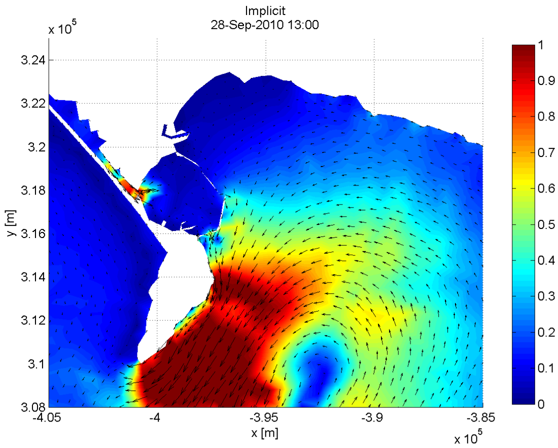

(c) Model results for the implicit version of FINEL2D. The Euler Implicit method has been applied.

Figure B.2: Results runs for different numerical flow models

Appendix C

Wind–induced current

In order to investigate the influence of the wind on the current pattern, several wind fields have been imposed to the numerical flow model, the ECSM model. The wind influence on the current pattern in the Weymouth and Portland area is discussed in Chapter 5, however, several of the model results have not been included in the main part of the report. These resulting water levels and flow velocities are presented here. For the sake of completeness, the results which have been presented in the main part of the report, are shown here as well. An overview of the presented results is given in table C.1 and table C.2.

In the figures that show the flow velocities in the Weymouth and Portland area, the first graph shows the current pattern in the area of interest, based on tide only. The second graph shows the current pattern which arises when the constant wind field is imposed to the model. The third graph shows the difference between the second and the first graph, and therefore shows the wind–induced currents only. To indicate to which extent the racing areas of the 2012 Olympic Sailing Competition are influenced by the wind, the racing areas have been indicated with red circles in the figures.

Wind conditions			Drag coefficient [−]	Figure
Speed [m/s]	Speed [bft]	Direction [°]		
19	8	180	0.0026	C.3, C.4
12.3	6	180	0.0026	C.5, C.6
7	4	180	0.0026	C.7, C.8
2.5	2	180	0.0026	C.9, C.10
12.3	6	0	0.0026	C.11, C.12
12.3	6	90	0.0026	C.13, C.14
12.3	6	270	0.0026	C.15, C.16

Table C.1: Overview of the presented resulting flow velocities for model runs where wind is accounted for

Wind conditions			Drag coefficient [−]	Figure
Speed [m/s]	Speed [bft]	Direction [°]		
12.3	6	180 and 0	0.0026	C.1
12.3	6	90 and 27	0.0026	C.2

Table C.2: Overview of the presented resulting water levels for model runs where wind is accounted for

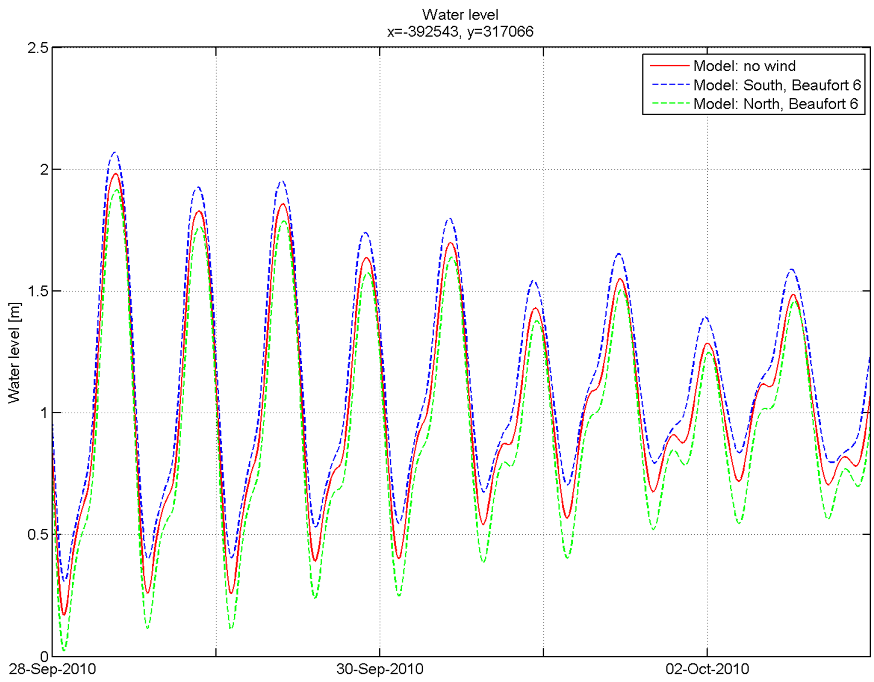

Figure C.1: Water level at Weymouth in case of no wind, a southern wind and a northern wind. The wind speed is Beaufort 6.

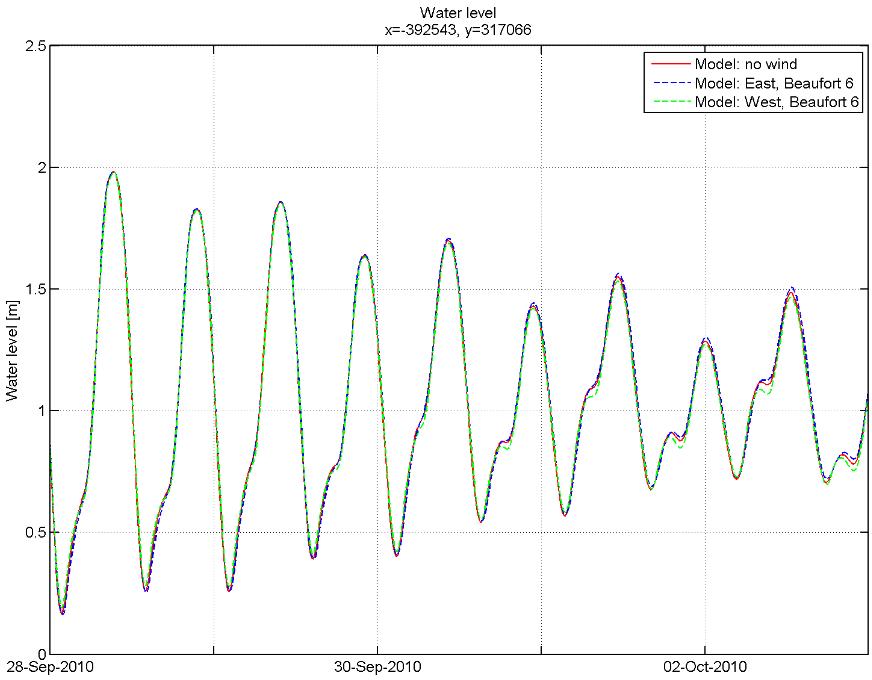

Figure C.2: Water level at Weymouth in case of no wind, a eastern wind and a western wind. The wind speed is Beaufort 6.

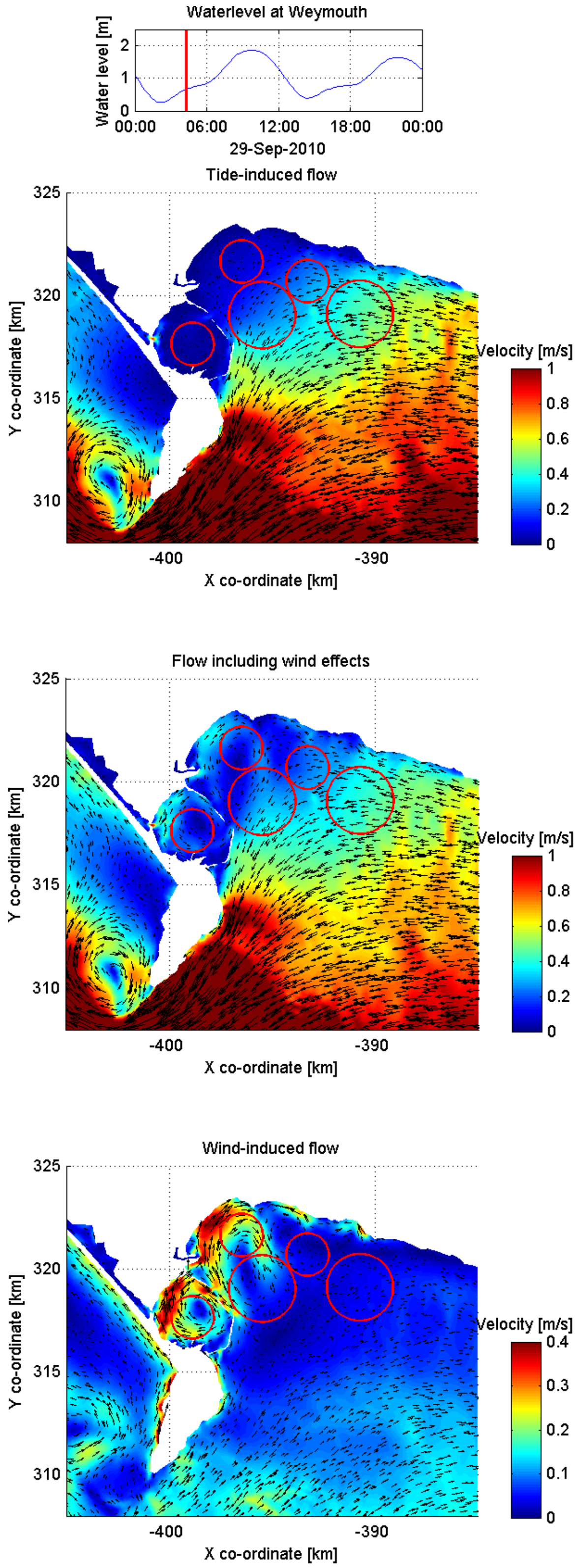

Figure C.3: Model results for the maximum ebb flow during spring tide for a southern wind, Beaufort 8.

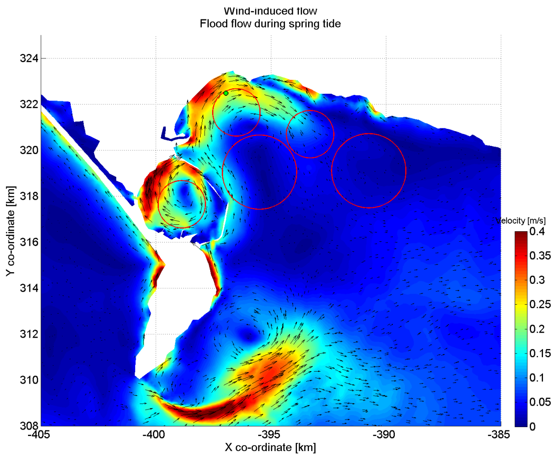

(a) Maximum flood flow during spring tide

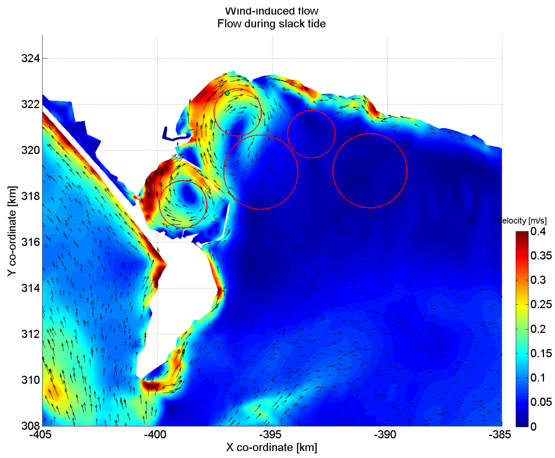

(b) Flow during slack tide

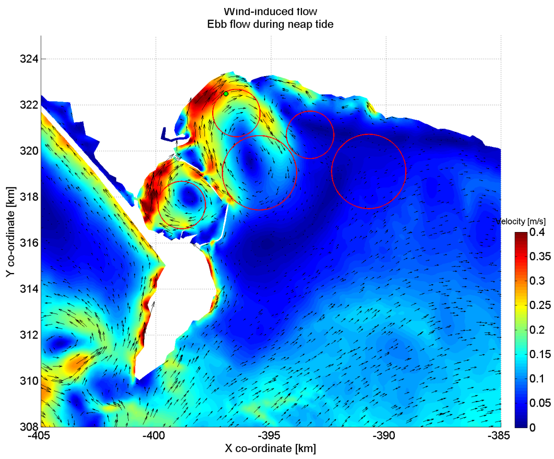

(c) Maximum ebb flow during neap tide

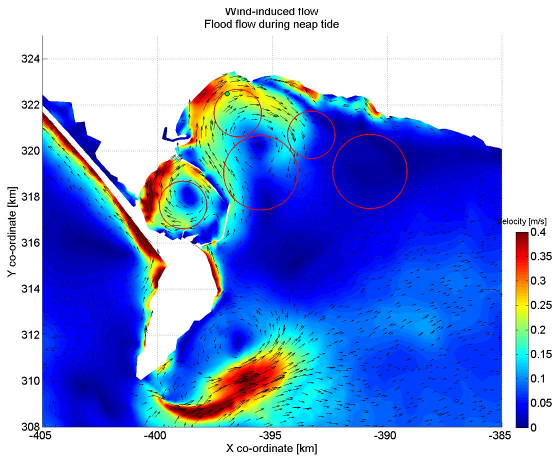

(d) Maximum flood flow during neap tide

Figure C.4: Model results for the flow for a southern wind, Beaufort 8.

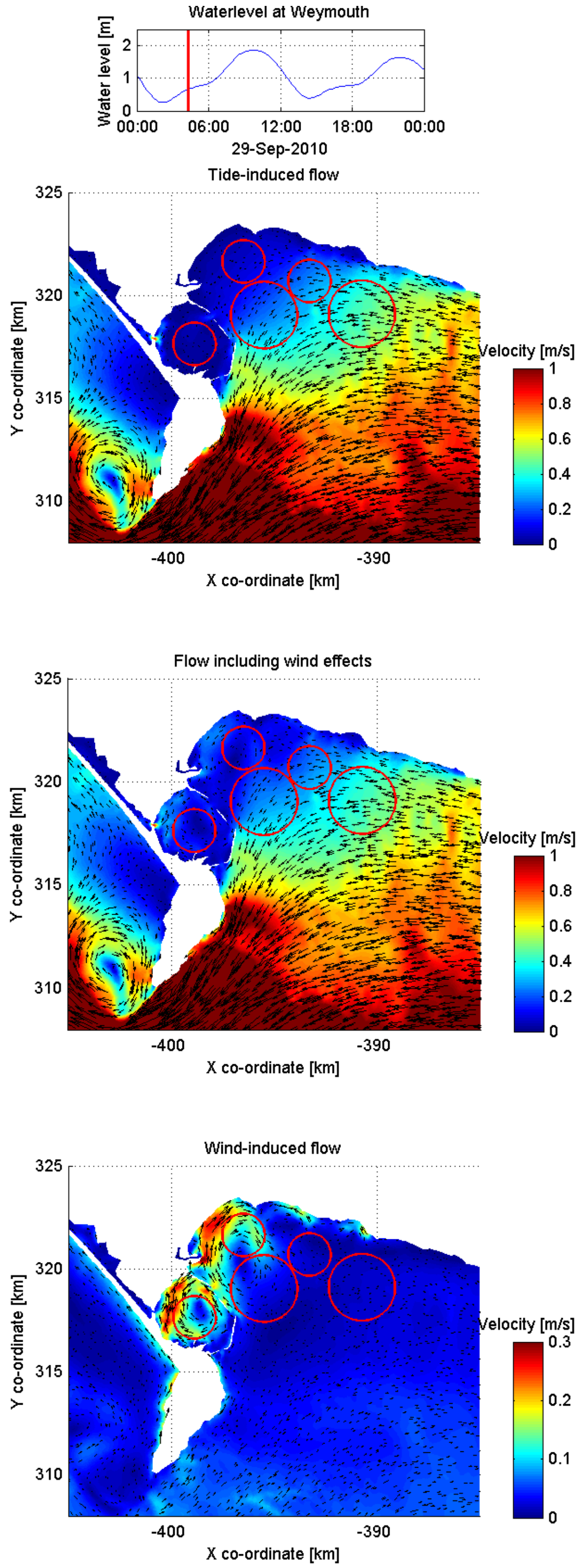

Figure C.5: Model results for the maximum ebb flow during spring tide for a southern wind, Beaufort 6.

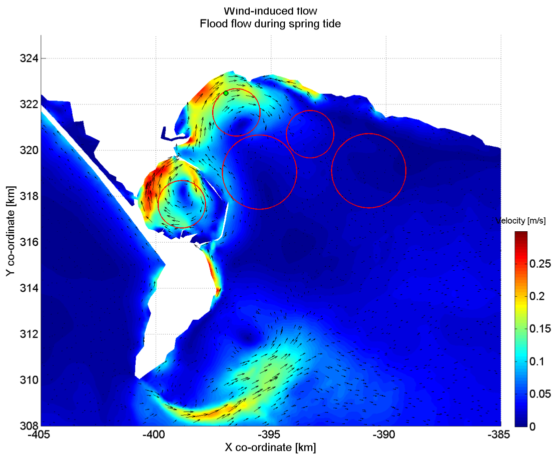

(a) Maximum flood flow during spring tide

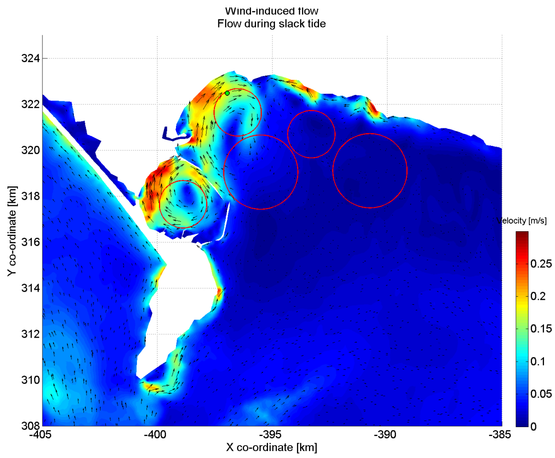

(b) Flow during slack tide

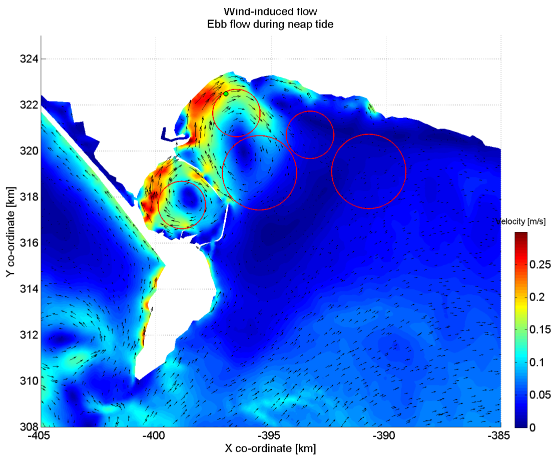

(c) Maximum ebb flow during neap tide

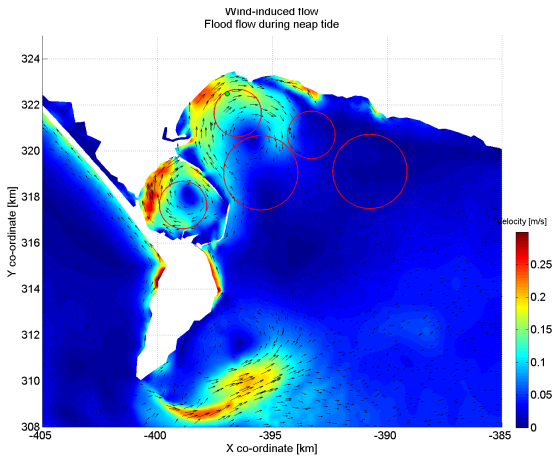

(d) Maximum flood flow during neap tide

Figure C.6: Model results for the flow for a southern wind, Beaufort 6.

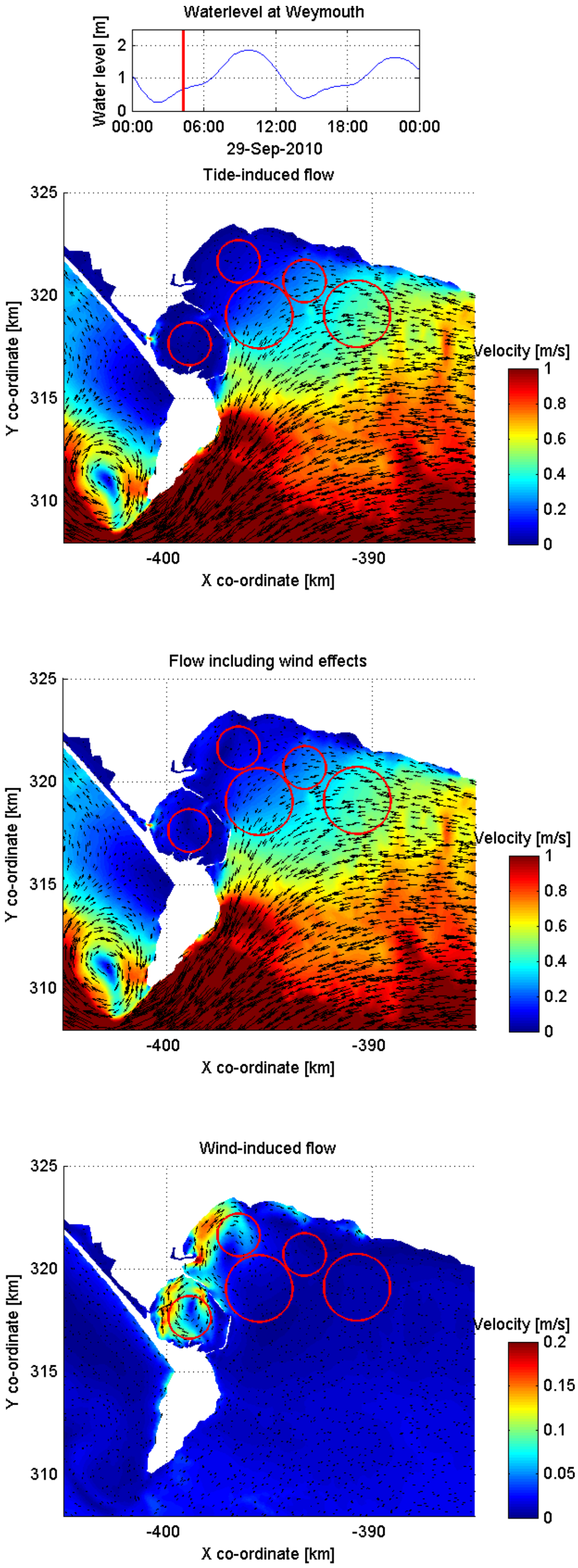

Figure C.7: Model results for the maximum ebb flow during spring tide for a southern wind, Beaufort 4.

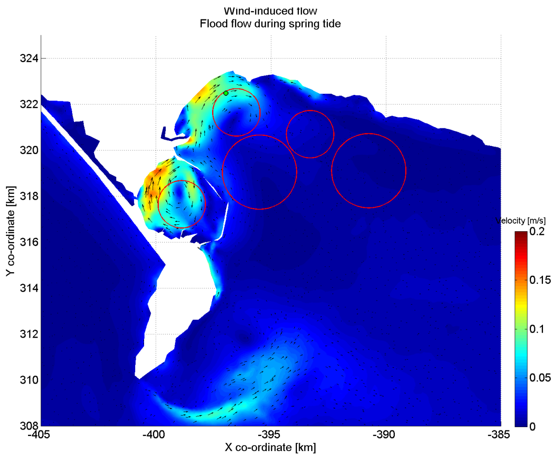

(a) Maximum flood flow during spring tide

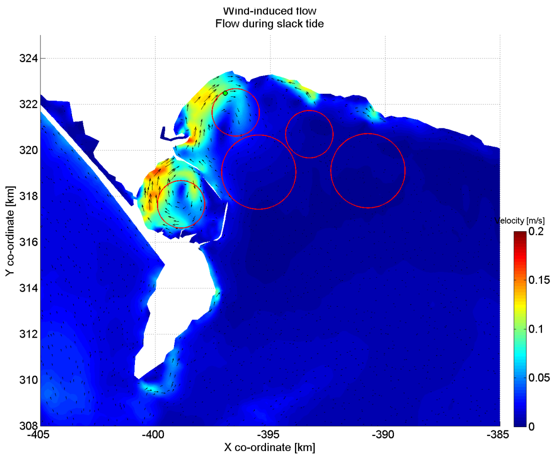

(b) Flow during slack tide

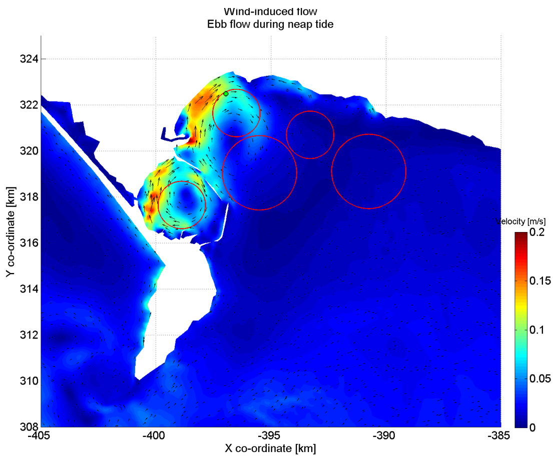

(c) Maximum ebb flow during neap tide

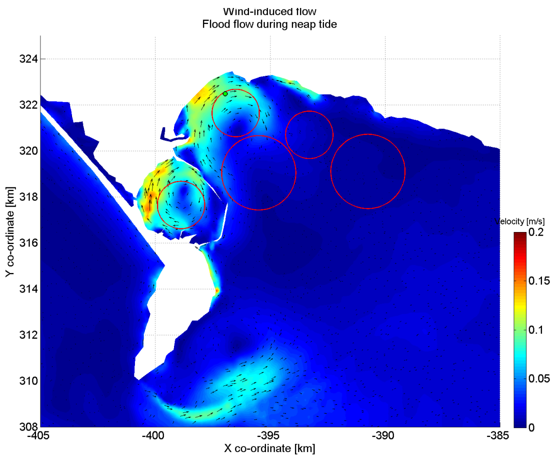

(d) Maximum flood flow during neap tide

Figure C.8: Model results for the flow for a southern wind, Beaufort 4.

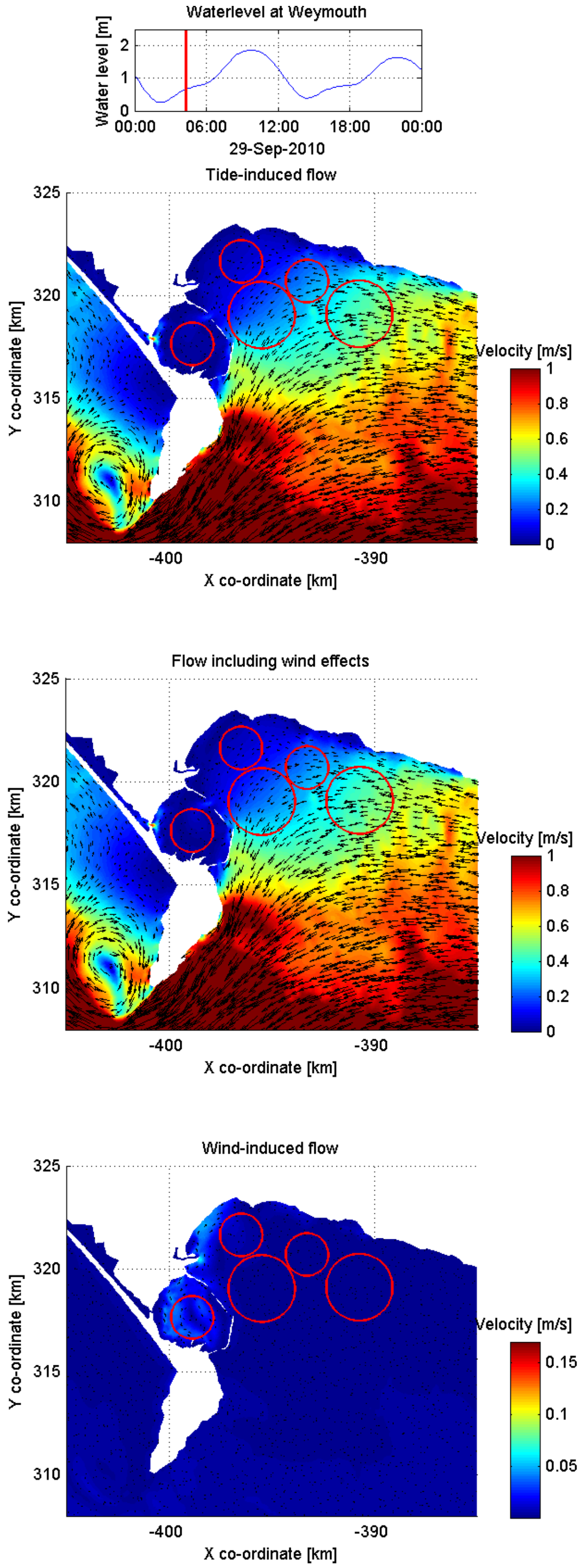

Figure C.9: Model results for the maximum ebb flow during spring tide for a southern wind, Beaufort 2.

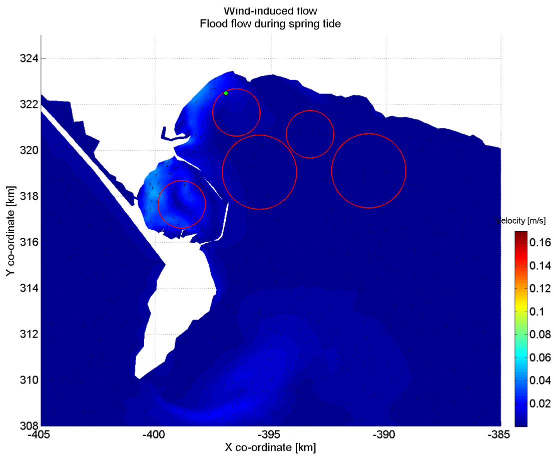

(a) Maximum flood flow during spring tide

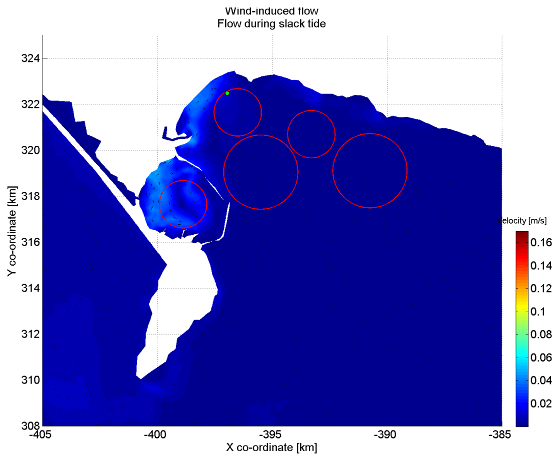

(b) Flow during slack tide

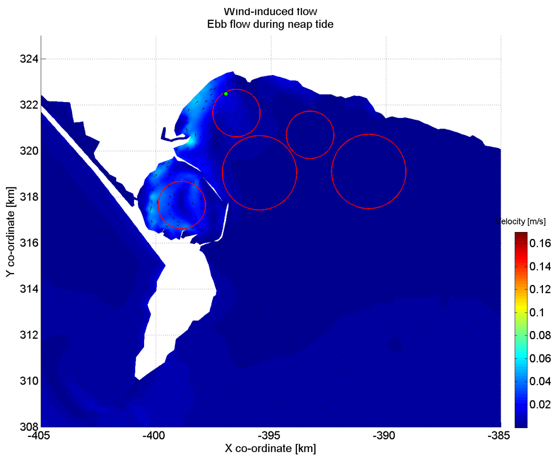

(c) Maximum ebb flow during neap tide

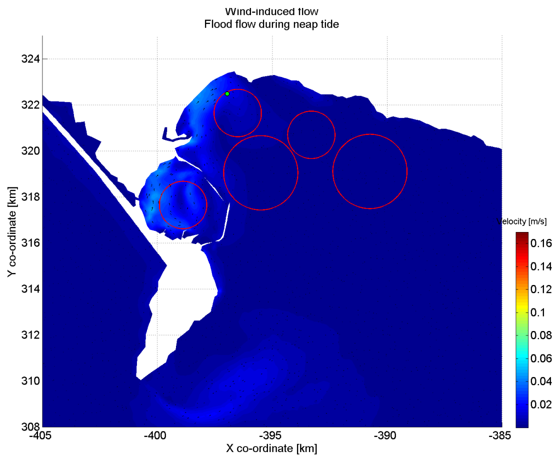

(d) Maximum flood flow during neap tide

Figure C.10: Model results for the flow for a southern wind, Beaufort 2.

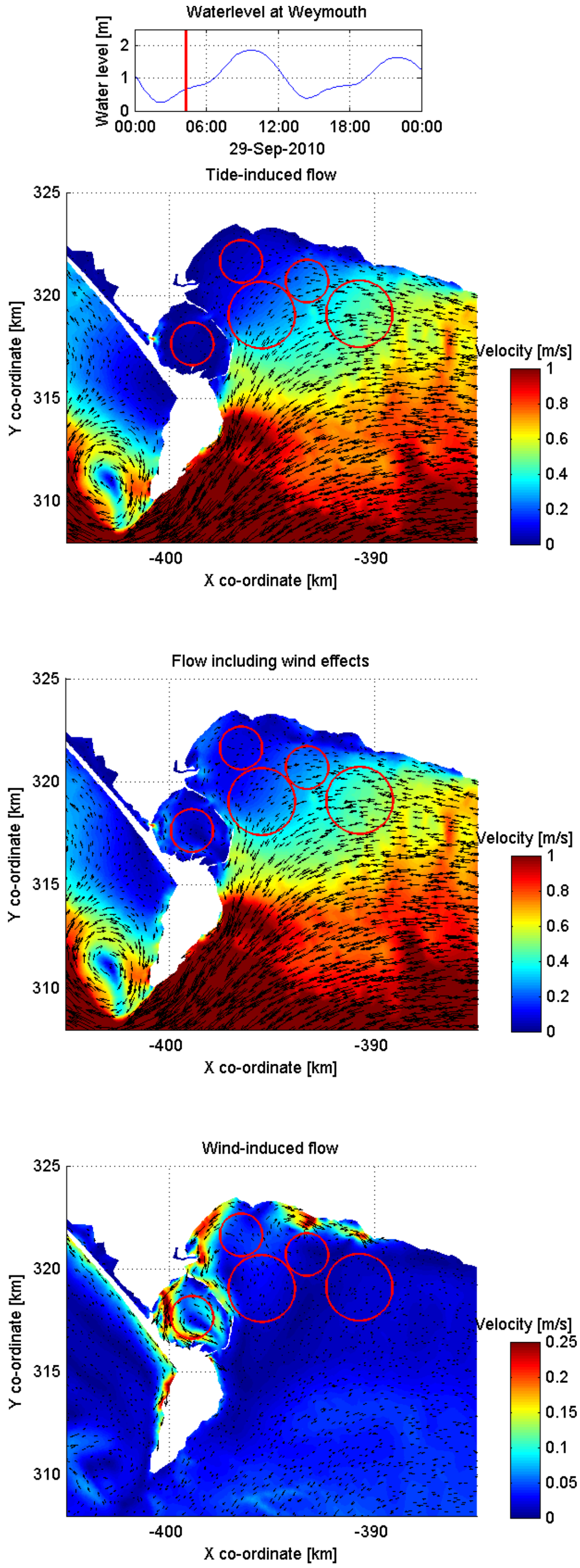

Figure C.11: Model results for the maximum ebb flow during spring tide for a northern wind, Beaufort 6.

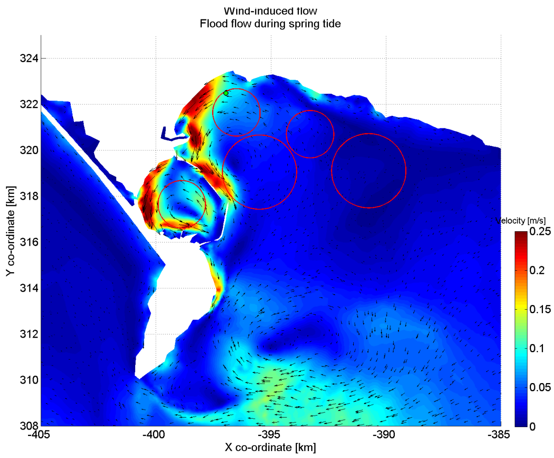

(a) Maximum flood flow during spring tide

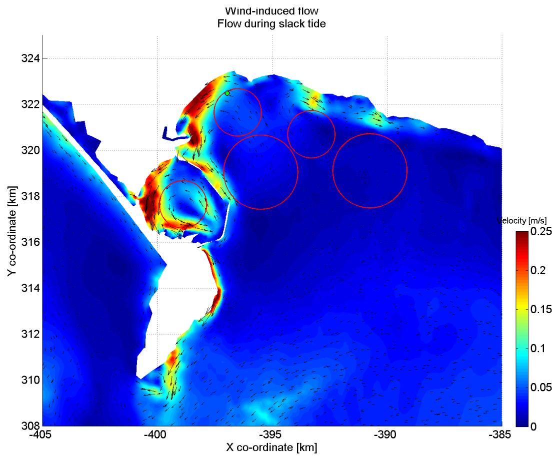

(b) Flow during slack tide

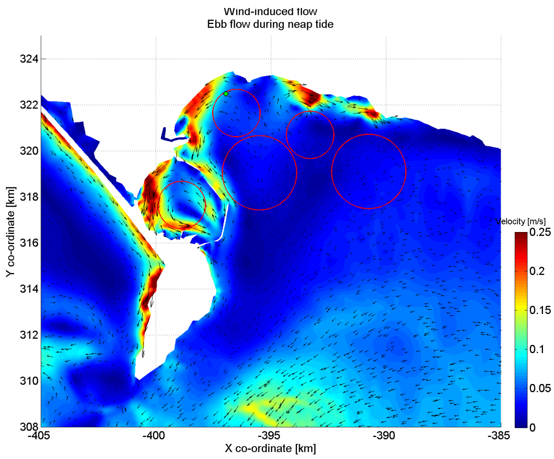

(c) Maximum ebb flow during neap tide

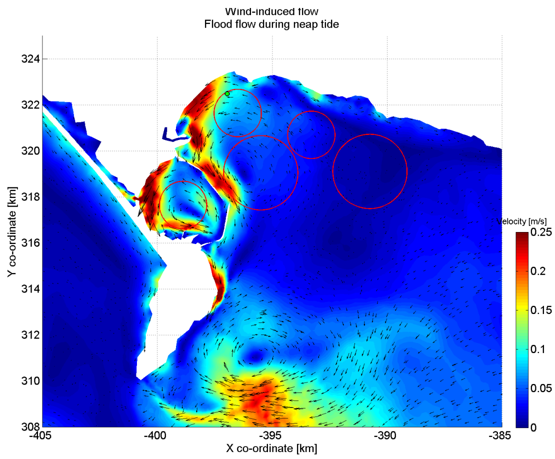

(d) Maximum flood flow during neap tide

Figure C.12: Model results for the flow for a northern wind, Beaufort 6.

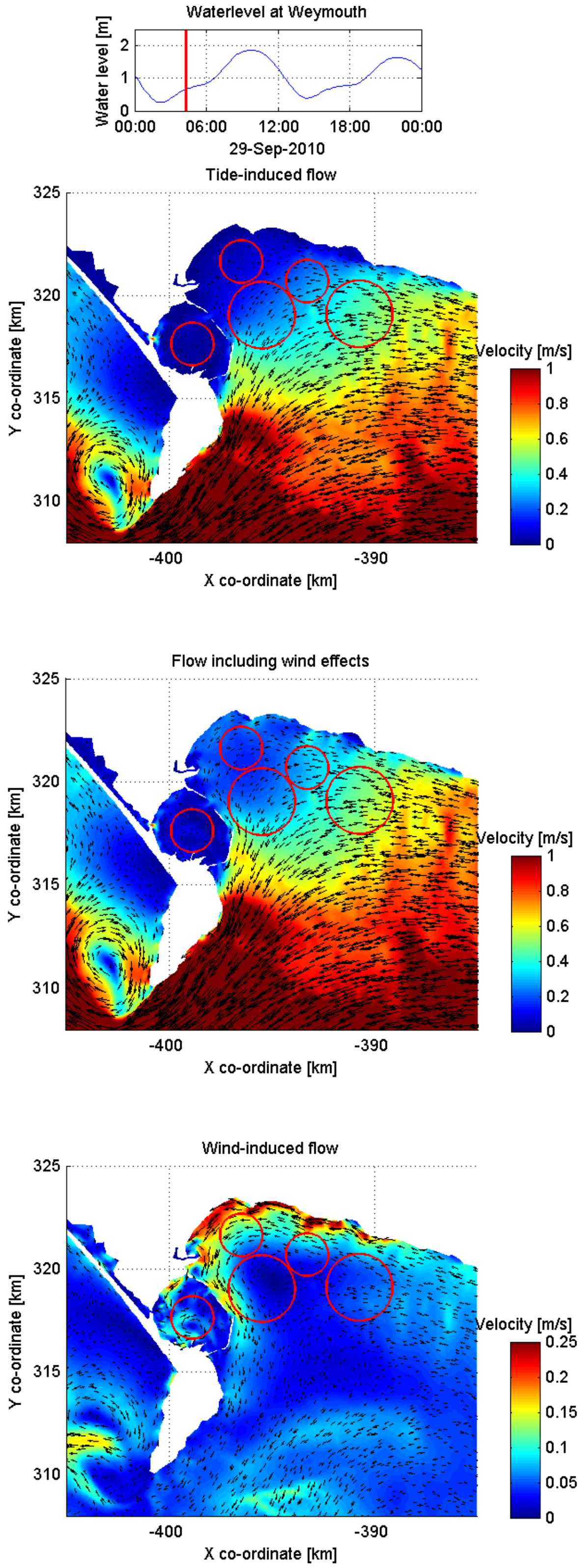

Figure C.13: Model results for the maximum ebb flow during spring tide for an eastern wind, Beaufort 6.

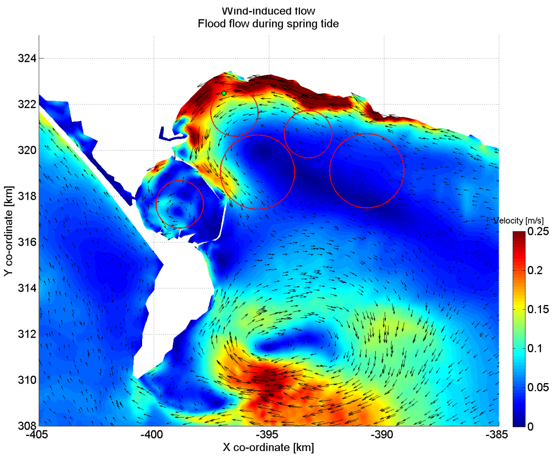

(a) Maximum flood flow during spring tide

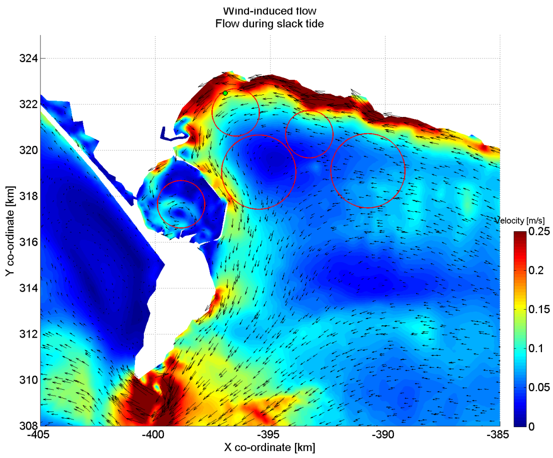

(b) Flow during slack tide

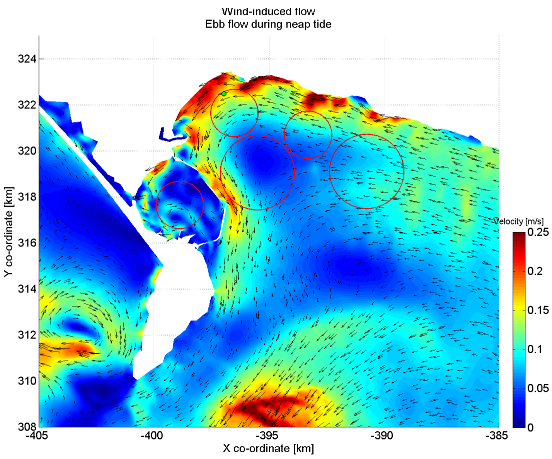

(c) Maximum ebb flow during neap tide

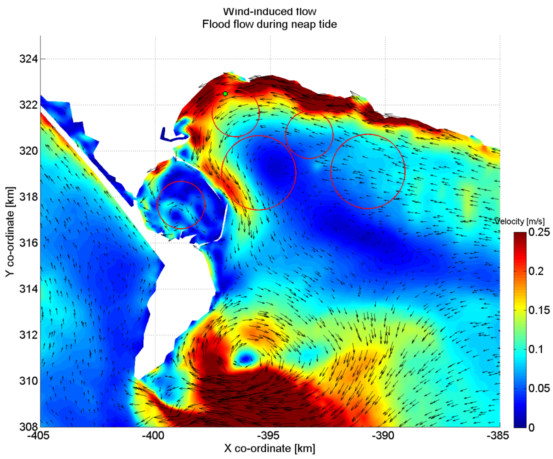

(d) Maximum flood flow during neap tide

Figure C.14: Model results for the flow for an eastern wind, Beaufort 6.

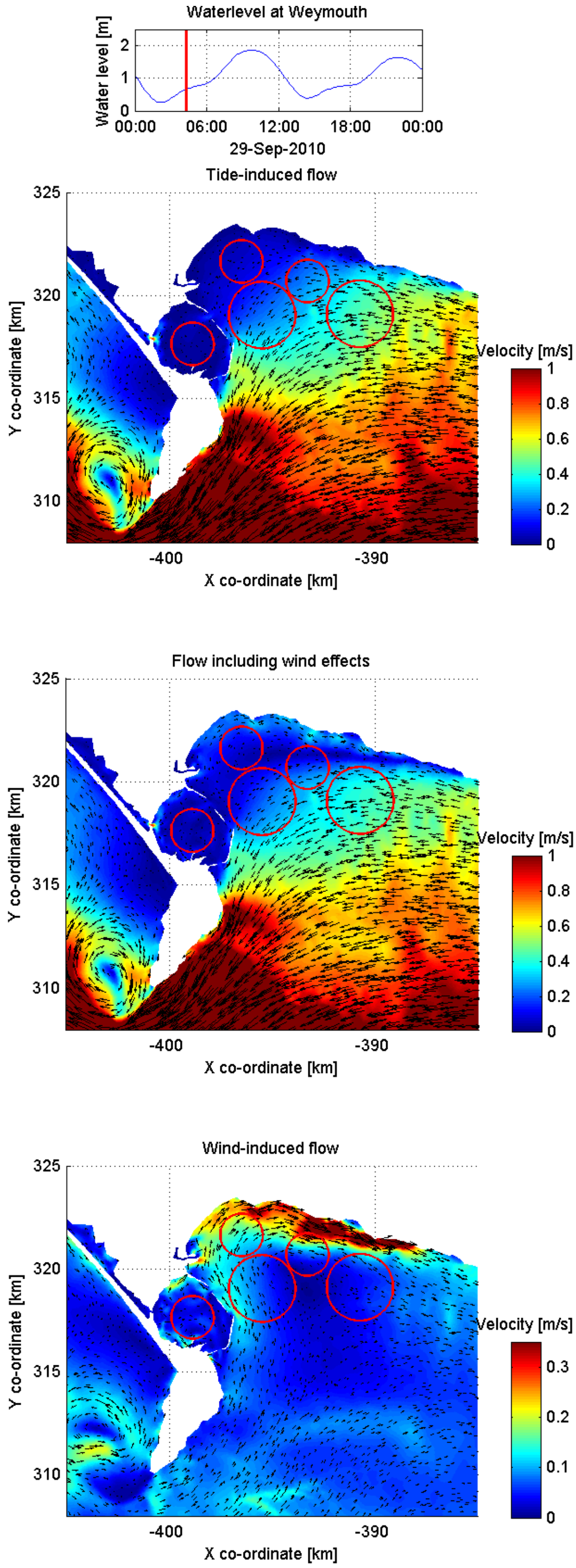

Figure C.15: Model results for the maximum ebb flow during spring tide for a western wind, Beaufort 6.

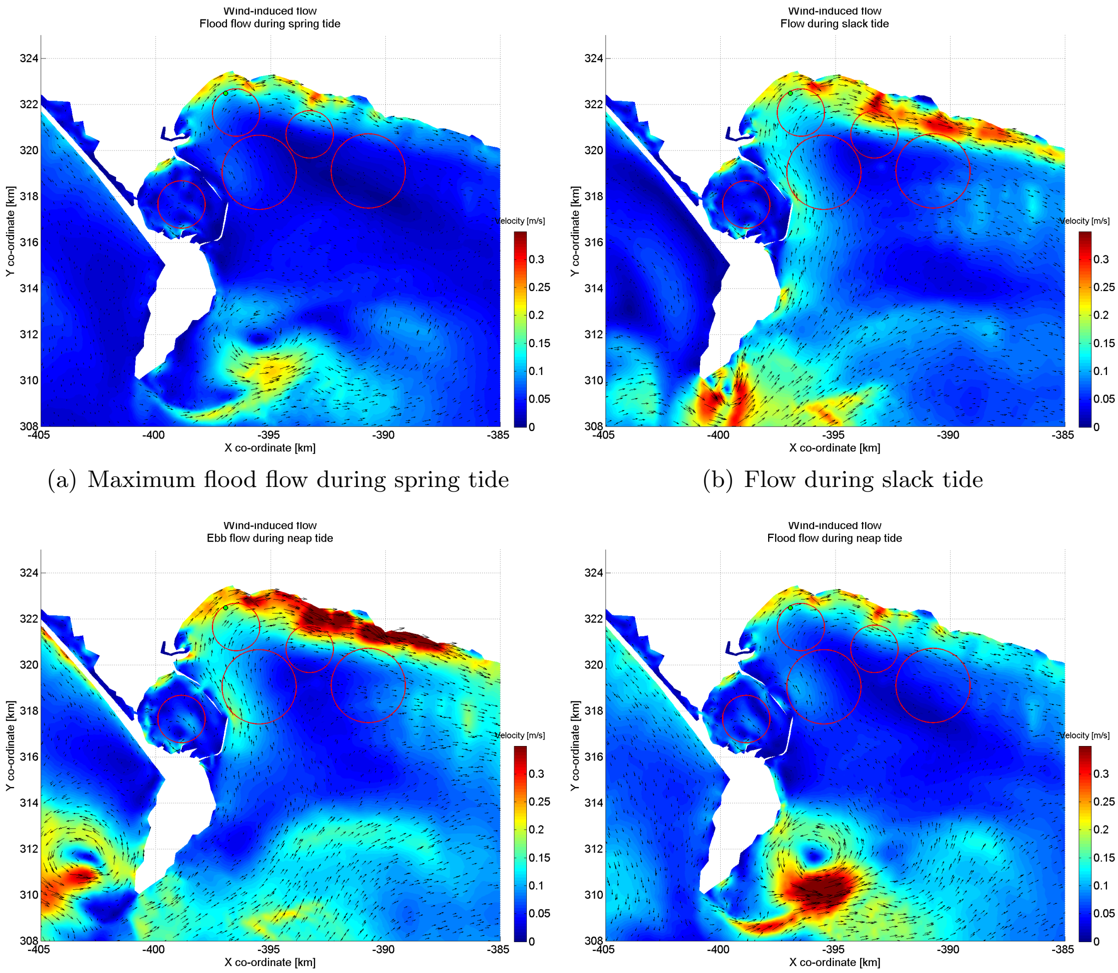

(a) Maximum flood flow during spring tide

(b) Flow during slack tide

(c) Maximum ebb flow during neap tide

(d) Maximum flood flow during neap tide

Figure C.16: Model results for the flow for a western wind, Beaufort 6.

Appendix D

Survey report

This appendix serves as a survey report of the survey performed in Weymouth Bay, UK, from September 27^{th} until October 2^{nd}. The survey has been performed within the framework of the 2012 Olympic Sailing Competition Support project. Both water level measurements and sailed current measurements have been performed.

General

The sailed current measurements have been performed by means of an Acoustic Doppler Current Profiler (ADCP), along the transects given in table D.2. The ADCP has been fixed to the sailing vessel during the measurements, the Antares, Scheveningen. By linking the ADCP to a gyro and a GPS system with DGPS, the current data is automatically corrected for the vessel speed. The data has been processed by means of the so–called SurveyVM software, version 1.45.

The measurements have been performed during several days; table D.1 shows an overview of which transect has been sailed on each day. In principle, measurements have been performed during 13 successive hours, in order to measure an entire tidal cycle. On October 1^{st} however, the weather was heavy to such an extent, that the measurements have been performed over a shorter period. The transects sailed on September 30^{th} have been extra. An overview of the sailed transects per day can be found in table D.3 until table D.7.

The water level has been measured with a Valeport pressure sensor. By also measuring the water temperature and salinity, and by measuring the air pressure with another pressure sensor, the measured pressure can be converted into the water level. The data from both pressure sensors is processed by means of the Diver Office software, version 2010.1.

Date	Activity
27/09/2010	Preparations
28/09/2010	Transect A
29/09/2010	Transect B
30/09/2010	Portland Harbour. Sailed Transect B once
01/10/2010	Transect C
02/10/2010	Transect B

Table D.1: Overview of the performed surveys

Transect	Direction	From	To
A	North–South	50°34′48″N 2°23′30″W	50°37′48″N 2°23′30″W
B	East–West	50°35′00″N 2°24′00″W	50°35′00″N 2°19′00″W
C	North–South	50°35′00″N 2°23′00″W	50°32′00″N 2°23′00″W

Table D.2: Lines of direction

Transect	**No.**	**Tidal phase**	**Start time**	**End time**	**Direction**
A	1	Flood	9.49	10.41	180
A	2	Slack	10.47	11.32	0
A	3	Slack	11.37	12.27	180
A	4	Ebb	12.32	13.21	0
A	5	Ebb	13.26	14.15	180
A	6	Ebb	14.20	14.59	0
A	7	Ebb	15.02	15.40	180
A	8	Ebb	15.43	16.21	0
A	9	Ebb	16.25	17.03	180
A	10	Ebb	17.07	17.21	0
A	11	Ebb	17.21	17.33	180

Table D.3: Overview sailed transects - September 28^{th}

Transect	**No.**	**Tidal phase**	**Start time**	**End time**	**Direction**
B	1	Flood	7.18	7.58	90
B	2	Flood	8.00	8.51	270
B	3	Flood	8.54	9.31	90
B	4	Flood	10.05	10.49	270
B	5	Ebb	12.34	13.03	270
B	6	Ebb	13.06	13.50	90
B	7	Ebb	13.52	14.30	270
B	8	Ebb	14.33	15.20	90
B	9	Ebb	15.22	15.59	270
B	10	Ebb	16.01	16.50	90
B	11	Ebb	16.52	17.31	270

Table D.4: Overview sailed transects - September 29^{th}

Transect	**No.**	**Tidal phase**	**Start time**	**End time**	**Direction**
B	1	Ebb	13.41	14.25	90
B	2	Ebb	14.27	15.11	270

Table D.5: Overview sailed transects - September 30^{th}

Transect	**No.**	**Tidal phase**	**Start time**	**End time**	**Direction**
C	1	Ebb	12.18	13.16	180
C	2	Ebb	13.20	13.51	0
C	3	Ebb	13.56	14.53	180
C	4	Ebb	14.57	15.34	0
C	5	Ebb	15.38	16.17	180
C	6	Ebb	16.21	16.55	0
C	7	Ebb	16.58	17.33	180
C	8	Ebb	17.37	18.13	0
C	9	Ebb	18.13	18.36	180
C	10	Ebb	18.40	19.20	0

Table D.6: Overview sailed transects - October 1^{st}

Transect	**No.**	**Tidal phase**	**Start time**	**End time**	**Direction**
B	1	Ebb	7.07	7.23	90
B	2	Ebb	7.26	8.05	270
B	3	Ebb	8.08	8.55	90
B	4	Ebb	8.57	9.38	270
B	5	Slack	9.41	10.26	90
B	6	Flood	10.28	11.14	270
B	7	Flood	11.17	11.59	90
B	8	Flood	12.01	12.52	270
B	9	Flood	12.55	13.34	90
B	10	Flood	13.36	14.24	270
B	11	Flood	14.26	15.08	90
B	12	Slack	15.10	15.53	270
B	13	Ebb	15.56	16.43	90
B	14	Ebb	16.45	17.25	270
B	15	Ebb	17.28	18.25	90

Table D.7: Overview sailed transects - October 2^{nd}

Tide levels Portland – 50°34′N 2°26′W	
Height in meters above datum	
Mean High Water Spring	2.1
Mean High Water Neap	1.4
Mean Low Water Neap	0.8
Mean Low Water Spring	0.1

Table D.8: Tide levels in the Weymouth and Portland area according to Admiralty Chart 2255

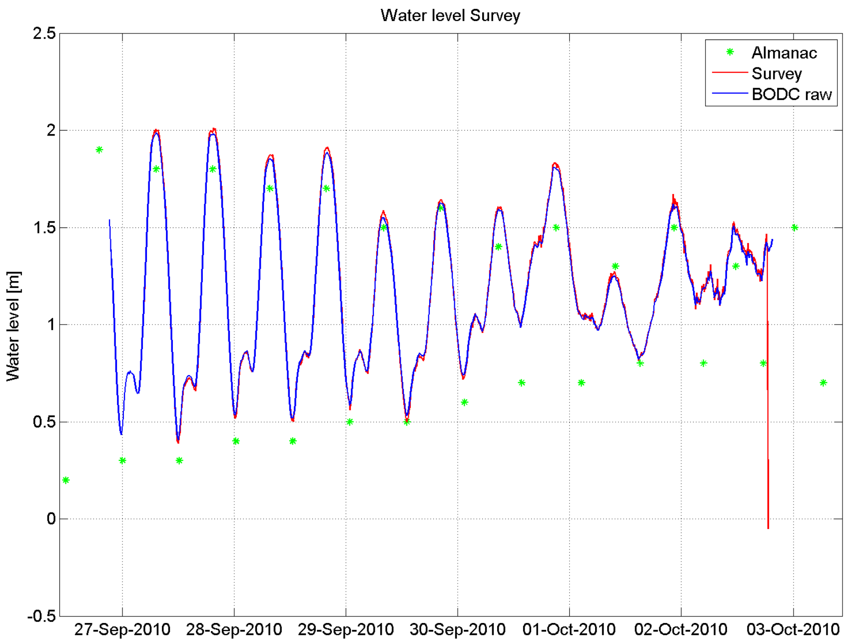

Figure D.1: Measured and (by means of a tidal analysis) predicted water levels at Weymouth [15]

Tide

As already mentioned in the previous section, water levels have been measured by means of measuring the pressure with a Valeport pressure sensor. Besides, the Weymouth tide gauge, part of the extended UK Tidal Gauge Network, has measured the water levels as well. The results from both devices are shown in figure D.1. The graph shows the high and low waters according to the Reeds Nautical Almanac 2010 as well. The high and low waters from the Almanac are predictions, predicted by means of performing an extensive analysis of the tide first. The mean tide levels according to Admiralty Chart 2255 are shown in table D.8.

Conditions

The wave and wind conditions during the survey are obtained from a local weather station and the Weymouth wave buoy. The wind speed and wind direction are shown in figure D.2. Both the significant wave height, the wave direction and the peak period are shown in figure D.3. Besides, the wind conditions according to the GFS0.5 forecast model and wind and wave conditions according to the NWW3 hindcast model are shown.

Results

The measured depth–averaged flow velocity and direction along the sailed transects are presented in figure D.4 until figure D.17. On each page, a maximum of 4 sailed transects is

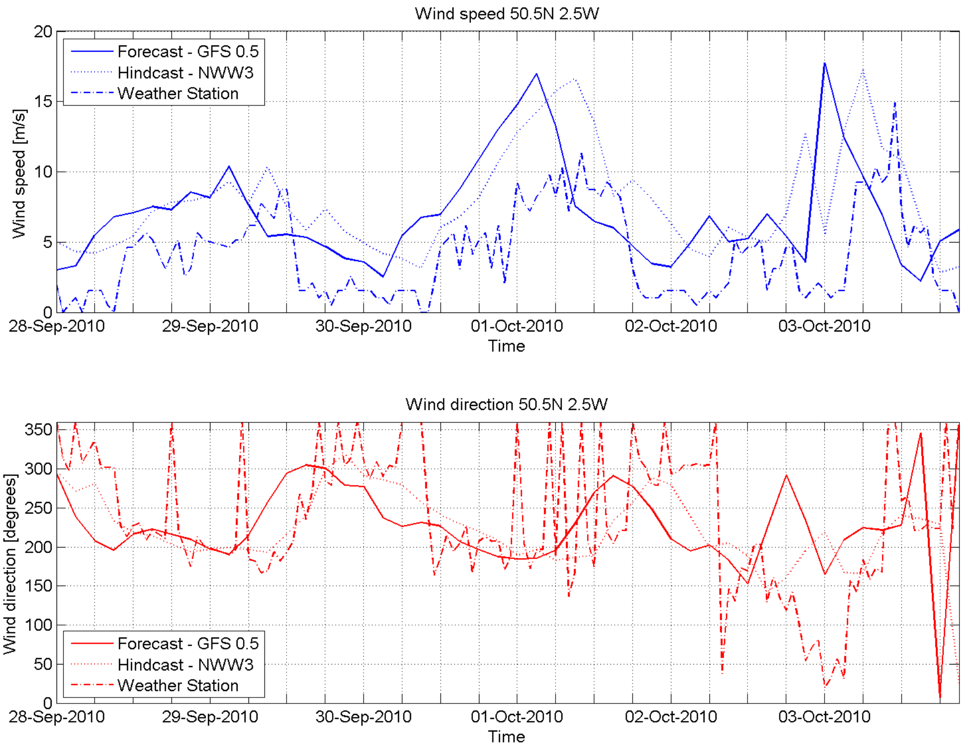

Figure D.2: Wind conditions during survey

presented. Furthermore, the vertical velocity profile for each transect is presented in figure D.18 until figure D.22. These figures consist of three graphs, which represent:

1 The vertical velocity profile;

2 The vertical velocity profile on a semi–logarithmic scale;

3 The flow direction.

For each transect, only one vertical velocity profile is shown. During the survey, every 20 s a velocity sample was produced, which is the average over those 20 s. Since the time span is very short, fluctuations due to turbulence are not averaged out of the results. These fluctuations clearly visible in for instance the vertical velocity distribution, which becomes very jagged. To determine whether for instance 3D–effects have been measured, it is desirable to filter these fluctuations out of the signal. Each vertical velocity profile therefore represents the average velocity profile of a single transect.

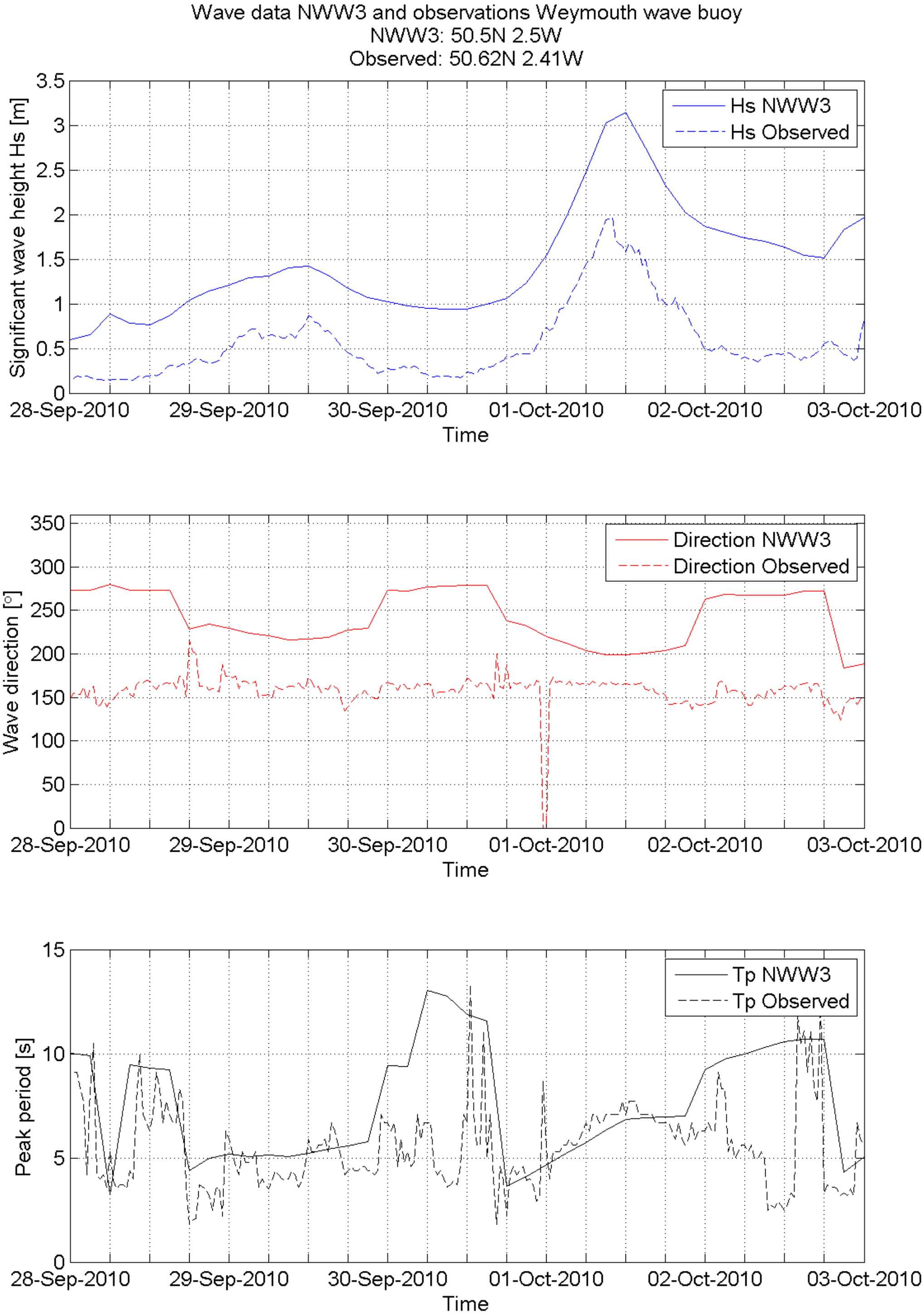

Figure D.3: NWW3 wave data and observed wave data

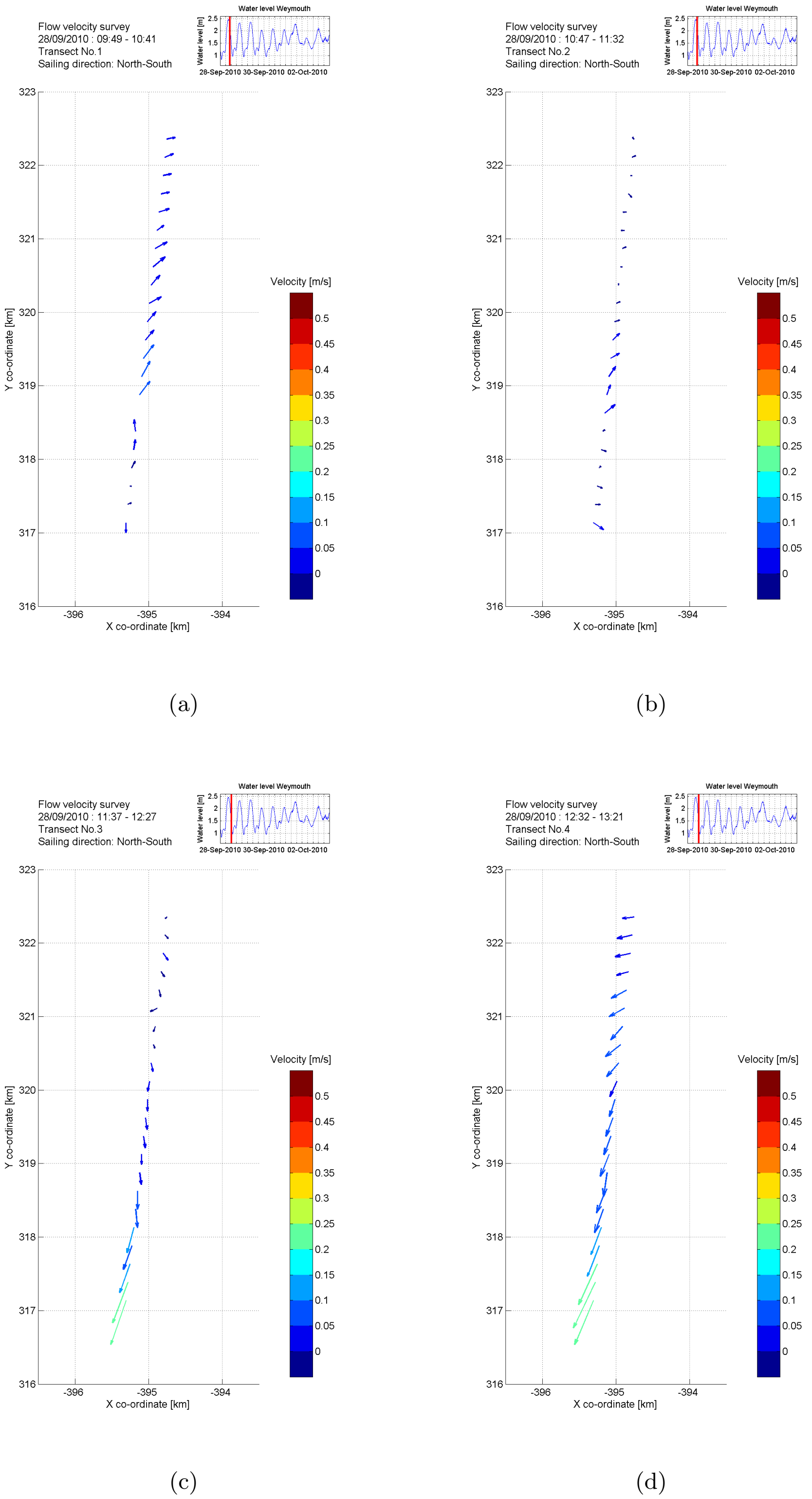

Figure D.4: Measured flow velocity along transect A at September 28^{th}, part (1)

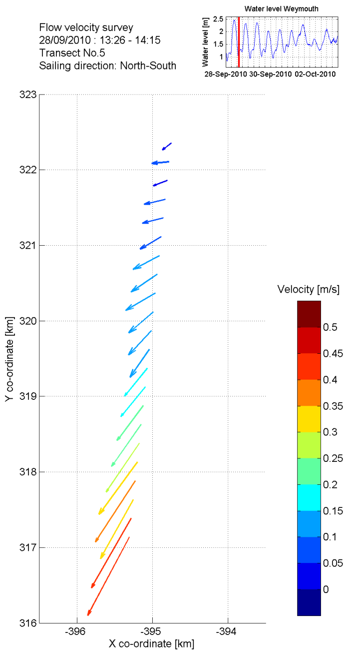

(a)

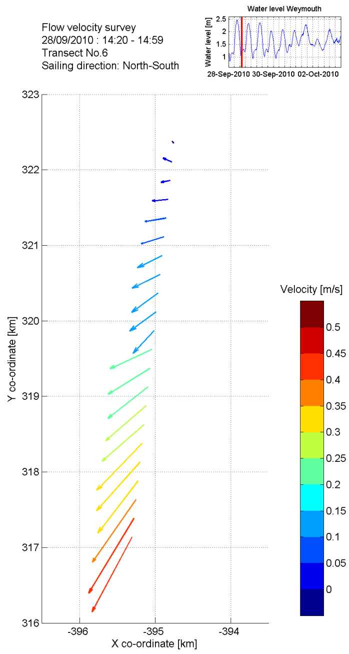

(b)

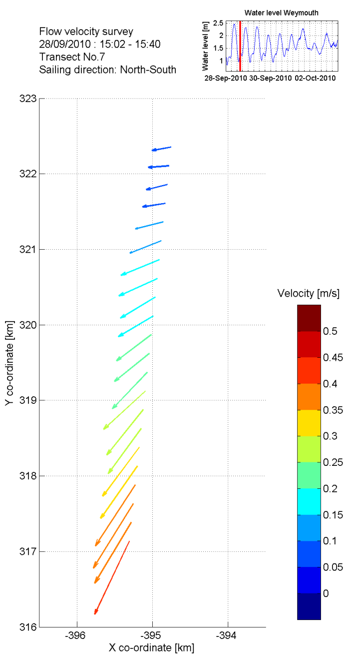

(c)

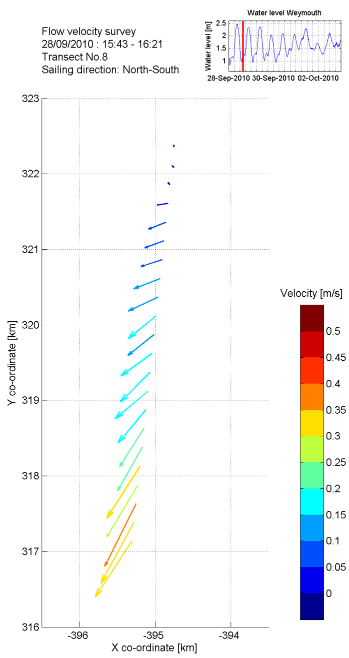

(d)

Figure D.5: Measured flow velocity along transect A at September 28^{th}, part (2)

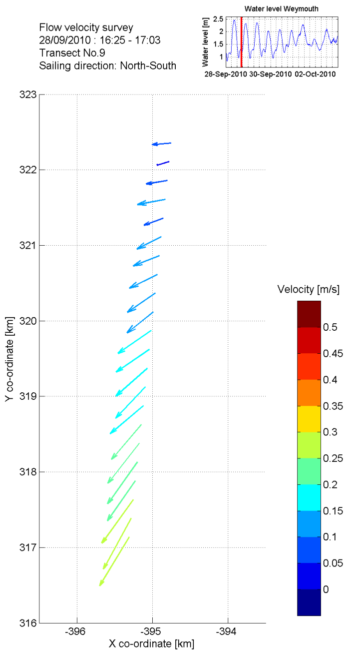

(a)

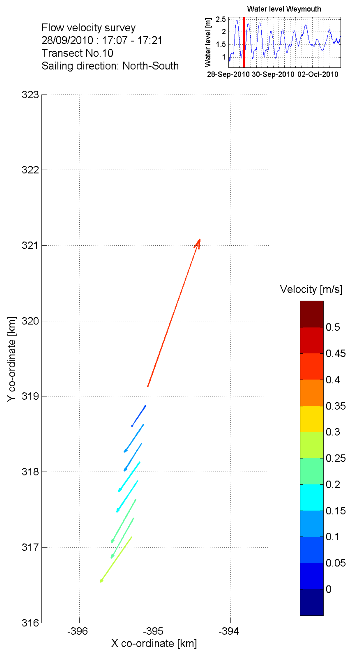

(b)

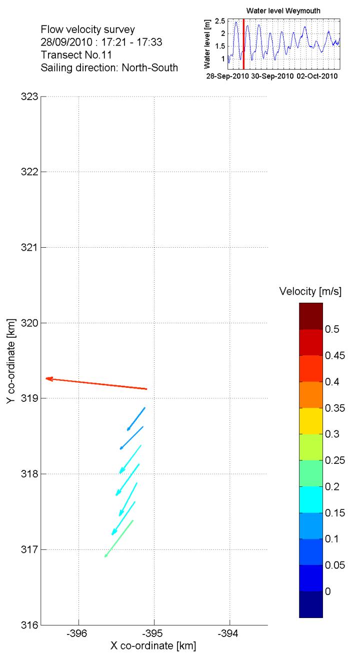

(c)

Figure D.6: Measured flow velocity along transect A at September 28^{th}, part (3)

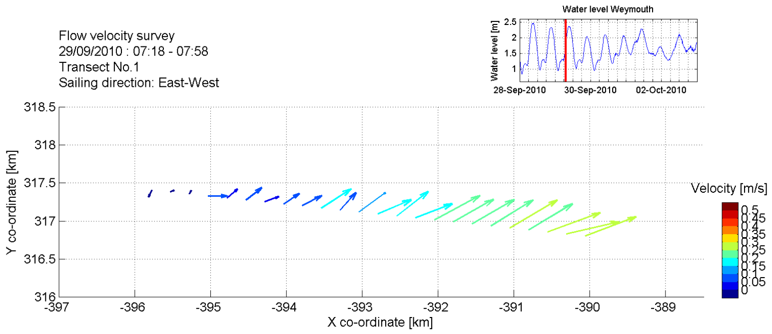

(a)

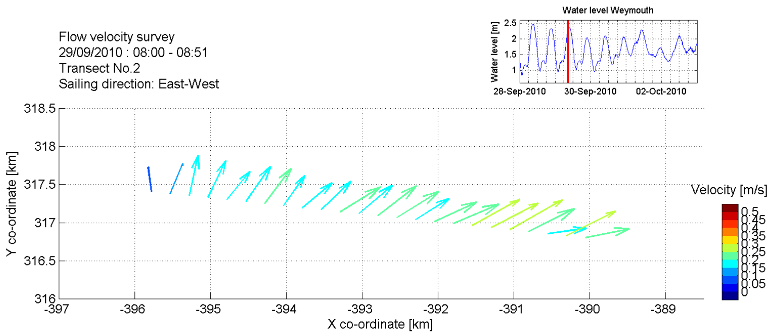

(b)

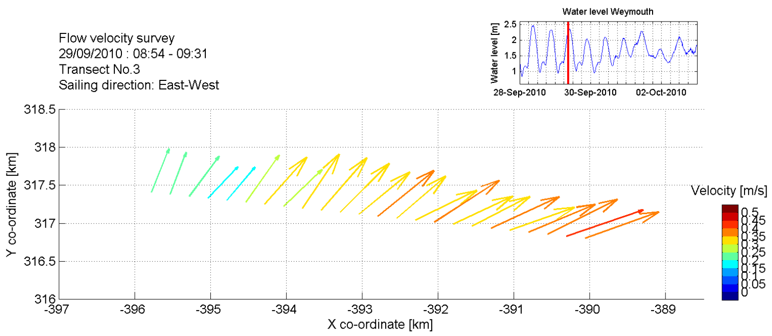

(c)

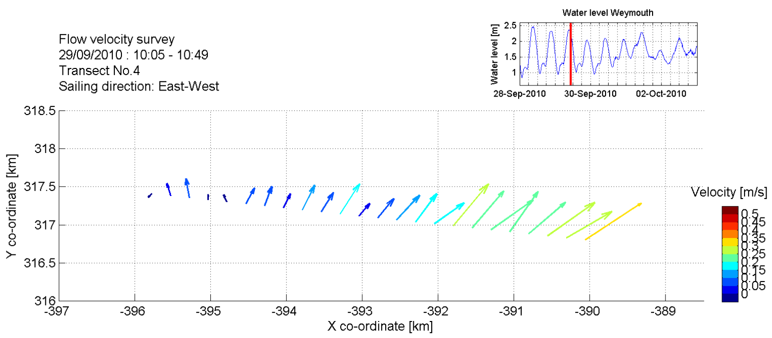

(d)

Figure D.7: Measured flow velocity along transect B at September 29^{th}, part (1)

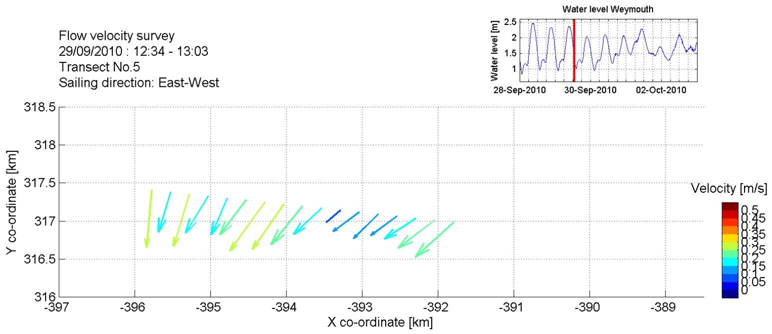

(a)

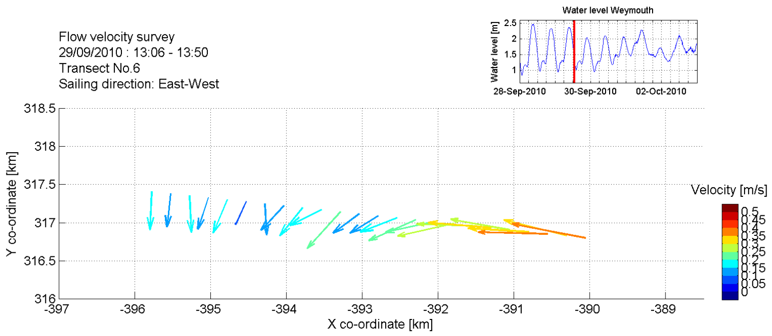

(b)

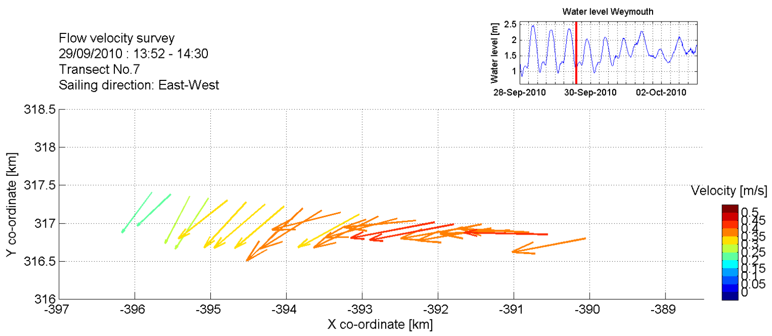

(c)

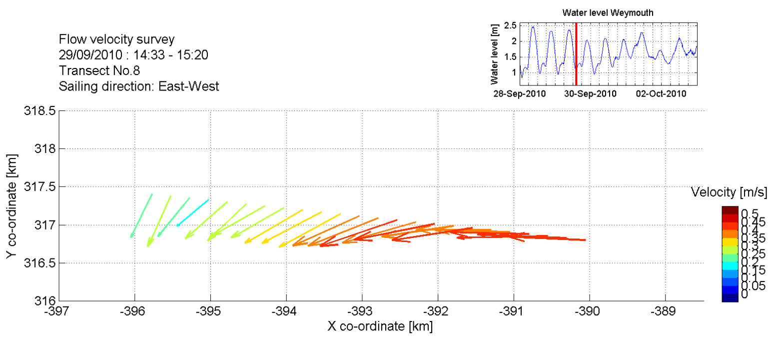

(d)

Figure D.8: Measured flow velocity along transect B at September 29^{th}, part (2)

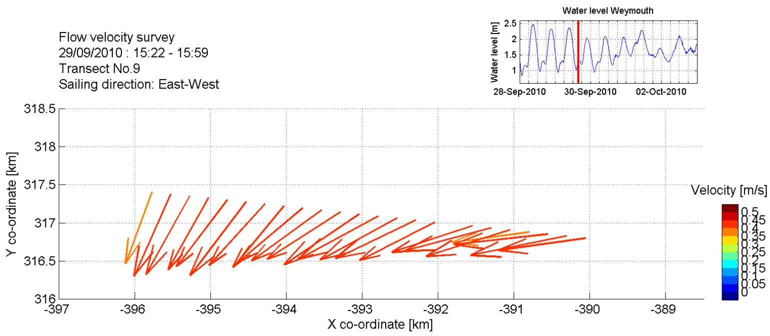

(a)

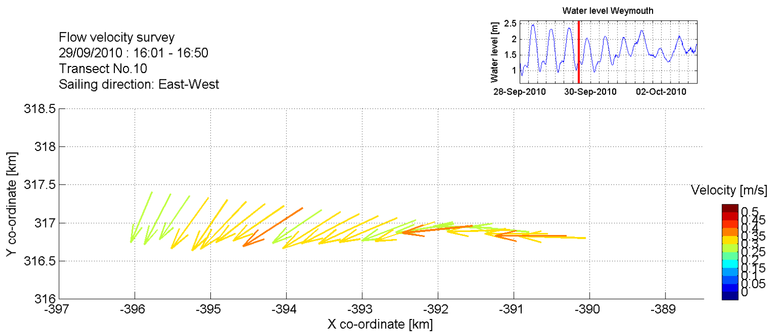

(b)

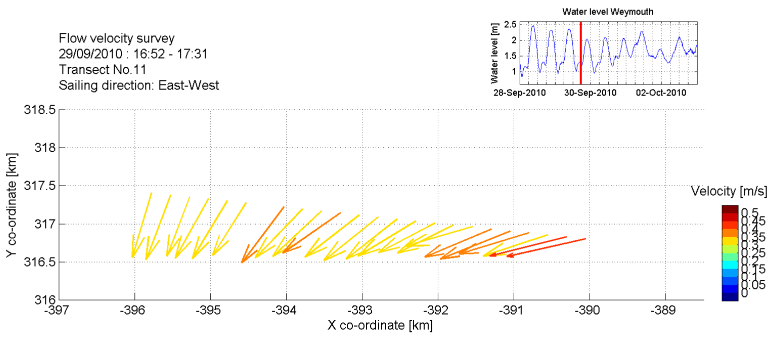

(c)

Figure D.9: Measured flow velocity along transect B at September 29^{th}, part (3)

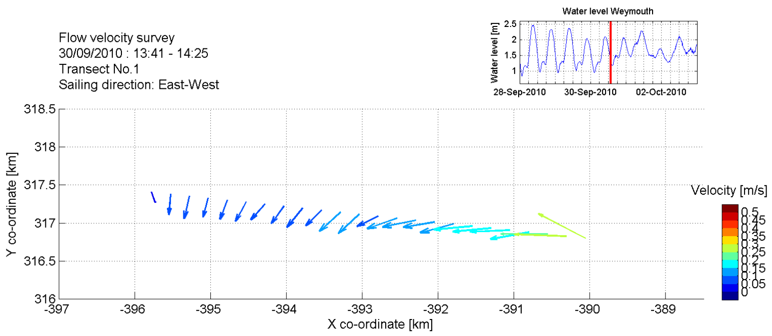

(a)

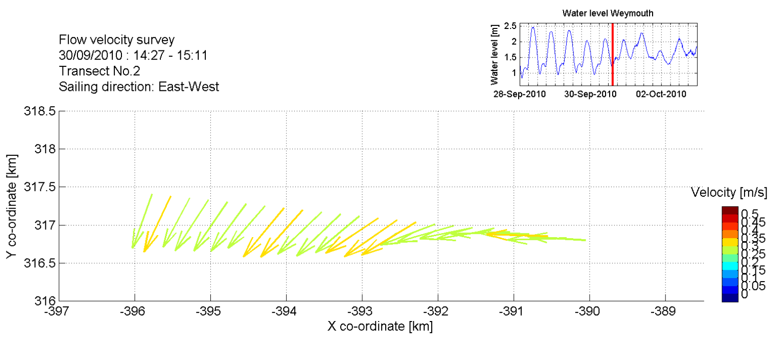

(b)

Figure D.10: Measured flow velocity along transect B at September 30^{th}

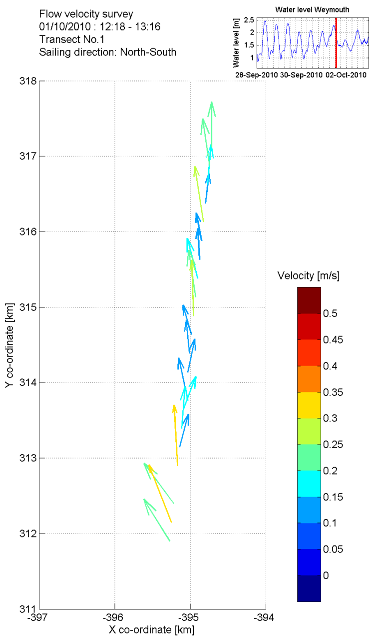

(a)

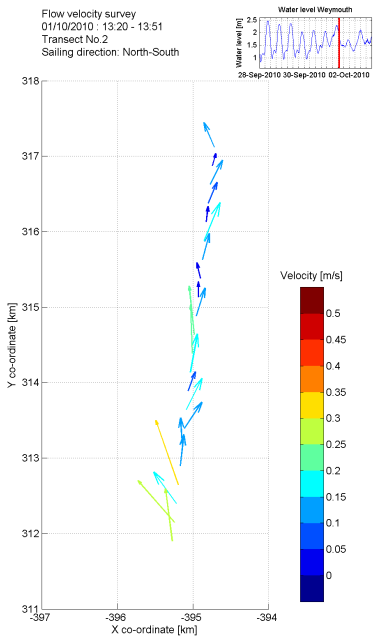

(b)

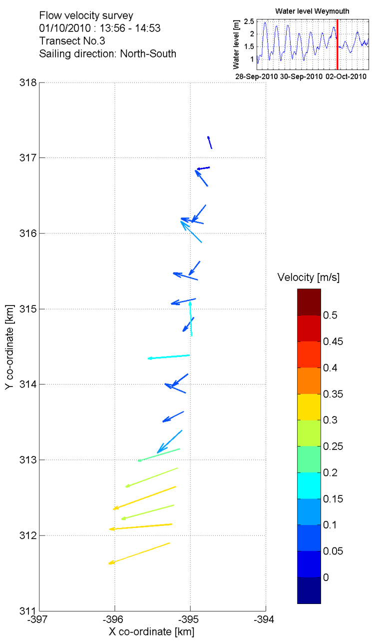

(c)

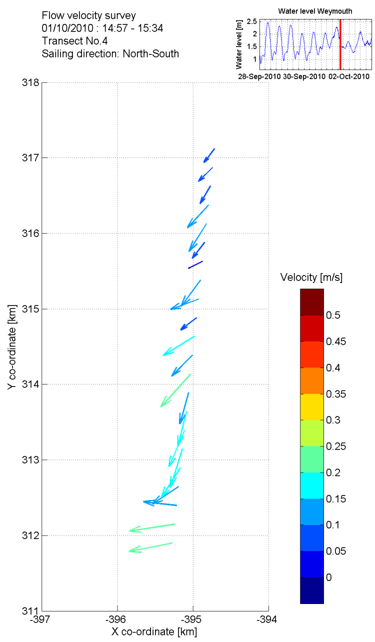

(d)

Figure D.11: Measured flow velocity along transect C at October 1^{st}, part (1)

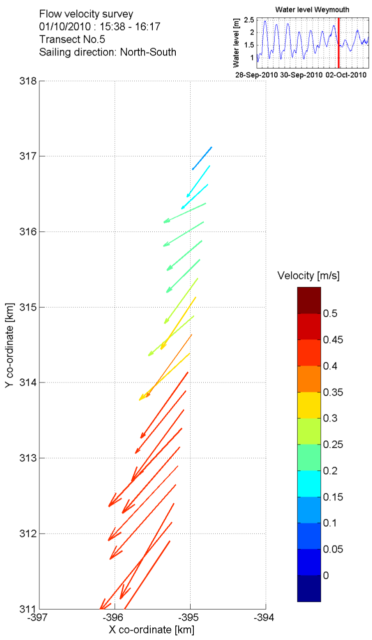

(a)

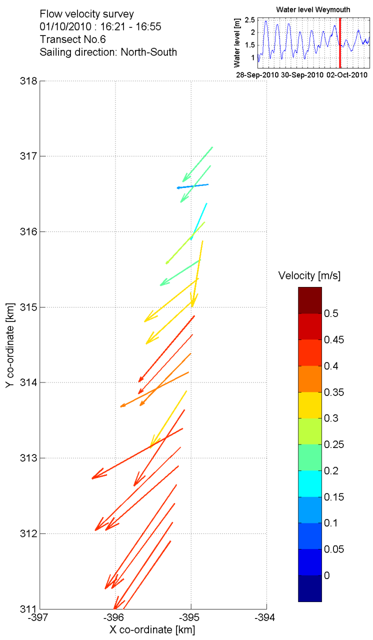

(b)

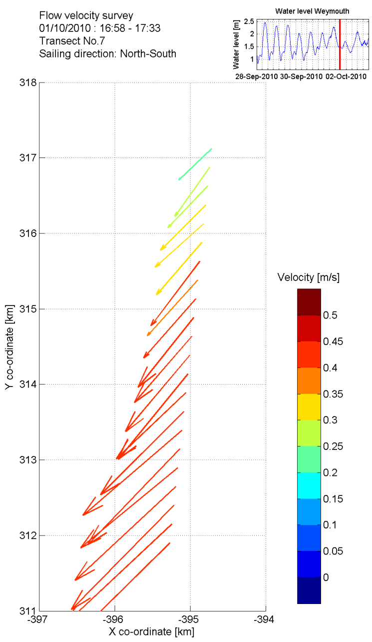

(c)

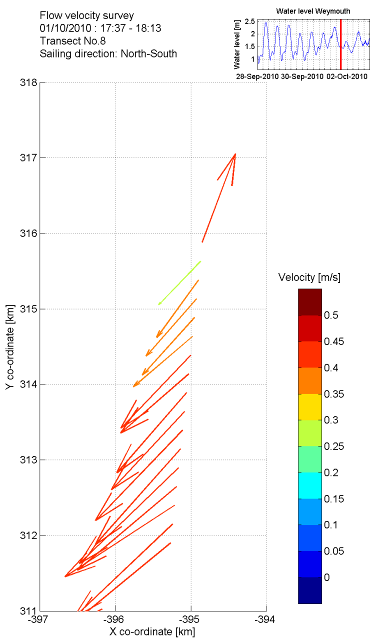

(d)

Figure D.12: Measured flow velocity along transect C at October 1st, part (2)

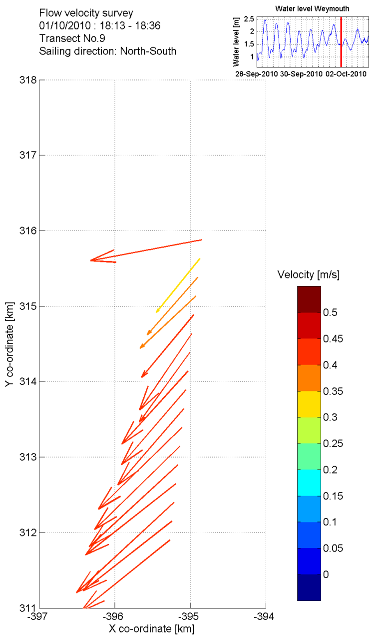

(a)

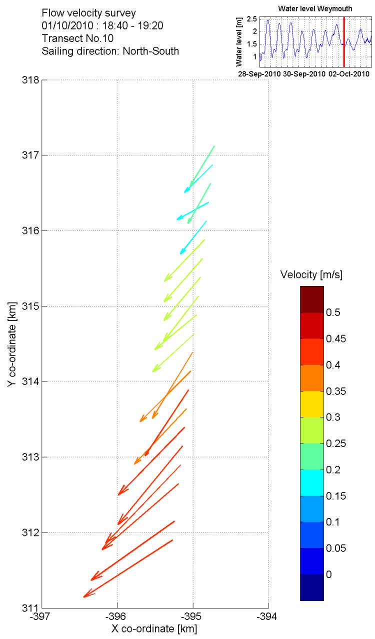

(b)

Figure D.13: Measured flow velocity along transect C at October 1st, part (3)

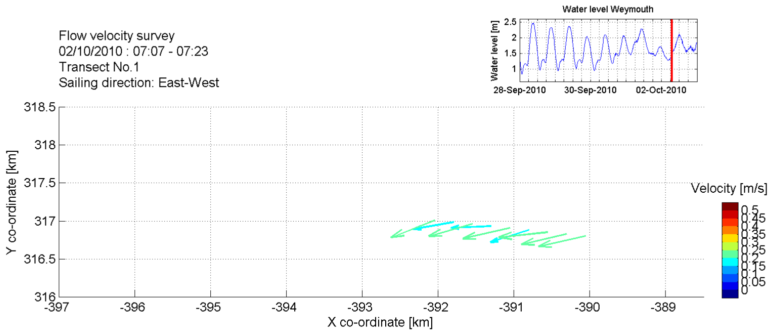

(a)

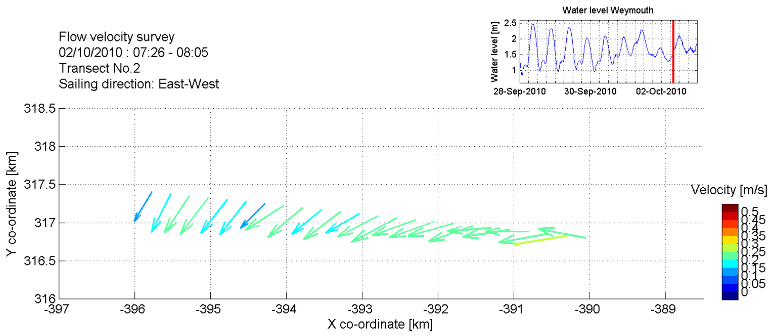

(b)

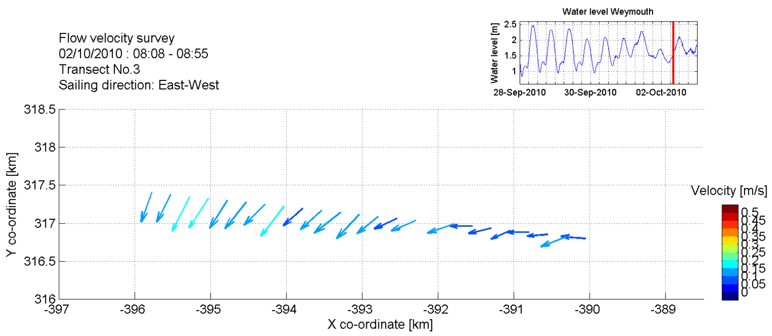

(c)

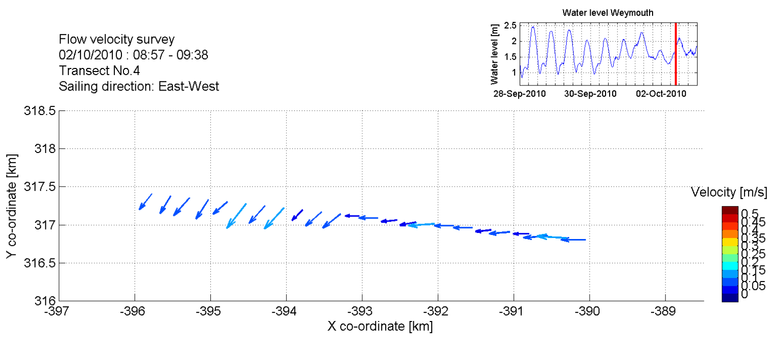

(d)

Figure D.14: Measured flow velocity along transect B at October 2^{nd}, part (1)

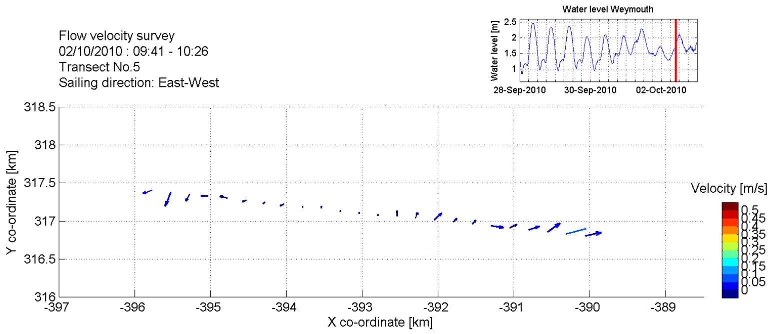

(a)

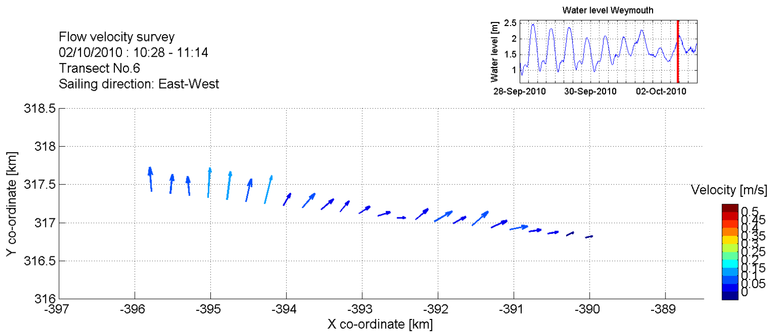

(b)

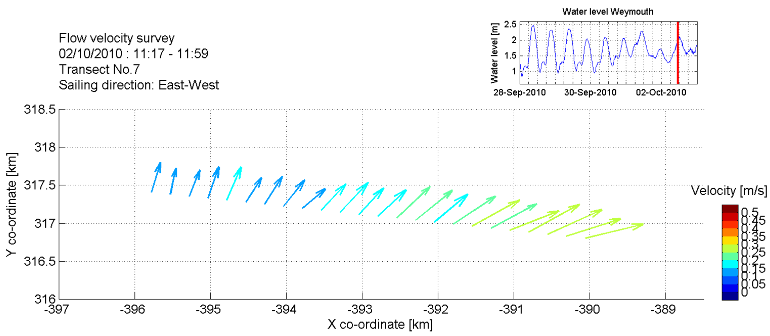

(c)

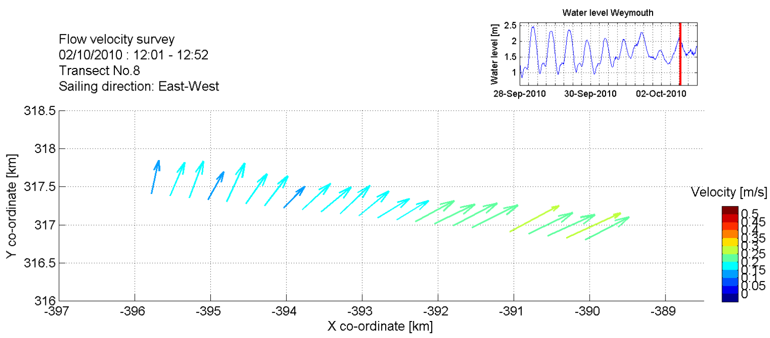

(d)

Figure D.15: Measured flow velocity along transect B at October 2^{nd}, part (2)

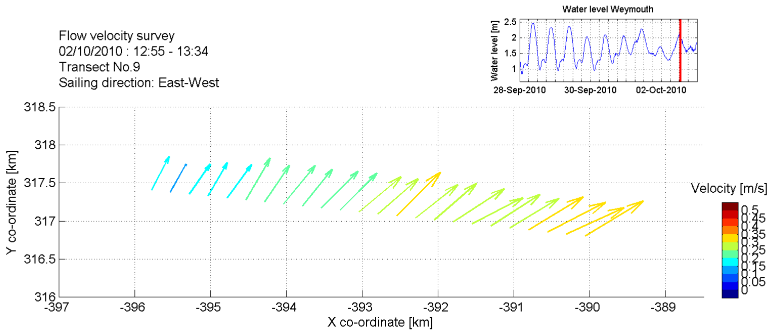

(a)

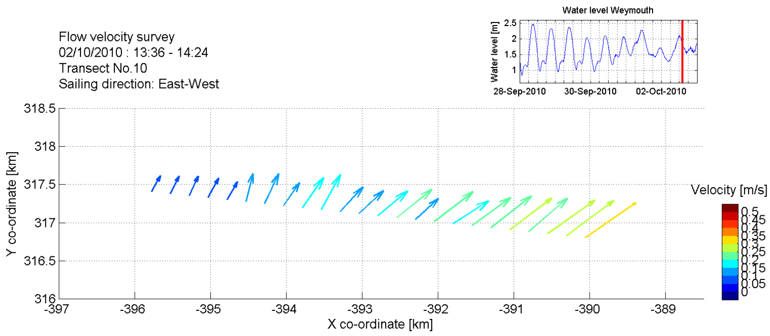

(b)

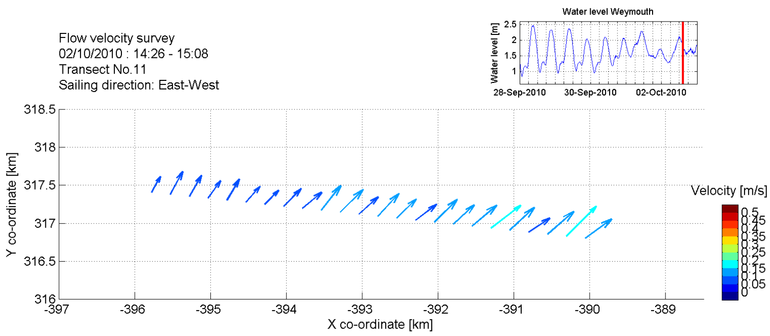

(c)

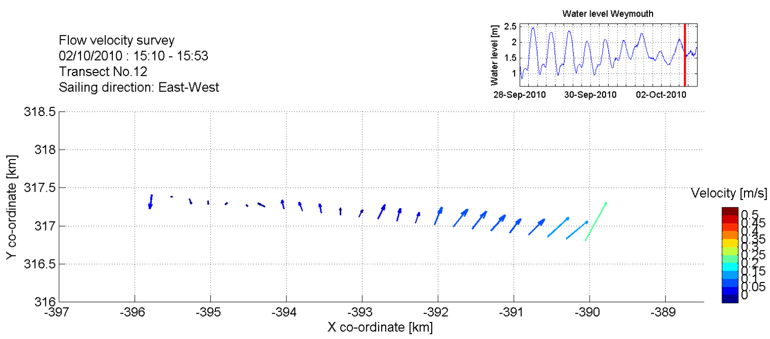

(d)

Figure D.16: Measured flow velocity along transect B at October 2^{nd}, part (3)

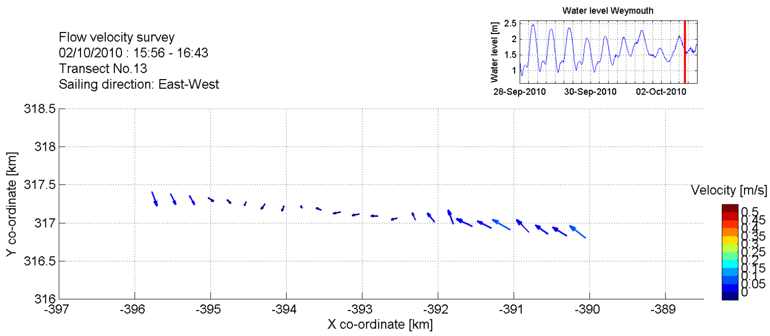

(a)

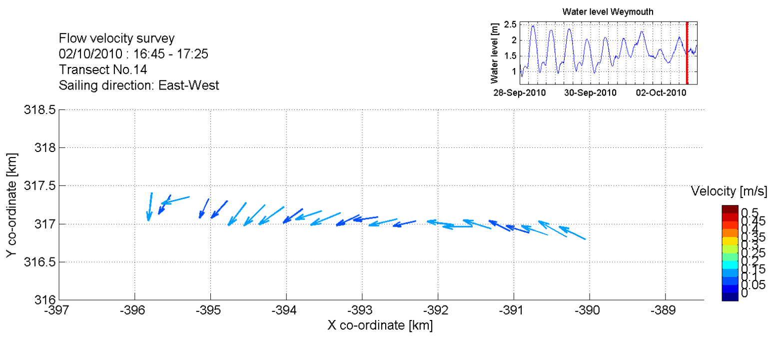

(b)

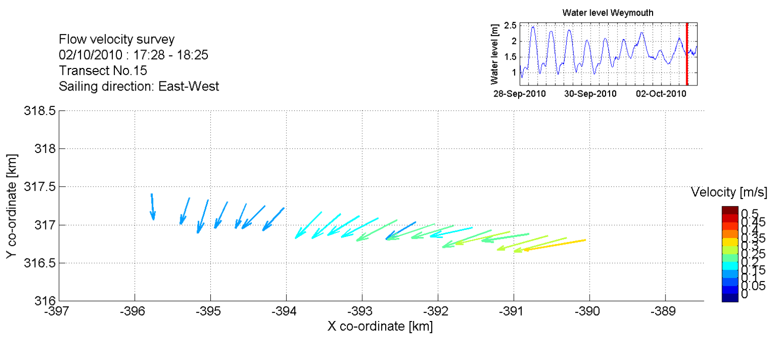

(c)

Figure D.17: Measured flow velocity along transect B at October 2^{nd}, part (4)

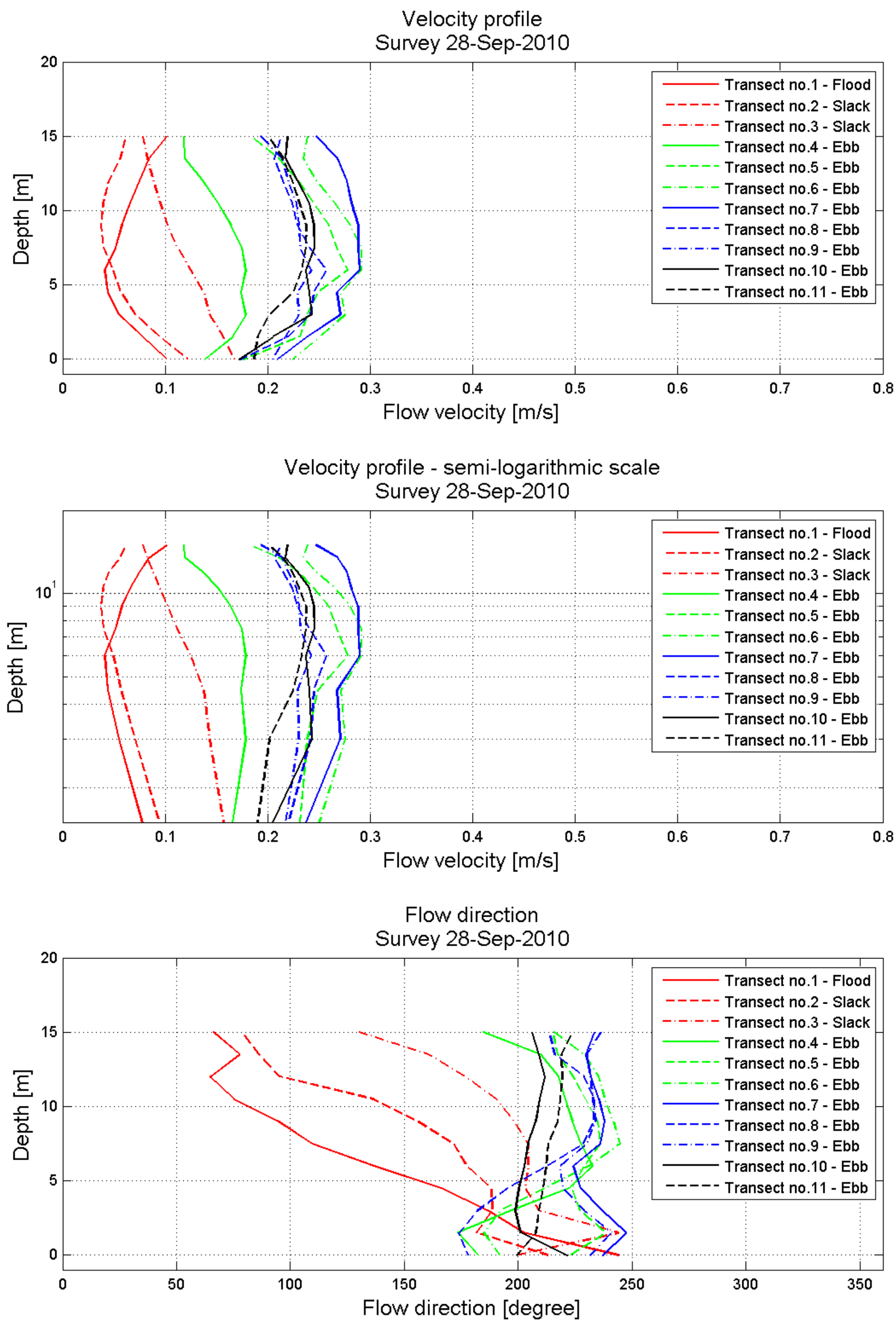

Figure D.18: Measured vertical velocity distribution for the transects A sailed on September 28^{th}

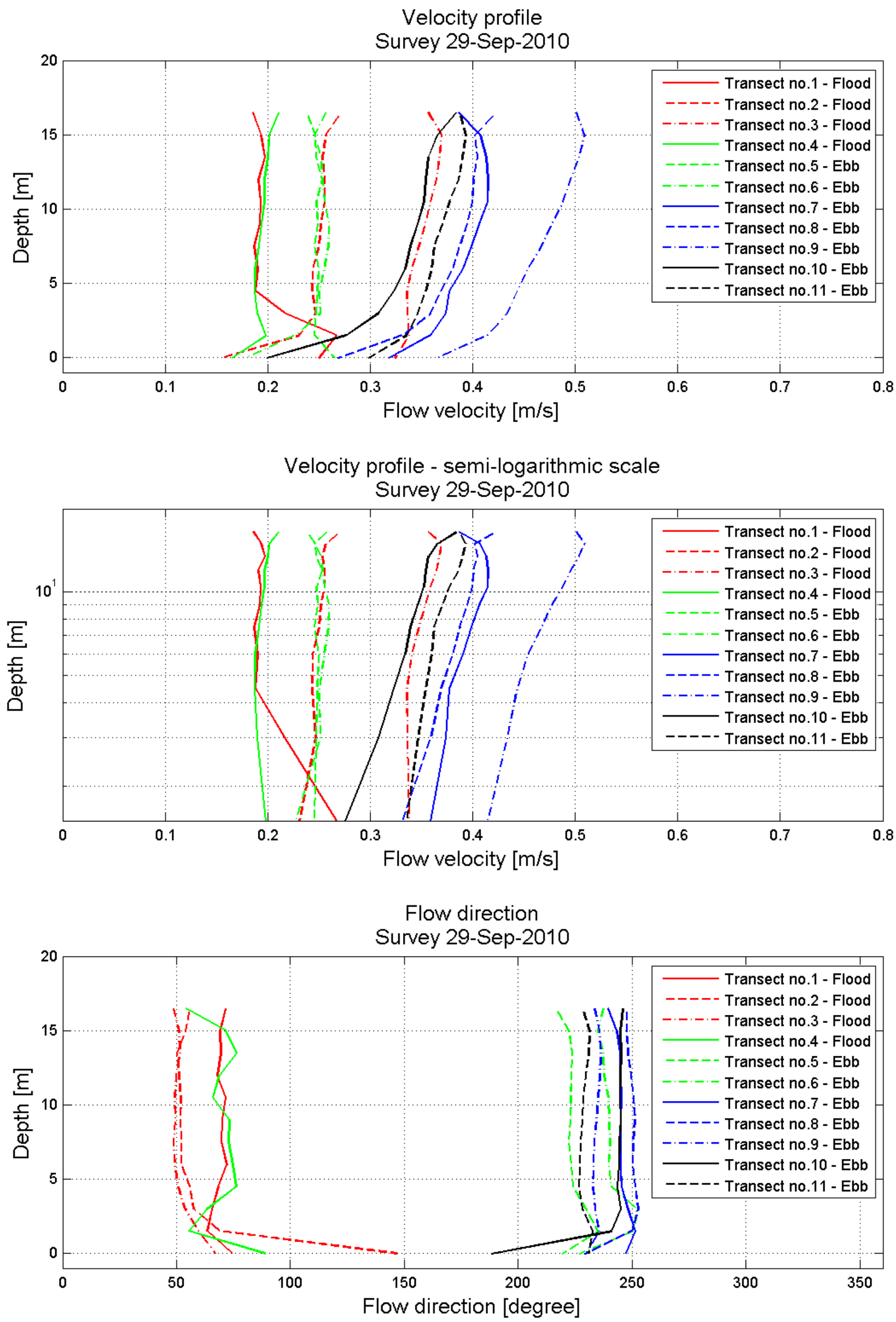

Figure D.19: Measured vertical velocity distribution for the transects B sailed on September 29^{th}

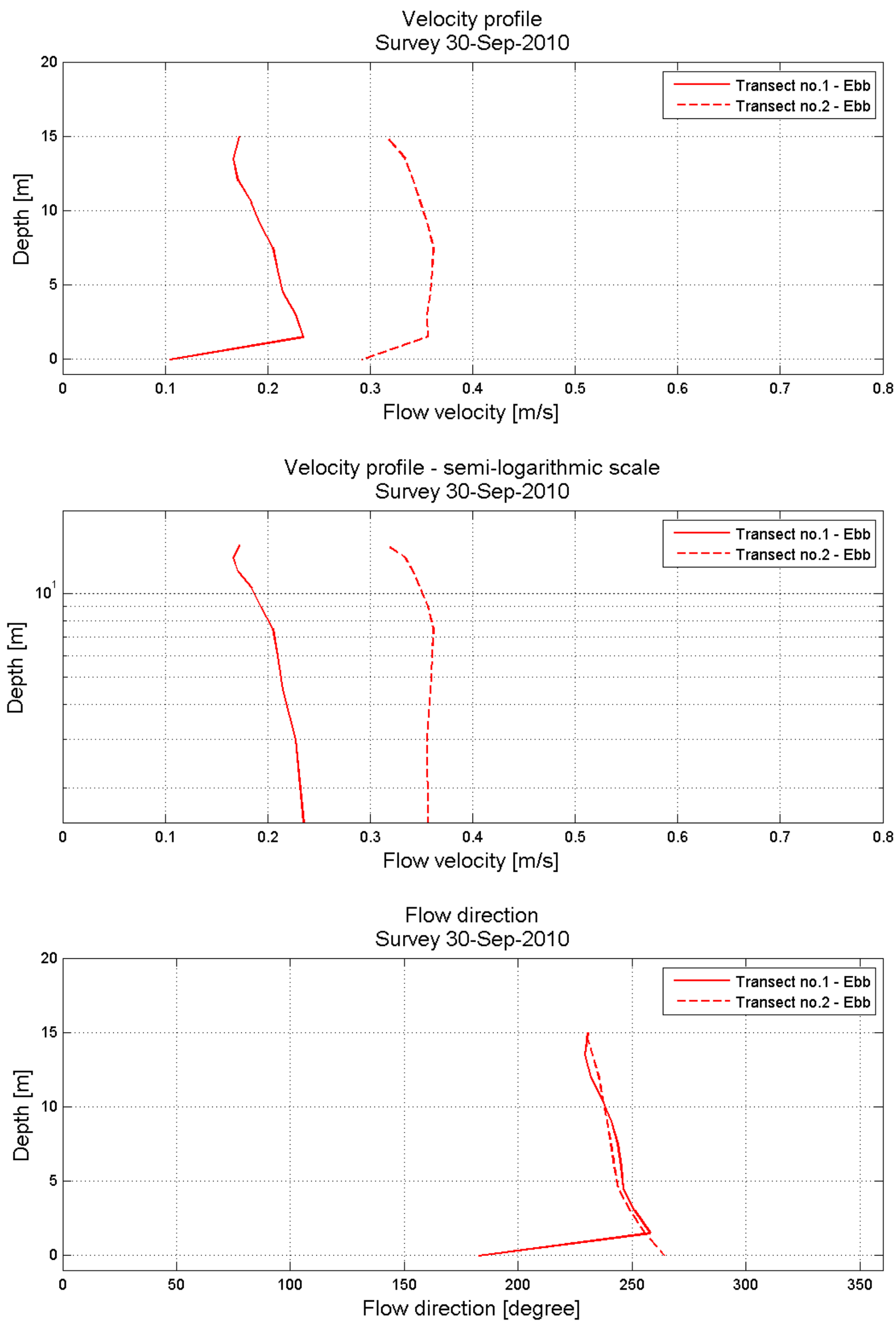

Figure D.20: Measured vertical velocity distribution for the transects B sailed on September 30^{th}

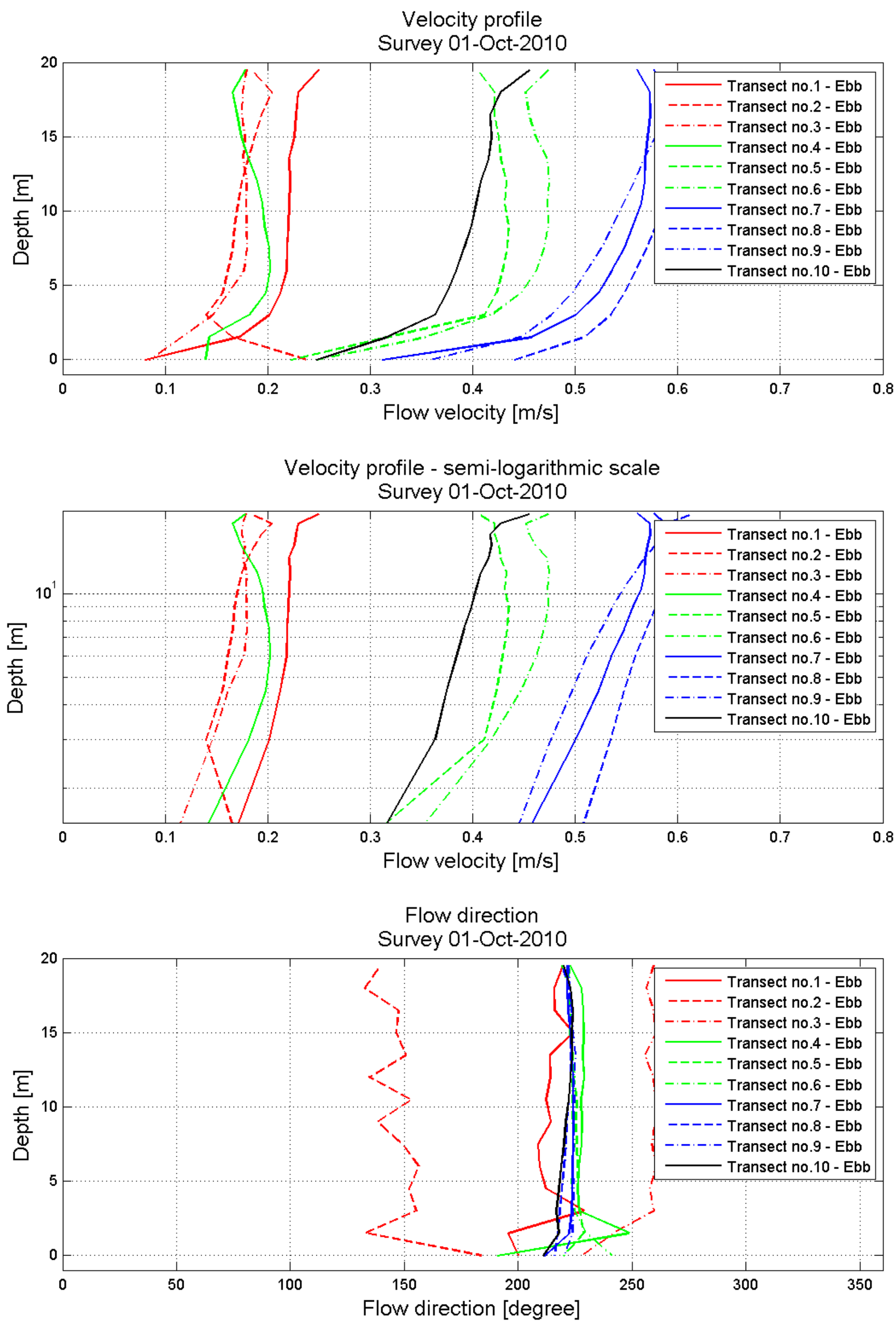

Figure D.21: Measured vertical velocity distribution for the transects C sailed on October 1^{st}

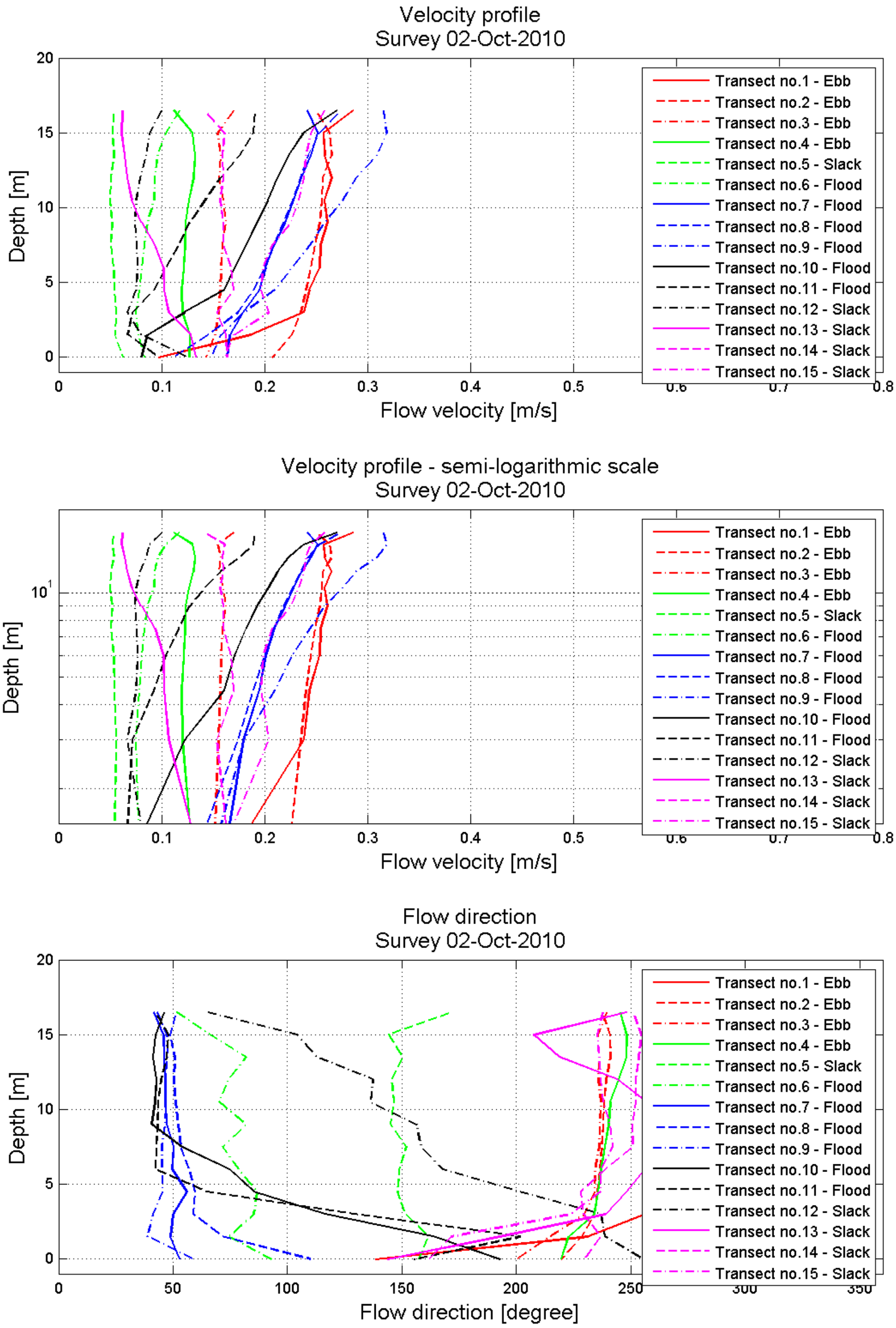

Figure D.22: Measured vertical velocity distribution for the transects B sailed on October 2^{nd}

Appendix E

Spatial comparison of measured and modelled flow

The modelled flow velocities and directions along the transects have been compared to the measured flow velocities and directions along the transects. Examples of the results of the comparison of the measured and modelled flow velocities and directions have been discussed in section 4.4. The results for all during the survey sailed transects are given in this Appendix. An overview of the during the survey sailed transects is given in table D.3 until table D.7 of Appendix D.

Separate graphs of both the flow velocity and flow direction are given in the two top figures, in order indicate the absolute difference in velocity and direction. In the bottom figure, the flow is visualised by means of vectors, by which the direction of the vector indicates the flow direction, and both the colour and the length of the vector indicate the flow velocity. The figures show that the model results correspond fairly well to the measured flow velocities and directions as well.

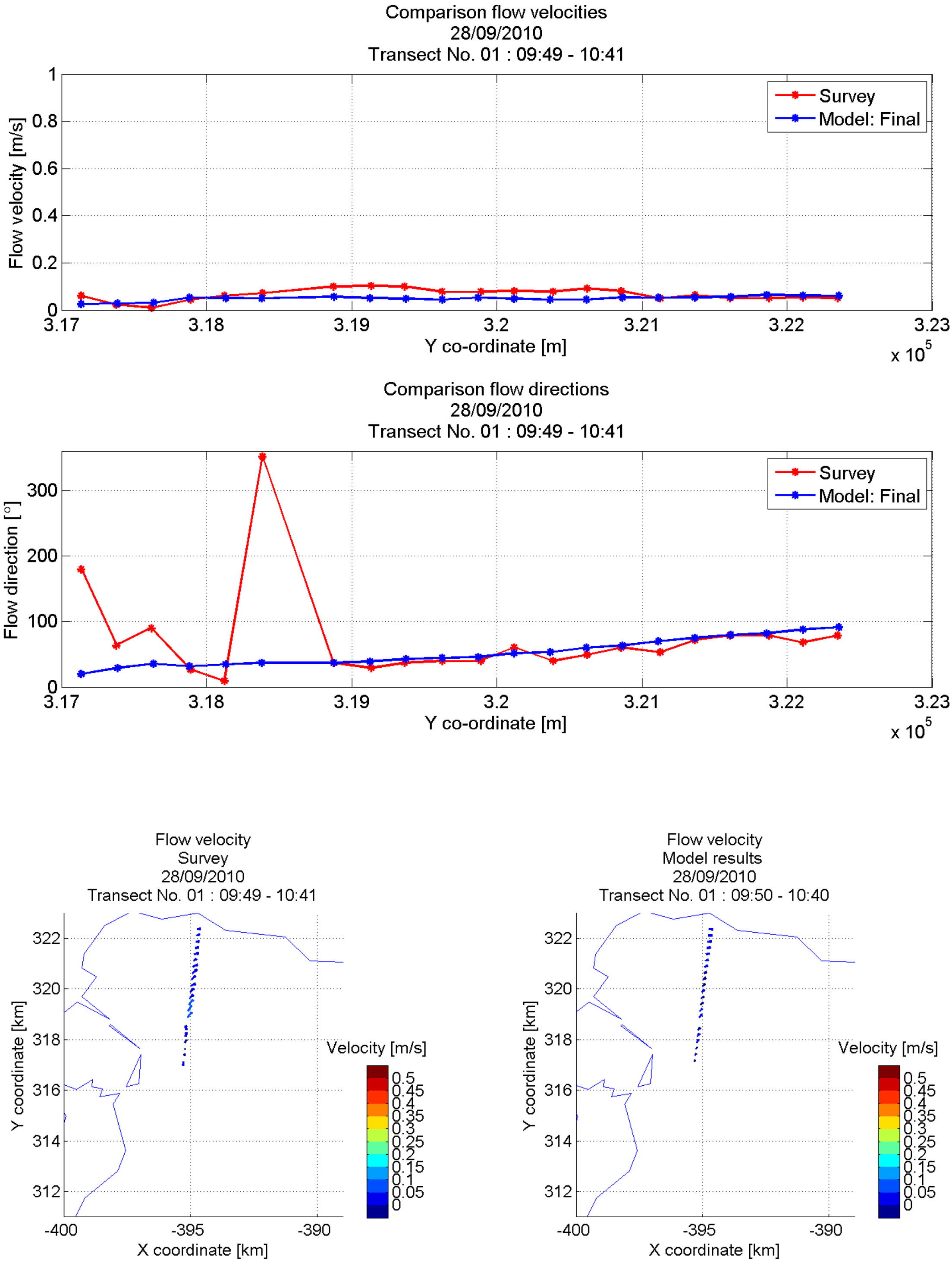

Figure E.1: Measured and modelled flow velocity and direction along transect A during flood tide

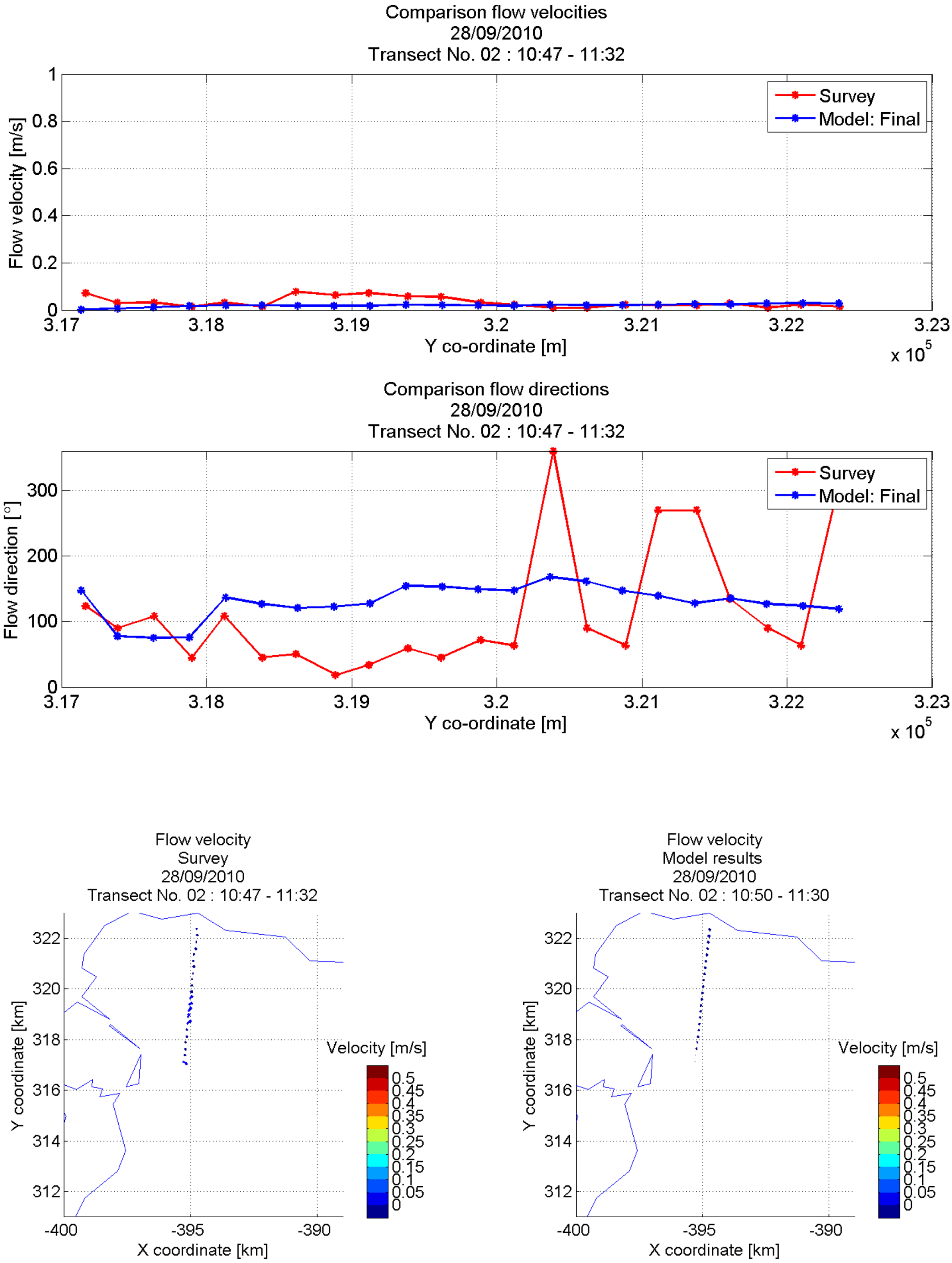

Figure E.2: Measured and modelled flow velocity and direction along transect A during slack tide

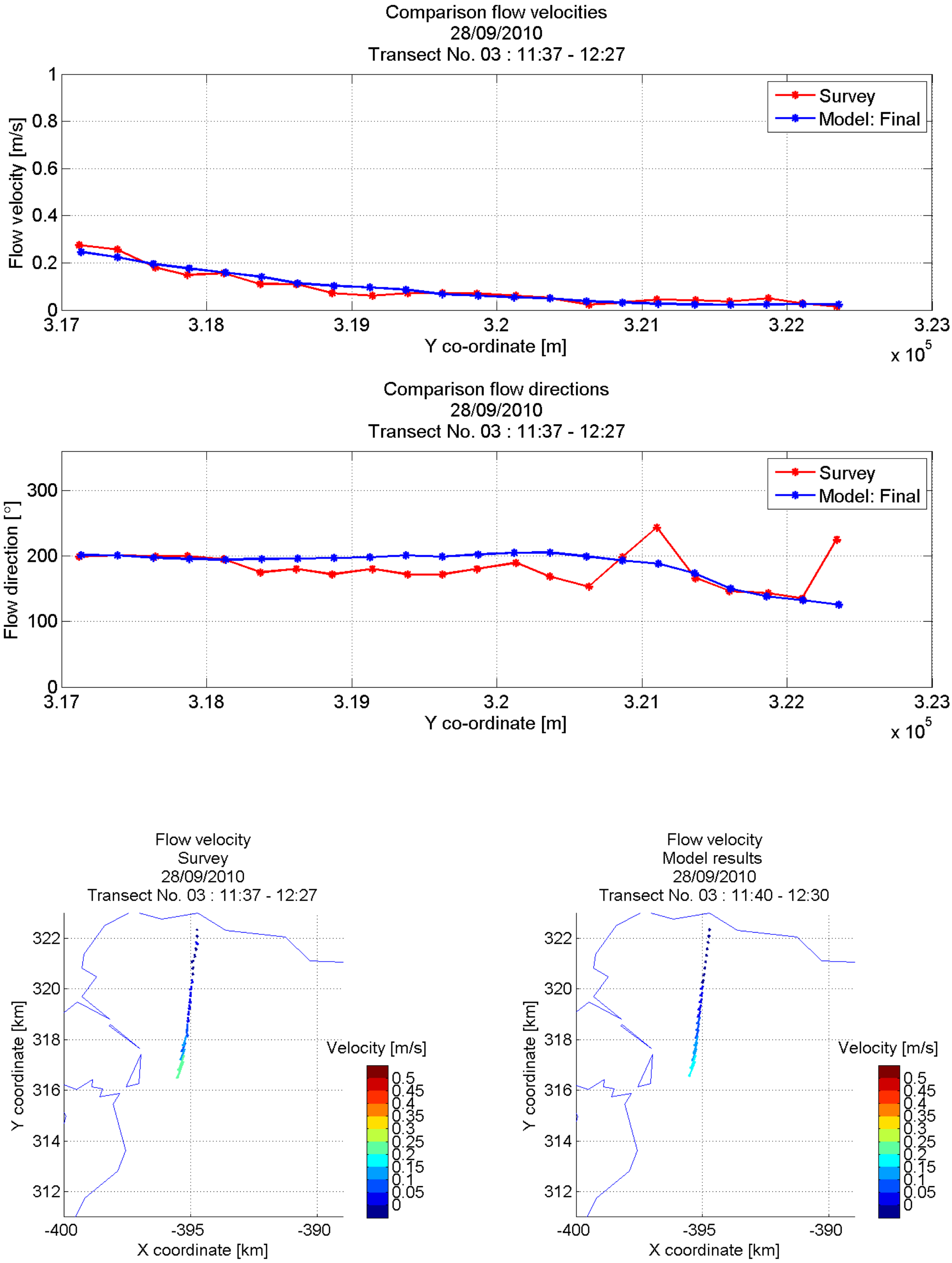

Figure E.3: Measured and modelled flow velocity and direction along transect A during slack tide

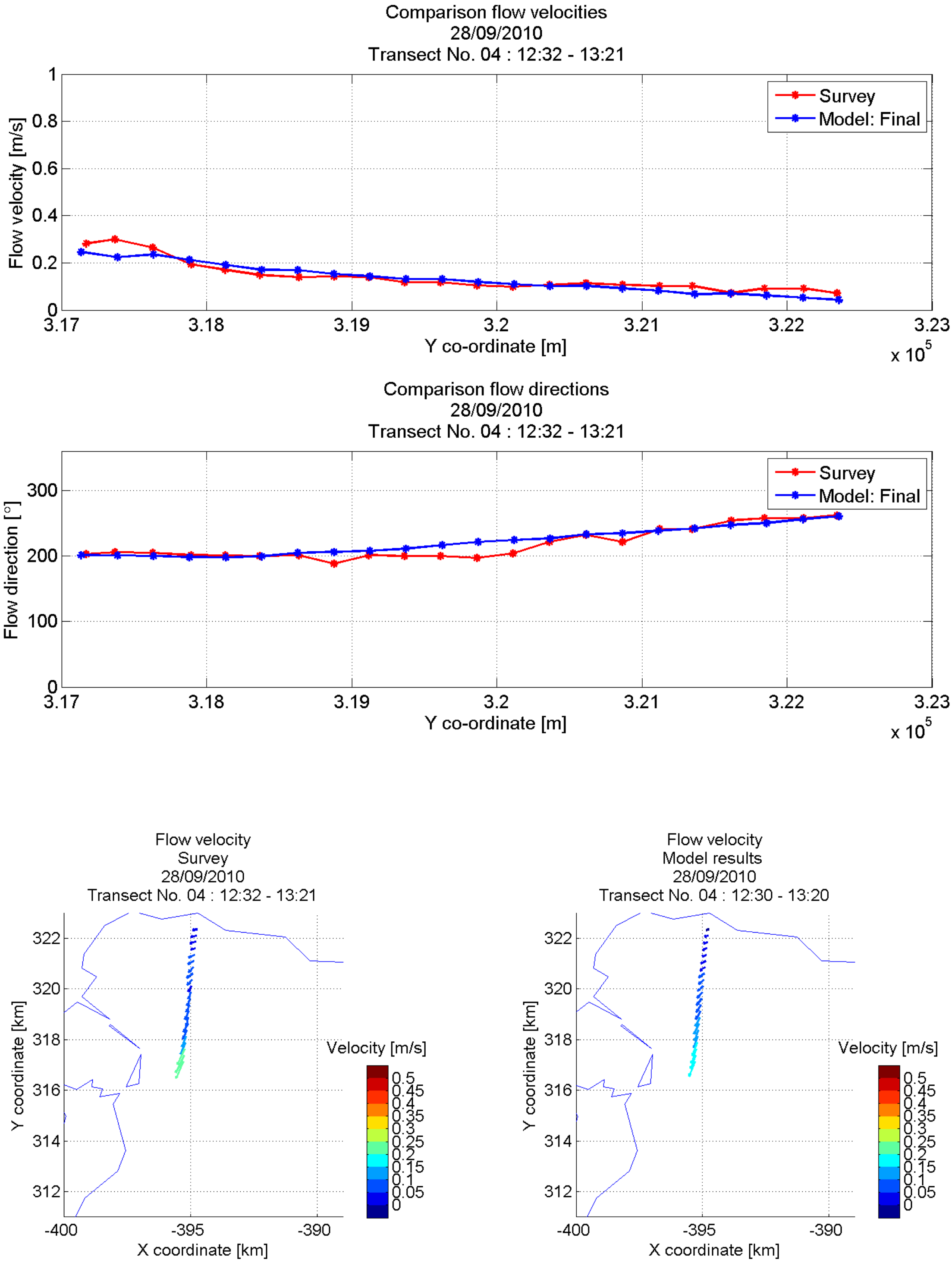

Figure E.4: Measured and modelled flow velocity and direction along transect A during ebb tide

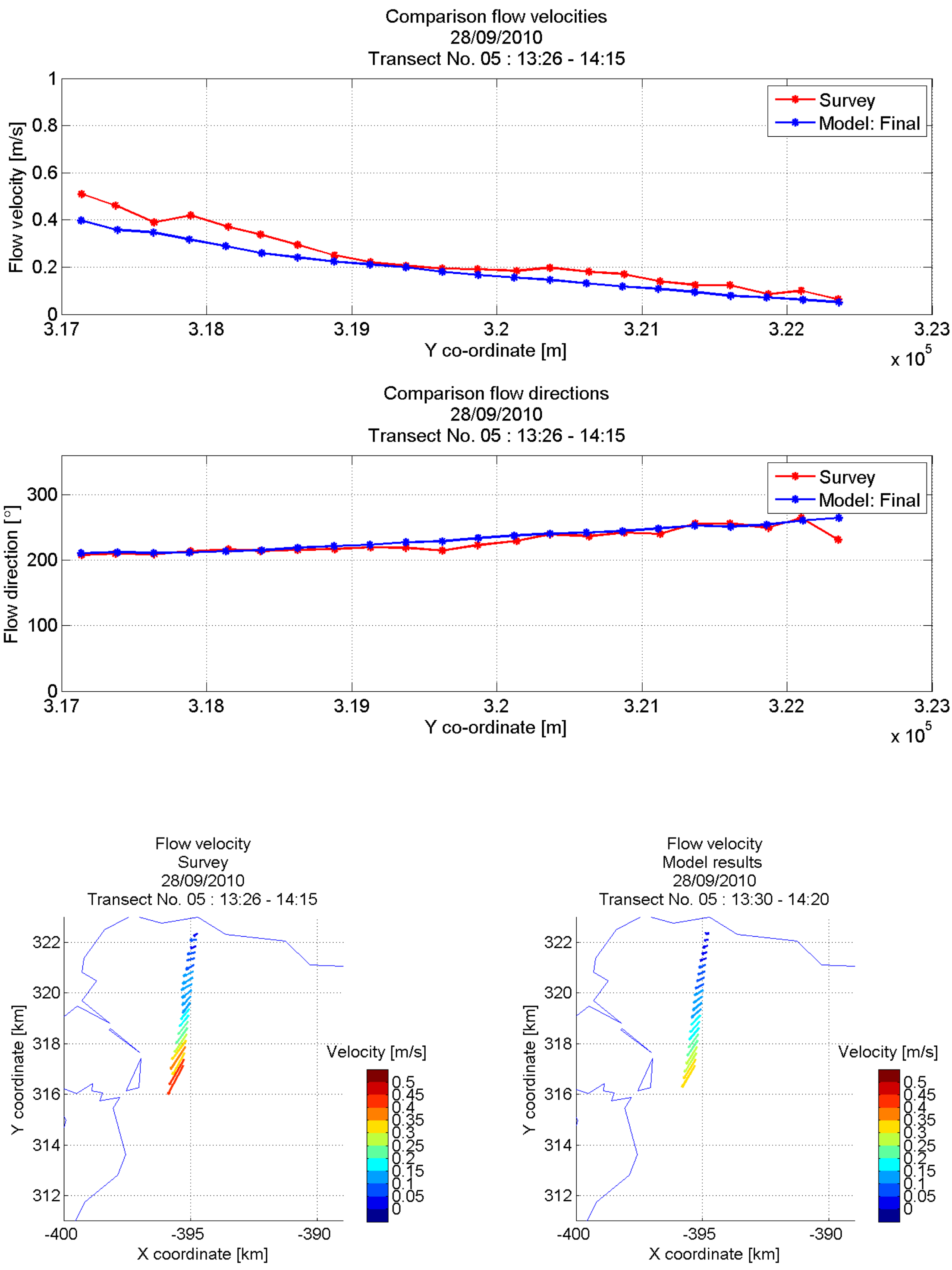

Figure E.5: Measured and modelled flow velocity and direction along transect A during ebb tide

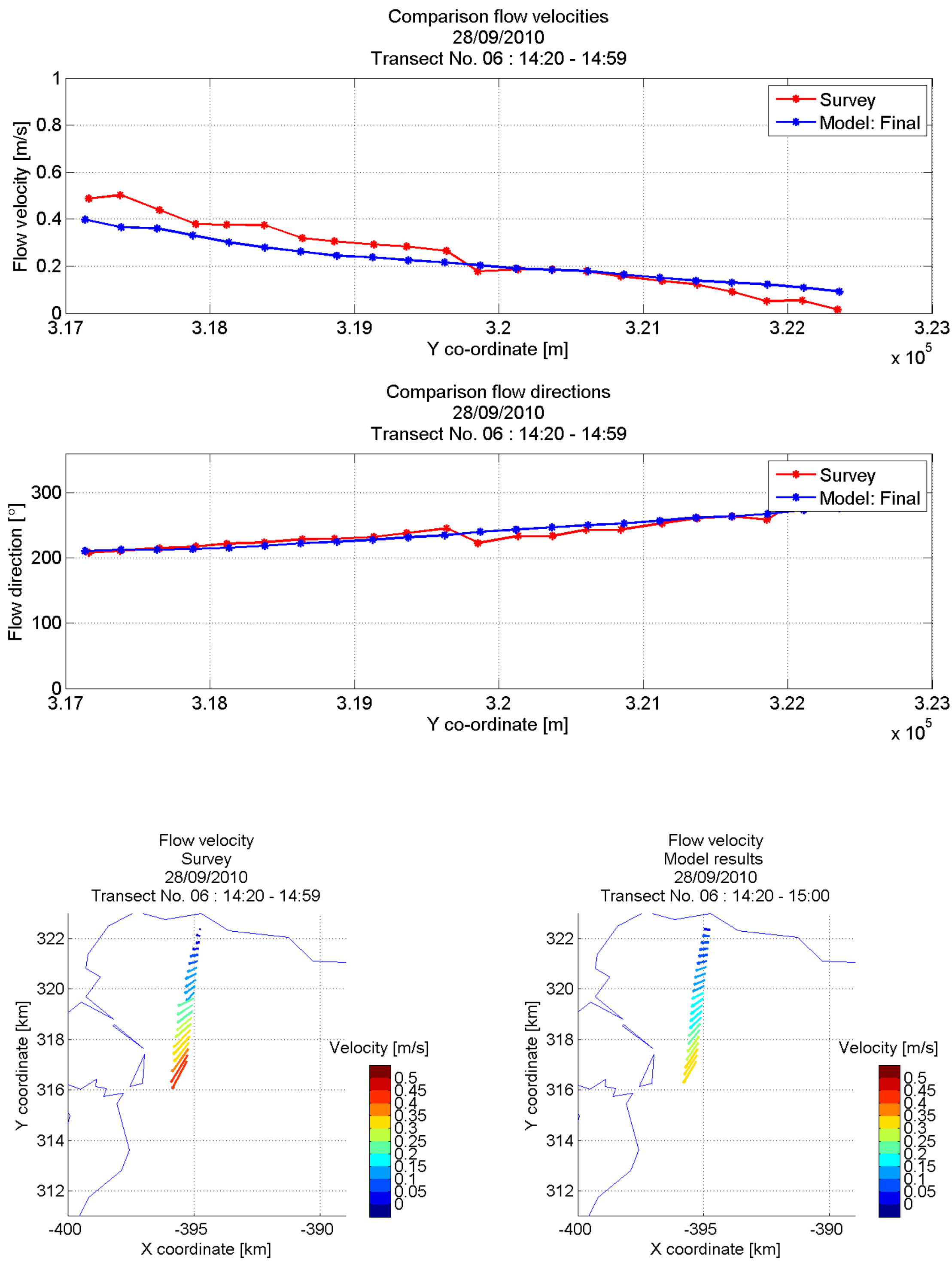

Figure E.6: Measured and modelled flow velocity and direction along transect A during ebb tide

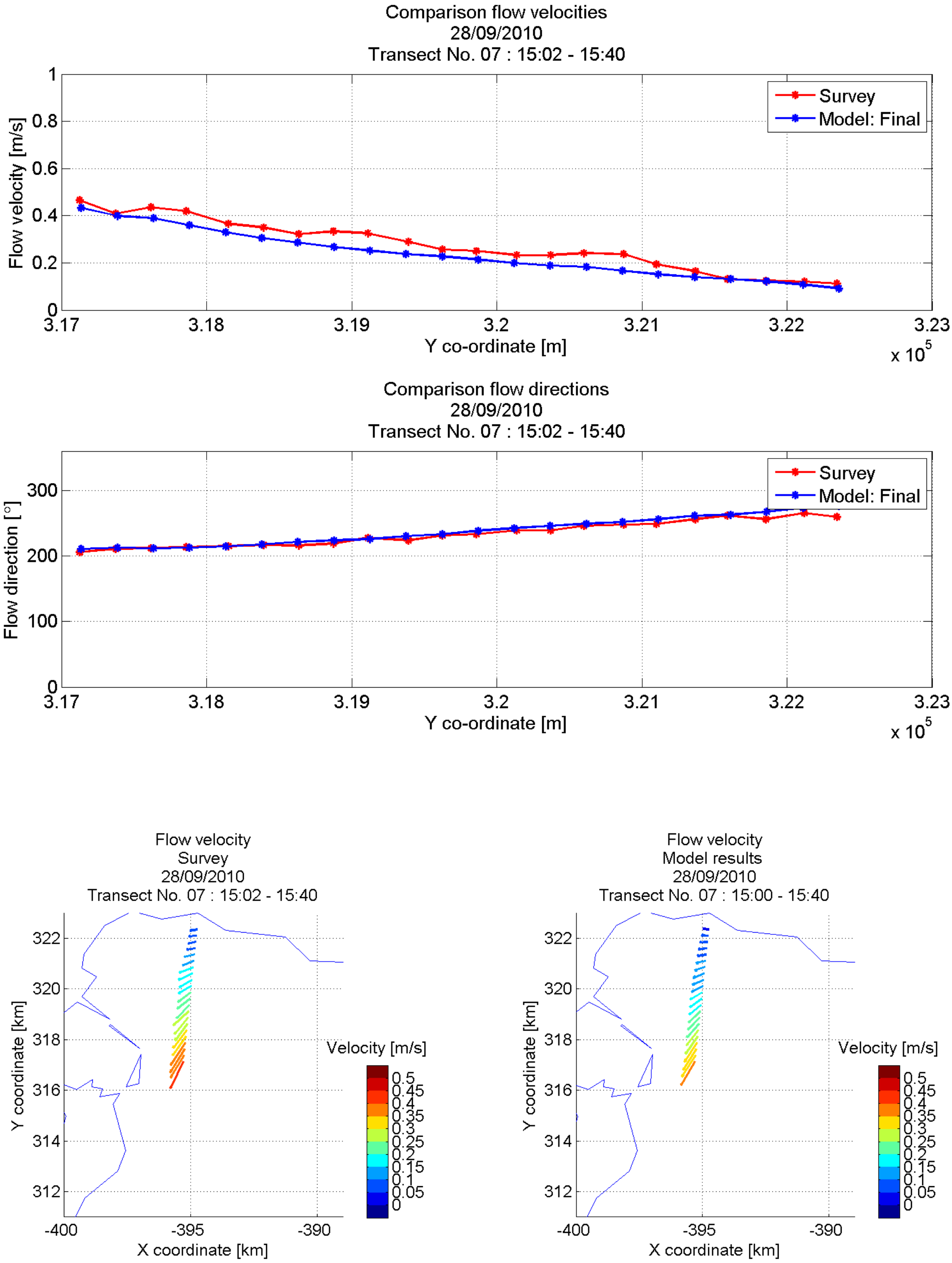

Figure E.7: Measured and modelled flow velocity and direction along transect A during ebb tide

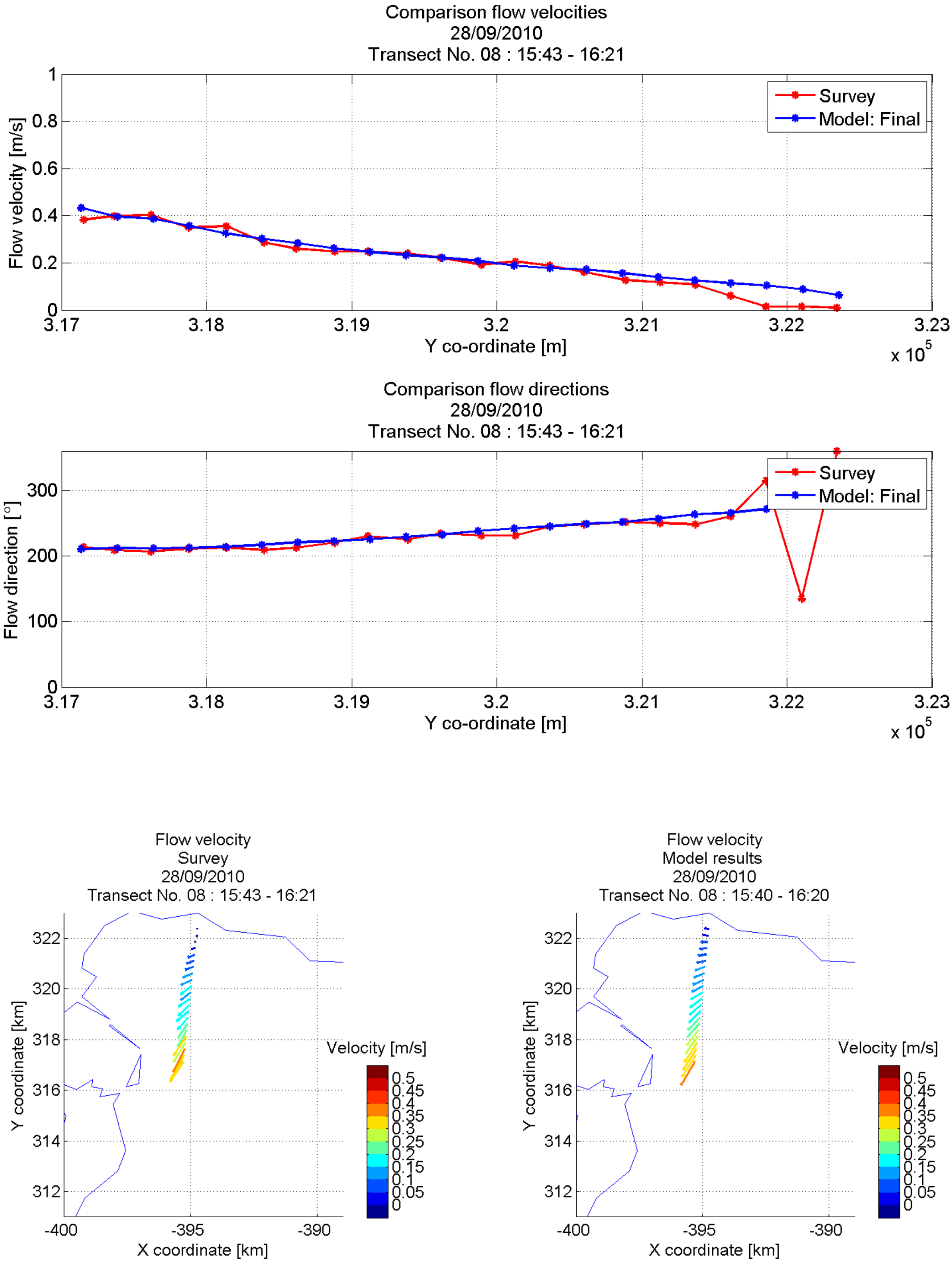

Figure E.8: Measured and modelled flow velocity and direction along transect A during ebb tide

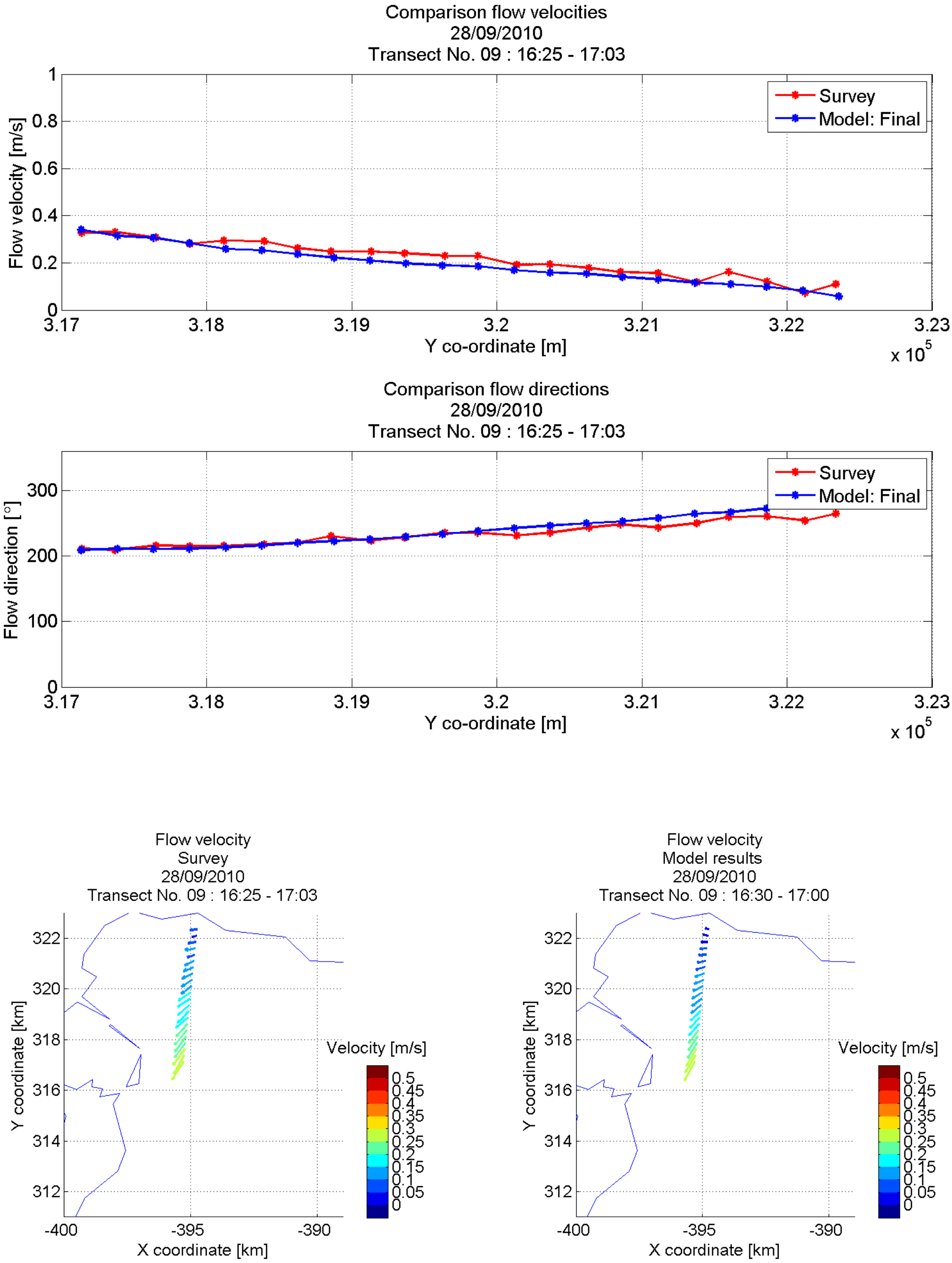

Figure E.9: Measured and modelled flow velocity and direction along transect A during ebb tide

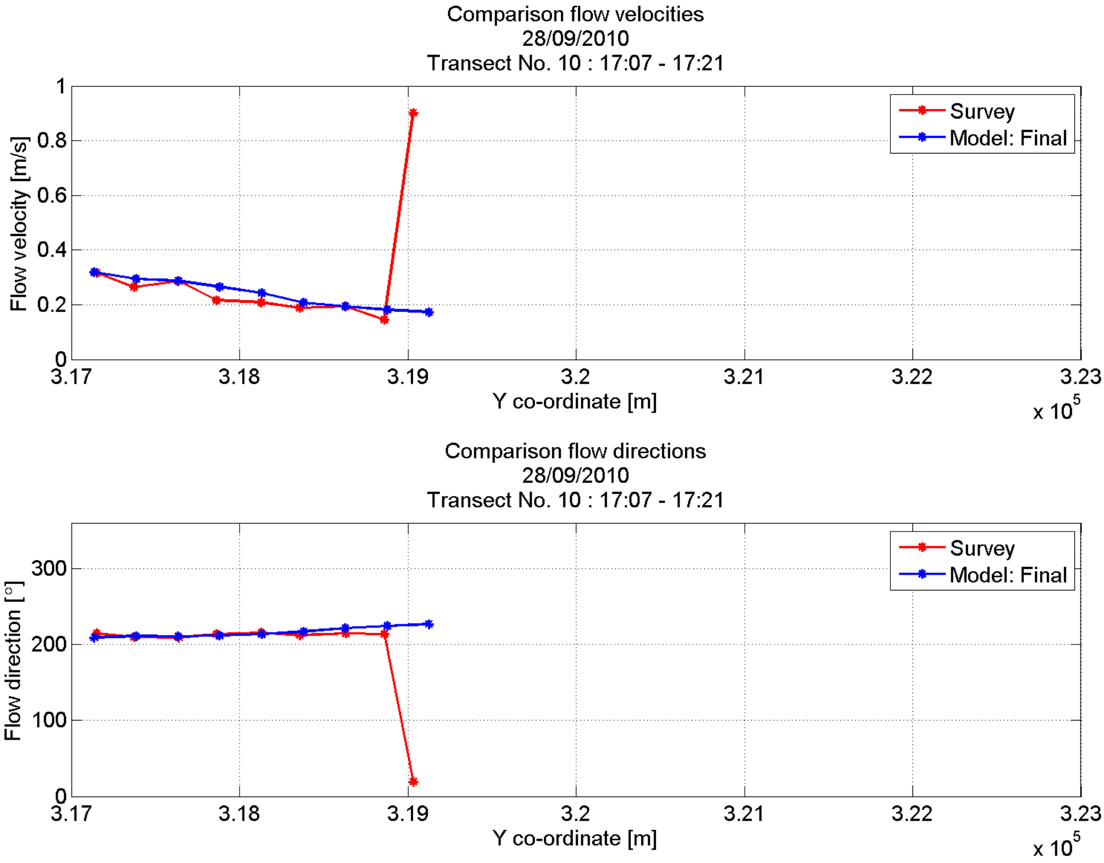

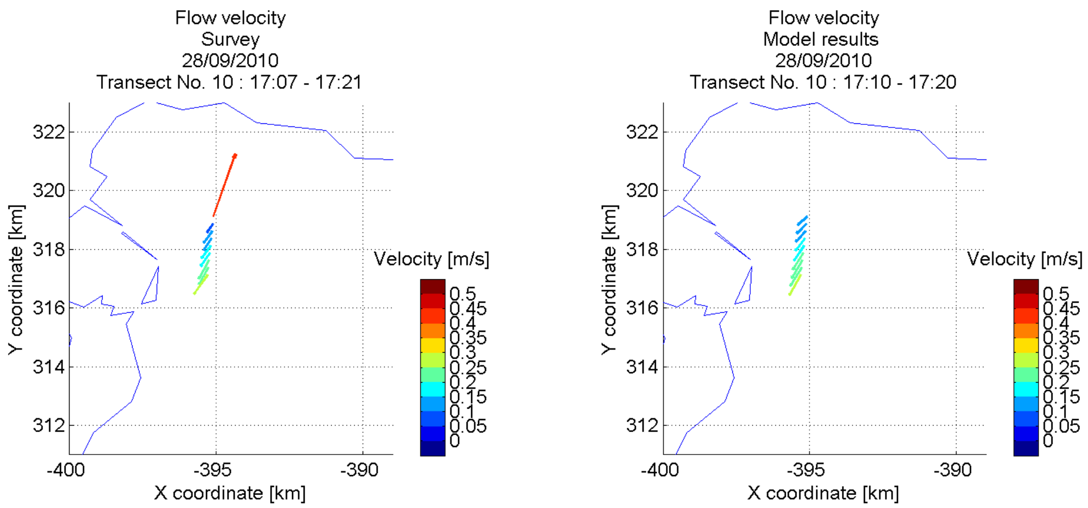

Figure E.10: Measured and modelled flow velocity and direction along transect A during ebb tide

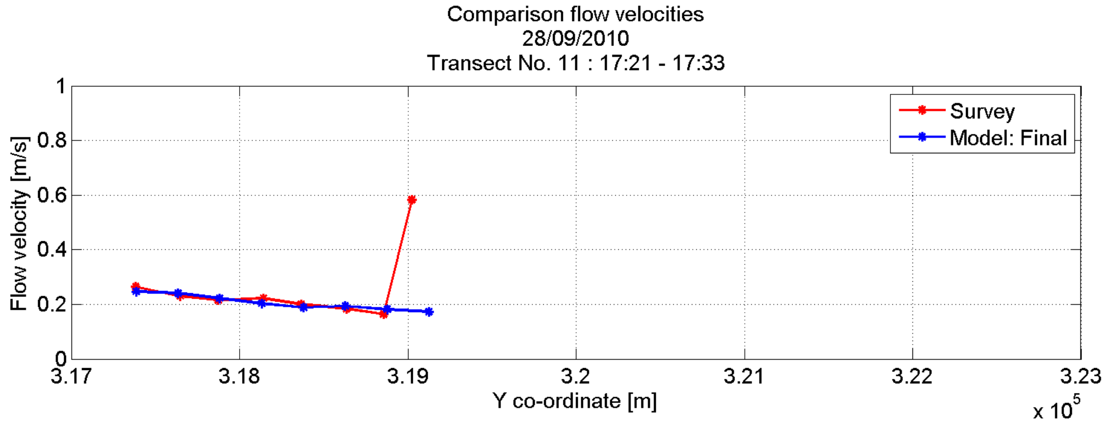

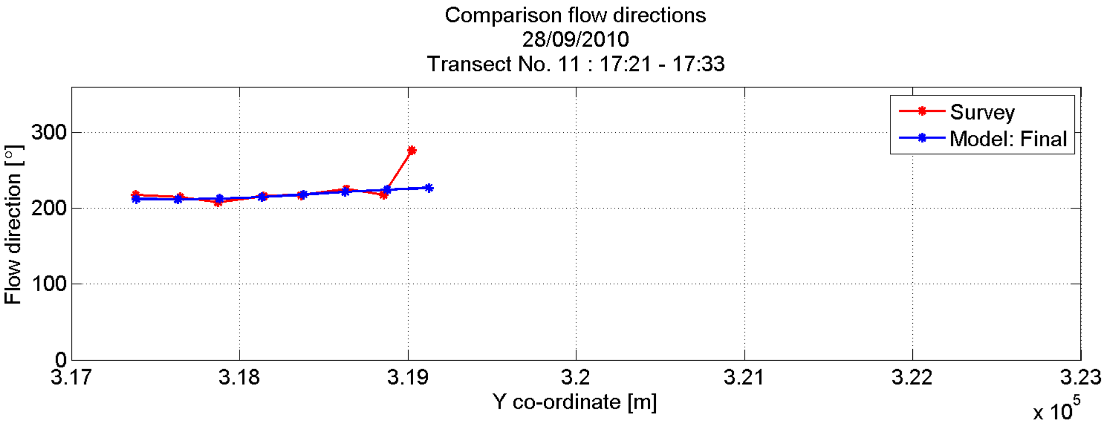

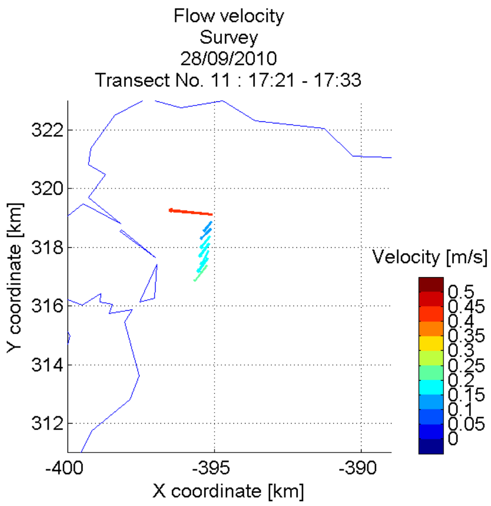

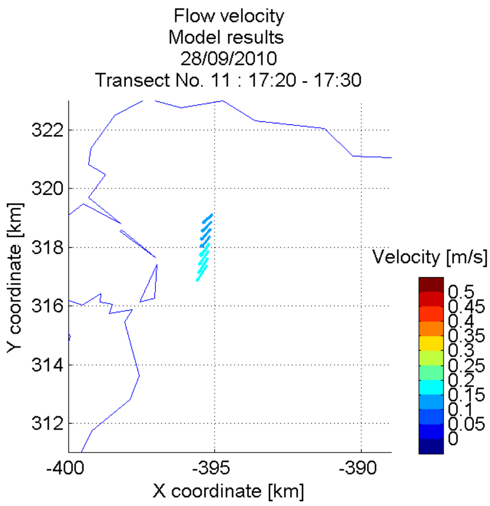

Figure E.11: Measured and modelled flow velocity and direction along transect A during ebb tide

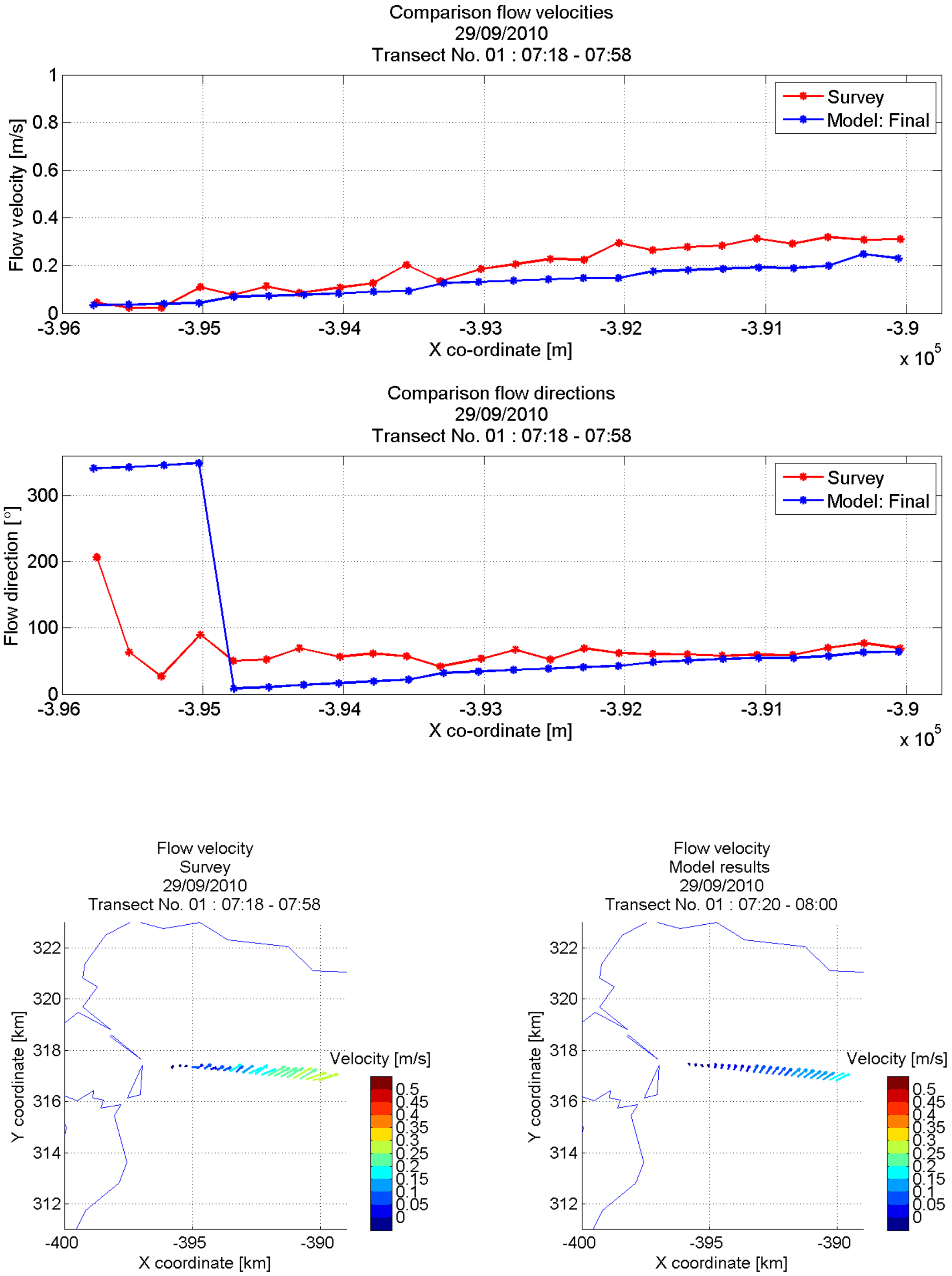

Figure E.12: Measured and modelled flow velocity and direction along transect B during flood tide

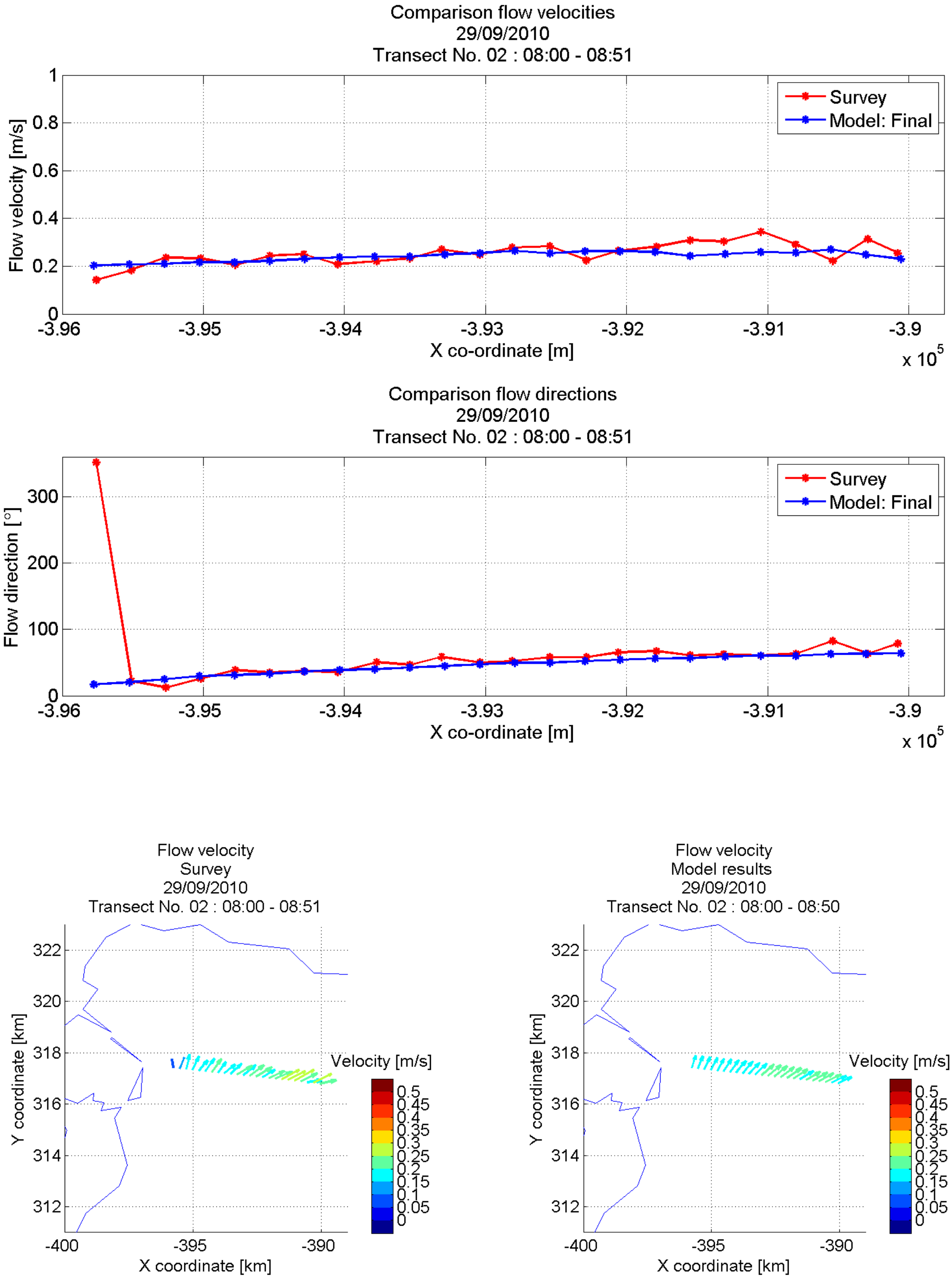

Figure E.13: Measured and modelled flow velocity and direction along transect B during flood tide

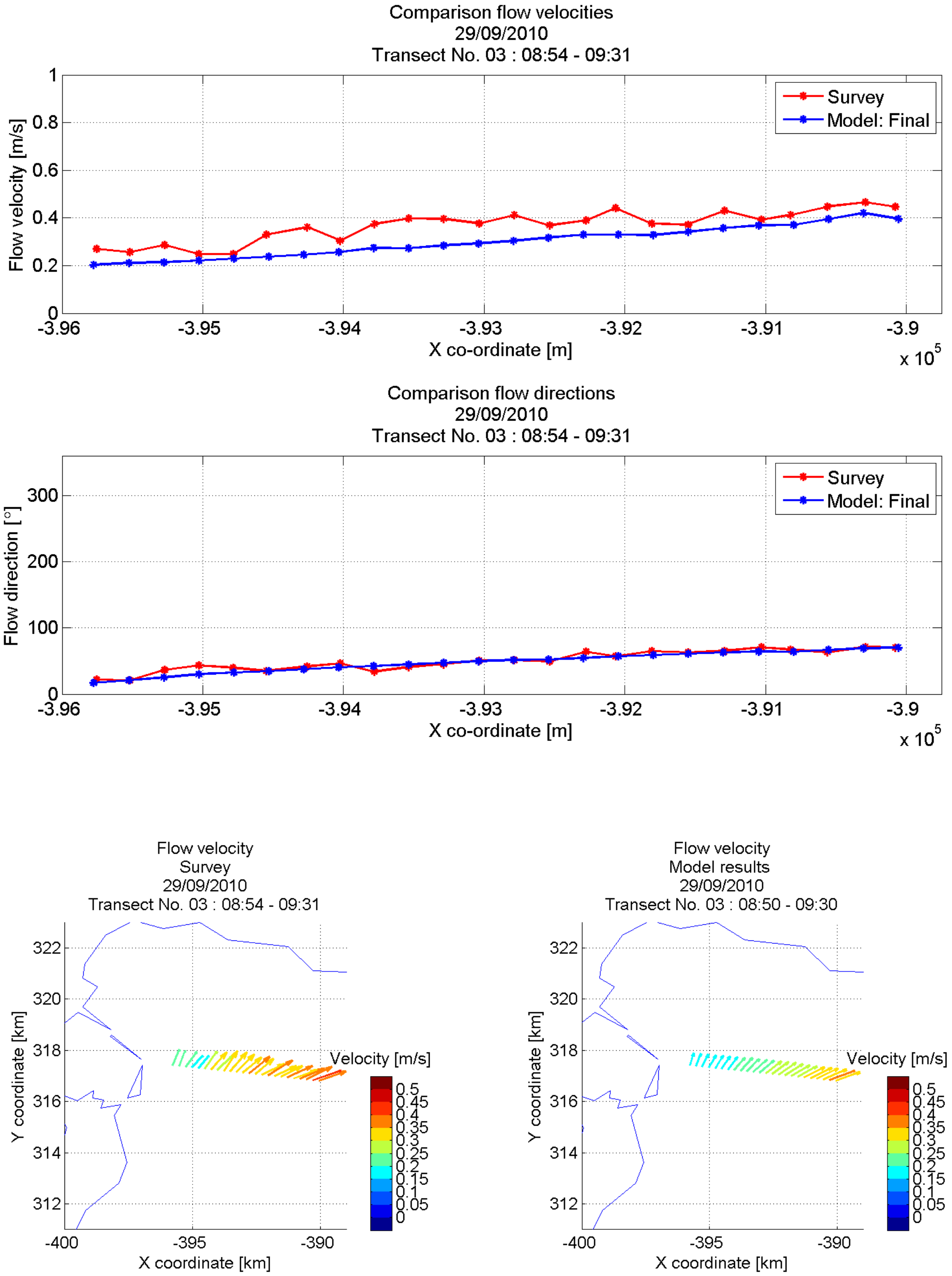

Figure E.14: Measured and modelled flow velocity and direction along transect B during flood tide

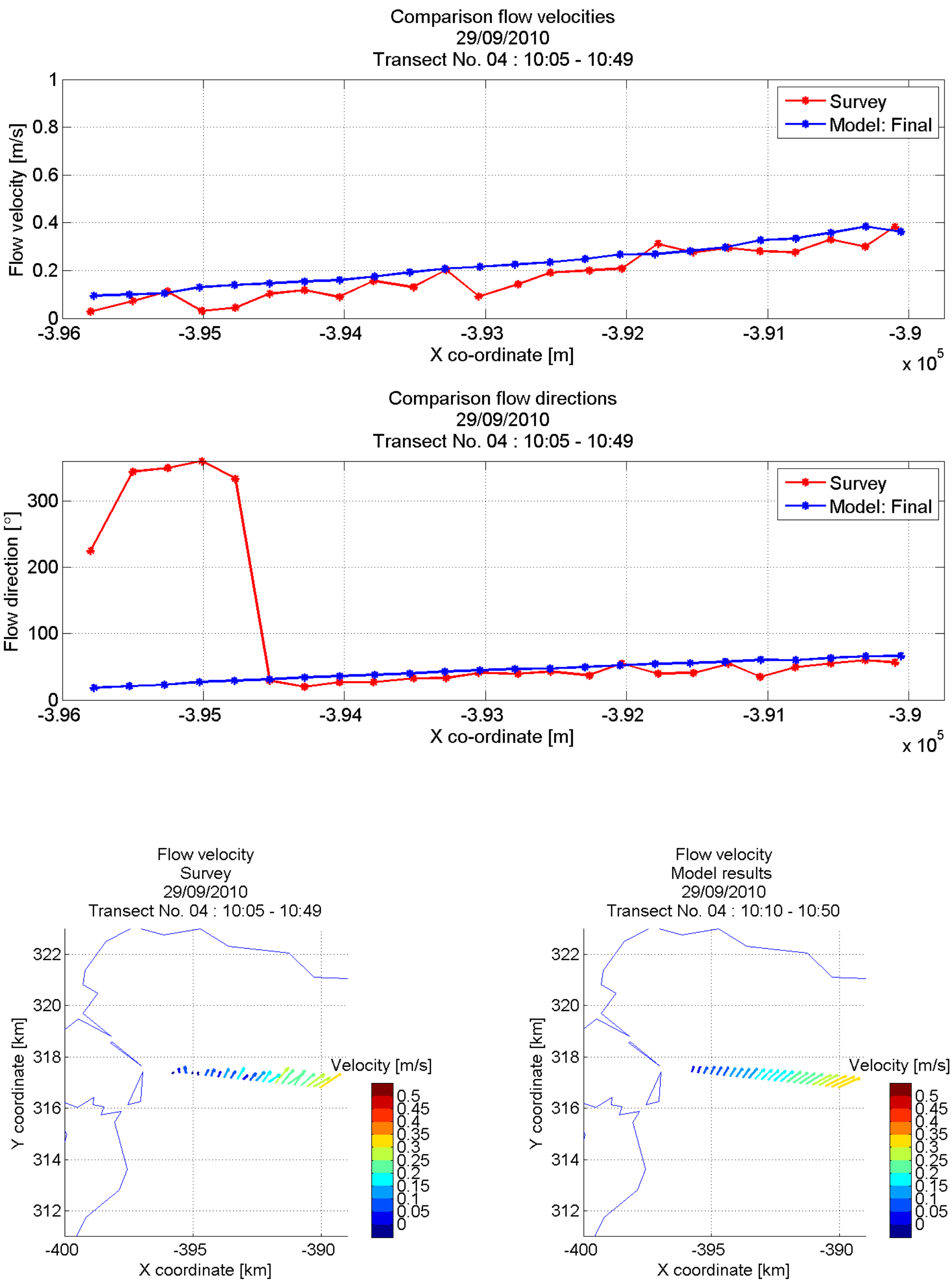

Figure E.15: Measured and modelled flow velocity and direction along transect B during flood tide

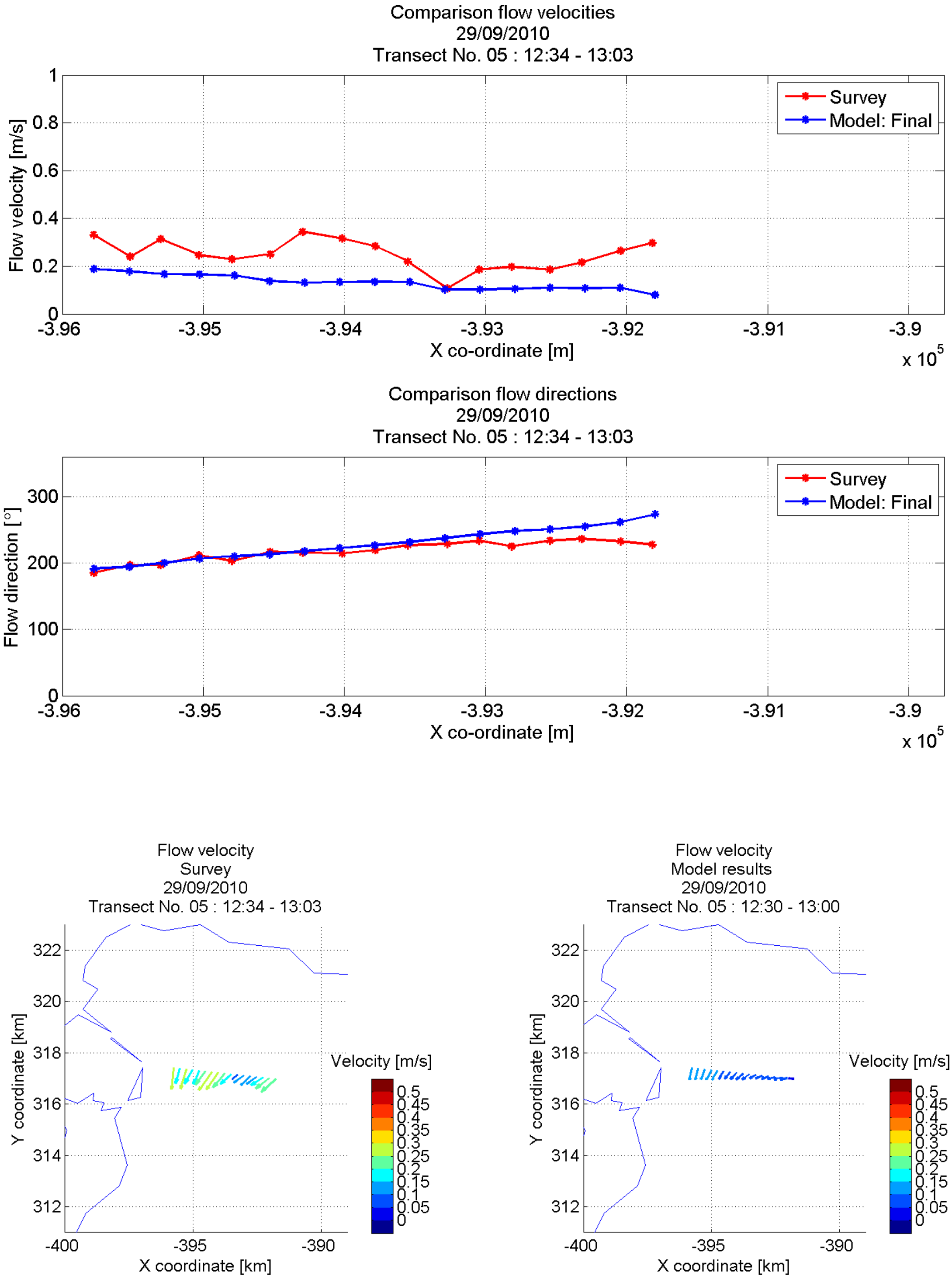

Figure E.16: Measured and modelled flow velocity and direction along transect B during ebb tide

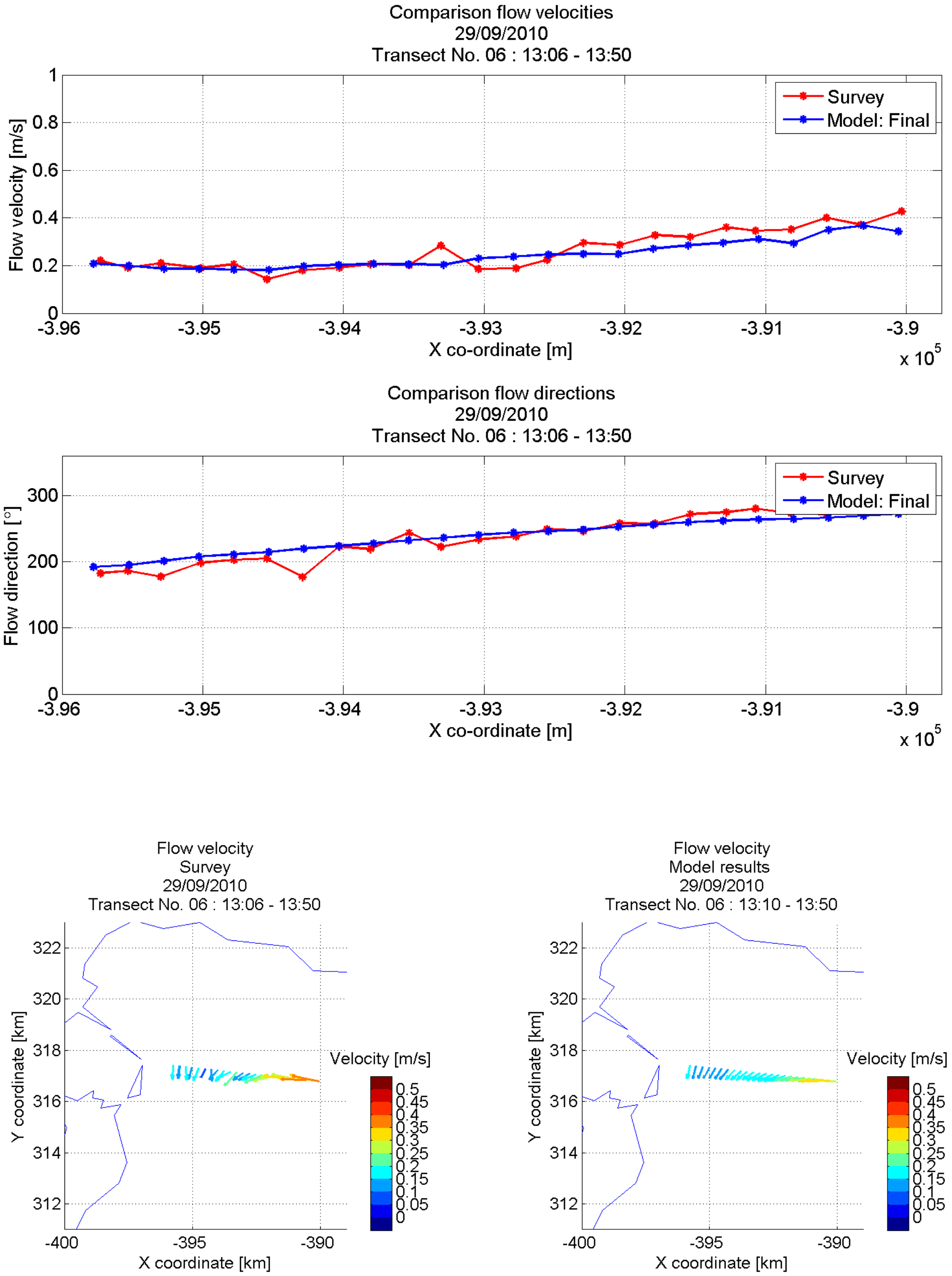

Figure E.17: Measured and modelled flow velocity and direction along transect B during ebb tide

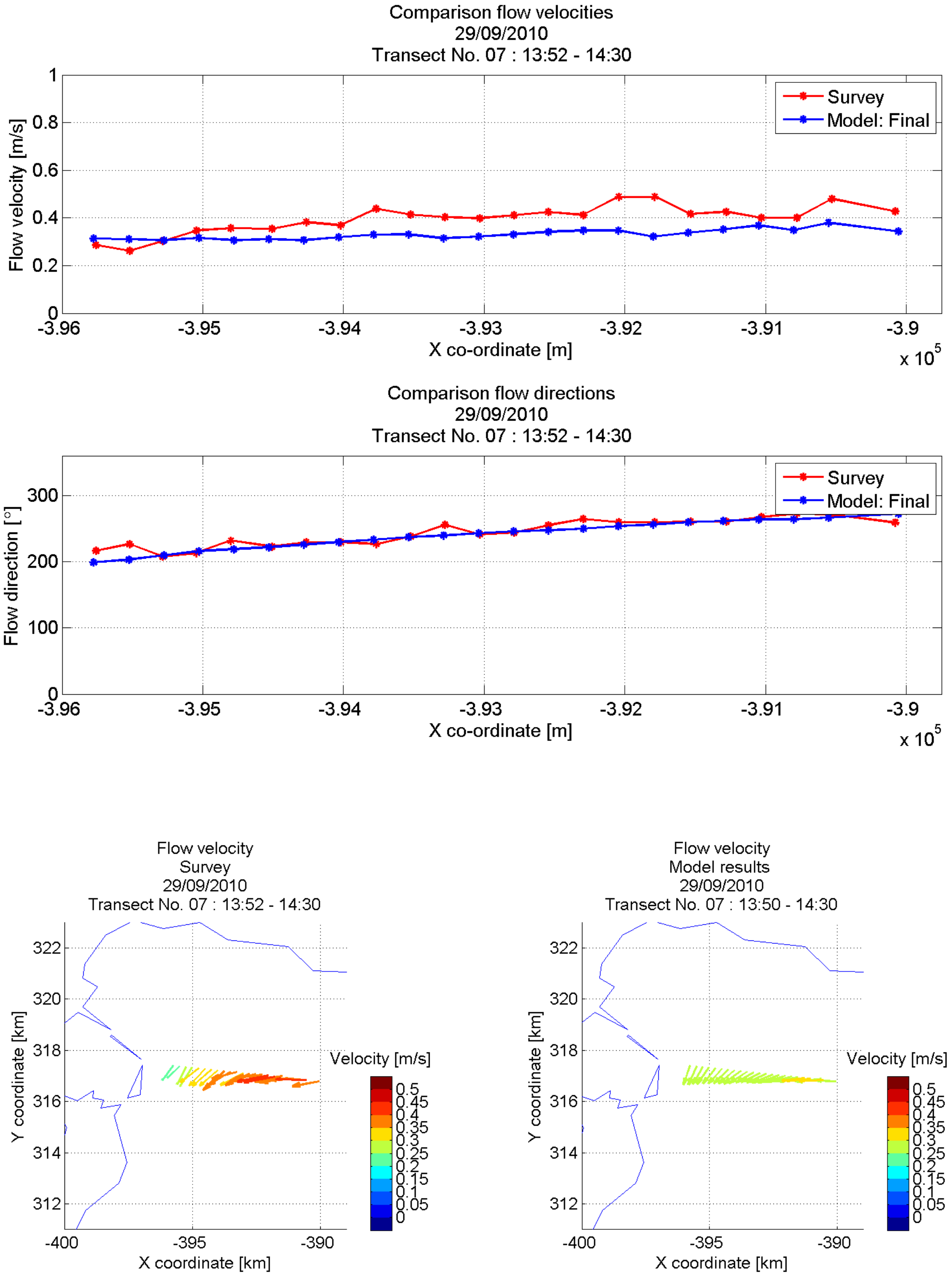

Figure E.18: Measured and modelled flow velocity and direction along transect B during ebb tide

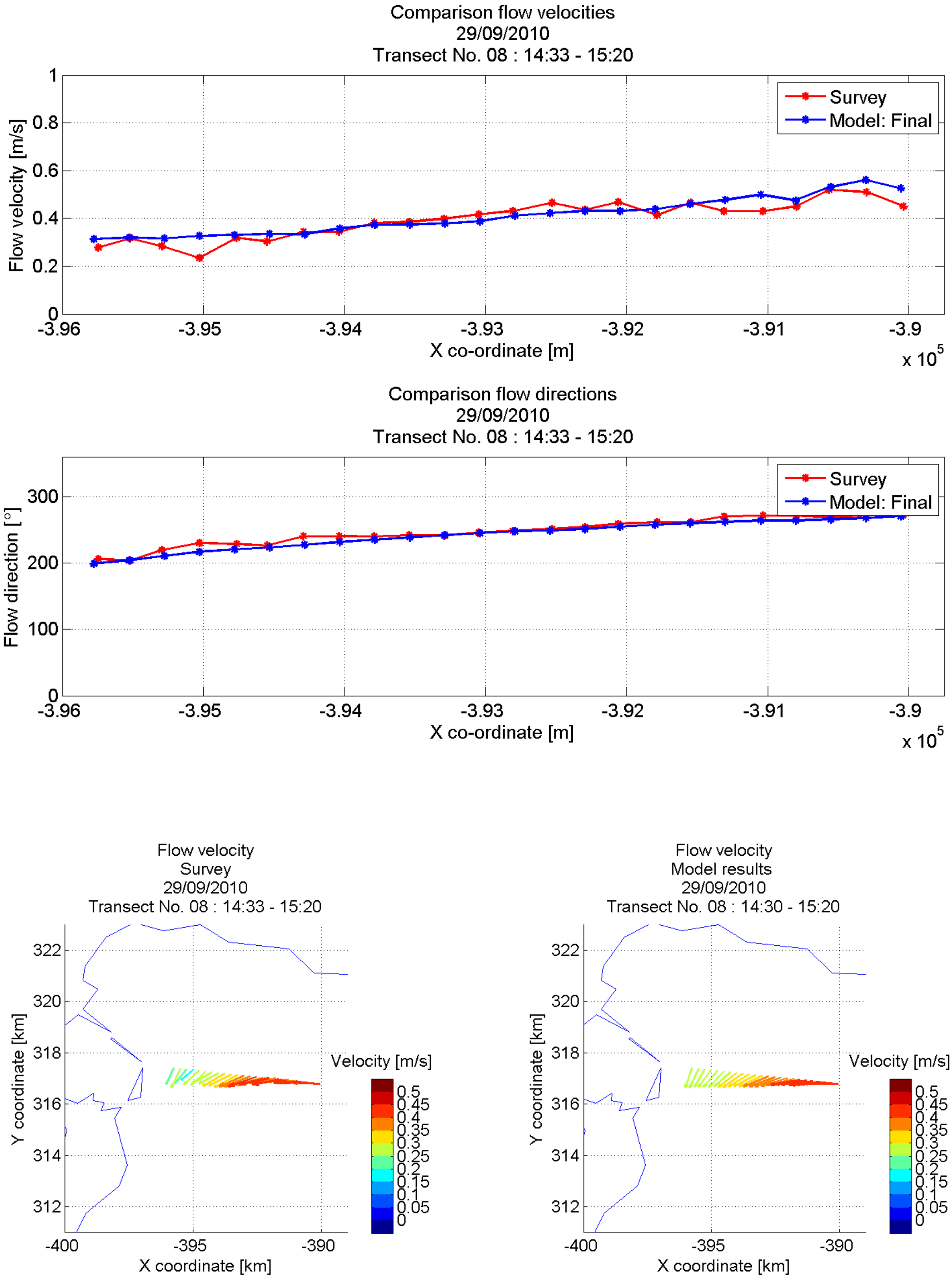

Figure E.19: Measured and modelled flow velocity and direction along transect B during ebb tide

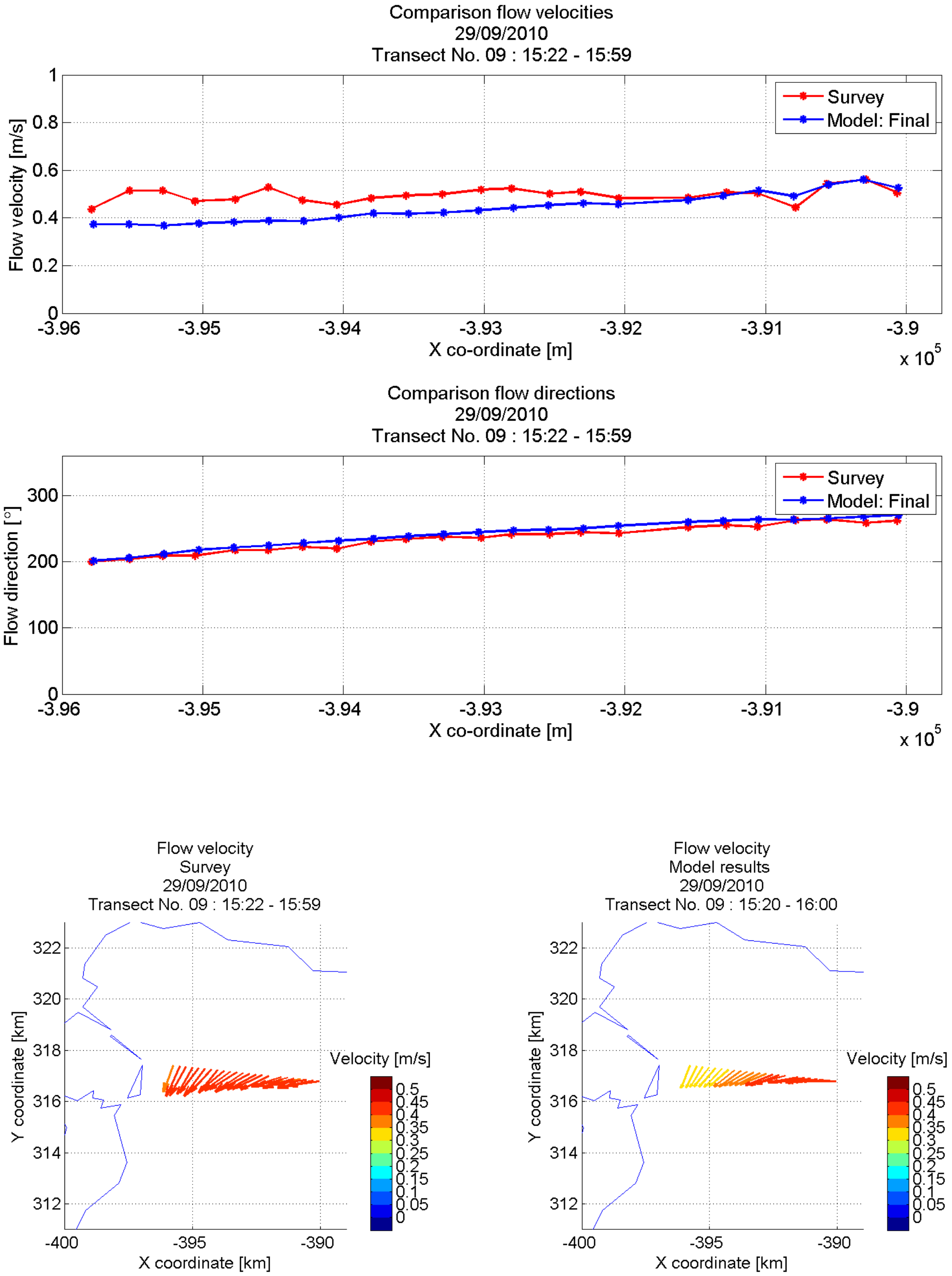

Figure E.20: Measured and modelled flow velocity and direction along transect B during ebb tide

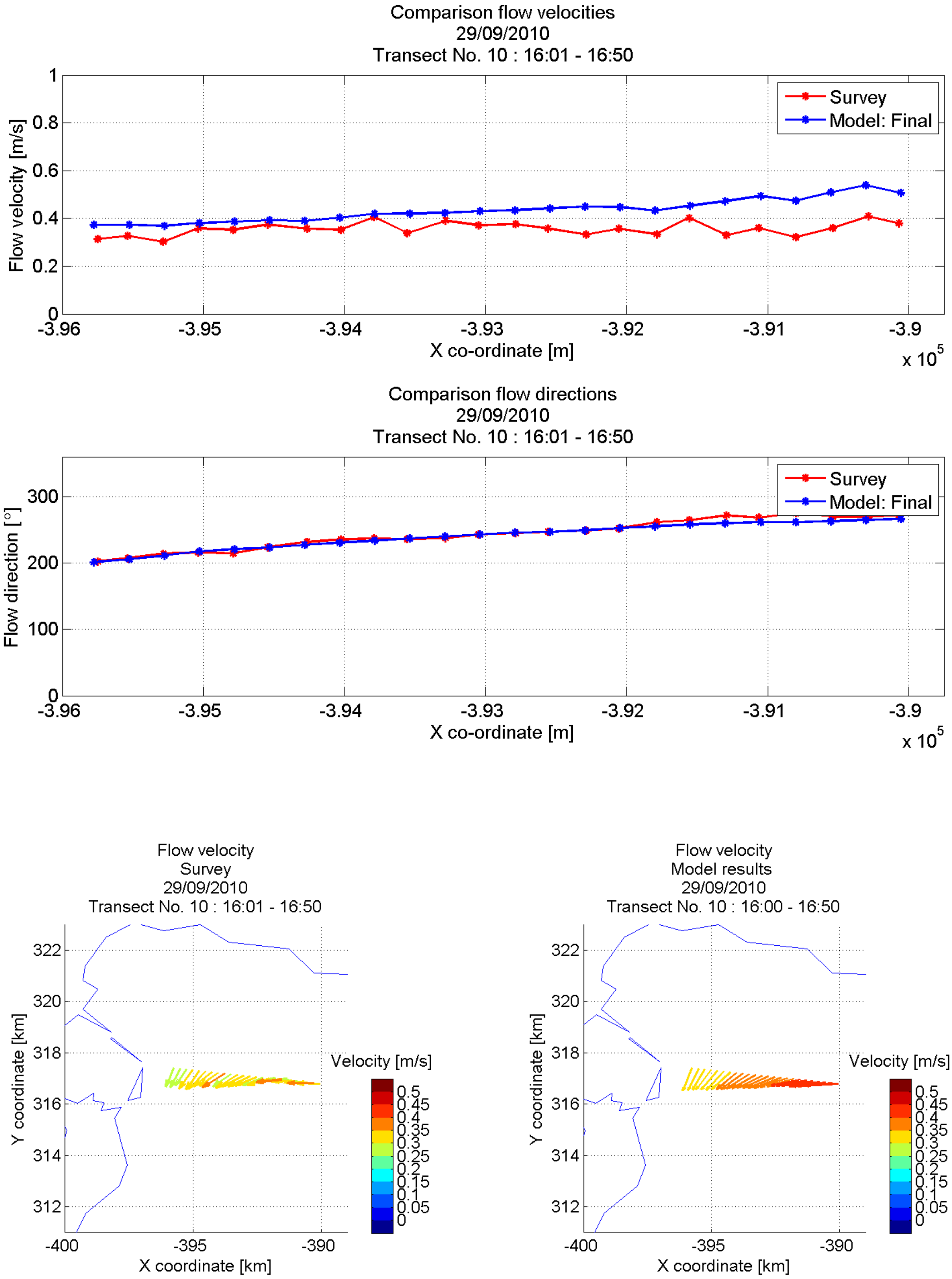

Figure E.21: Measured and modelled flow velocity and direction along transect B during ebb tide

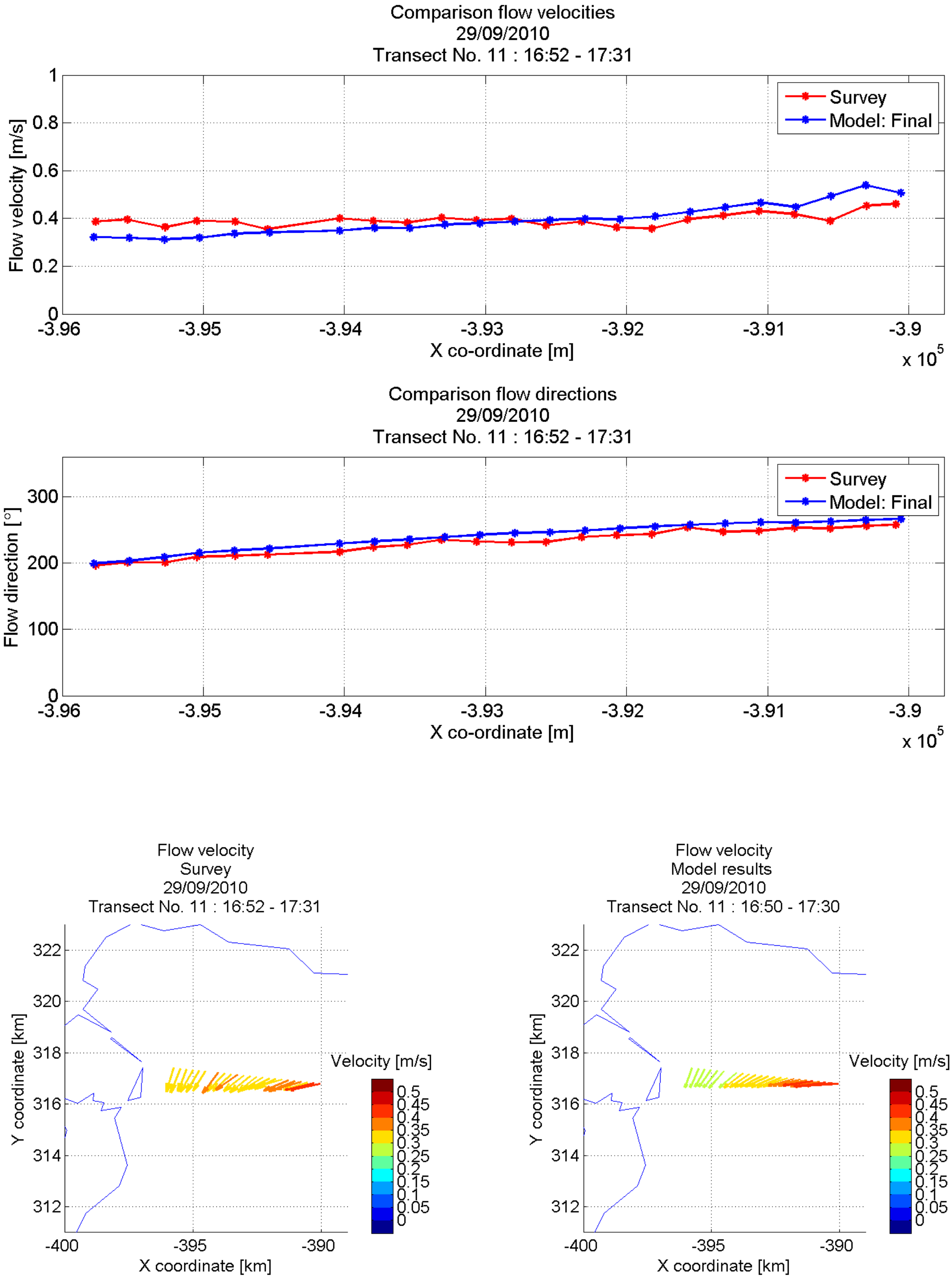

Figure E.22: Measured and modelled flow velocity and direction along transect B during ebb tide

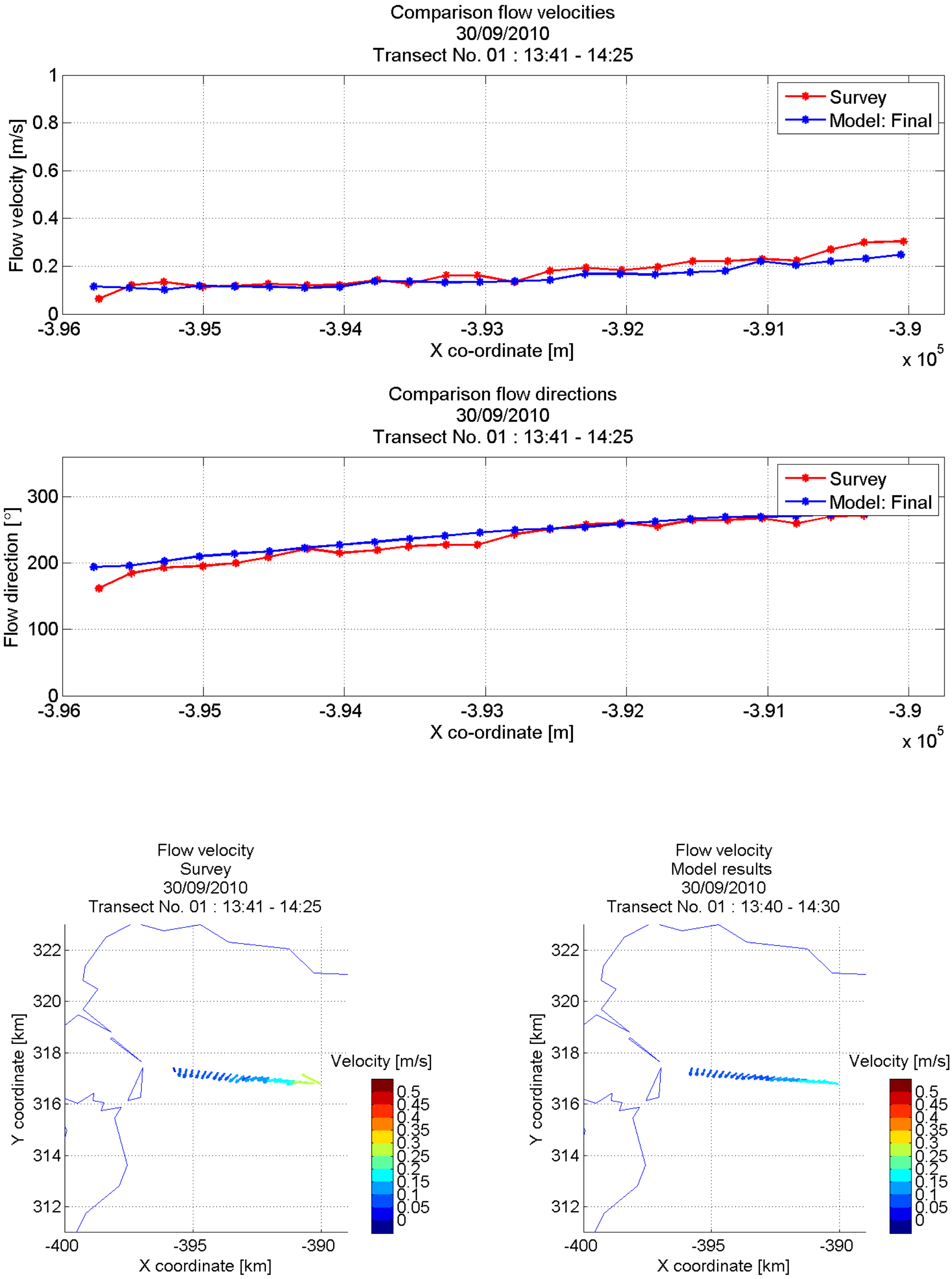

Figure E.23: Measured and modelled flow velocity and direction along transect B during ebb tide

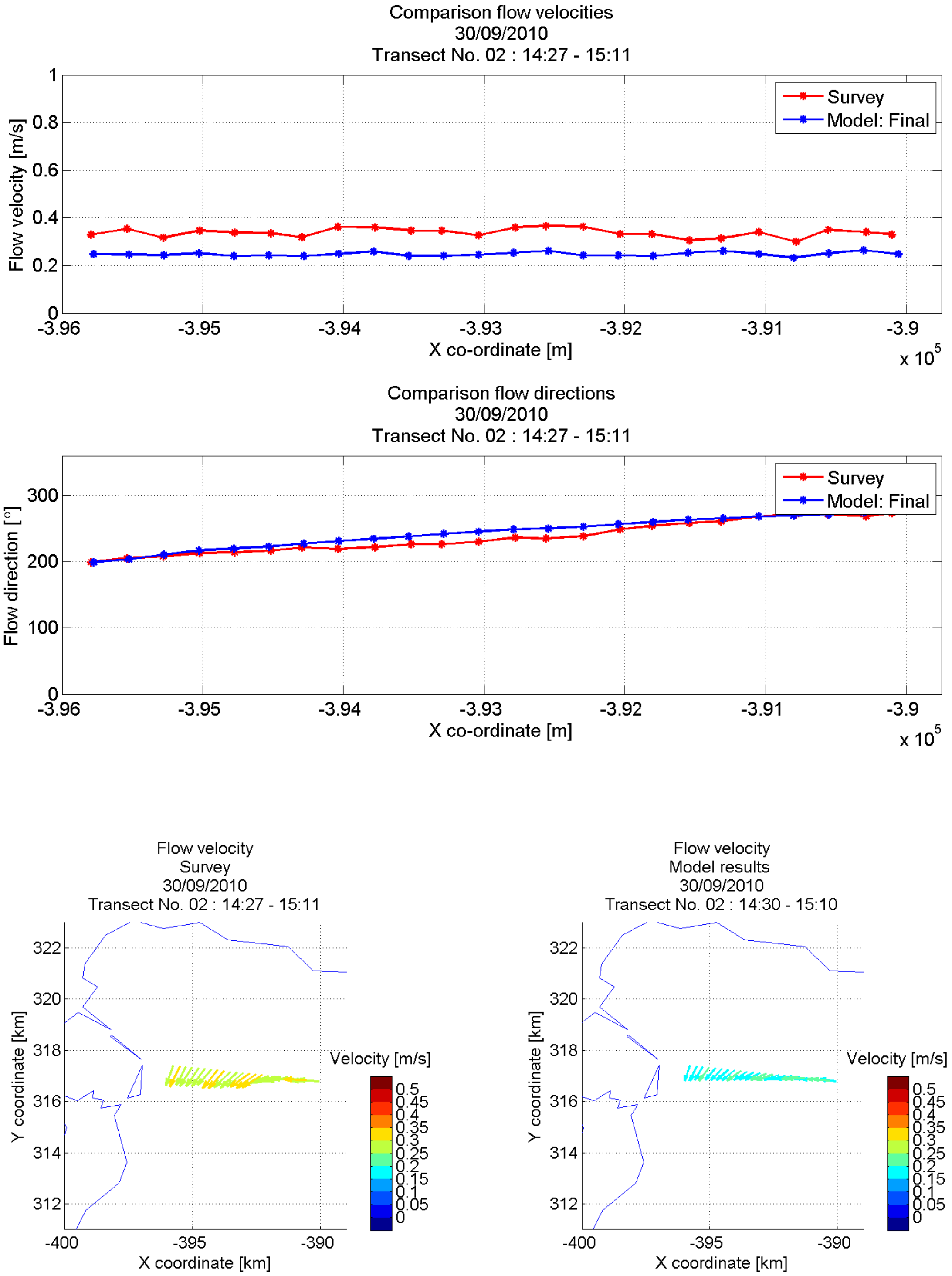

Figure E.24: Measured and modelled flow velocity and direction along transect B during ebb tide

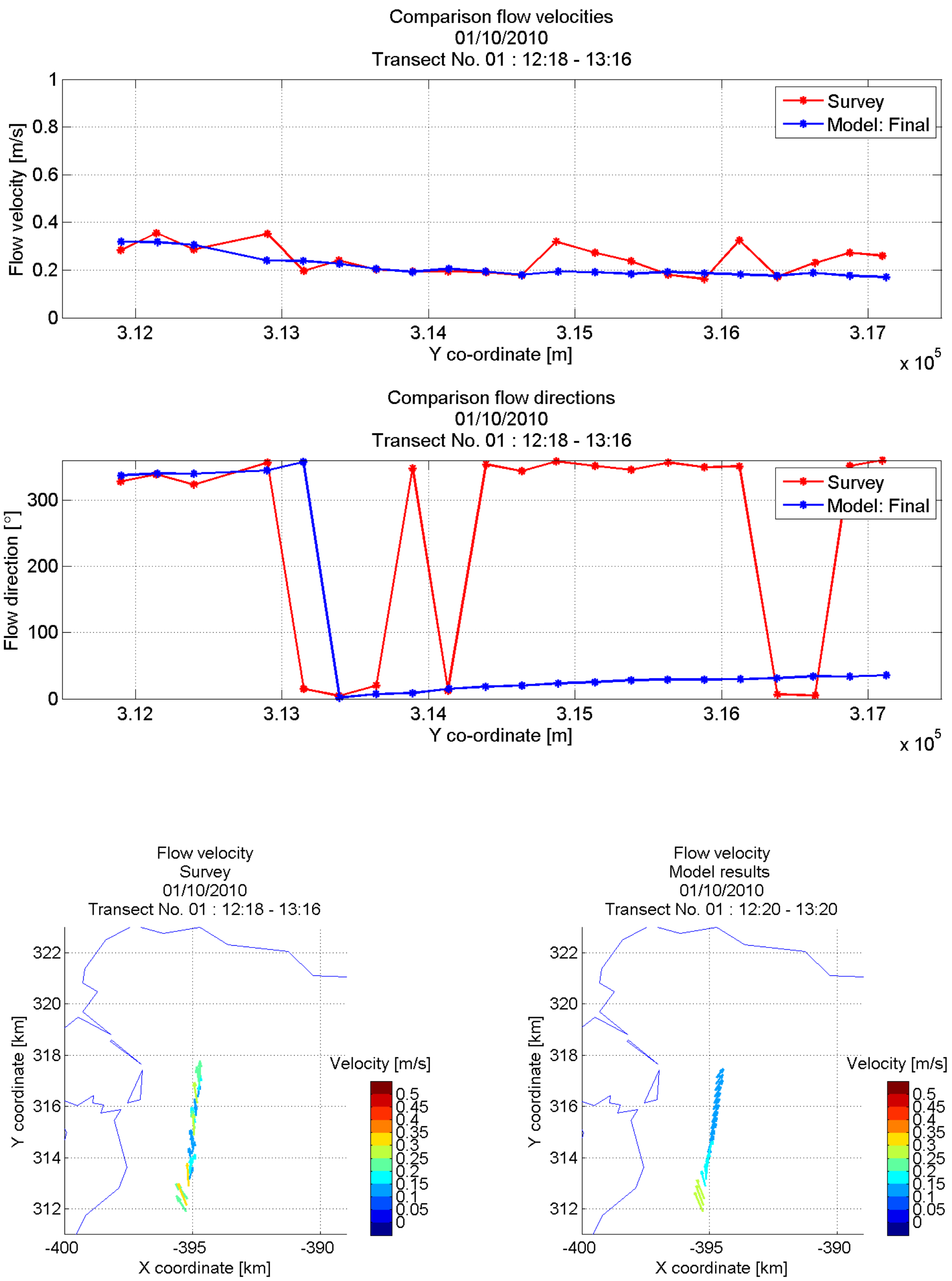

Figure E.25: Measured and modelled flow velocity and direction along transect C during ebb tide

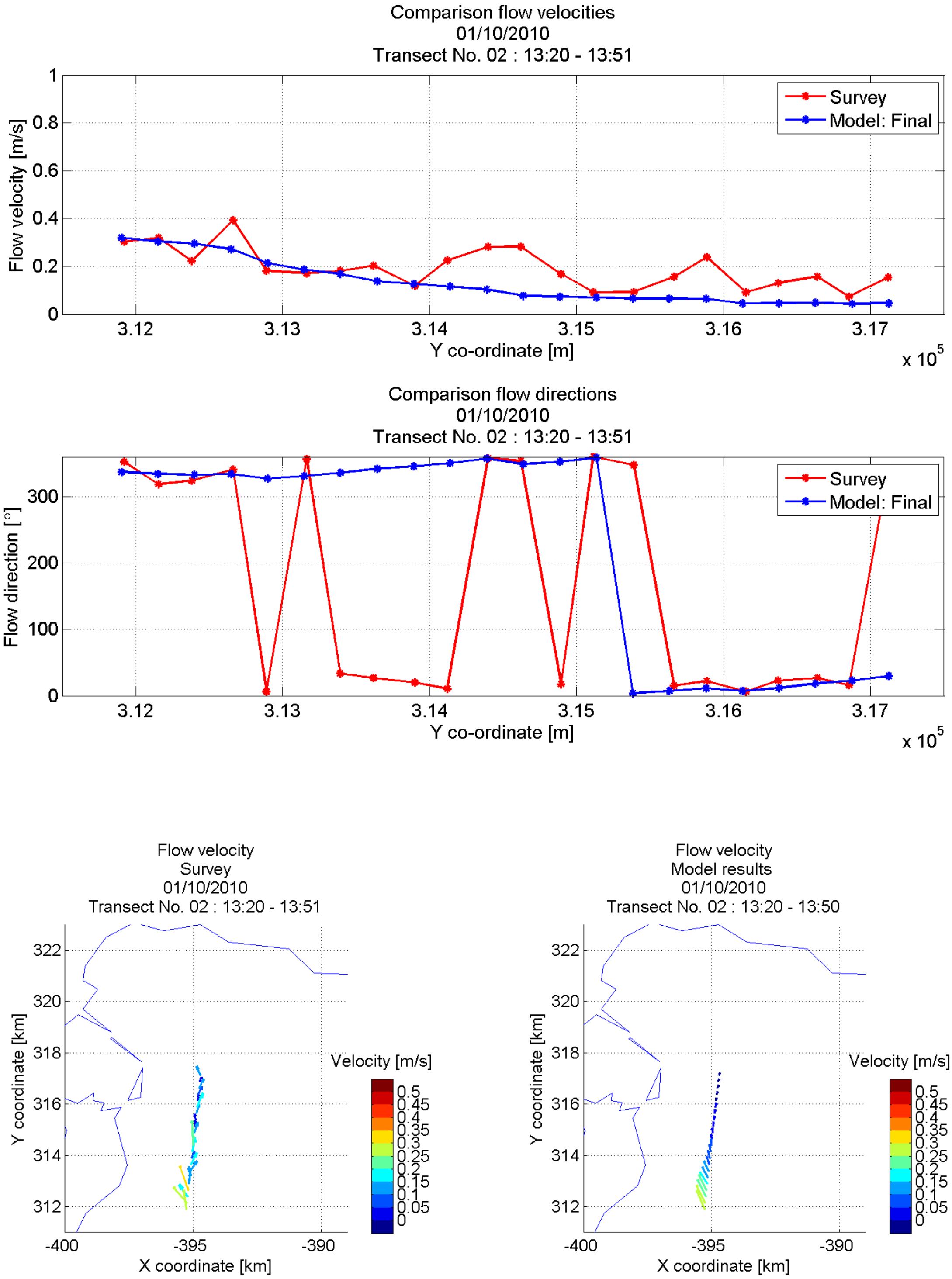

Figure E.26: Measured and modelled flow velocity and direction along transect C during ebb tide

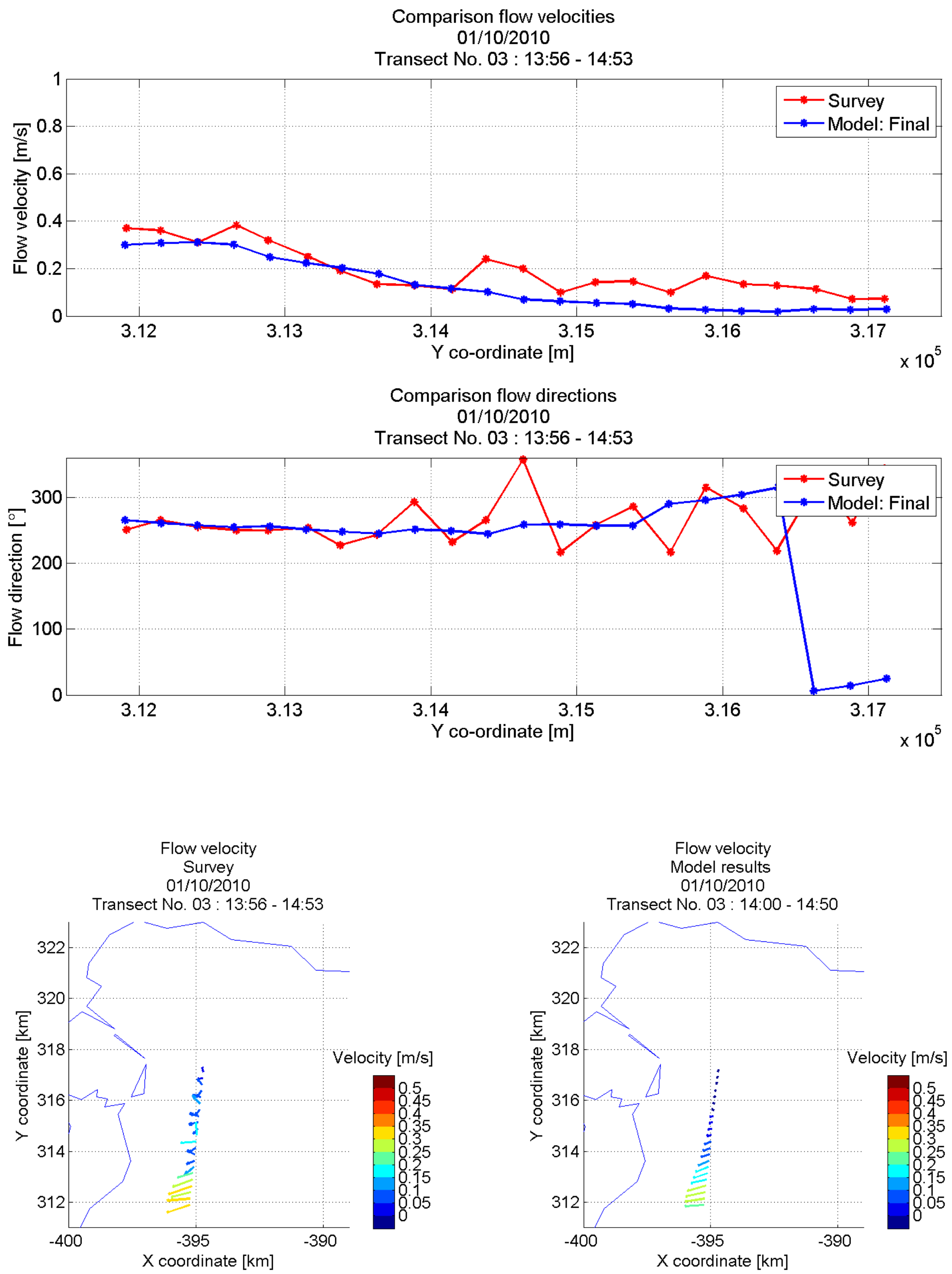

Figure E.27: Measured and modelled flow velocity and direction along transect C during ebb tide

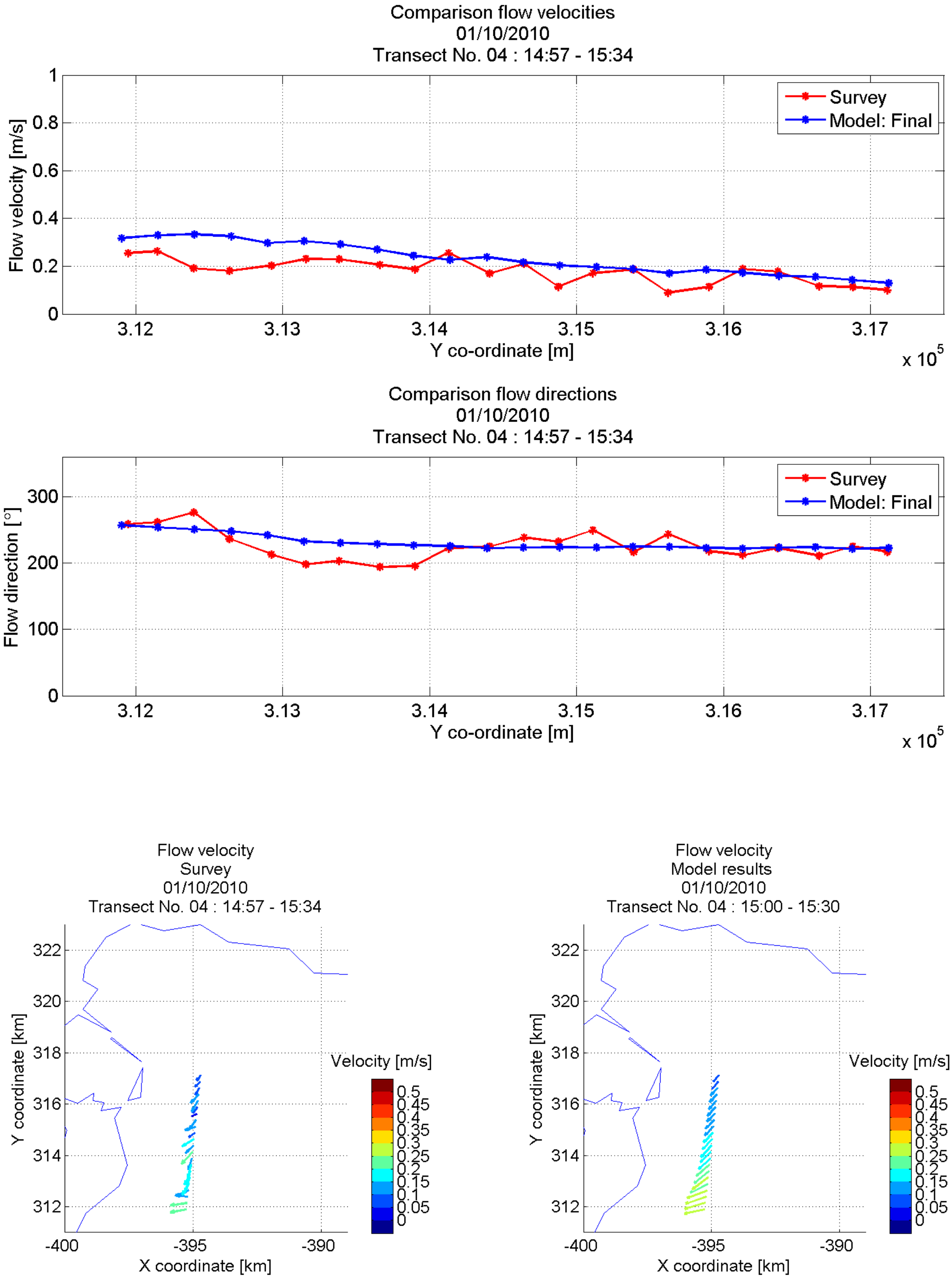

Figure E.28: Measured and modelled flow velocity and direction along transect C during ebb tide

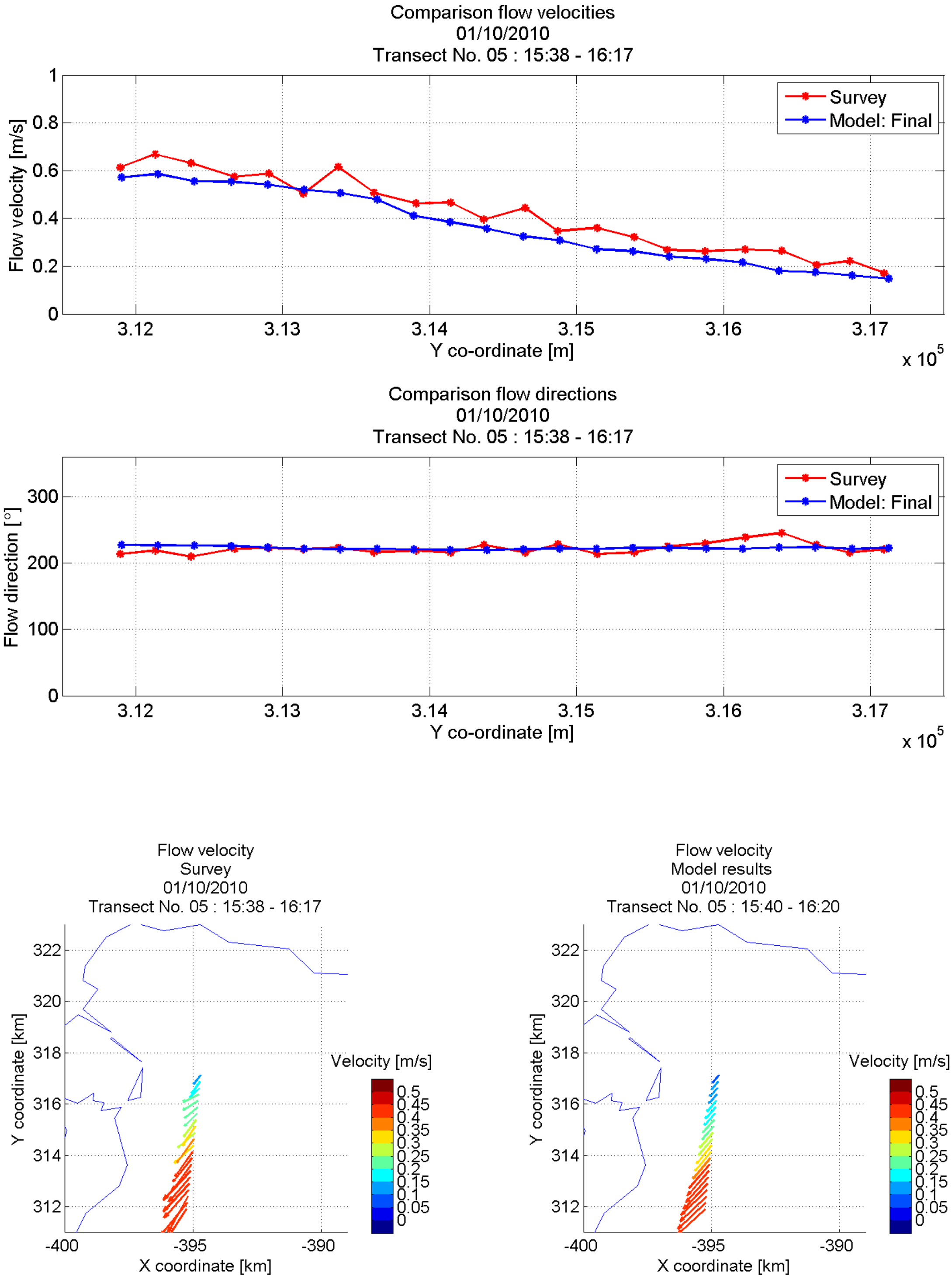

Figure E.29: Measured and modelled flow velocity and direction along transect C during ebb tide

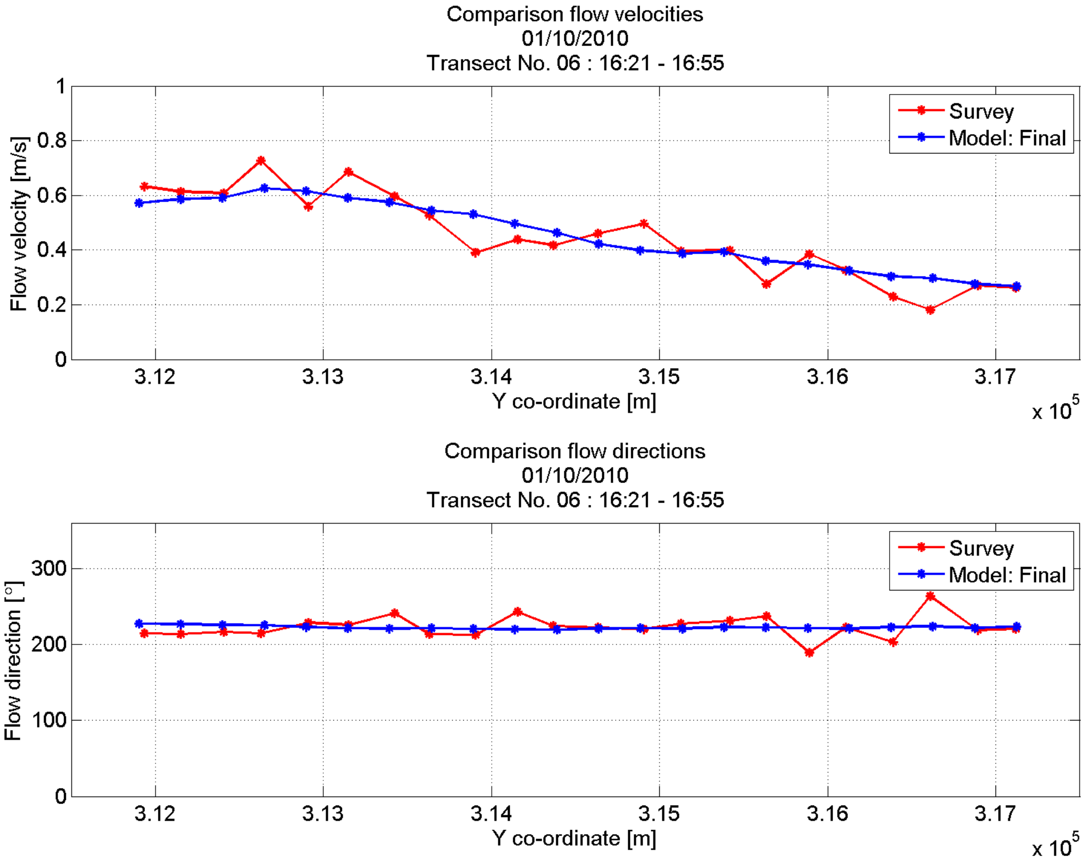

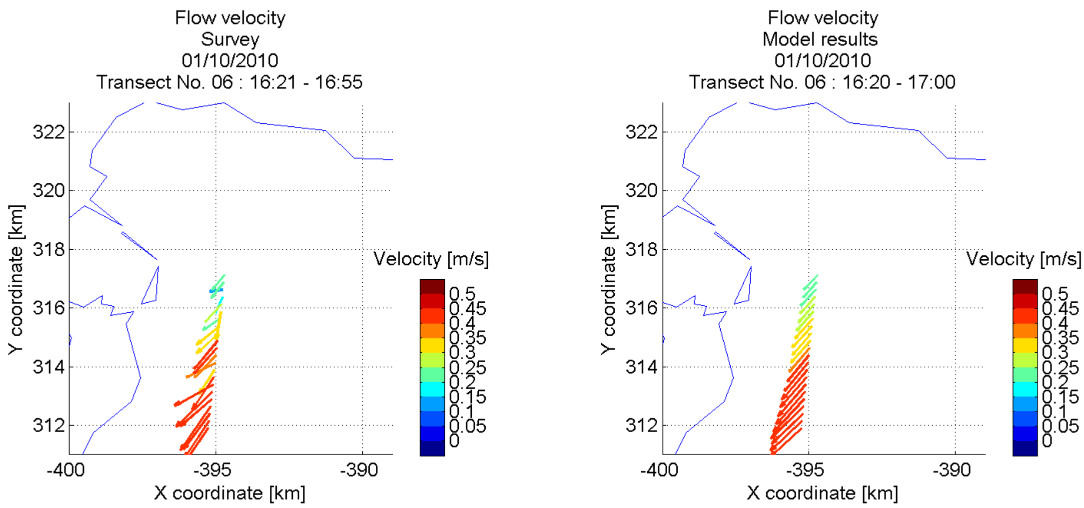

Figure E.30: Measured and modelled flow velocity and direction along transect C during ebb tide

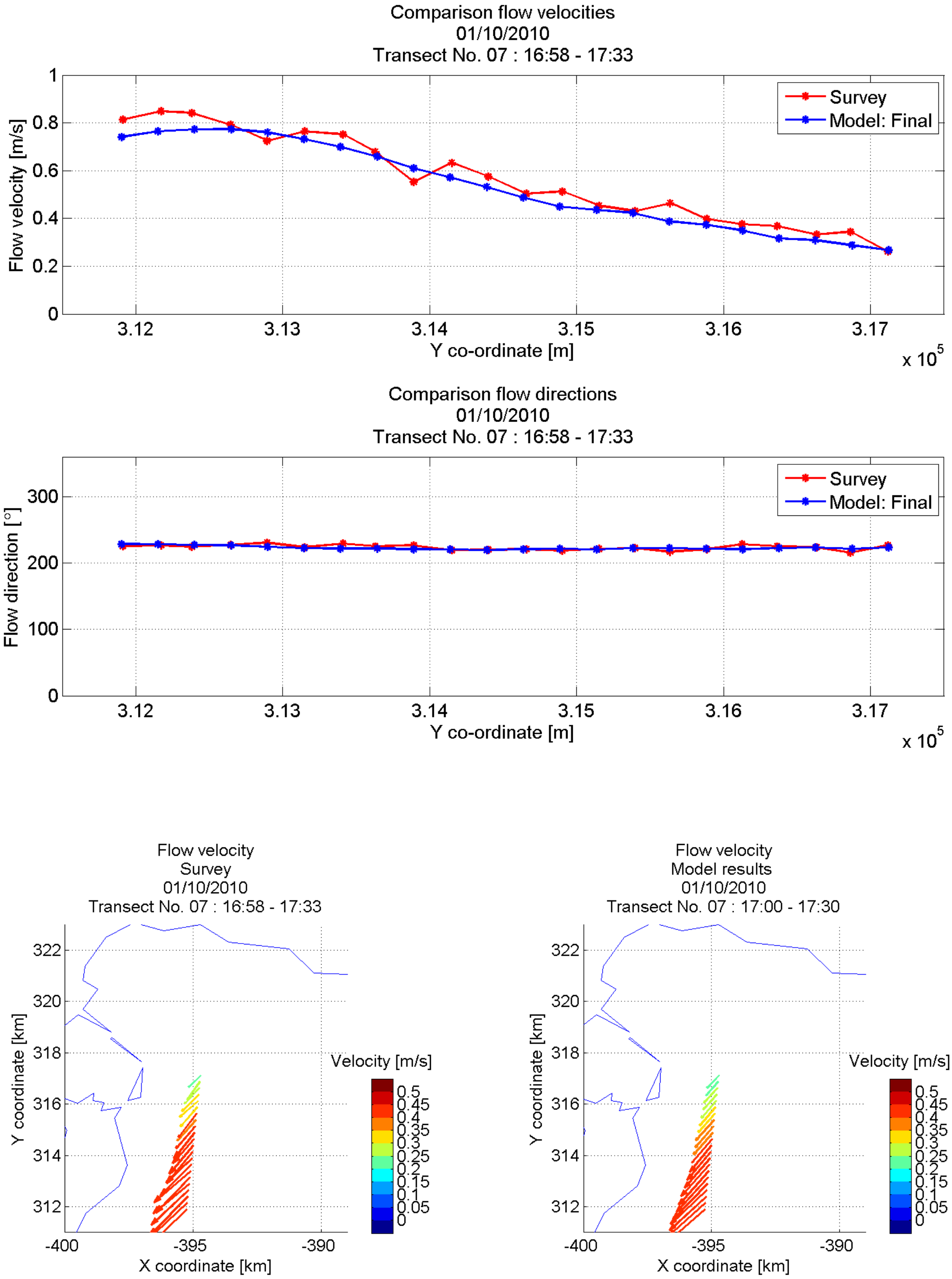

Figure E.31: Measured and modelled flow velocity and direction along transect C during ebb tide

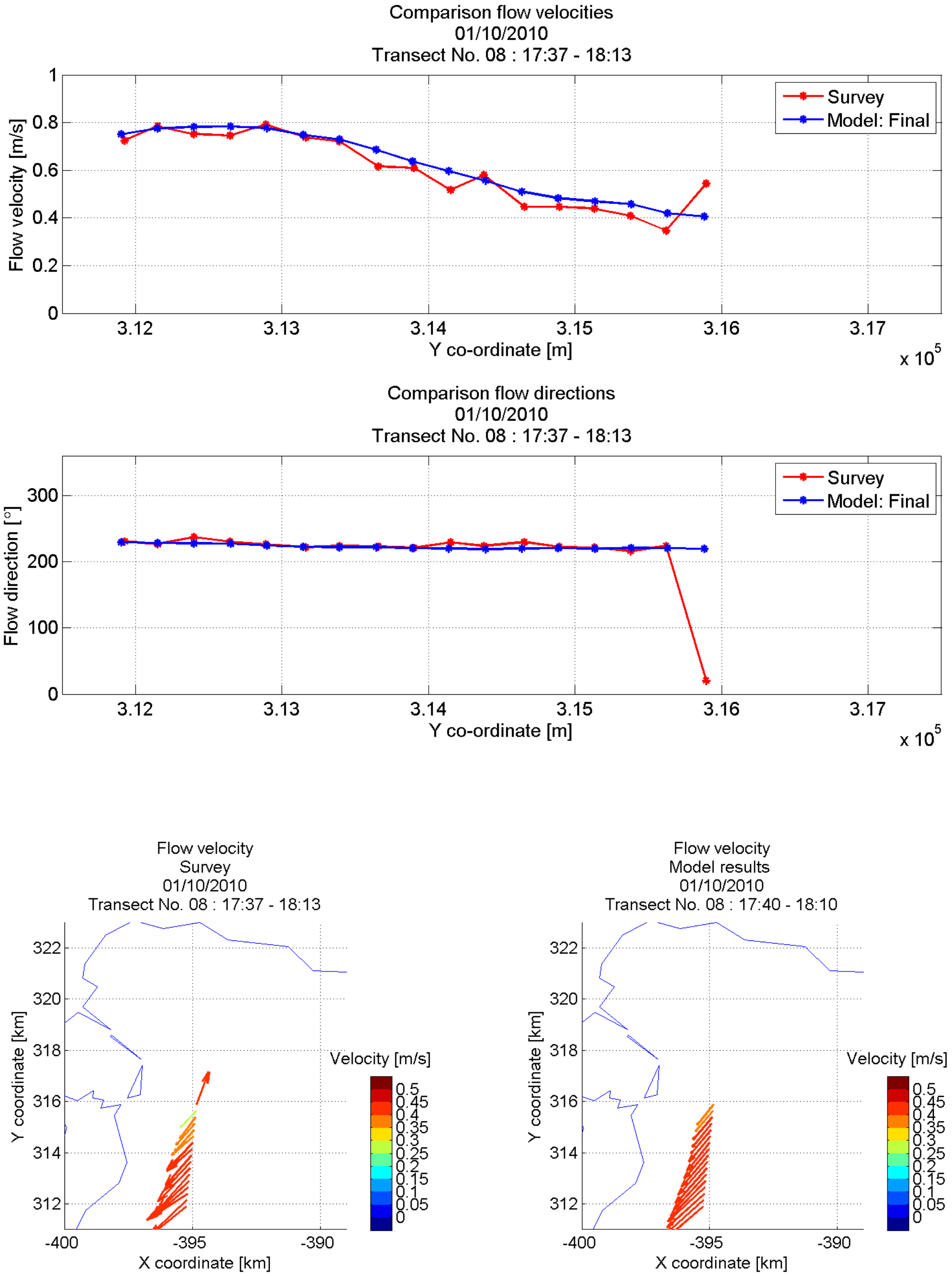

Figure E.32: Measured and modelled flow velocity and direction along transect C during ebb tide

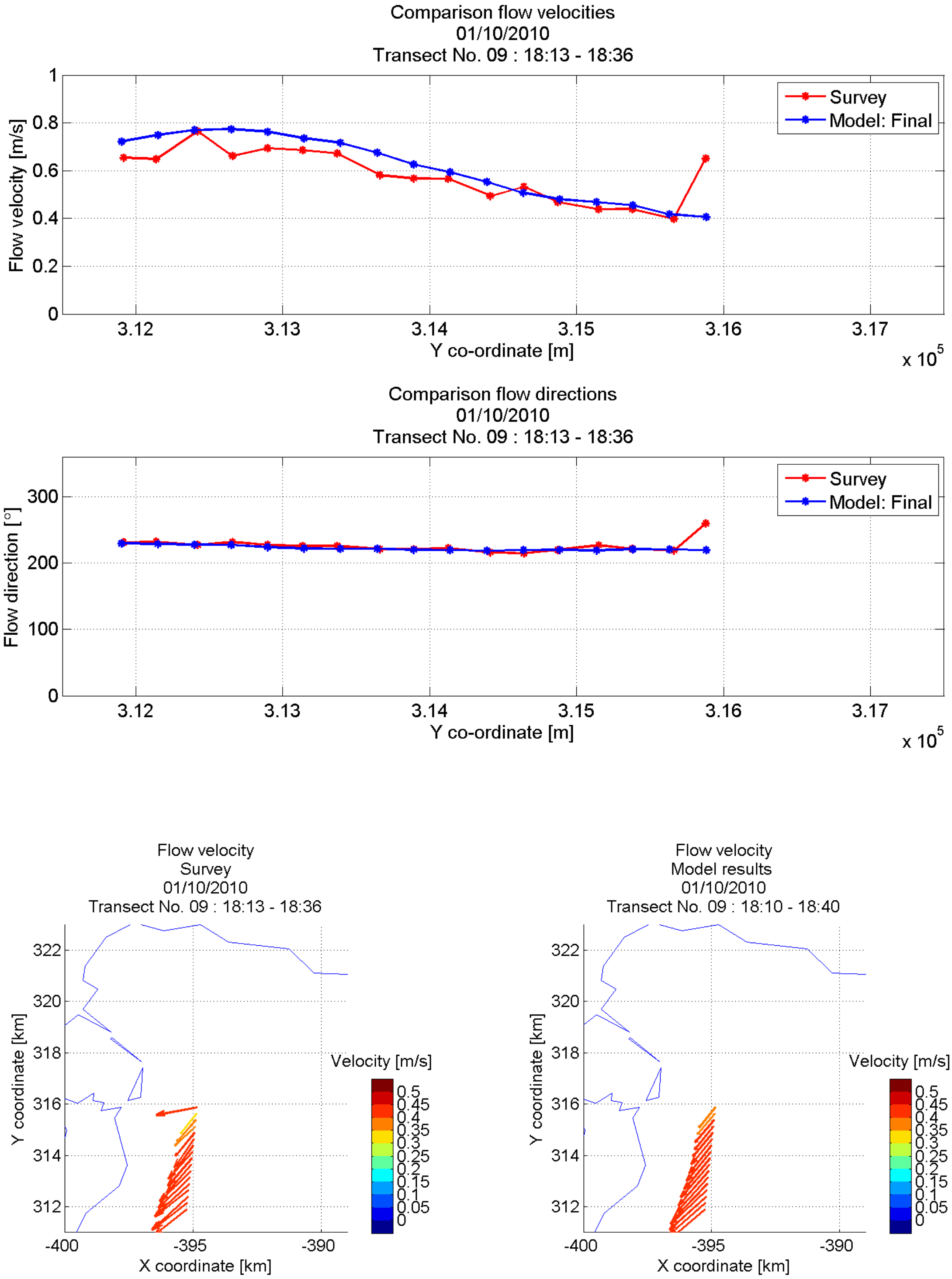

Figure E.33: Measured and modelled flow velocity and direction along transect C during ebb tide

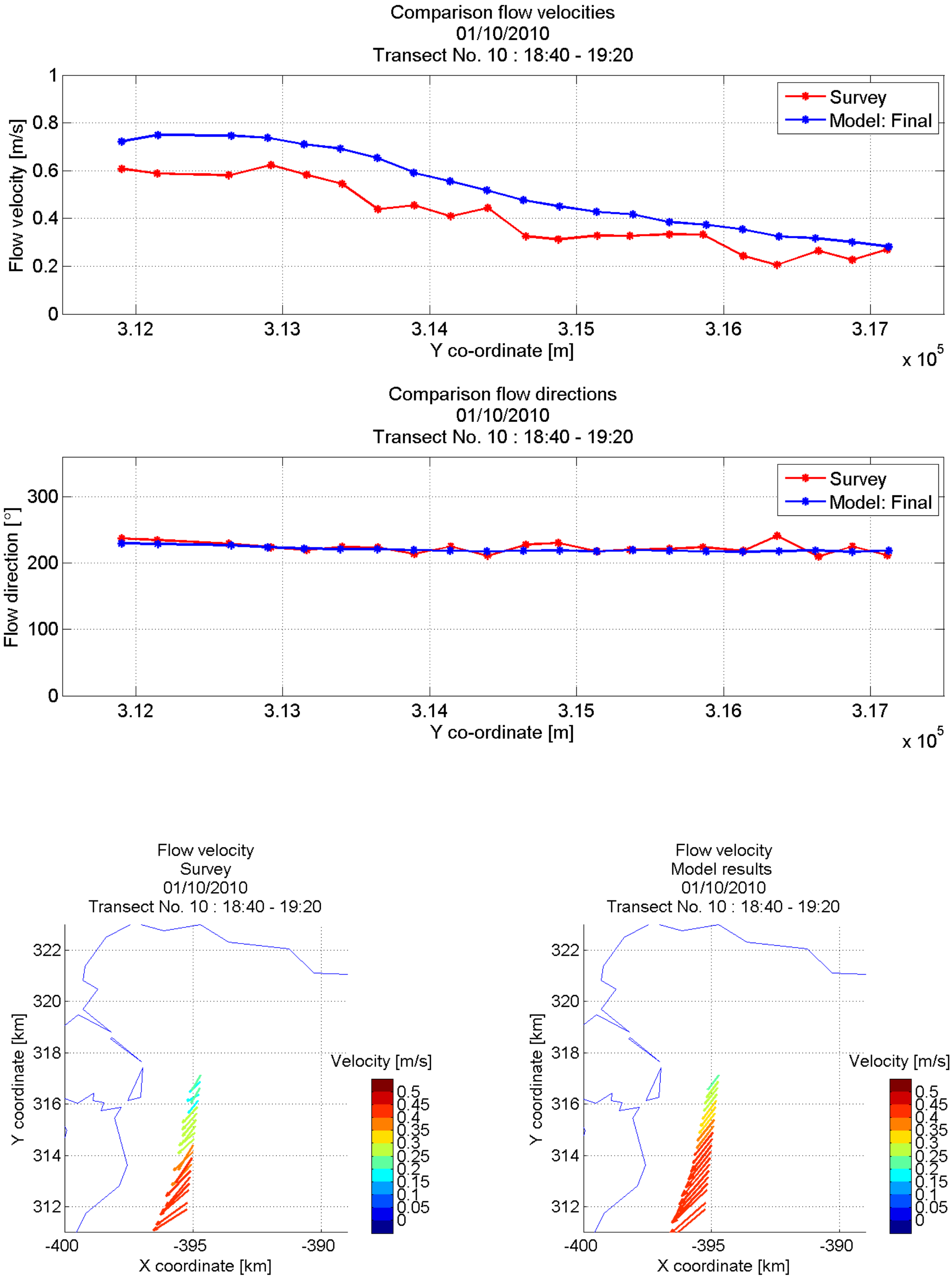

Figure E.34: Measured and modelled flow velocity and direction along transect C during ebb tide

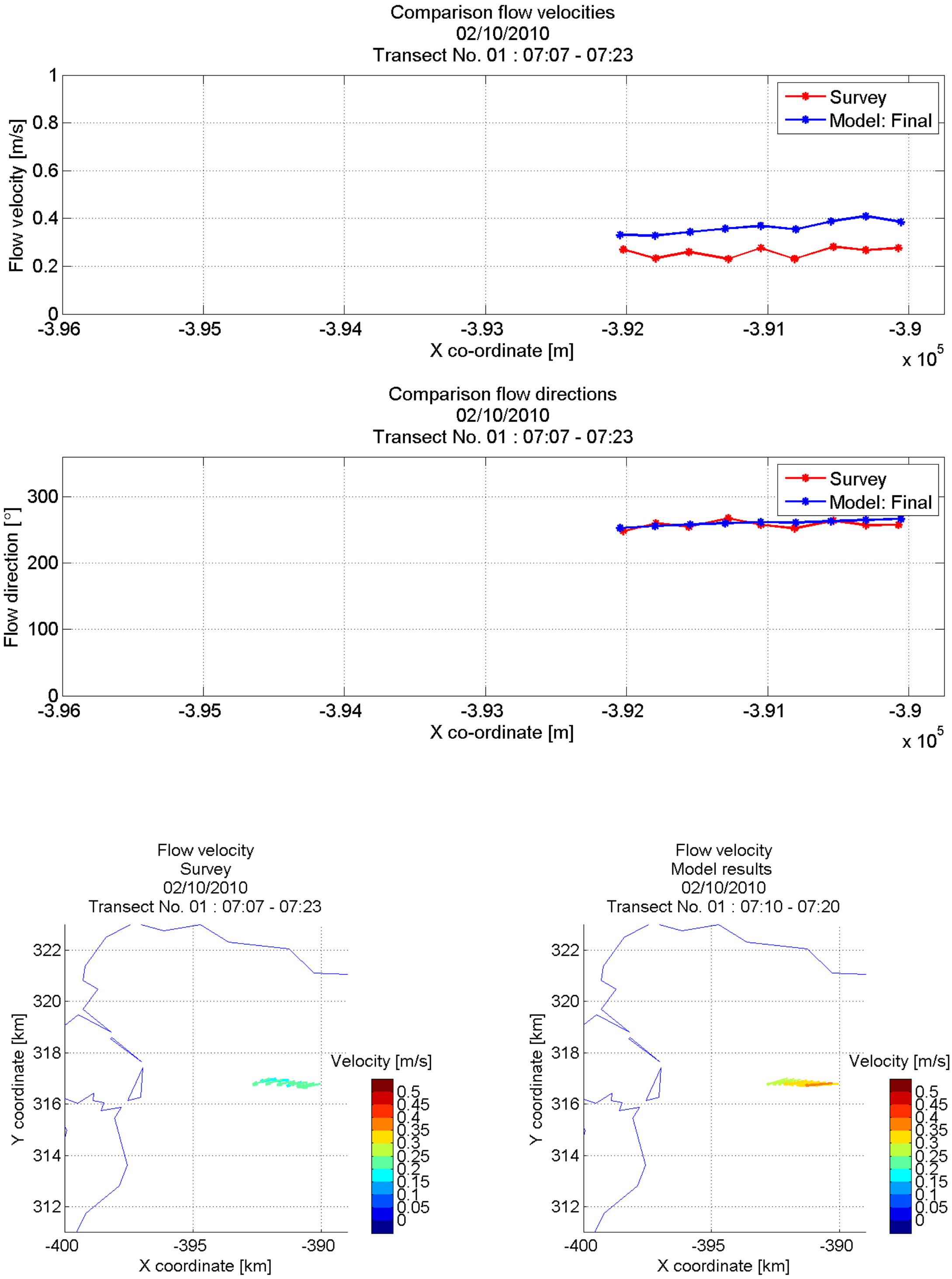

Figure E.35: Measured and modelled flow velocity and direction along transect B during ebb tide

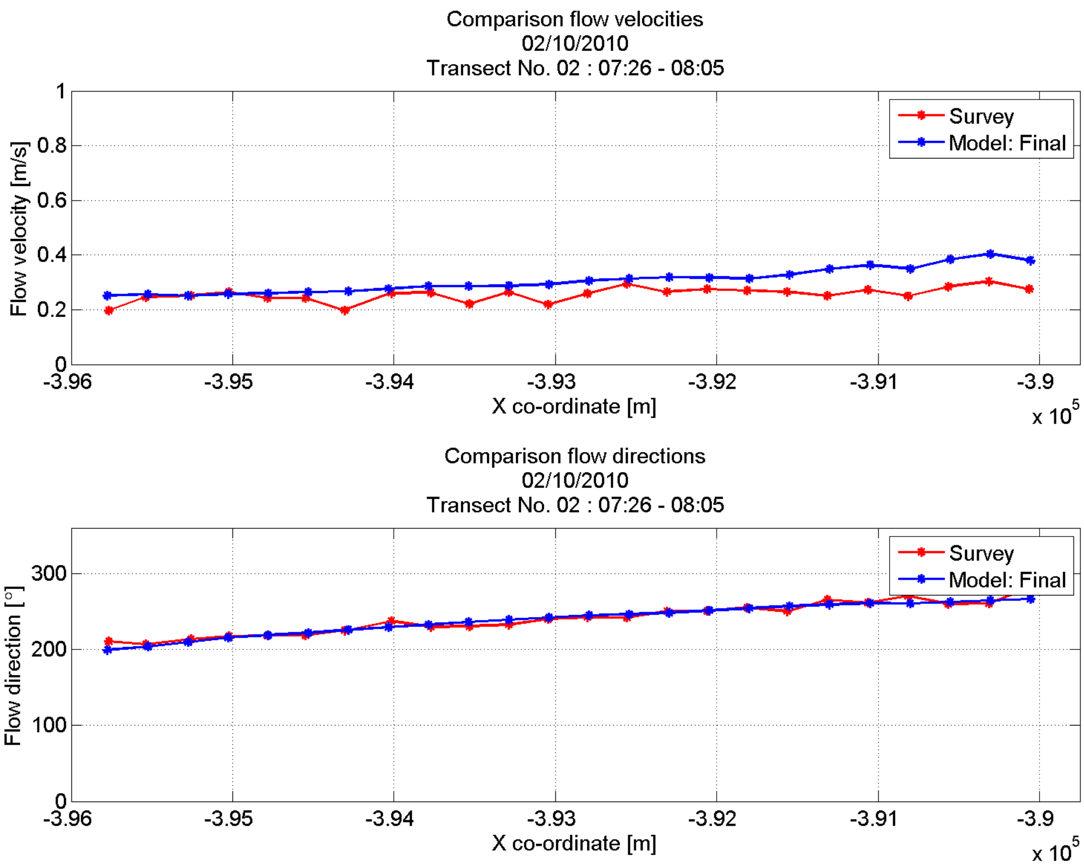

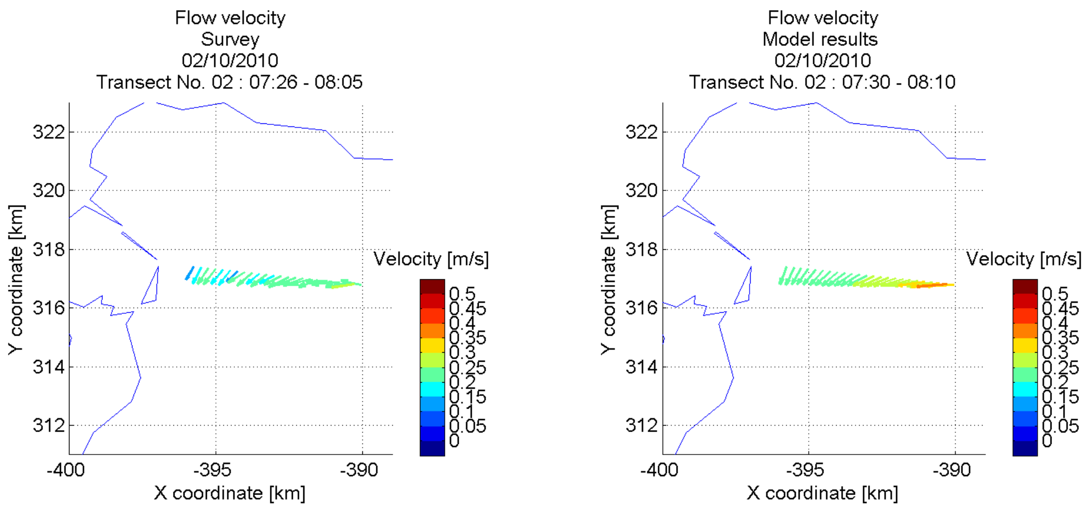

Figure E.36: Measured and modelled flow velocity and direction along transect B during ebb tide

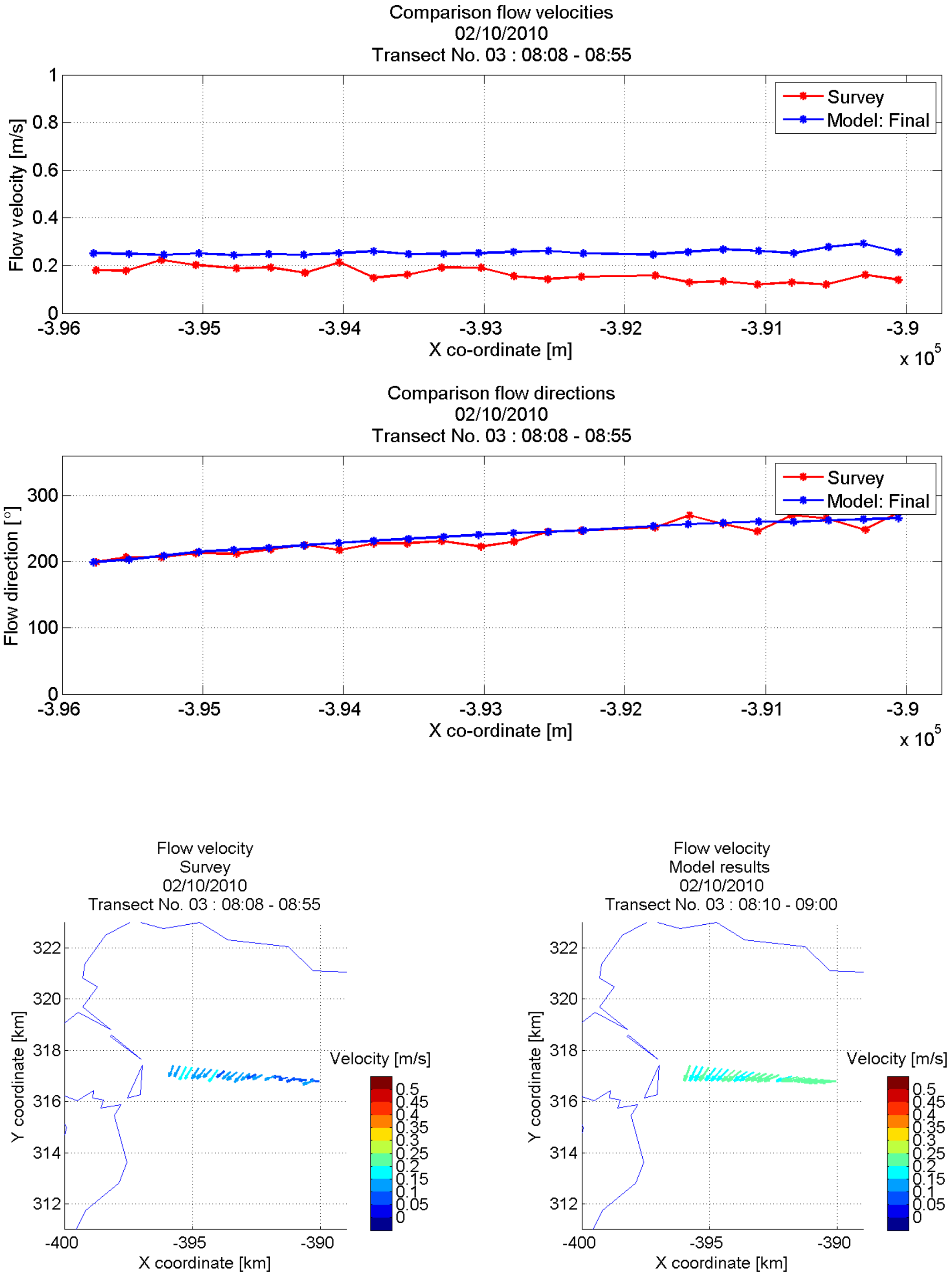

Figure E.37: Measured and modelled flow velocity and direction along transect B during ebb tide

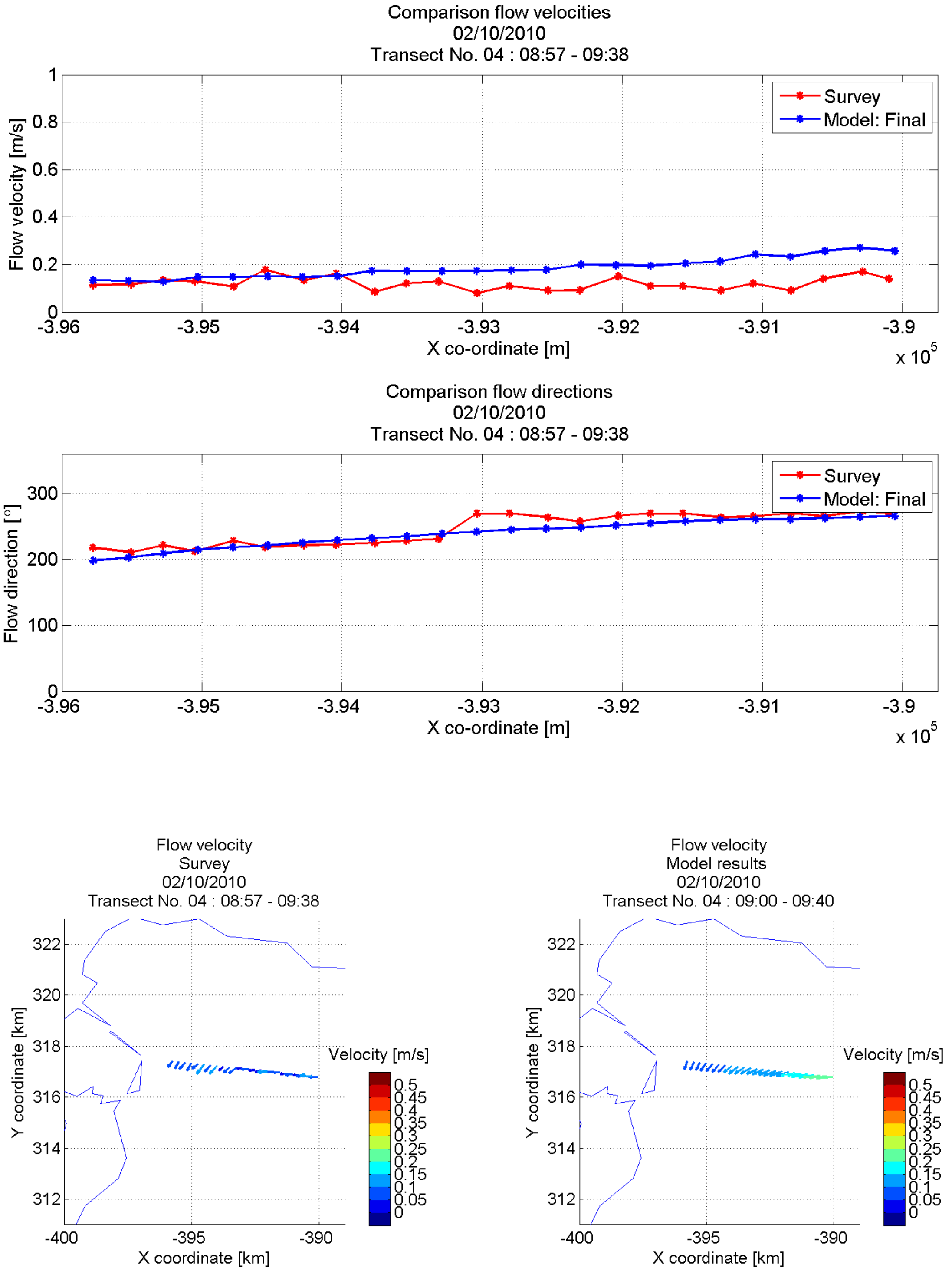

Figure E.38: Measured and modelled flow velocity and direction along transect B during ebb tide

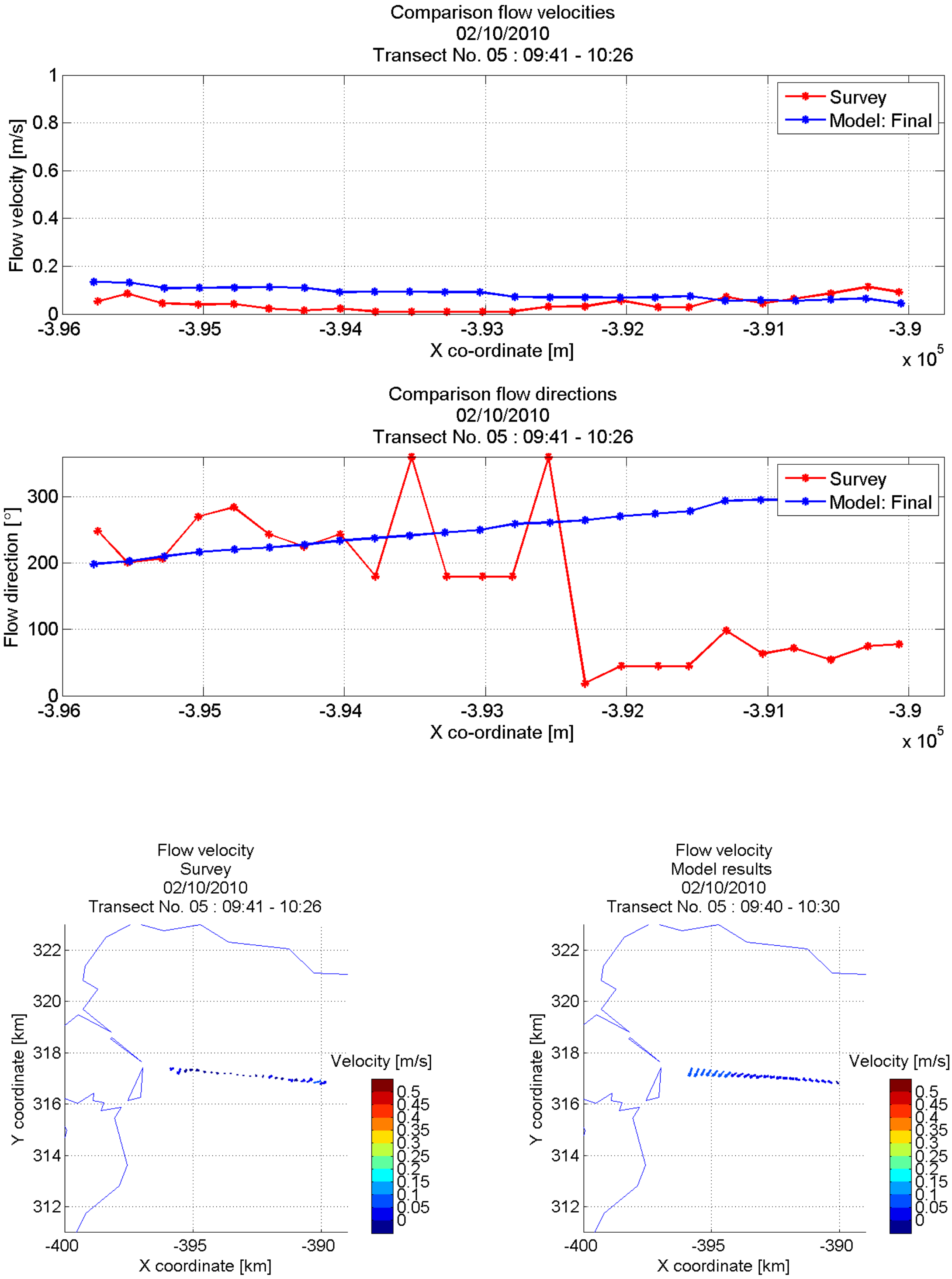

Figure E.39: Measured and modelled flow velocity and direction along transect B during slack tide

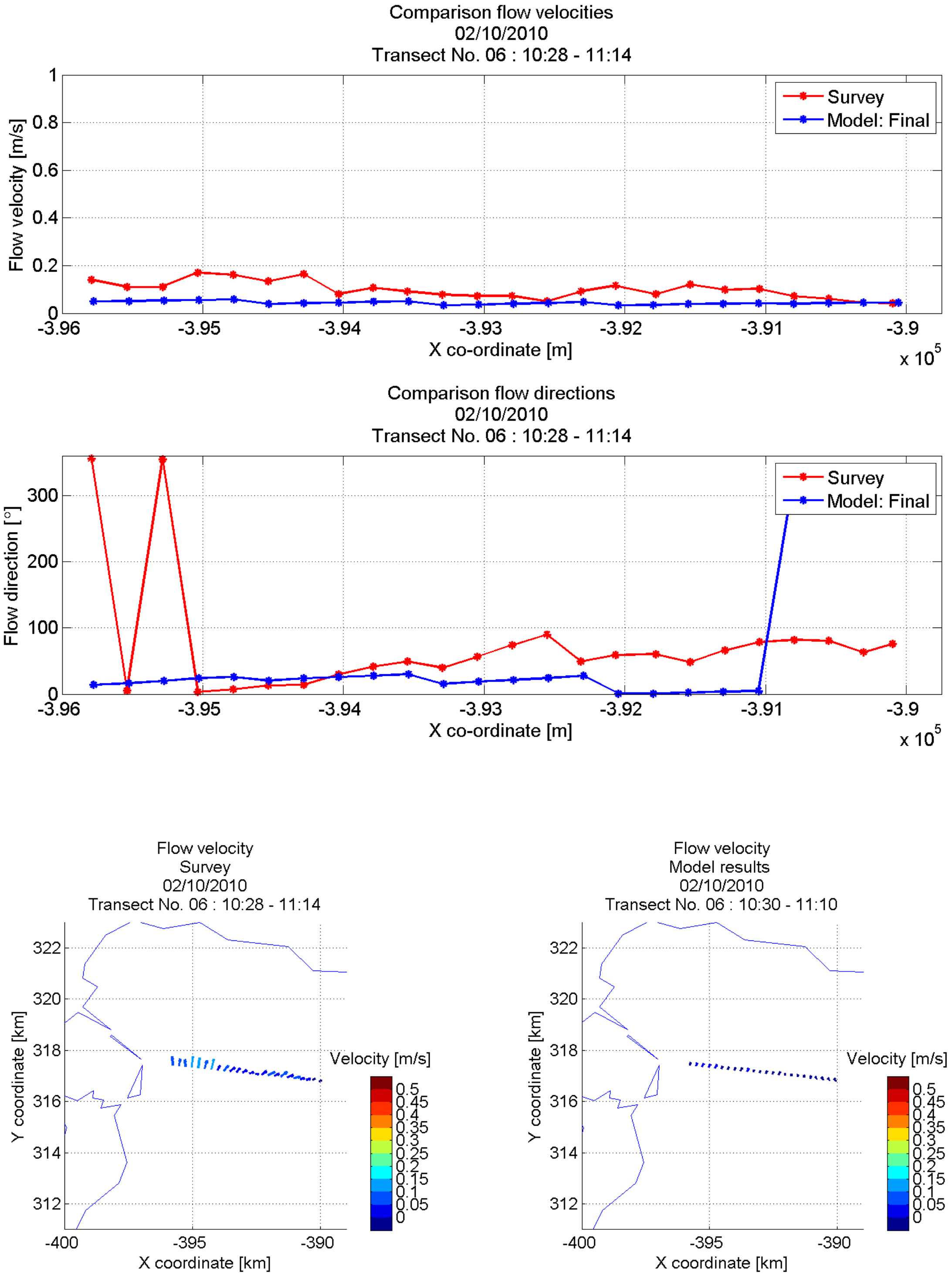

Figure E.40: Measured and modelled flow velocity and direction along transect B during flood tide

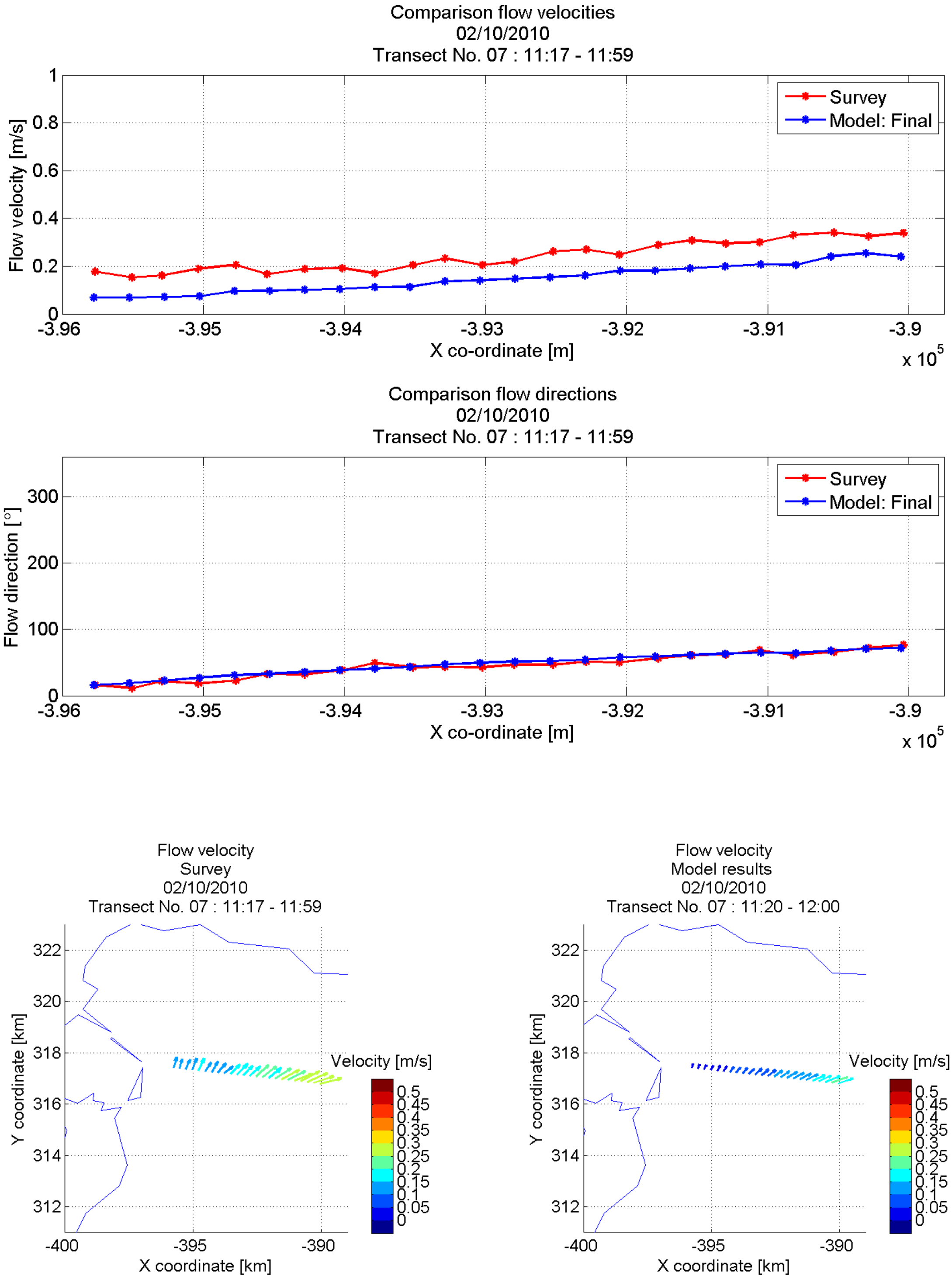

Figure E.41: Measured and modelled flow velocity and direction along transect B during flood tide

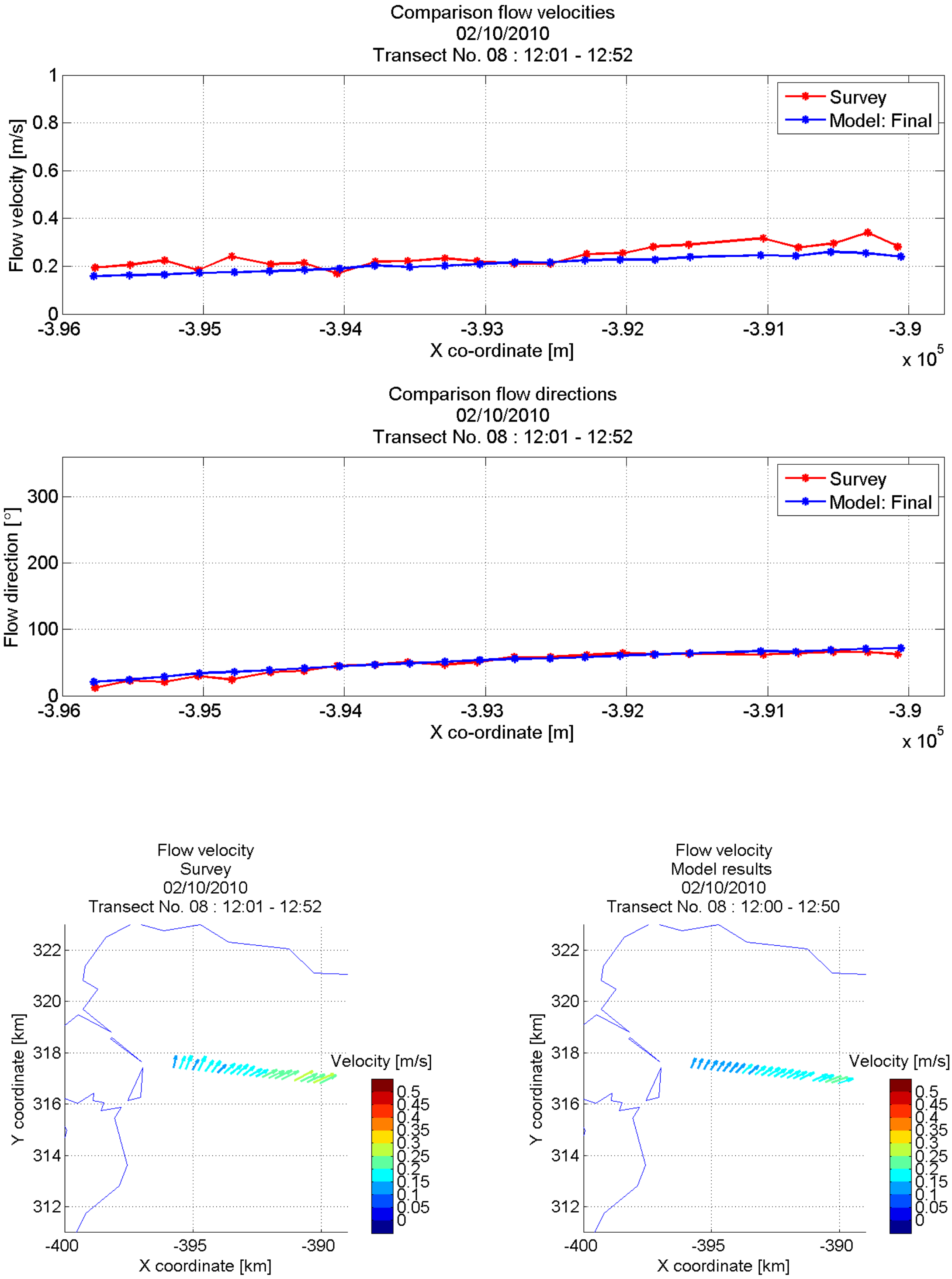

Figure E.42: Measured and modelled flow velocity and direction along transect B during flood tide

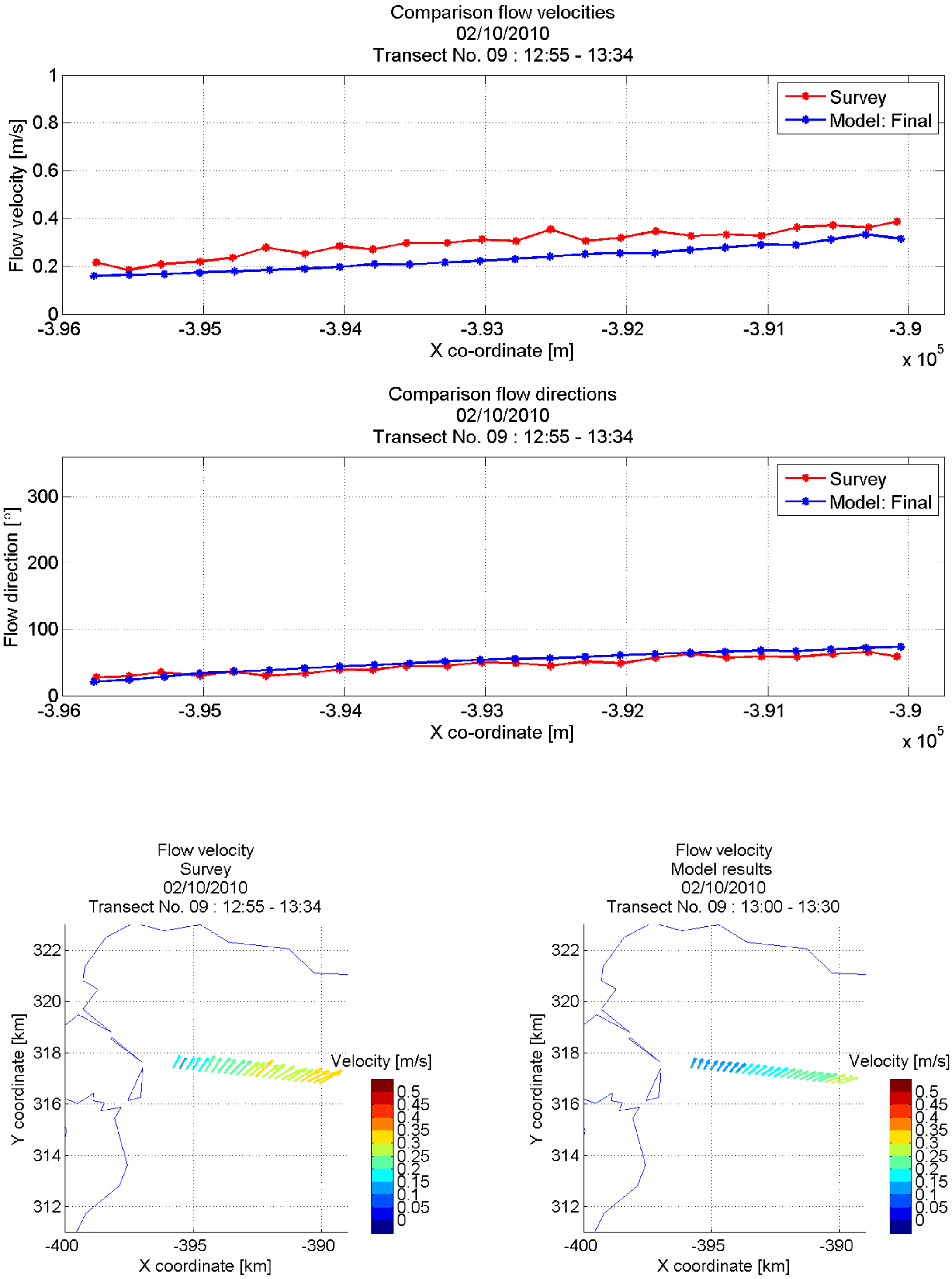

Figure E.43: Measured and modelled flow velocity and direction along transect B during flood tide

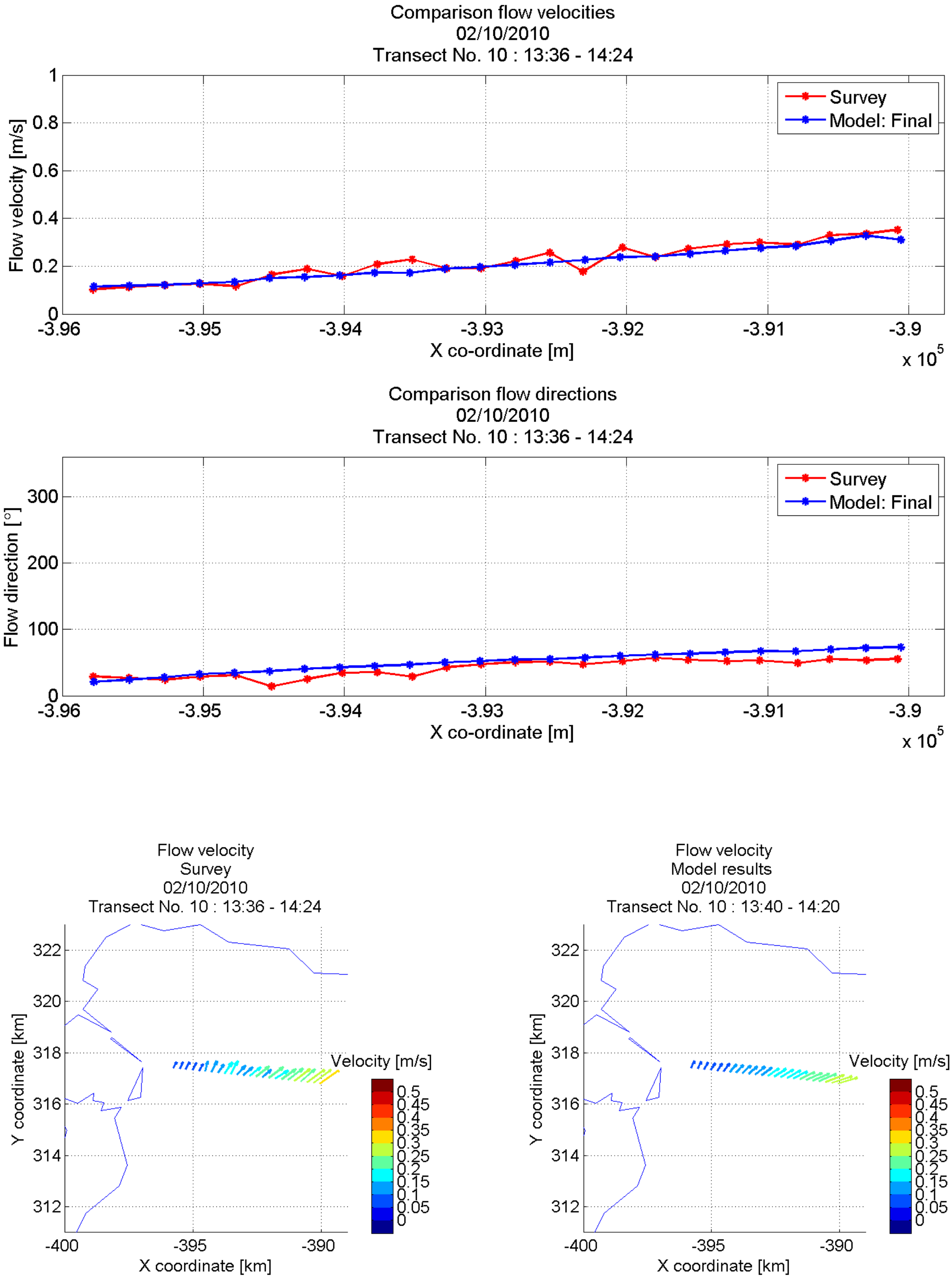

Figure E.44: Measured and modelled flow velocity and direction along transect B during flood tide

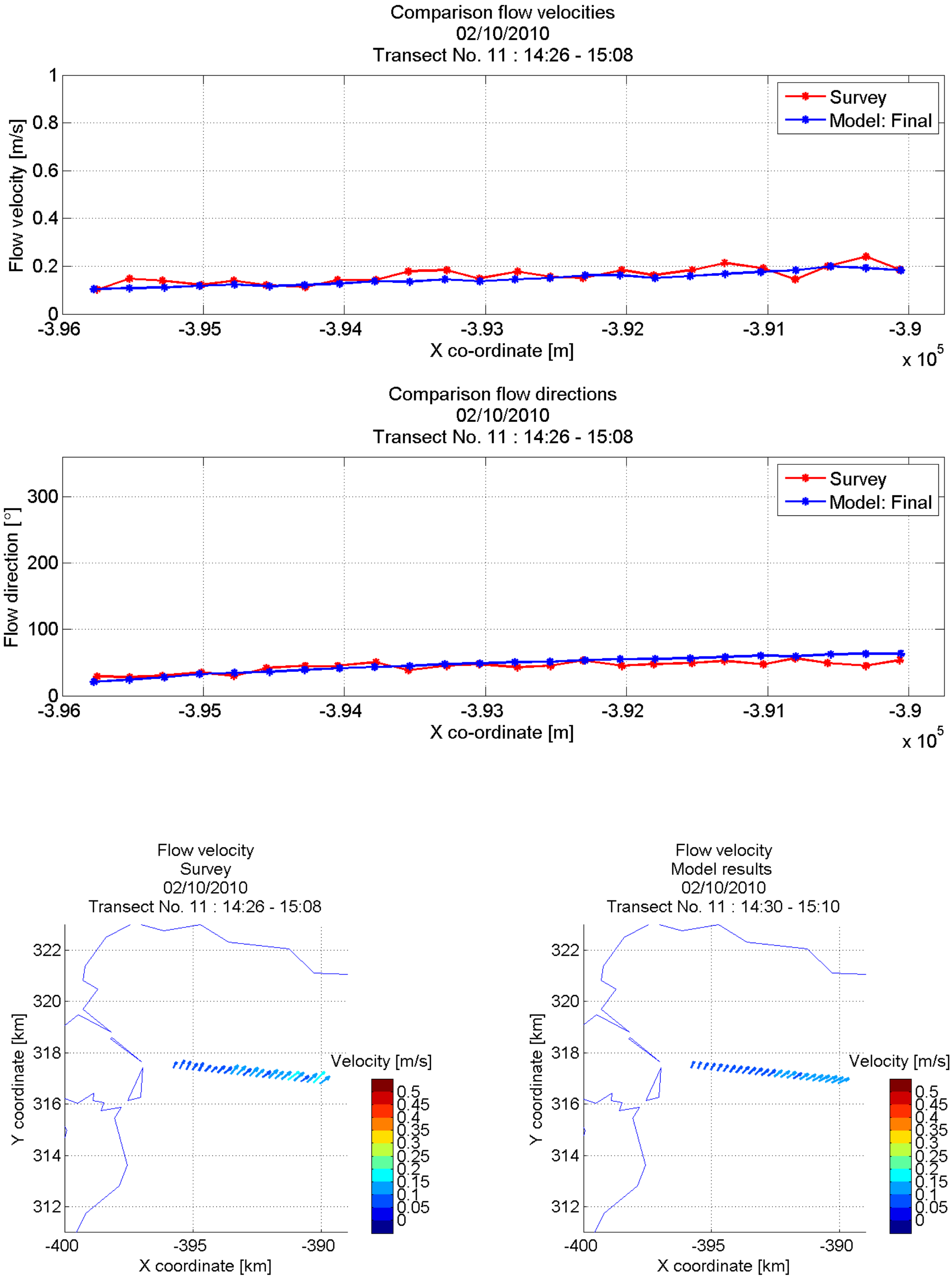

Figure E.45: Measured and modelled flow velocity and direction along transect B during flood tide

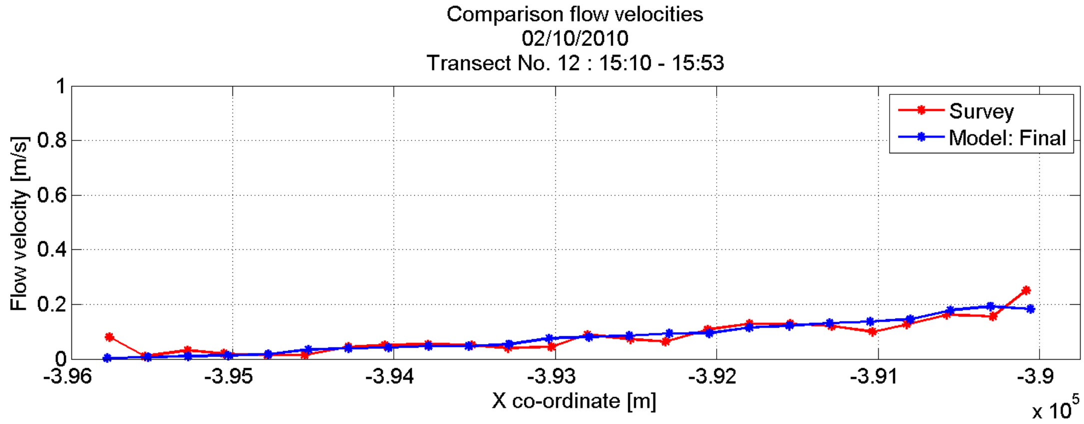

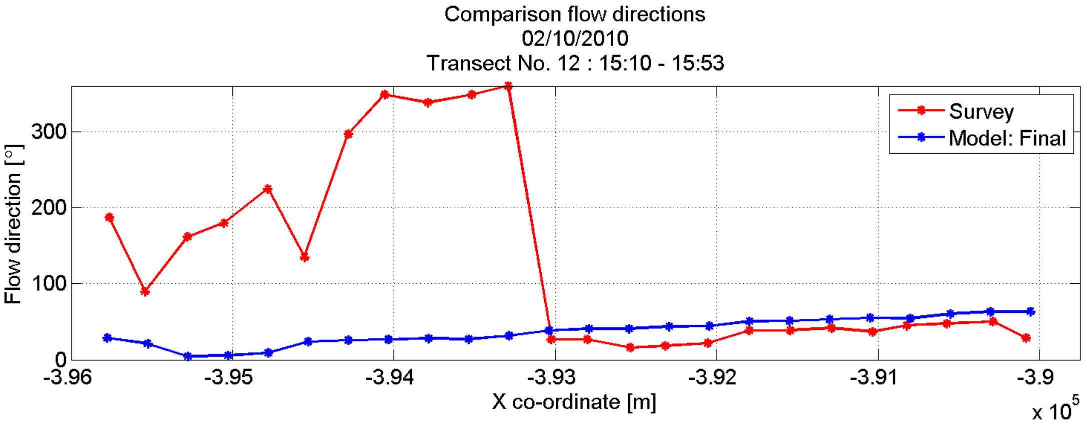

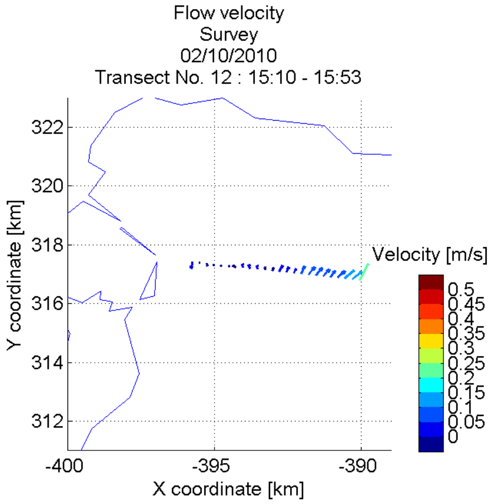

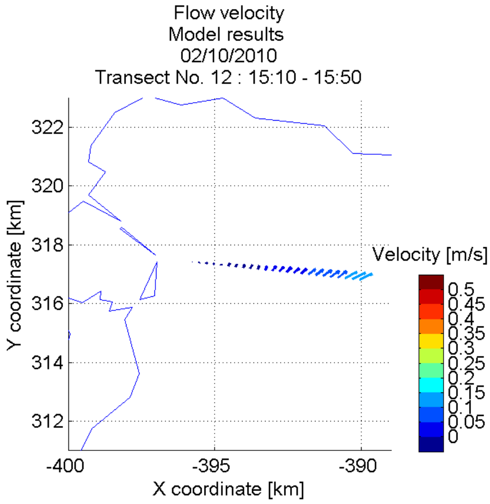

Figure E.46: Measured and modelled flow velocity and direction along transect B during slack tide

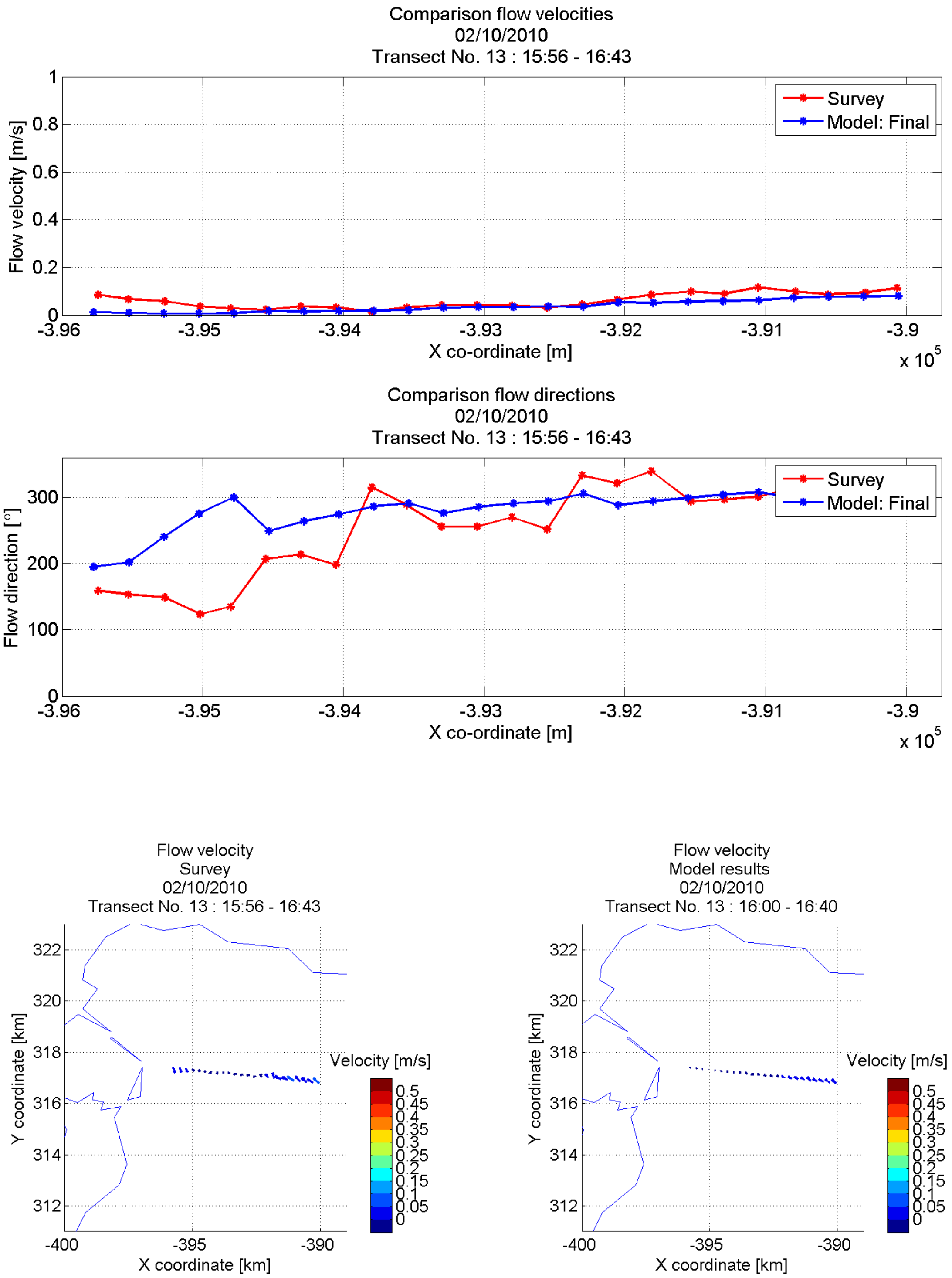

Figure E.47: Measured and modelled flow velocity and direction along transect B during ebb tide

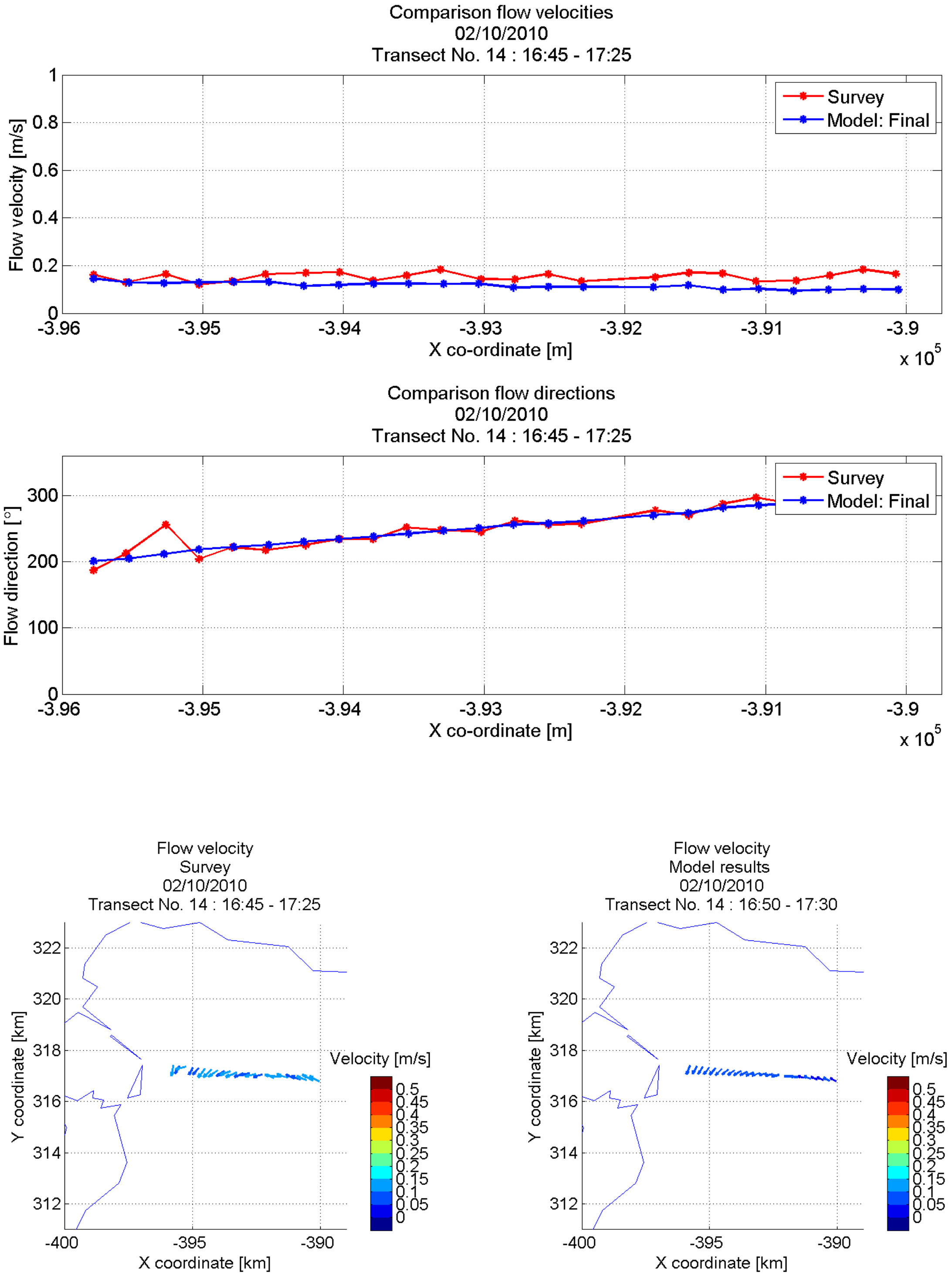

Figure E.48: Measured and modelled flow velocity and direction along transect B during ebb tide

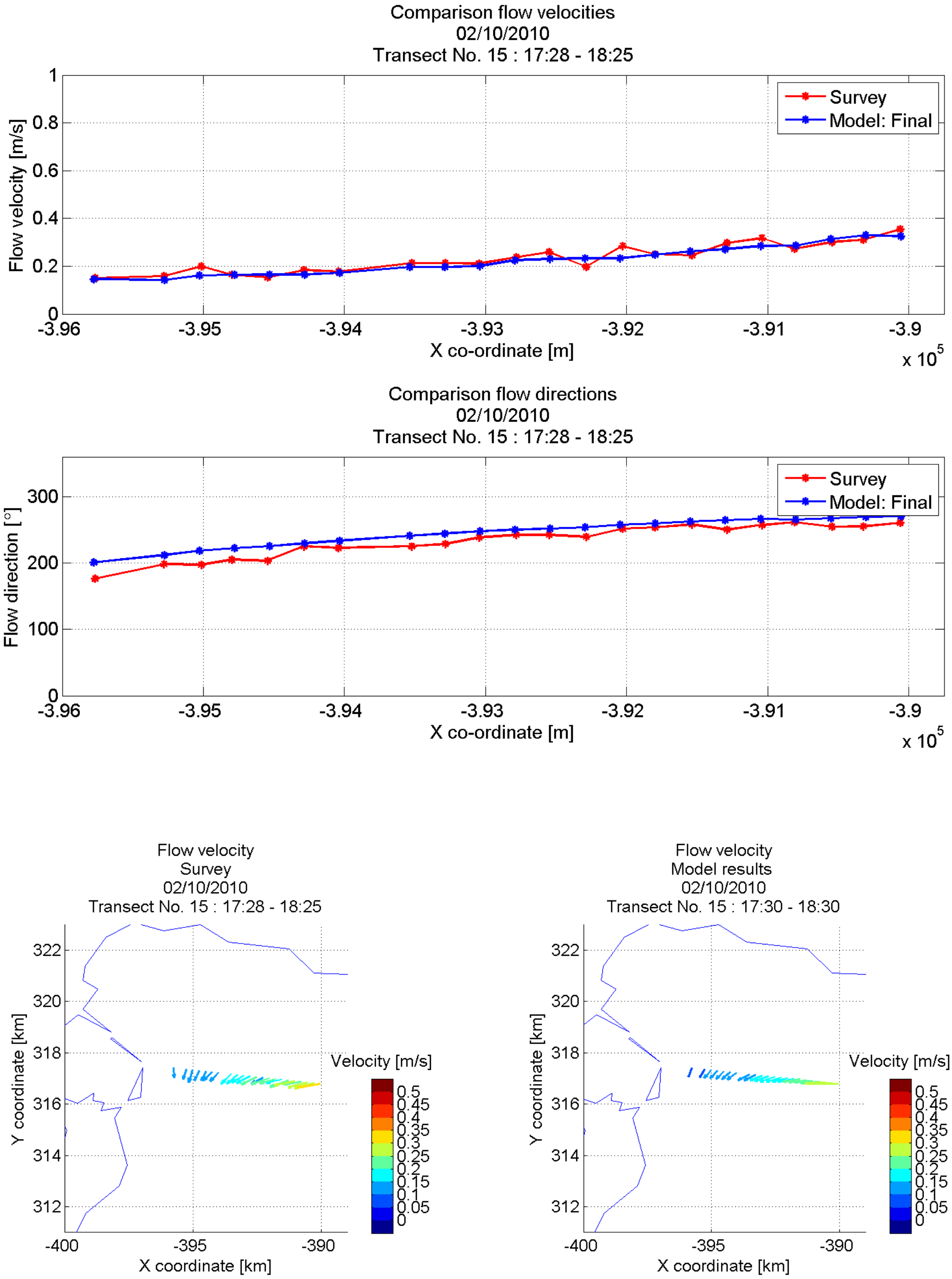

Figure E.49: Measured and modelled flow velocity and direction along transect B during ebb tide